

RICE UNIVERSITY

**One- and two-photon photoassociative  
spectroscopy using ultracold strontium**

by

**James Allen Aman**

A THESIS SUBMITTED  
IN PARTIAL FULFILLMENT OF THE  
REQUIREMENTS FOR THE DEGREE

**Doctor of Philosophy**

APPROVED, THESIS COMMITTEE:

---

Thomas C. Killian, Chair  
Professor of Physics and Astronomy

---

Randall G. Hulet  
Fayez Sarofim Professor of Physics and  
Astronomy

---

Kevin F. Kelly  
Associate Professor of Electrical and  
Computer Engineering

Houston, Texas

April, 2019

## ABSTRACT

One- and two-photon photoassociative spectroscopy using ultracold strontium

by

James Allen Aman

”Lorem ipsum dolor sit amet, consectetur adipiscing elit, sed do eiusmod tempor incididunt ut labore et dolore magna aliqua. Ut enim ad minim veniam, quis nostrud exercitation ullamco laboris nisi ut aliquip ex ea commodo consequat. Duis aute irure dolor in reprehenderit in voluptate velit esse cillum dolore eu fugiat nulla pariatur. Excepteur sint occaecat cupidatat non proident, sunt in culpa qui officia deserunt mollit anim id est laborum.”

## Acknowledgments

It is difficult to over state how much I have learned during my time in grad school. Not only pertaining to physics, engineering, and computer science but also about myself, my friends, and my communities.

I owe so much to Brian DeSalvo for being an inspiration. It was Brian who showed me my first Bose-Einstein condensate

I bugged him relentlessly as a naive undergraduate with so many questions.

# Contents

Abstract	ii
Acknowledgments	iii
List of Illustrations	ix
List of Tables	xiii
<b>1 Introduction</b>	<b>1</b>
1.1 Few-body physics . . . . .	1
1.2 Halo molecules . . . . .	2
1.3 Properties of strontium . . . . .	4
1.4 Thesis Outline . . . . .	4
<b>2 The Neutral apparatus</b>	<b>7</b>
2.1 Experimental procedure . . . . .	8
2.1.1 Characteristic performance . . . . .	12
2.2 Vacuum system and atom source . . . . .	15
2.3 Laser systems . . . . .	26
2.3.1 Wideband cooling stage: 461 nm . . . . .	26
2.3.1.1 Overview . . . . .	26
2.3.1.2 922 nm master . . . . .	30
2.3.1.3 Zeeman subsystem . . . . .	35
2.3.1.4 MOT subsystem . . . . .	36
2.3.2 Narrowband cooling stage: 689 nm . . . . .	44
2.3.2.1 Overview . . . . .	44
2.3.2.2 689 nm Master . . . . .	47

2.3.2.3	Neutral red system . . . . .	48
2.3.3	Optical dipole trap: 1064 nm . . . . .	54
2.3.3.1	Modeling the potential . . . . .	56
2.3.3.2	Trap frequency calibration . . . . .	61
2.3.4	Optical lattice trap: 532 nm . . . . .	67
2.3.4.1	Background . . . . .	67
2.3.4.2	Setup and alignment . . . . .	70
2.3.4.3	Measurement and results . . . . .	80
2.3.5	Optical toolbox . . . . .	86
2.3.5.1	Absorption imaging system . . . . .	86
2.3.5.2	Highly tunable 689 nm spectroscopy system . . . . .	91
2.3.5.3	Spin-manipulation laser with dynamic polarization control . . . . .	98
2.4	Apparatus interface . . . . .	100
2.4.1	Software . . . . .	100
2.4.2	Hardware control and measurement systems . . . . .	101
2.4.3	Ancillary laboratory systems . . . . .	105
2.4.3.1	MOT coils . . . . .	105
2.4.3.2	Trim coils . . . . .	105
2.4.3.3	Zero crossing AC line trigger . . . . .	107
2.4.3.4	Pneumatic actuated mirror mounts . . . . .	110

### **3 Photoassociation in ultracold gases** 113

3.1	Introduction . . . . .	113
3.2	Theoretical description of trapped boson gases . . . . .	115
3.2.1	Extracting data from column densities . . . . .	119
3.3	Characterizing collisions . . . . .	125
3.3.1	Classical . . . . .	126

3.3.2	Single channel scattering . . . . .	126
3.3.2.1	Low energy results . . . . .	127
3.3.3	Multichannel scattering . . . . .	129
3.4	Modeling of photoassociation lineshapes . . . . .	135
3.4.1	One-photon excitation of free to bound transitions . . . . .	136
3.4.1.1	PAS near narrow intercombination transitions . . . . .	136
3.4.2	Extension to two-color spectra . . . . .	137
<b>4</b>	<b>Strongly coupled PAS of a weakly bound molecule</b>	<b>140</b>
4.1	Probing the ground state potential . . . . .	140
4.2	Experimental setup . . . . .	141
4.3	Estimating the halo binding energy . . . . .	148
4.3.1	Frequency dependence of the AC Stark shift . . . . .	149
4.4	Multi-photon loss processes . . . . .	153
<b>5</b>	<b>Binding energy of the <math>^{86}\text{Sr}_2</math> halo molecule</b>	<b>154</b>
5.1	Experimental setup . . . . .	155
5.2	Modeling the PA spectra . . . . .	158
5.2.1	Consideration of the trap depth . . . . .	158
5.2.2	Fitting the trap-averaged thermal lineshape . . . . .	160
5.3	Determination of energy shifts . . . . .	166
5.3.1	AC Stark shift due to excitation lasers . . . . .	166
5.3.2	Density-dependent frequency shift . . . . .	170
5.3.3	AC Stark Shift due to Trapping Lasers . . . . .	172
5.4	Discussion of the halo binding energy . . . . .	174
5.4.1	Calculating the $\text{X}^1\Sigma_g^+$ $\text{C}_6$ coefficient . . . . .	178
<b>6</b>	<b>Progress towards studies of quantum magnetism</b>	<b>183</b>
6.1	Spin manipulation of $^{87}\text{Sr}$ . . . . .	183

6.2 Search for narrowline PA molecules using various spin mixtures . . . . .	186
<b>7 Conclusion</b>	<b>187</b>
<b>Bibliography</b>	<b>189</b>
<b>Appendices</b>	<b>202</b>
<b>A Two-particle momentum probability distribution</b>	<b>203</b>
A.1 Standard form . . . . .	203
A.2 Truncated form . . . . .	204
<b>B Imagefit analysis routine</b>	<b>209</b>
B.1 Background removal . . . . .	209
B.1.1 Principal component analysis . . . . .	209
B.1.2 Comparison of PCA implementations . . . . .	211
B.2 Fitting the spatial distribution . . . . .	211
B.3 Evaluating fit parameters . . . . .	211
B.3.1 Writing new plug-ins . . . . .	211
B.3.2 Suggested improvement . . . . .	211
<b>C neuKLEIN - Killian lab experimental interface</b>	<b>213</b>
C.1 Labview code . . . . .	213
C.2 FPGA code . . . . .	213
C.3 Possible improvements . . . . .	214
<b>D Experimental control computer hardware</b>	<b>216</b>
D.1 Overview of status . . . . .	216
D.2 Migration to a new machine . . . . .	216
D.3 PixelFly camera system . . . . .	216

<b>E Neutral apparatus</b>	<b>217</b>
E.1 Opening vacuum - data and process . . . . .	217
E.2 Nozzle redesign - neuNozzle 2018 . . . . .	217
<b>F Gaussian Beam Programs</b>	<b>220</b>
F.1 Simple beam propagation . . . . .	220
F.2 Laser beam profile fitting . . . . .	220
F.2.1 Data taking template . . . . .	220
<b>G Concise derivation of effective volumes</b>	<b>221</b>
<b>H Repair of 922 Lynx master</b>	<b>222</b>
<b>I Doppler Free Spectroscopy</b>	<b>228</b>
I.1 Common setup . . . . .	228
I.2 Addition of Zeeman shift . . . . .	230
<b>J Bose-Hubbard model</b>	<b>231</b>
<b>K Shallow angle Bragg setup</b>	<b>234</b>

# Illustrations

1.1 Properties of strontium. Left: Natural abundances and s-wave scattering lengths for all mixtures of Sr. Right: Simplified energy level diagram of Sr showing the relevant states used for trapping and cooling of the atomic gas . . . . .	4
1.2 Partial energy level diagram of strontium . . . . .	5
1.3 Properties of strontium . . . . .	6
2.1 Neutral apparatus vacuum system . . . . .	16
2.2 Source assembly - side view . . . . .	17
2.3 Source assembly - rear view . . . . .	17
2.4 2D collimator assembly . . . . .	18
2.5 Cryo tower assembly . . . . .	18
2.6 Typical fluorescence of Zeeman beam looking down 2D collimator . .	22
2.7 Atom oven and nozzle construction . . . . .	24
2.8 Ablating strontium coating from window . . . . .	26
2.9 461 nm light generation system . . . . .	28
2.10 922 nm master optical schematic . . . . .	31
2.11 922 nm doubling cavity length stabilization feedback diagram . . . .	32
2.12 922 nm frequency stabilization block diagram . . . . .	33
2.13 Zeeman subsystem optical schematic . . . . .	35
2.14 MOT subsystem optical schematic . . . . .	37
2.15 461 nm MOT schematic . . . . .	40

2.16	461 nm saturated absorption setup	41
2.17	689 nm light generation system	45
2.18	689 nm master system	49
2.19	Neutral 689 nm trapping and cooling setup	50
2.20	1064 nm optical dipole trap schematic	55
2.21	Two-level avoided crossing	57
2.22	Modeling an optical dipole potential	60
2.23	Example center-of-mass oscillations	62
2.24	1D band structure as a function of lattice depth	69
2.25	Lattice optical schematic	73
2.26	Lattice Arm A profile	74
2.27	Lattice Arm B profile	74
2.28	Lattice Arm C profile	75
2.29	Center-of-mass amplitude suppression when overlapping traps	77
2.30	Observation of breathing mode oscillation	78
2.31	Evolution of plane wave population using Kapitza-Dirac	81
2.32	Oscillation period between $n = 0 \rightarrow n = 2$ band at $q = 0$	82
2.33	Lattice depth calibration	82
2.34	Characterization of heating in the optical lattice	85
2.35	Absorption imaging and blow away pulser optical schematic	87
2.36	Timing diagram of PixelFly doubleshutter mode	88
2.37	Comparison of background subtraction methods	91
2.38	Optical schematic: 689 spectroscopy laser	92
2.39	Infinite sample and holding timing diagram	94
2.40	Characterization of the OPLL performance	97
2.41	Zeroing residual magnetic fields	106
2.42	Circuit diagram of the zero crossing AC line trigger	108
2.43	Comparison of pulseblaster timing jitter	109

2.44 Pneumatic actuators diagram . . . . .	111
3.1 Ballistic expansion of particles . . . . .	120
3.2 Strontium interatomic wavefunctions . . . . .	129
3.3 Schematic representation of a Feshbach resonance . . . . .	131
4.1 Strontium PAS potential . . . . .	142
4.2 Schematic of PAS light generation . . . . .	145
4.3 Histogram of PAS beam intensity variation . . . . .	147
4.4 Characteristic view of the PA beatnote . . . . .	148
4.5 Estimate of bound-bound coupling via isolated resonance model . . . . .	152
5.1 Strontium two-photon photoassociation . . . . .	157
5.2 PAS laser setup . . . . .	159
5.3 Variation of 1064 nm trap depth . . . . .	167
5.4 Variation of 689 nm excitation . . . . .	168
5.5 Fit of 689 nm AC Stark shift . . . . .	169
5.6 Measurement of halo state susceptibility, $\chi_{1064}$ . . . . .	173
5.7 Determination of 86 scattering length . . . . .	176
5.8 Variation of halo susceptibility as a function of $\Delta_1$ . . . . .	177
6.1 $^{87}\text{Sr } ^1S_0 \rightarrow ^3P_1$ hyperfine structure . . . . .	185
H.1 Damaged 922 master PZT . . . . .	223
H.2 Removing the circuit board of the 922 master . . . . .	224
H.3 Reference image of the spring terminal connections . . . . .	225
H.4 Newly installed 922 master PZT . . . . .	226

J.1 Calculated interaction energies and tunneling rates for each isotope of strontium . . . . .	232
---	-----

## Tables

2.1	Sample trapping performance of $^{84}\text{Sr}$	13
2.2	Sample trapping performance of $^{86}\text{Sr}$	13
2.3	Sample trapping performance of $^{88}\text{Sr}$	14
2.4	Example trapping performance of $^{87}\text{Sr}$	14
2.5	461 nm system AOM details	29
2.6	689 nm system AOM details	46
2.7	Lattice optics details	72
2.8	Arbitrary waveform generation details	102

# Chapter 1

## Introduction

The ability to engineer and manipulate quantum states lies at the heart of modern atomic physics experiments using ultracold gases [12, 46, 54? ? ? ]. Two important tools for this pursuit are Feshbach resonances [15, 45] and optical lattices [? ]. This proposal will detail our recent work building and characterizing a three-dimension optical lattice for use with ultracold and quantum degenerate gases of neutral strontium. Furthermore, we will present the first experiment we hope to pursue with the optical lattice; the creation of Feshbach molecules using an optical Feshbach resonance. We will also briefly discuss other future plans such as the production of highly excited ground state  $\text{Sr}_2$  dimers through adiabatic internal state transfer.

Should probably mention somewhere that this is long-range PA, in contrast to short-range stuff being explored now.

Julienne form of the corss section 6.16 in CM. Discuss how important the phase space density is, the timescale for interactions, and the complex

[32]

### 1.1 Few-body physics

field of photoassociation in ultracold gases, wherein studies of molecular structure have revealed the most accurate descriptions of atomic interactions and have become

a fundamental probe of the ultracold toolbox [41].

## 1.2 Halo molecules

Mostly studied in helium

Comes from bound state of the dirac potential. Unsure how much detail I want right here

Check out CM Juleinne pg 229. He has a ref

Weakly bound ground-state dimers are of great interest in ultracold atomic and molecular physics.

In the extreme case of a scattering resonance, the least-bound state represents an example of a quantum halo system [39] with spatial extent well into the classically forbidden region.

Halo molecules show universality, meaning that molecular properties such as size and binding energy can be parameterized by a single quantity, the *s*-wave scattering length  $a$ , independent of other details of the atom-pair interaction [10? ].

For potentials that asymptote to a van-der-Waals form, an additional parameter, the van der Waals length  $l_{\text{vdW}}$ , can be introduced for a more accurate description.

Efimov trimers also exist in systems near a scattering resonance, influencing dimer and atomic scattering properties and introducing additional universal phenomena [11, 61].

Ultracold halo molecules are often associated with magnetic Feshbach resonances [? ], for which the scattering state and a bound molecular state can be brought near resonance by tuning a magnetic field.

This is a naturally occurring halo molecule, meaning it exists in the absence of tuning with a magnetic Feshbach resonance. A well-known example of a naturally occurring halo molecule is the  ${}^4\text{He}_2$  dimer [49, 69? ]. Moreover, the least-bound vibrational level of the ground state of  ${}^{40}\text{Ca}_2$ , which was recently studied using similar methods [63], is similarly related to this regime.

There are important differences between halo molecules associated with magnetic Feshbach resonances and the naturally occurring halo molecule in  ${}^{86}\text{Sr}$ . With magnetic Feshbach resonances, the relevant scattering and bound molecular states lie on different molecular potentials, and single-photon magnetic-dipole transitions can be used to measure molecular binding energies with RF or microwave spectroscopy [16? ? ]. Typically, this is done by first forming molecules through magneto-association and then driving bound-free or bound-bound transitions converting the halo molecule into a different state. Other methods include spectroscopy with an oscillating magnetic field [? ], a modulated optically controlled Feshbach resonance [20], and Ramsey-type measurements of atom-molecule oscillation frequencies [21]. It is also possible to efficiently populate halo states with a magnetic-field sweep [29] or evaporative cooling [40] near a magnetic Feshbach resonance [? ]. These are powerful techniques for manipulating quantum gases of alkali metals and other open-shell atoms, for which there are many magnetic Feshbach resonances. Strontium, however, due to its closed-shell electronic structure, lacks magnetic Feshbach resonances in the electronic ground state.

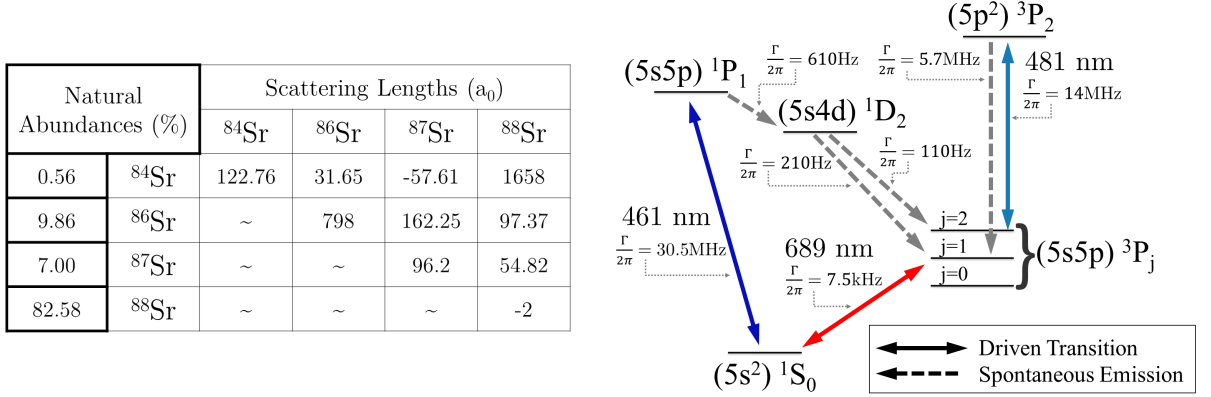


Figure 1.1 : Properties of strontium. Left: Natural abundances and s-wave scattering lengths for all mixtures of Sr. Right: Simplified energy level diagram of Sr showing the relevant states used for trapping and cooling of the atomic gas

### 1.3 Properties of strontium

The experiments in this proposal will be realized using an ultracold gas of atomic strontium. Fig. 1.3 shows all of the stable isotopes of strontium, their natural abundance, as well as their inter-particle scattering lengths. The isotopic differences in strontium have important implications for their use in certain experiments. For example, none of the bosonic isotopes of strontium ( $^{88}\text{Sr}$ ,  $^{86}\text{Sr}$ , or  $^{84}\text{Sr}$ ) display hyperfine structure since they have no nuclear spin,  $\mathbf{I} = 0$ . However, the fermionic isotope  $^{87}\text{Sr}$  has a large nuclear spin,  $\mathbf{I} = 9/2$ , which makes it an ideal candidate for exploring exotic phases of quantum magnetism [5, 14? ]. In the studies presented in this proposal, we are sensitive to the isotopic shifts of the bosonic photoassociation lines along the  $^1S_0 \rightarrow ^3P_1$  transition as well as the various interspecies scattering lengths.

### 1.4 Thesis Outline

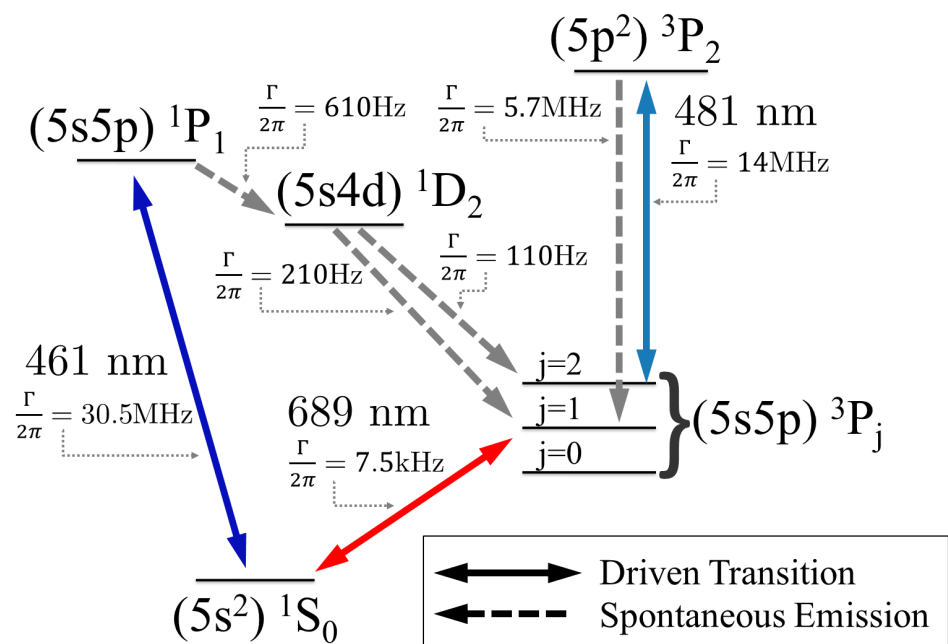


Figure 1.2 : Partial energy level diagram of strontium

Shown are the relevant transitions and decay rates utilized to perform laser cooling and spectroscopy.

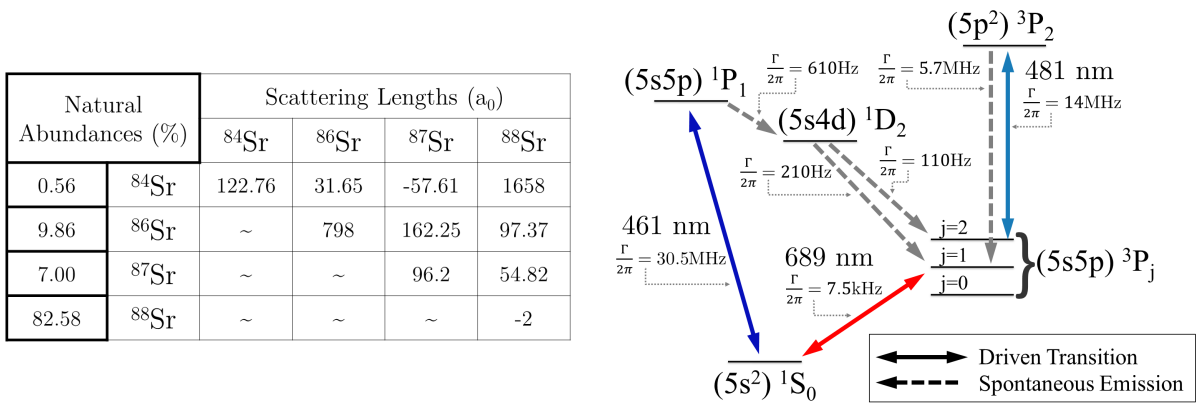


Figure 1.3 : Properties of strontium

Properties of strontium. Left: Natural abundances and s-wave scattering lengths for all mixtures of Sr. Right: Simplified energy level diagram of Sr showing the relevant states used for trapping and cooling of the atomic gas

## Chapter 2

### The Neutral apparatus

The Neutral apparatus has been one of the pioneering experiments for the trapping, cooling, and creation of quantum degenerate gases of neutral strontium BEC refs. As such, there is a plethora of previous theses and publications which extensively outline the details for how to achieve these goals. refs. In particular, we refer the reader to the PhD theses of previous Killian lab students: Francisco Camargo, Brian DeSalvo, Mi Yan, Pascal Mickelson, Natali Martinez de Escobar, and Sarah Nagel. Additionally, the PhD work of Simon Stellmer [71] and review of strontium quantum degenerate gases are also highly recommended reading [72].

Building upon this previous work, this chapter will forego an extensive review of the basic laser cooling techniques for strontium. We refer the reading to the works listed above for a formal discussion of the theory behind laser cooling and trapping. Instead, we will focus on the systems and processes which are crucial to the operation of the experiment with an emphasis on technical findings and changes which remain, as of yet, mostly undocumented.

Furthermore, it has been nearly a decade since the last broad apparatus overview [52] and the experiment has grown significantly in complexity in the intervening years. Therefore, the goal of this chapter is to serve as a reference for future work and students. In this spirit, this chapter will be highly technical and provide an in-depth review of the operation and current status of the Neutral apparatus. Where

appropriate we will refer the reader to the relevant original thesis or published work.

We will begin with a brief overview of our trapping procedure in order to contextualize the remaining sections focusing on the hardware including the vacuum system, various laser systems, and experimental control software, hardware, and electronics.

## 2.1 Experimental procedure

Our experiments begin by cooling and trapping atomic strontium utilizing well-established atomic physics techniques [7, 22, 35, 37, 42, 48, 51, 58, 60, 73, 74, 78]. Fig. 1.2 shows the simplified energy level diagram employed in our cooling process. Once cooled, we typically obtain bulk samples in an optical dipole trap containing on the order of  $10^6$  atoms at temperatures  $< 1\mu\text{K}$  and densities between  $10^{12} - 10^{15} \text{ cm}^{-3}$  depending upon the isotope.

The procedure outlined below is generally followed for trapping all isotopes of strontium with the major difference being timescales and laser frequencies. Trapping of the bosonic isotopes of strontium is nearly identical across isotopes while fermionic  $^{87}\text{Sr}$  presents a greater challenge due to its high nuclear spin,  $I = 9/2$ . For a thorough and detailed discussion of the relevant physics of trapping  $^{87}\text{Sr}$  in the red MOT, we refer the interested reader to the fermion portion of section 2.7.3 in the PhD thesis of Simon Stellmer [71] and section 2.2.1 of Pascal Mikelson's PhD thesis [57]. In short, due to the change in spin between the singlet and triplet series, there is a mismatch in the Zeeman shifts of the  $^1S_0$  and  $^3P_1$  states which results in anti-trapped edge states causing atoms to be expelled from the MOT laser acting on the  $^1S_0 (F = 9/2) \rightarrow ^3P_1 (F = 11/2)$  transition. The complication can be overcome by

adding an additional laser addressing the  $^1S_0 (F = 9/2) \rightarrow ^3P_1 (F = 9/2)$  transition to randomize the  $m_F$  populations in the  $^1S_0$  ground state.

---

The trapping process begins with vaporizing metallic strontium loaded in an oven heated to approximately 400 °C. This strontium vapor escapes through thin collimating tubes to produce a partially collimated beam with a mean velocity of  $\sim$ 450 m/s. To aid in collimation, the atoms undergo a stage of transverse two dimensional optical molasses which is elongated and retro-reflected. This helps increase the atom flux into the Zeeman slowing stage and we typically observe an approx. 7x improvement in trapped atom number with the 2D collimator versus without. The majority of cooling is done using 461 nm light acting on the strongest dipole allowed transition between the  $^1S_0 \rightarrow ^1P_1$  states. The excited state lifetime of 5 ns ( $\Gamma = 30.5$  MHz) and large energy separation between the states results in a hefty saturation intensity of 40.5 mW/cm<sup>2</sup> for this transition. Therefore laser powers on the order of 100 mW are necessary to produce large optical forces and rapid cooling rates.

Upon entering the magnetic field of the Zeeman slower, the highest velocity atoms begin to scatter photons from the Zeeman beam red detuned by approx. 16x the natural linewidth. Large detunings help to eliminate unwanted photon scattering from the Zeeman beam once atoms have been sufficiently cooled and are accumulating

in the MOT fields of the science chamber\*. After reducing the atoms velocity down to approx. 30 m/s, the atoms exit the Zeeman slower and are captured in a 461 nm magneto-optical trap (MOT) also using the  $^1S_0 \rightarrow ^1P_1$  transition. Typically the MOT operates at a detuning of approximately  $-3\Gamma/2 \approx -45$  MHz, however, the optimal trapping frequency is slightly varied for each isotope using our tunable sat. abs described in Sec. 2.3.1.4.

MOT operation along the broad dipole allowed  $^1S_0 \rightarrow ^1P_1$  transition comes with the significant drawback that the Doppler temperature is relatively high at  $T_D \approx 1$  mK and the number of trapped atoms saturates quickly. Fortunately, this transition is not completely closed as shown in Fig. 1.2. The leak to the  $^3P_2$  state results in population of magnetically trappable low-field seeking  $m_j$  states. These atoms are trapped by the anti-Helmholtz field of the MOT and are dark to the 461 nm light [natali refs (I think) [78, 79, 80, 65]. This allows us to take advantage of the long lifetime of the metastable  $^3P_2$  state and accumulate a large number of atoms which can then be repumped back down to the  $^1S_0$  ground state. The lifetime of the magnetic trap is typically limited by background pressure (approx. 15 - 25s) and therefore the maximum number of atoms which can be held by the magnetic trap is much greater than in the MOT. On average, an atom will fall into the  $^3P_2$  state after scattering  $10^5$  photons from

---

\*While the functioning of a Zeeman slower only relies on the magnitude of the B-field, the anti-Helmholtz MOT field and the decaying field outside of the Zeeman slower may lead to a local maxima or minima near the interface of the Zeeman and science chamber dependent on the orientation of the Zeeman B-field. This subtle detail can greatly affect trapping efficiency as we found around 2014 when the current direction of the Neutral Zeeman slower was reversed and a subsequent 2x increase in trapped atom number was observed.

the  $^1S_0 \rightarrow ^1P_1$  transition. However, only 2 out of 5 of the magnetic sub-levels are trappable which can lead to long load times when trapping less abundant isotopes.

Repumping from the  $^3P_2$  state is achieved via a 481 nm transition along the  $(5s5p)^3P_2 \rightarrow (5p^2)^3P_2$  transition for approx. 50ms. During the repumping exposure we continue to illuminate the cloud with 461 nm light but reduce the light intensity by an order of magnitude. We refer to this stage as the "cold" blue MOT and find that reduction of the intensity, while maintaining consistent laser detuning, significantly increases the transfer efficiency into the red MOT stage. <sup>†</sup>

Once the atoms have been returned to the ground state, we begin a second MOT stage using the narrow intercombination transition  $^1S_0 \rightarrow ^3P_1$  to cool below 1 mK. The  $(5s5p)^3P_1$  state has a reasonably long lifetime of  $21\ \mu s$  ( $\Gamma/2\pi = 7.5\ \text{kHz}$ ). Thus the narrow line MOT operates in a different regime compared to typical dipole allowed MOTs, as the narrow linewidth means that only a thin shell of the atomic cloud is resonant at a given laser detuning and magnetic field value. We simulate the behavior of a broad transition by frequency modulating the 689 nm light using voltage controlled RF sources coupled to the light via an acousto-optic modulator (AOM) during the initial stages of cooling. Additionally, the overall laser detuning, amplitude of modulation, and laser intensity begin at large values in order to trap the initially hotter atoms from the blue MOT stage. As cooling with the 689 nm light becomes effective, we dynamically vary these three parameters along with the magnetic field gradient in order to efficiently cool and compress the entire sample. Ultimately, the

---

<sup>†</sup>We have explored ramping the laser intensity closer to atomic resonance as we expected reduced intensity at farther red-detuning to result in a weakened trapping force. However, we did not find any improvement with the added complexity of varying the blue laser frequency during this stage.

red MOT is reduced to single frequency operation near resonance at extremely low laser intensity to achieve final temperatures between  $1 - 2 \mu\text{K}$  after 400 ms of cooling.

During the last 50 - 100 ms of the 689 MOT (typically during single frequency operation) we additionally overlap the high intensity 1064 nm optical dipole trap (ODT). The red MOT can then cool atoms into the typically  $10 \mu\text{K}$  deep ODT with transfer efficiencies as high as 75%. After loading, we subsequently extinguish the red MOT and allow a period ( $\sim 10 - 100 \text{ ms}$ ) of free evaporation for the sample to equilibrate in the ODT before beginning forced evaporative cooling to produce our final sample of ultracold or quantum degenerate gas.

The end of the evaporation typically marks the beginning of the experimental phase and the divergence of our protocol into the specific procedures necessary. These may include ramping or pulsing on lattice beams, exciting a collective mode, probing the gas with PAS laser, shelving, etc. Once we have completed the experimental phase, we measure the cloud characteristics via absorption imaging along the  $^1S_0 \rightarrow ^1P_1$  transition. Typically we perform absorption imaging following a time-of-flight to measure both the atom number and temperature at the time of release. However, this is not strictly necessary and certain experiments may result in low atomic densities which are not amenable to a time-of-flight due to their low optical depth.

### 2.1.1 Characteristic performance

The following tables outline sample trapping performance at various stages of the cooling procedure for each isotope. Note, that while we have recently demonstrated the ability to dual trap 84 and 87, full characterization and optimization of this process is currently the subject of investigation.

Date	Load Time [s]	Magnetic trap ( $\times 10^6$ )	BB Red MOT		SF Red MOT		ODT	
			Num. ( $\times 10^6$ )	Temp. [ $\mu\text{K}$ ]	Num. ( $\times 10^6$ )	Temp. [ $\mu\text{K}$ ]	Num. ( $\times 10^6$ )	Temp. [ $\mu\text{K}$ ]
1/18/16	5	–	–	–	3.5	1.7	2	1.4
	15	–	–	–	6	1.7	4.3	1.4
8/11/16	5	–	–	–	3.2	2.1	1.4	2.1
	15	–	–	–	7.6	2.1	3.3	1.9
3/15/18	5	–	2.2	4.5	2.2	1.8	1.6	1.5
	15	–	4	4.2	3.8	1.8	2.6	1.5
5/23/18	5	5.8	3.1	5.8	2.6	2.2	1.3	1.6
	15	13.3	5.5	8	4.5	2.3	2.3	1.6
8/3/18	5	–	3.3	5.1	2.8	1.7	–	–
	15	–	5.8	5.2	5.2	1.9	–	–

Table 2.1 : Sample trapping performance of  $^{84}\text{Sr}$ 

Date	Load Time [s]	Magnetic trap ( $\times 10^6$ )	BB Red MOT		SF Red MOT		ODT	
			Num. ( $\times 10^6$ )	Temp. [ $\mu\text{K}$ ]	Num. ( $\times 10^6$ )	Temp. [ $\mu\text{K}$ ]	Num. ( $\times 10^6$ )	Temp. [ $\mu\text{K}$ ]
11/29/16	1	–	–	–	9.5	2	7.4	1.7
	3	–	–	–	23	2.5	15	2
1/20/17	1	–	–	–	5	1.7	4	1.6
	3	–	–	–	9.1	2	7.7	1.7
3/30/17	1	–	–	–	6.6	2	5	1.7
	3	–	–	–	12.8	2.7	9	1.9
11/15/18	1	7.9	9.7	4.7	7.3	3.4	6.1	3.5
	3	24	21.5	5.1	14.4	3.5	11.4	3.7

Table 2.2 : Sample trapping performance of  $^{86}\text{Sr}$

Date	Load Time [s]	Magnetic trap ( $\times 10^6$ )	BB Red MOT		SF Red MOT		ODT	
			Num. ( $\times 10^6$ )	Temp. [ $\mu\text{K}$ ]	Num. ( $\times 10^6$ )	Temp. [ $\mu\text{K}$ ]	Num. ( $\times 10^6$ )	Temp. [ $\mu\text{K}$ ]
6/14/17	0.5	–	–	–	3.2	1.6	–	–
	1.5	–	–	–	5	1.6	–	–
2/1/18	0.5	–	–	–	10	2.1	5	1.4
	1.5	–	–	–	19	2.2	6.5	1.4
2/12/18	0.5	25	–	–	–	–	–	–
	1.5	54.1	–	–	–	–	–	–

Table 2.3 : Sample trapping performance of  $^{88}\text{Sr}$ 

Date	Load Time [s]	Magnetic trap ( $\times 10^6$ )	BB Red MOT		SF Red MOT		ODT	
			Num. ( $\times 10^6$ )	Temp. [ $\mu\text{K}$ ]	Num. ( $\times 10^6$ )	Temp. [ $\mu\text{K}$ ]	Num. ( $\times 10^6$ )	Temp. [ $\mu\text{K}$ ]
8/15/17	5	–	–	–	0.7	3	0.22	1.7
	15	–	–	–	1.6	2.6	0.5	1.7
9/8/17	5	–	–	–	1	1.8	0.6	1.6
	15	–	–	–	1.8	1.6	1	1.4
	40	–	–	–	1.8	1.6	1.5	1.4
5/1/18	5	8	5.5	8.4	1.8	1.1	1.5	1.1
	15	17	10	11	2.6	1.2	2.2	1.2
12/13/18	5	15	10.3	8.1	2.65	2.3	1.8	2
	15	31	18.7	8.5	4	2.2	2.6	2.1
2/26/19	5	13	8.5	9.9	1.7	1.9	1.25	1.6
	15	21	12	12	2.5	2	–	–

Table 2.4 : Example trapping performance of  $^{87}\text{Sr}$

## 2.2 Vacuum system and atom source

### Overview

The Neutral apparatus is built around a custom stainless steel chamber positioned above the table to facilitate optical access. Typical pressures are in the ultrahigh vacuum regime,  $< 1 \times 10^{-10}$  torr. Details on the original construction can be found in Natali (App. A.10) and Pascal's theses [52, 57]. The master's of Francisco Camargo [13] outlines the construction of the similar Rydberg apparatus. This more recent apparatus has benefited from the many lessons learned during the early life of the Neutral experiment.

Figure 2.1 shows a complete overview of the assemblies which form the Neutral vacuum system. Figures 2.2 - 2.5 show various views of the atom source, 2D collimator, and cryo tower assemblies. Note the red markers and green arrows denote the positions of heater bands and thermo-couples respectively. For more information please see App. E.

From right to left, the system starts with an oven source based around a custom nozzle design which uses a rod heater to vaporize elemental strontium. Next, there is a 6 way tee used for the optical molasses step which we refer to as the 2D collimator. From here atoms pass through a narrow differential pumping tube and into the entry port of the Zeeman slower where a majority of the laser cooling takes places as atoms traverse the one dimensional cooling stage. Following the Zeeman slower, atoms enter the science chamber where a plethora of lasers are used to manipulate and probe their behavior. Chief among these laser systems are the MOT sequences and high intensity far off-resonant optical dipole traps used for the final stage of confinement. Lastly, the

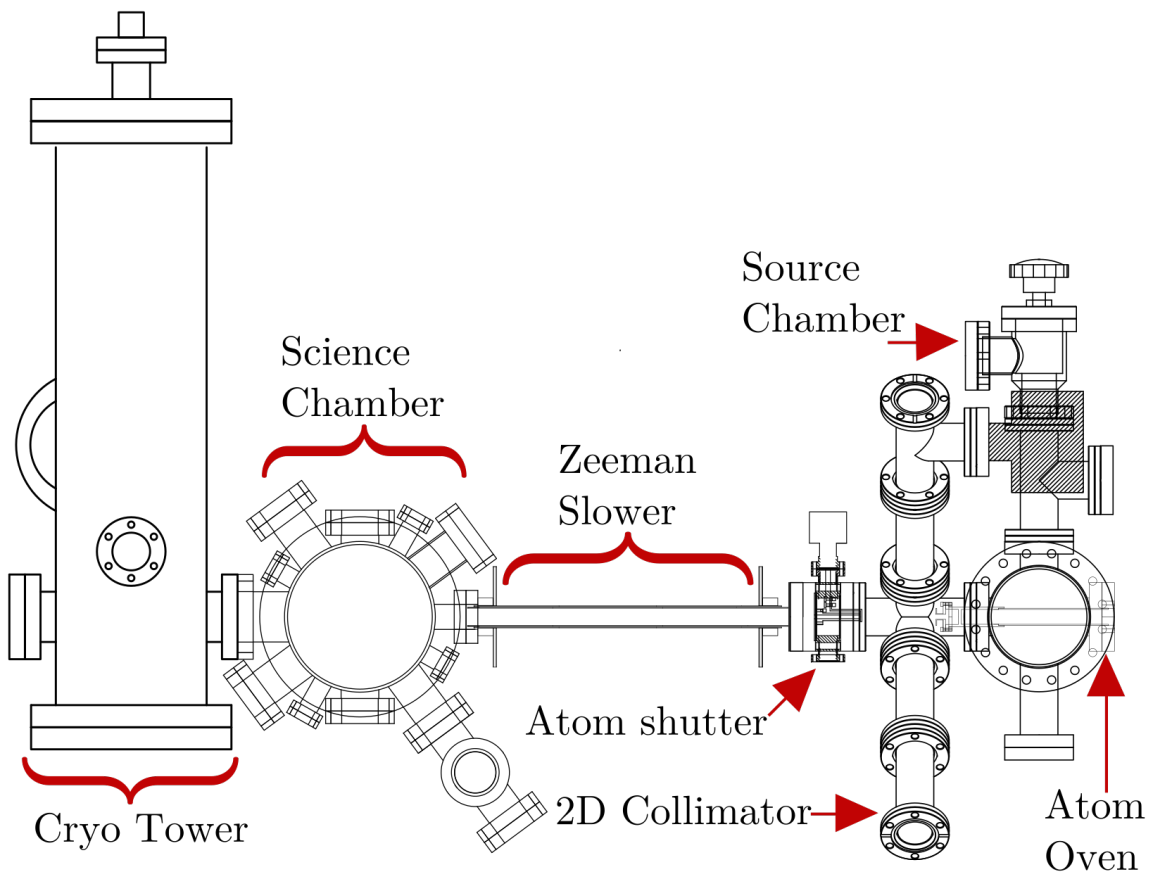


Figure 2.1 : Neutral apparatus vacuum system

Some components are rotated to provide easier identification. Not shown are the bellows which extend from the upper angle valve of the source chamber to the metal valve shown in Fig. 2.5.

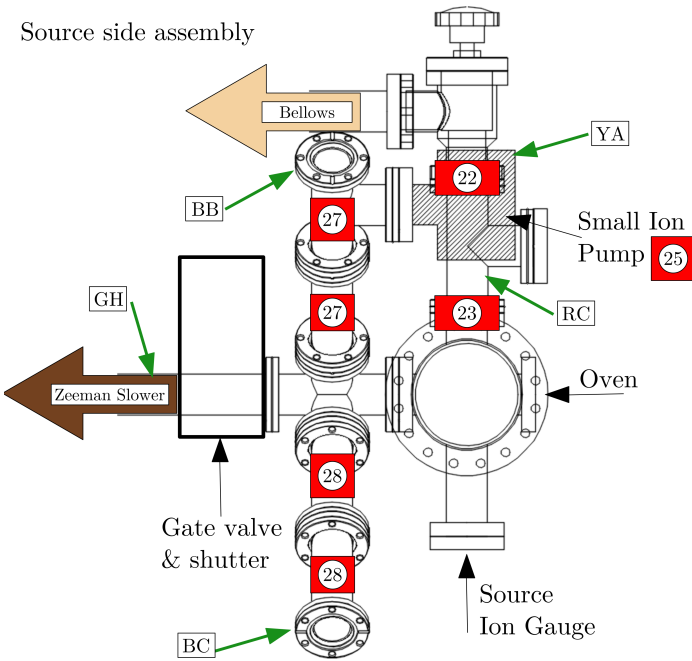


Figure 2.2 : Source assembly - side view

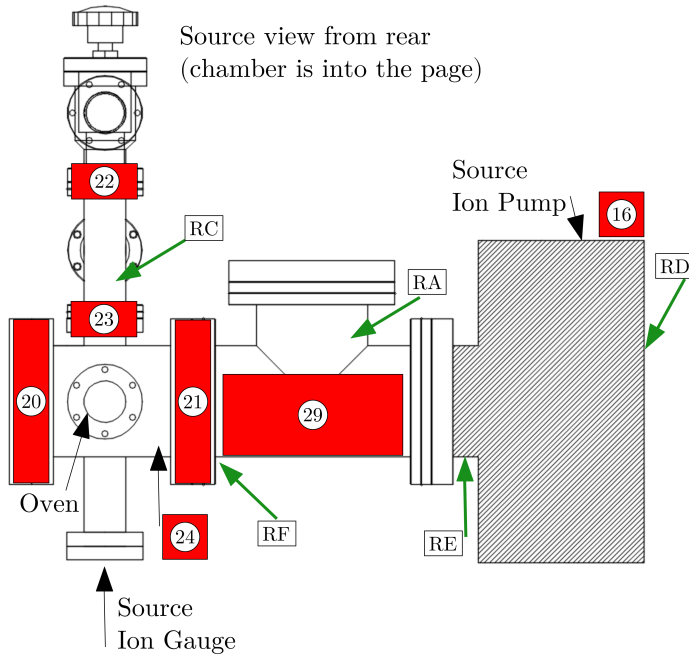


Figure 2.3 : Source assembly - rear view

2D Collimator view from rear  
(source is out of page and chamber is into page)

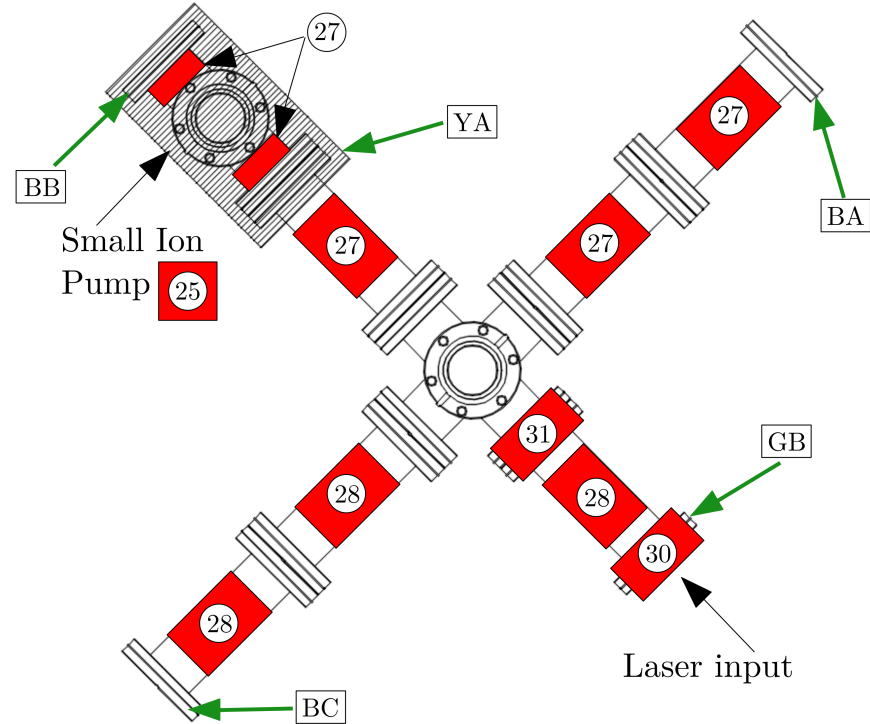
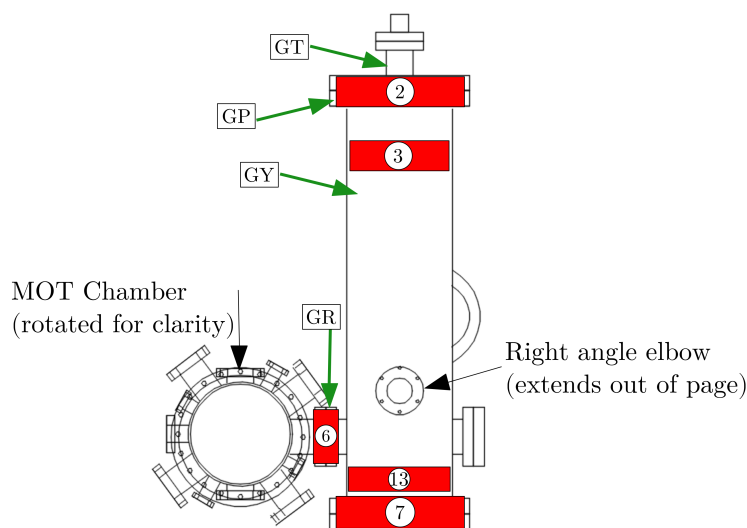


Figure 2.4 : 2D collimator assembly

Right view of tower



Left view of tower

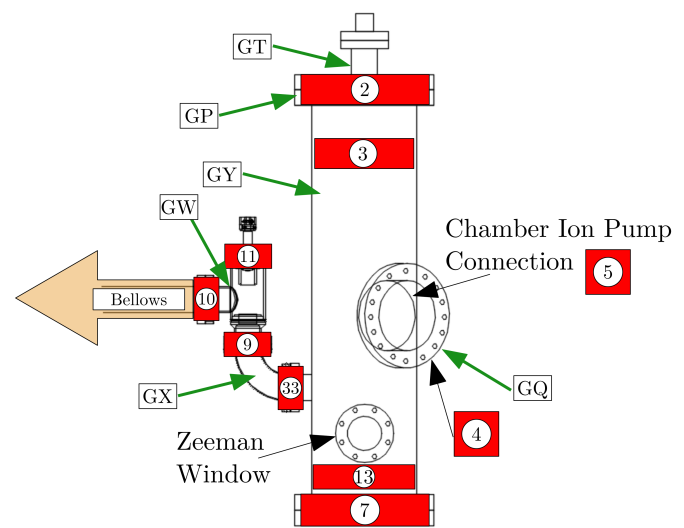


Figure 2.5 : Cryo tower assembly

body of the science chamber is supported by the cryo tower which houses a titanium sublimation cartridge (model: Varian 916-0061 series) and is the entry point for the Zeeman laser. It is worth explicitly noting that this Zeeman window is necessarily directly opposite the atomic source and therefore is subject to a flux of hot atomic strontium which will eventually coat the vacuum side. A brief note on a possible solution to this problem is explored at the end of this section.

While the source and science chamber have remained largely unchanged since the publication of Natali's thesis, several key improvements and events have occurred over the last few years\*. The original drawings of these components can be found in App. A.10 of [52] along with detailed information on the window coatings.

### Recent changes

**Addition of platform:** While exploring routes to produce quantum degenerate gases of strontium, it was determined that different geometries of traps were necessary to achieve efficient forced evaporation. The task of redesigning the optical dipole traps was undertaken by Ying Huang and is detailed in her master's thesis [36]. As part of this project, a raised platform was designed and built around the chamber to facilitate beam shaping and launching of the ODT laser. Details of the platform are available in the main apparatus CAD drawing.

The raised platform has become the primary method for directing lasers into the

---

\*As of April 2019, the most up to date CAD drawing for the Neutral apparatus is located at KillianDrobo:\Neutral\Laboratory Systems\Vacuum Chamber\Neutral Chamber\2017.12.26\_strontiumvacuum35\_latticetable.dwg. Additionally, please consult the README file located in this folder for further information.

chamber including the 1064 nm bulk optical dipole trap and the 532 nm optical lattice, both of which are outlined below. During installation of the free space optical lattice we observed heating and hypothesized that relative movement of the platform and chamber may be a cause. Supporting struts were then added beneath the chamber in an attempt to secure it to the platform around 2016. However, the extreme sensitivity of cold atoms and occasional observation of shot to shot fluctuations persists the concern of relative movement between non-rigid components.

These concerns were reinforced when we observed increased stability with the addition of a partial cover over the platform optics for the optical dipole and lattice traps. Initially meant as an optical safety measure for enclosing the high power beams, the cover led to a marked decrease in shot to shot fluctuations of the cloud position after a time of flight. With further testing we were able to attribute the increased stability to a mitigation of air currents caused by close proximity of the platform optics to the ventilation system meant to thwart dust accumulation inside the experimental enclosure.

**Running out of strontium:** In the winter of 2017 the neutral apparatus had been under vacuum for approx 8 years when suddenly we were no longer able to trap a significant number of atoms <sup>†</sup>. After extensive testing, we hypothesized that we had run out of elemental strontium within the atomic source. This led us to break vacuum, reload strontium, and perform a light bakeout procedure to reestablish the requisite ultrahigh vacuum for experiments. Details of this bakeout procedure can

---

<sup>†</sup>It was expected any trapping loss due to low strontium would be gradual and we were not able to determine the cause of the abrupt behavior.

be found in App. E. Through this process we confirmed our hypothesis that lack of strontium was the cause of the issue. Figure 2.6 shows the atom beam fluorescence after refilling the oven. This image was taken while using the Zeeman laser to cause photon scattering and looking down the 2D collimator. Prior to this event the Neutral apparatus enjoyed lifetimes of approximately 25 s as measured by background lifetimes measurements within the IR optical dipole trap. Approximately a year after restoring vacuum we have measured lifetimes on the order of 15s, the cause of the discrepancy is not rigorously known.

During the process of breaking vacuum we attempted several upgrades to the apparatus including adding a gate valve between the cryo tower and the Zeeman window and redesigning the atom nozzle source to incorporate a fixed heat shield around the heating element. Details of the nozzle design can also be found in App. E. Unfortunately, multiple issues arose during construction which led us to re-establish vacuum without these upgrades in place. Therefore, they are documented in the appendices for potential future use.

Finally, after removing the atom oven to replace strontium, we placed a temporary viewport to facilitate alignment of the Zeeman beam through the length of the vacuum system. While aligning we observed an unexpected partial occlusion of the Zeeman beam and upon further investigation learned that the differential pumping tube is noticeably not parallel to the atom trajectory. We were not able to determine the severity of the misalignment since the tube is not easily accessible and replacement is problematic as the tube is attached to a copper gasket held between flanges connecting the atom source chamber and the 6-way tee of the 2D collimator. The main readily measurable symptom is the occlusion of the Zeeman beam, which with an input

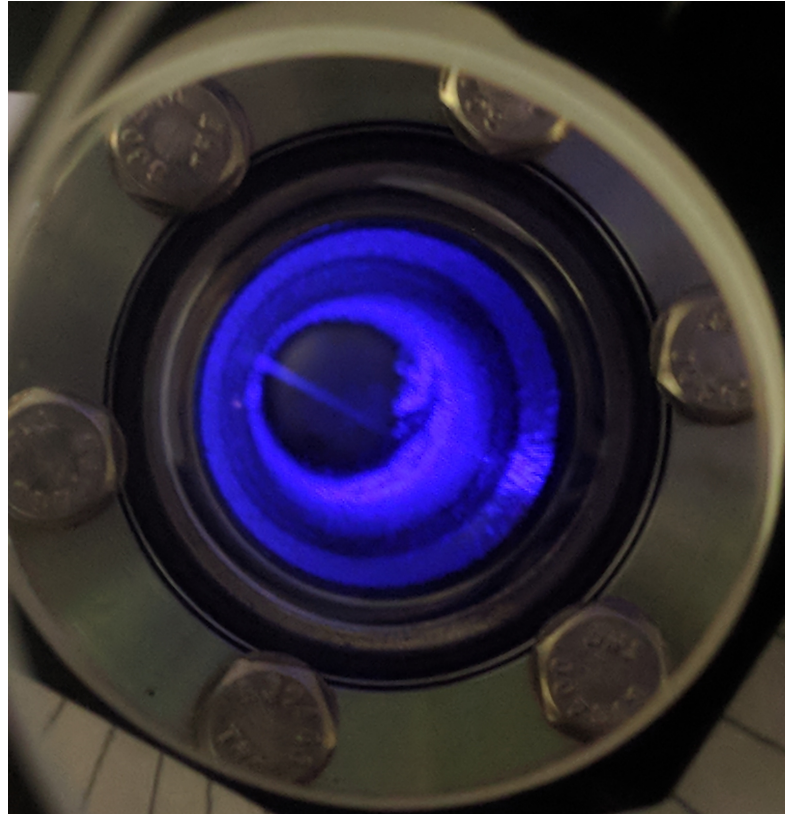


Figure 2.6 : Typical fluorescence of Zeeman beam looking down 2D collimator

This view is found using a 2 in mirror aligned along the path of the first pass of the 2D collimator and looking down the collimator tube. While looking at this angle, we are able to see the Zeeman beam move across the atom column when moving the last turning mirror. Reduction in this fluorescence signal from that shown was the primary indicator of lack of strontium in the source.

power of  $\sim 120$  mW before expansion optics and entering the chamber, only measures  $\sim 60$  mW of transmitted power through the length of the vacuum system. As adequate repair of the tube necessitates a drastic and practically infeasible deconstruction of the vacuum system our goal here is to document the issue for future students. It is currently hypothesized that this problem is the primary cause of the much longer load times needed in the Neutral apparatus compared to the newly designed Rydberg machine.

### Clarifications from de Escobar thesis

**HV version 1 & 2:** As a point of clarification, Natali's thesis [52] presents two versions of the HV chamber in figures A.42 - A.47 while referencing that the original construction proceeded with version 1. However, version 2 (the cryo tower) was installed around 2011 and is currently in use. Version 2 is shown in Fig. 2.5 and details are available in the apparatus CAD drawing.

**Collimating array in nozzle:** Once more, Natali's thesis refers to the installation of an improved nozzle design incorporating an array of collimating tubes constructed from  $2 \mu\text{m}$  hypodermic needles. Modeling and construction of this design was done by Anton Mazurenko, [53], with the goal of improving the angular discrimination of the oven assembly to produce a better collimated beam of atoms. Figure 2.7 shows the improved nozzle design  $\ddagger$ . The original assembly of this oven also incorporated a heat shield that would insert over the construction shown in Fig. 2.7b

---

$\ddagger$ For reference, this nozzle design is labeled "new nozzle summer 2010" in the apparatus CAD file to distinguish it from the other nozzle drawings also present.

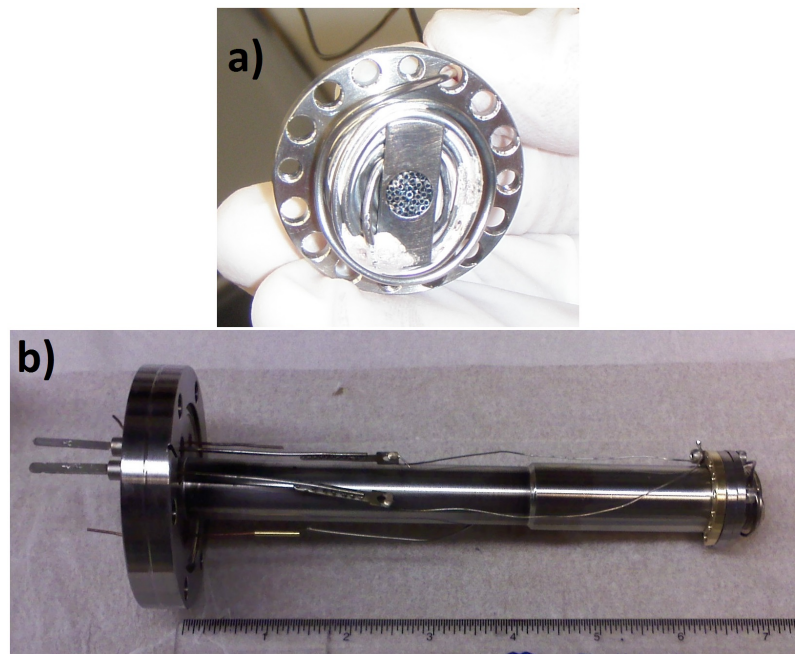


Figure 2.7 : Atom oven and nozzle construction

- a) The nozzle through which vaporized strontium enters the experiment. Here we see the array of collimating tubes behind which solid strontium is packed. b) The complete oven construction which houses the cartridge heater and the nozzle at the tip.

but this shield is not currently installed on the source oven.

### Ablating strontium off window

While not directly related to any experiment or typical procedure, here we summarize a brief side project where we used pulsed 532 nm Verdi to ablate strontium from a window.

As discussed previously, a common problem faced by strontium experiments is the accumulation of strontium on the Zeeman entry port. These deposits may then act as a partial mirror leading to attenuation of the crucially important Zeeman beam. It was shared through private communication with professor Killian, that pulsed 532 nm light (such as from a q-locked Verdi system like that used in the Plasma laboratory) might vaporize the strontium off the window and restore any loss in transmission. Using a test apparatus we were able to verify that indeed we could ablate the strontium off of an uncoated window, as shown in figure 2.8. This promising test led us to install an optical traversal port connecting the Plasma and Neutral labs. Unfortunately, while flashing the Verdi on a small section of the Neutral Zeeman window we found that the energy needed to ablate the strontium was accompanied by deformation of the substrate. We discontinued the ablation upon observing this behavior to avoid further damage and subsequently replaced the window after breaking vacuum as previously noted.



Figure 2.8 : Ablating strontium coating from window

Comparison of the before (left) and after (right) when using a pulsed 532 nm Verdi to ablate strontium. The residue visible in the after image we hypothesize to be caused by high pulse energy. We reduced the pulse energy as we moved towards the center of the window.

## 2.3 Laser systems

The heart of any atomic physics experiment are the laser systems which form the basis for laser cooling and various probes. Our lab has transitioned to primarily using diode laser system and relies heavily upon the use of injection locked master - slave setups. [ref](#) Below we will outline the specifics of our light generation setups.

### 2.3.1 Wideband cooling stage: 461 nm

#### 2.3.1.1 Overview

As discussed in the experimental overview, the majority of our laser cooling is done using 461 nm light. We generate and control these photons by amplifying and frequency doubling 922 nm light from a master ECDL diode laser. Fig. 2.9 shows an

overview of how we generate and use the 461 nm light. We will explore each of these sections in detail below, with emphasis on the MOT subsystem since it is the basis for many different components of the overall 461 generation.

In conjunction with the block diagram, Table 2.5 shows the details of the frequency shifts and AOM details. The position of these AOMs is represented by the numbered grey squares, while the labeled red squares define the system frequencies at various points along the system. The primary frequency relations for trapping and imaging are schematically represented in the lower portion of Fig. 2.9 and are determined via Eq. 2.1. Table 2.5 defines the shift variables used in these equations.

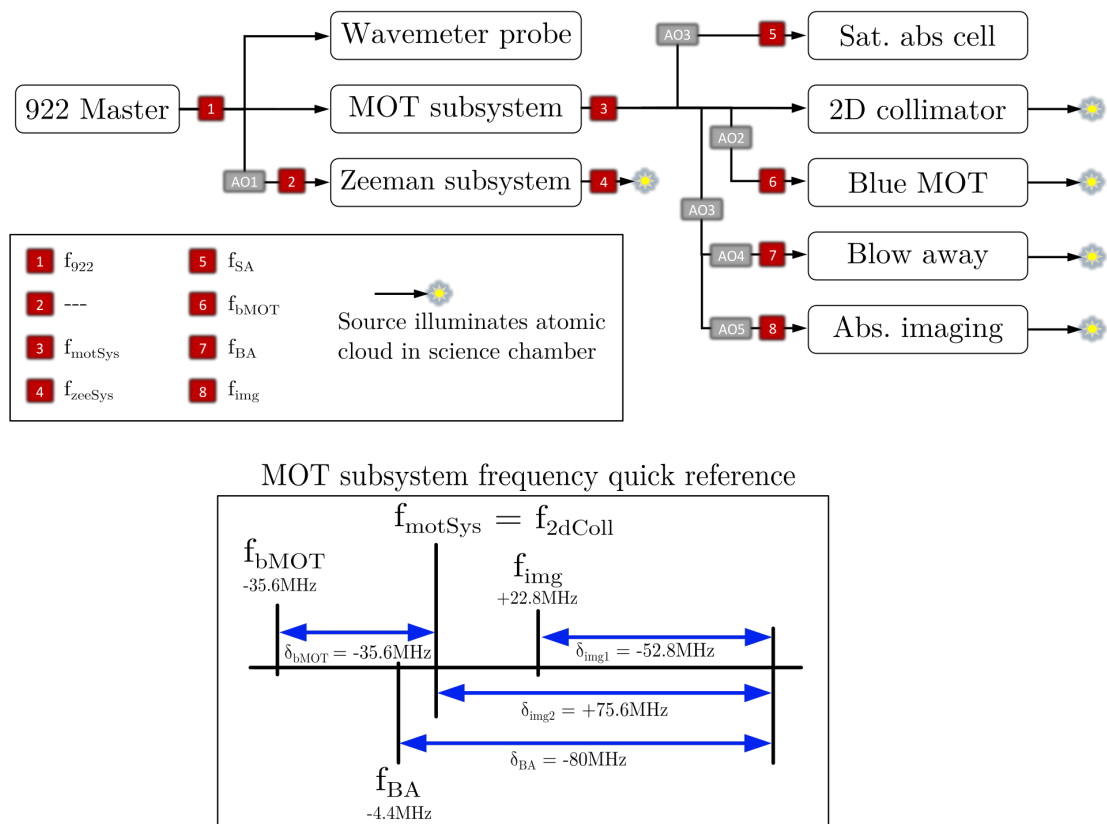


Figure 2.9 : 461 nm light generation system

Top - Block schematic showing the relations of the various systems, AOMs, and frequencies used to lock the system for 461 nm trapping and spectroscopy. See Table 2.5 for information on the AOMs. Bottom - Relative frequencies of the MOT subsystem at various stages of the 461 system. Frequencies are quoted with respect to  $f_{\text{motSys}}$  which in turn is controlled via the tunable sat. abs. to address different isotopes.

Label	Ind.	System	Shift variable	Nominal Freq. [MHz]	Freq. Source	Freq. control	AOM Model
Zeeman	AO1	922 master	$\delta_{zeeman}$	-252.4	Mini Circuits ZOS-300	Static voltage	Crystal Tech. 3200-1113
Blue MOT	AO2	MOT	$\delta_{bMOT}$	-35.5	Mini Circuits ZOS-50	Static voltage	IntraAction AOM-402A1
Image 2	AO3	Abs. imaging & Blow away	$\delta_{img2}$	+75.6	Mini Circuits ZOS-75+	Static voltage	IntraAction ATM-1001A1
Image 1	AO4	Abs. imaging	$\delta_{img1}$	-52.8	Mini Circuits ZOS-150	Static voltage	IntraAction AOM-602A1
Blow away pulser	AO5	Blow away	$\delta_{BA}$	-80	IntraAction ME-801T7	Internal synth.	IntraAction ATM-802DA1
Sat. abs. shifter	AO6	Sat. abs	$\delta_{SA}$	+317.3	Mini Circuits ZOS-400+	Static voltage	Crystal Tech. 3200-141

Table 2.5 : 461 nm system AOM details

Ind. labels the AOMs as shown in Fig. 2.9. The sign of the nominal freq. indicates the AOM order used.

$$\begin{aligned}
f_{\text{motSys}} &= 2f_{922} & f_{\text{zeeSys}} &= 2(f_{922} + \delta_{\text{zeeman}}) \\
f_{\text{2dColl}} &= f_{\text{motSys}} & f_{\text{bMOT}} &= f_{\text{motSys}} + \delta_{\text{bMOT}} \\
f_{\text{img}} &= f_{\text{motSys}} + \delta_{\text{img2}} + \delta_{\text{img1}} & f_{\text{SA}} &= f_{\text{motSys}} + \delta_{\text{SA}} \\
f_{\text{BA}} &= f_{\text{motSys}} + \delta_{\text{img2}} + \delta_{\text{BA}}
\end{aligned} \tag{2.1}$$

Overall frequency control,  $f_{922}$ , is determined via the magnetically tunable saturated absorption cell. The use of magnetic tunability to control the 461 nm light frequency is well documented in section 2.2.1 of Natali's thesis [52] and section 2.1.1 of Pascal's thesis [57]. A more recent undergraduate project also explored optimizations of this scheme for the Rydberg apparatus [56].

### 2.3.1.2 922 nm master

The master 922 laser is derived from a Sacher Lynx 922 nm IR diode laser in a Littrow ECDL configuration. Fig. 2.10, shows a simplified optical schematic of the master setup.

Starting at the master output, the beam is shaped and sent through a two optical isolators before it is coupled into an optical fiber. The fiber output immediately goes through an AOM which detunes the diffracted order by approximately 250 MHz. The diffracted and zeroth order are then separated with the unshifted beam sent towards the MOT generation subsystem and the shifted light towards the Zeeman subsystem. We find it necessary to include dual isolators in front of the master laser and have found that inadequate alignment of these isolators can lead to significant instability in the frequency of the master which in turn may lead the doubling cavities to be

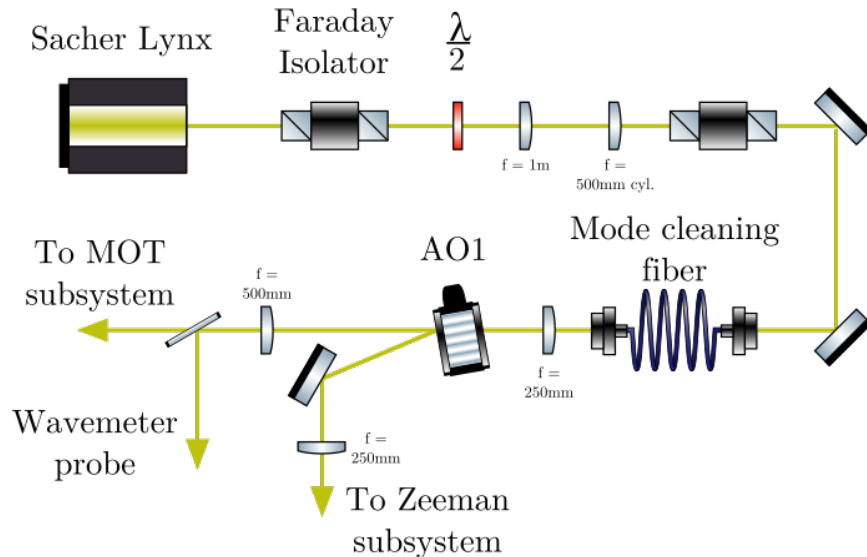


Figure 2.10 : 922 nm master optical schematic

unable to maintain a lock.

Fig. 2.11 shows a simplified schematic of the negative feedback path for stabilizing the length of the doubling cavities. Light out of the 922 master has sidebands added via a high bandwidth AC coupled current modulation directly to the laser diode \*. The doubling cavities of the MOT and Zeeman subsystems are length stabilized via these sidebands using the Pound-Drever-Hall (PDH) technique [refs](#). Currently, the reference oscillator RF source is a PTS 160 from Programmed Test Sources with an output power of 12 dbm and frequency of 39.55 MHz. This RF is sent to a 3-way power splitter which sends roughly a third of the power ( $\sim 4$  dbm) to each of the MOT

---

\*This direct coupling means the RF must be turned on prior to enabling the DC current. Conversely, the DC current should be disabled before turning off the RF source. Failure to follow this order may result in destruction of the laser diode.

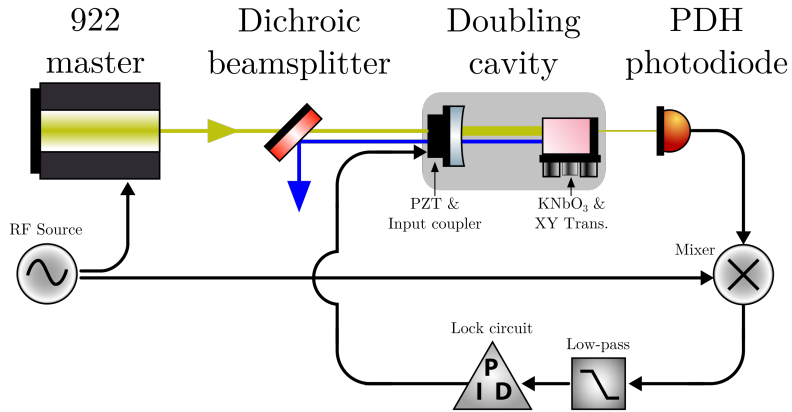


Figure 2.11 : 922 nm doubling cavity length stabilization feedback diagram

and Zeeman PDH mixers for demodulation. The remaining third is attenuated by 3db before coupling directly to the laser diode.

Once 461 nm light is available, we stabilize the frequency of the 922 nm using light from the MOT subsystem to interrogate a strontium heat pipe via frequency modulated Doppler-free saturated absorption from which an error signal of the  $^1S_0 \rightarrow ^1P_1$  transition is derived. As shown in Fig. 2.12, this error signal is sent into a homemade integrator circuit with a fast feedback path controlling the 922 nm diode current and a super low-bandwidth<sup>†</sup> path controlling for long term frequency drifts via the ECDL's internal PZT. We found that addition of this super low-bandwidth lock has significantly improved the continuous lock time of the 461 system. When enabled, the experiment may stay locked for upwards of 24 hours at a time. Additional details on the original construction of the 922 nm system can be found in App. A.8 of Natali's

---

<sup>†</sup>This super low-bandwidth lock is based on an Arduino PID controller with a long time constant and was built by Josh Hill. We refer the interested reader to Josh's forthcoming thesis for details of this general purpose slow lock.

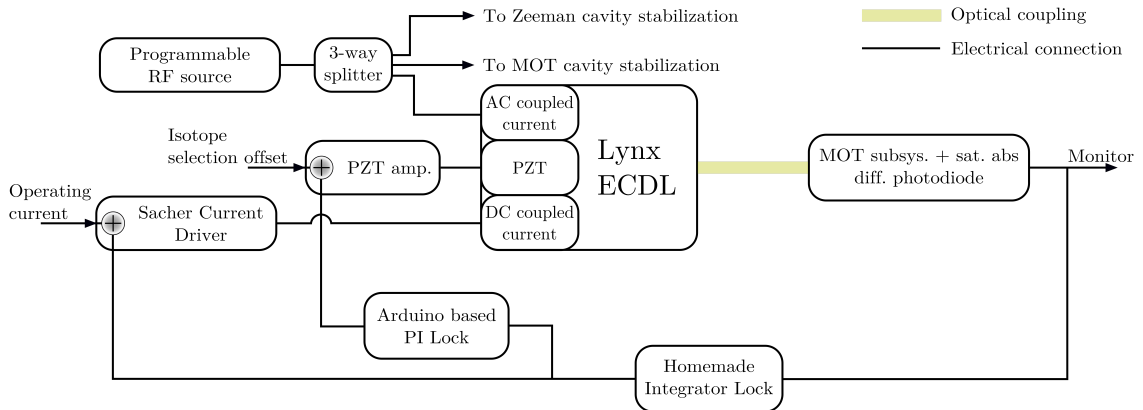


Figure 2.12 : 922 nm frequency stabilization block diagram

Multiple feedback paths allow for controlling the 922 master across disparate timescales. Note that the generation of the error signal used in the feedback is optically connected to the 922 master via the MOT subsystem and sat. abs. setup discussed in Sec. 2.3.1.4.

thesis [52].

### Historical notes and tips for usage

**PZT driver and replacement:** The PZT driver provided by Sacher has become problematic over the last few years. When varying the voltage we would occasionally hear a "clicking" noise from the Lynx laser as if the voltage was abruptly changing. We moved to a Thorlabs analog PZT driver (model: MDT694A) and have not had this issue since the switch<sup>‡</sup>.

---

<sup>‡</sup>We attempted to use the newer Thorlabs MDT694B which incorporates a digital potentiometer instead of the analog pot of the "A" model. However, we found the resolution of the digitization caused the laser frequency to jump and we were unable to maintain the frequency lock.

In early 2017, we found that the Lynx PZT was no longer responding to applied voltage. We believe this was caused by the afore mentioned "clicking" issue and was the motivation for changing PZT drivers. Details and pictures of the PZT replacement are available in App. H.

**Sacher temperature setpoint:** Care must be taken when attempting to change the set temperature of the laser diode as the internal potentiometer does not maintain full contact such that when attempting to turn it ever so slightly, the set point temperature may jump from approx 16 °C to 11 °C . Worse yet, we have observed that after changing the temperature there is a settling time during which the temperature setpoint may change while not be monitored. For these reasons we generally avoid touching this control as the present setpoint of 16.1 °C is adequate and no major improvements have been found when changing this temperature.

**Daily alignment:** The input coupler for the 922 cleanup fiber is not a reliable mount and tends to drift significantly from day-to-day. Therefore, we find it useful to peak up the alignment into this fiber while monitoring the output power at a fixed position after the fiber. Importantly, the positioning of the power meter head seems to effect the amount of power measured by the device (especially as the head ages). Thus, we use optical mounts in an attempt to reproduce the spatial position everyday and typically achieve a coupling efficiency of ~51% through the 922 mode cleaning fiber.

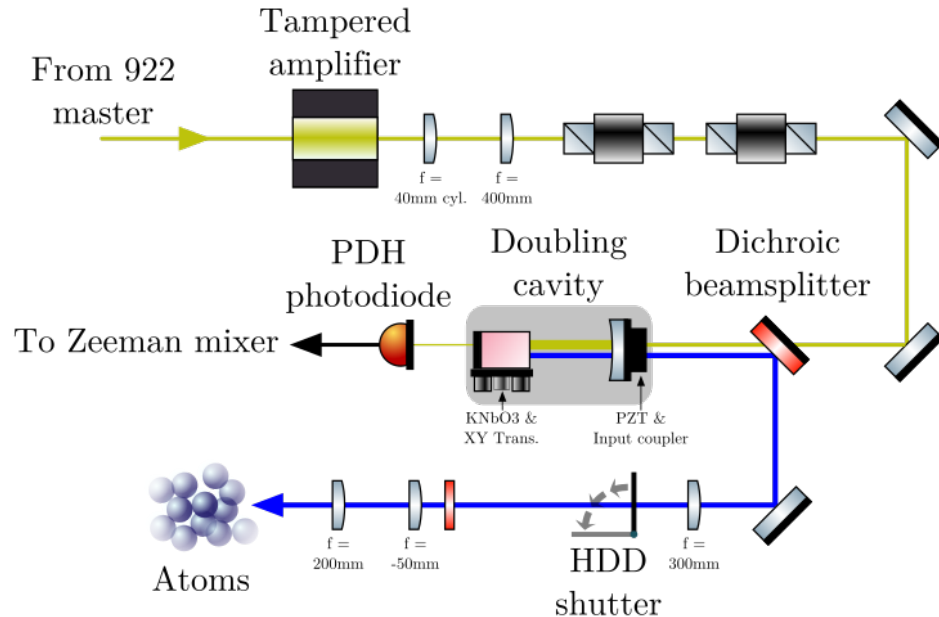


Figure 2.13 : Zeeman subsystem optical schematic

### 2.3.1.3 Zeeman subsystem

The Zeeman subsystem is a dedicated TA + doubling cavity for 461 nm light exclusively used for the one-dimensional Zeeman cooling stage. This system was originally constructed by Aaron Saenz [67] with additional details available in App A.8 of Natali's thesis [52]. Figure 2.13 shows a simplified optical schematic of this system. Light from the 922 master (approx. 20 mW) is shaped and coupled into a tapered amplifier to produce nearly 300 mW of 922 nm light. After being shaped further and passed through dual isolators, the light is then coupled into the homemade doubling cavity where a potassium niobate crystal is held within an optical resonance cavity to produce the 461 nm light. For approx. 300 mW into the cavity we are able to produce  $\sim$ 125 mW of 461 nm light. This light is sent through a final beam expander and into

the chamber where we have designed the system to focus the Zeeman beam just at the tip of the atom nozzle to maximize the spatial and temporal interaction between hot atoms and the Zeeman beam.

### Historical notes and tips for usage

**Mode hop:** Doubling cavities at short wavelengths are known to be mercurial aaron refs so stabilizing them can be difficult. We find that this cavity tends to become stable with approx. 300 mW of input power and increases of the power beyond this result in an initial cavity lock producing more 461 nm light but which quickly mode hops into a lower power mode. While we have seen cavity output powers of up to 150+ mW, these are not stable modes. Additionally, the locking circuit contains an auto re-lock feature that can occasionally result in locking to a lower power mode, usually around  $\sim$ 80 mW. We have found that power cycling the TA current driver is the least intrusive and quickest method to reattain the 125 mW output. If cycling does not work, then the TA current output may need to be adjusted or the cavity alignment tweaked.

#### 2.3.1.4 MOT subsystem

The MOT path generates light used for a multitude of processes as shown in Fig. 2.9. Here we detail the systems required for laser cooling and trapping, leaving the details of the blow away pulser and absorption imaging to be discussed in Sec. 2.3.5. Furthermore, we begin our discussion with a focus on the light generation of the MOT subsystem and next we will explore the child setups derived from this subsystem.

Fig. 2.14 shows a simplified optical schematic of the MOT subsystem which is

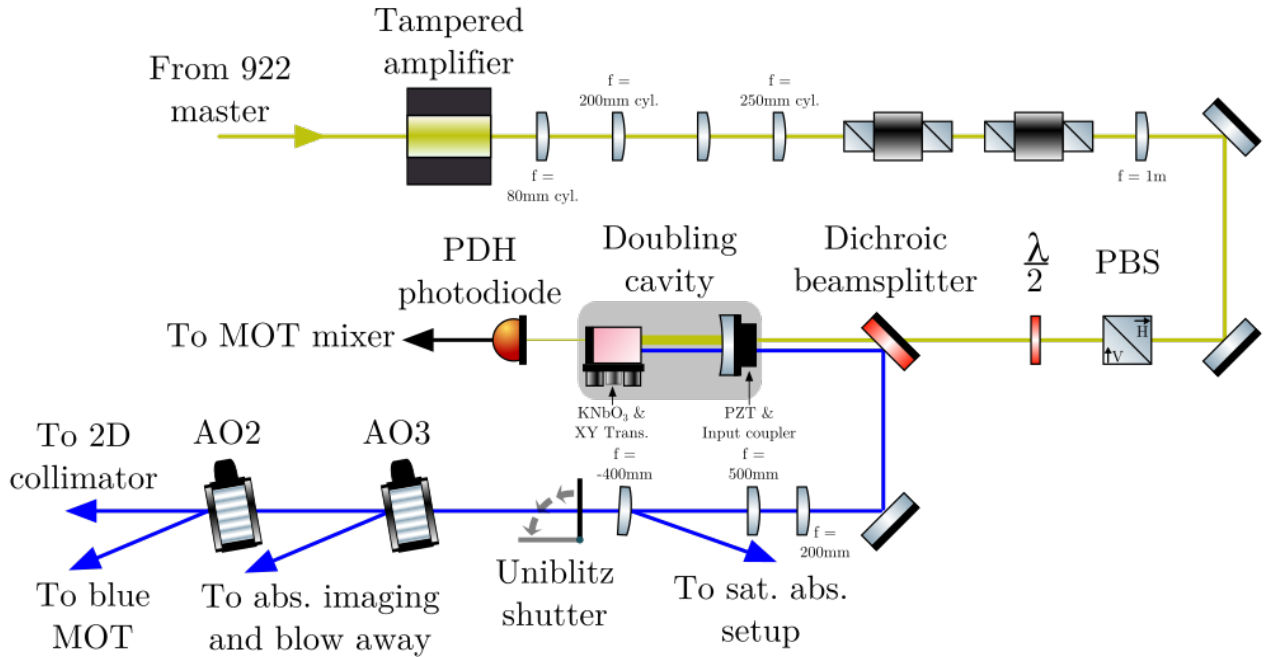


Figure 2.14 : MOT subsystem optical schematic

Note the sharing of power between the 2D collimator and blue MOT paths. While the blue MOT is power stabilized as shown in Fig. 2.15 the 2D collimator utilizes the remaining laser power.

modeled after the Zeeman setup described previously. Light from the 922 nm is shaped, amplified, and coupled into the doubling cavity where the same feedback mechanism shown in Fig. 2.11 is used to stabilize the cavity length. Since the MOT system is situated close to the experimental chamber, a "black-house" wall and shroud were constructed to minimize stray reflections (not shown in figure). This enclosure was placed around the MOT subsystem to mitigate stray 461 nm light which can

significantly hinder the achievement of quantum degenerate strontium gases<sup>§</sup>. Part of this enclosure is a fast ( $\sim 2$  ms) shutter (model: Uniblitz CS45) used to block the 461 nm light during the red MOT and evaporation stages. Additional hard drive (HDD) shutters are also placed along the MOT path behind the black-house shutter as leakage light through the blue MOT AOM (AO2) was seen to cause additional heating when utilizing the blow away pulser.

One concern we face with this MOT setup is the coupling of power between the various paths. Typically we do not operate the imaging & blow away pulser while trapping so all available power from the doubling cavity is available for these processes. However, the 2D collimator and 461 nm MOT operate concurrently during the first stages of trapping, thus the available laser power must be split between these two systems and an equilibrium found which balances the optimum trapping force of the MOT and the optical molasses of the collimator.

## 461 nm MOT

Fig. 2.15 gives an overview of the 461 nm MOT optics<sup>¶</sup>. Separation of the laser beams is performed on the table level where custom dichroics are used to combine the 461 and 689 MOT paths. Following the dichroics, the MOT beams are directed up to the platform layer via periscopes and subsequently pass through dual wavelength waveplates which retard 461 nm light by three-quarters of a period and 689 nm by

<sup>§</sup>Even stray reflected light off the glossy ceiling of the experimental enclosure has been found to cause atom heating!

<sup>¶</sup>The MOT arms are labeled as they are organized on the table, where Arm B is closest to the "computer side" of the table.

one-quarter. This setup allows us to maintain well defined polarization along the MOT paths.

### Saturated absorption

The saturated absorption cell is used to interrogate the  $^1S_0 \rightarrow ^1P_1$  transition to lock the frequency of the 922 master. App.I outlines a brief derivation for determining the lock point when a constant offset is added to the laser frequency, as is the case here. As outlined in the derivation, by utilizing the Zeeman tunability of magnetic sublevels, we can shift the resonance frequency of the atoms in the heat pipe. Thus, by interrogating and locking to the transition frequency of the most abundant isotope,  $^{88}\text{Sr}$ , we can shift it's resonance to cover the isotope shifts of the other strontium isotopes. This provides a simple method for trapping various isotopes and mixtures of strontium.

A detailed walkthrough of the construction and relevant physics of a blue sat. abs. cell can be found in the undergraduate report of Michael Viray [56]. Additionally, the original construction of the Neutral cell is covered in section 2.2.1 of Natali's thesis. Fig. 2.16 shows the optical setup used to generate the error signal and reference traces of Doppler bowl and frequency lock error signal. This error signal is generated by frequency modulating the magnetic field of the cell and performing Doppler-free saturated absorption.

### Historical notes and tips for usage

**Daily alignment of MOT TA:** The simplified optical schematic of the MOT subsystem in Fig. 2.14, does not reflect the approximately two meter lever arm which

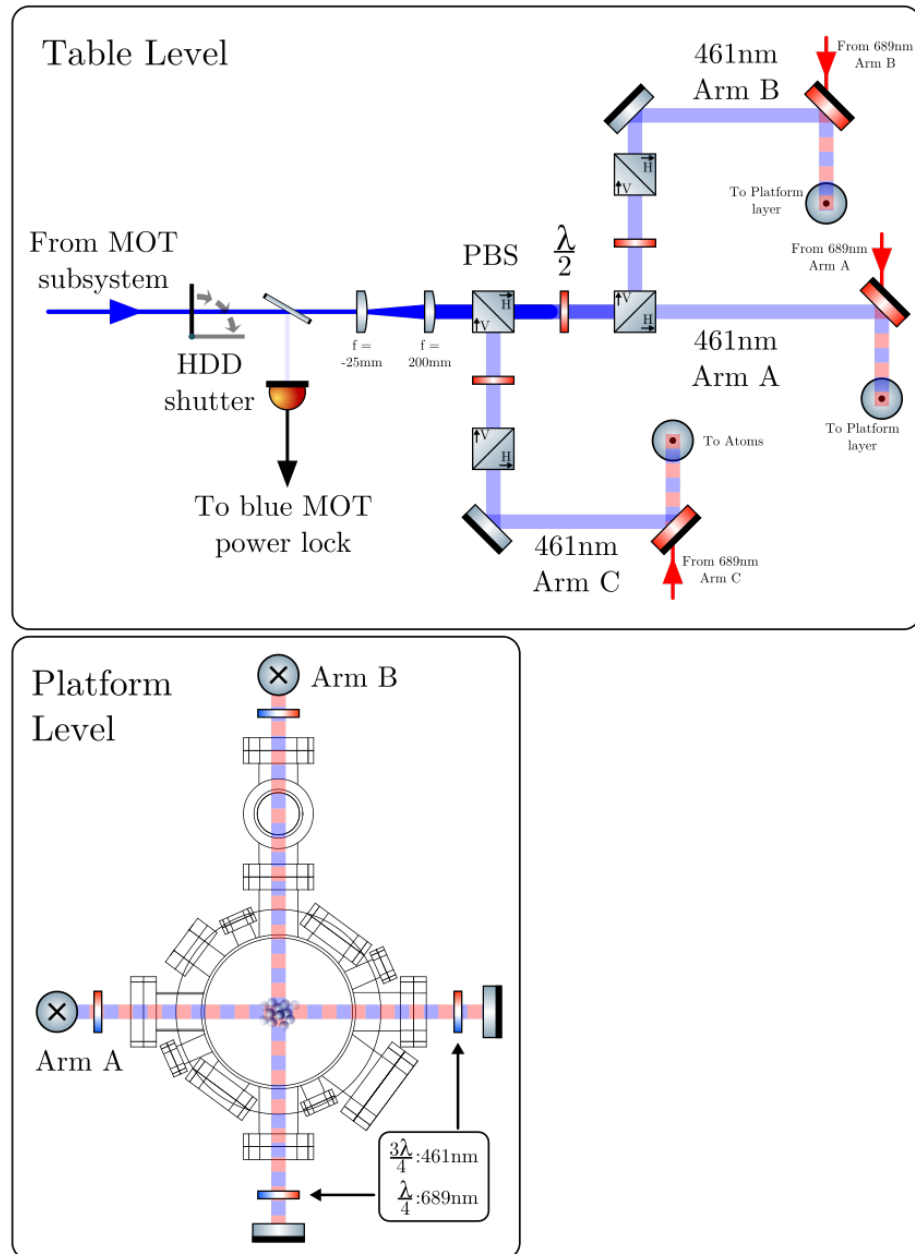


Figure 2.15 : 461 nm MOT schematic

Typical MOT setup with an additional HDD shutter to mitigate light leakage from AO2. Transparency of the laser beams represents the intensity. Note the 461 nm and 689 nm light follow the same path through the science chamber. Custom waveplates acting on both wavelengths are used to provide the appropriate polarization.

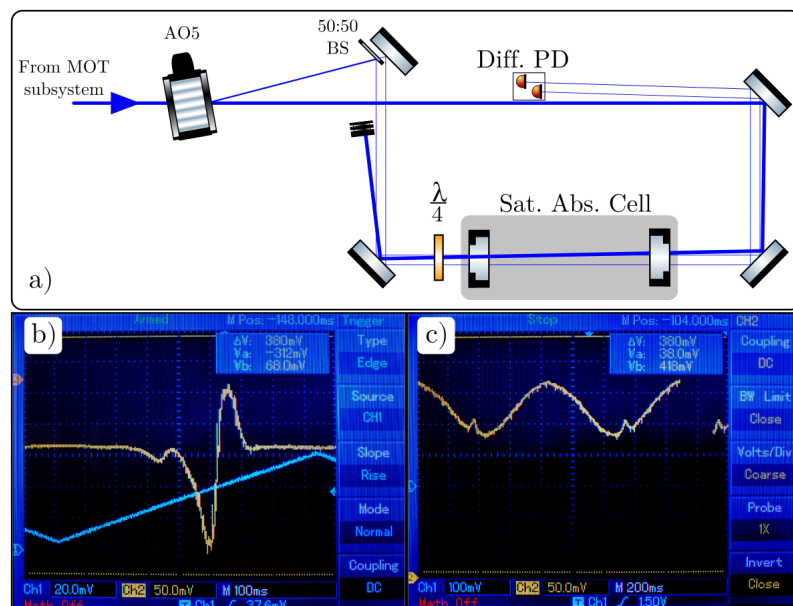


Figure 2.16 : 461 nm saturated absorption setup

a) Optical setup for frequency locking the 922 nm master. b) Example error signal. The cause of the asymmetry is unknown but occurs around approx.  $\pm 1.7\text{A}$  drive. The offset seen here can be nulled by balancing the amplification applied to the differential photodiode inputs. c) Example of the Doppler bowl where the Lamb dip can be seen. Note that the Lamb dip interacts with a specific velocity class determined by  $\delta_{SA}$ .

is present between the Zeeman split AOM and the input to the MOT TA due to the relative positions of the cavities. We have found this requires us to peak up the alignment of the 922 master beam into the MOT TA on a daily basis and is hypothesized to be the cause of large long time power variations ( $\sim 15\%$ ) on the output power of the MOT cavity which we observe throughout the course of the day. Typically with an input power of approx. 300 mW of 922 nm light we get between 100 - 115 mW out on a daily basis.

**Note on changing isotopes:** While the basic setup of the sat. abs has not changed over the many years, we have recently moved away from the original current source based on a home built high-current FET amplifier to a Bi-polar current source (BOP) (model: Kepco BOP-20-10DL). This change allows for more expansive coverage of the  $^1S_0 \rightarrow ^1P_1$  isotopes shifts. The previous current source limited our dual trapping capability to 87+88, and required an AOM to be tweaked and the sat. abs. to be realigned for trapping 84 and 86. Using the BOP, we can now easily shift the transition frequency over approx.  $\sim 200$  MHz which allows us to span the range between 84 and 87 within a single experimental cycle. Given the geometry of our solenoid, large currents are required to apply such large Zeeman shifts. We have observed that these large currents increase the heat load on the cell, which can lead to a reduction in the error signal. We mitigate this additional heating by varying the heater current to maintain approx. 50% absorption of the pump beam. As we expect, the timescale for these effects are minutes, so short term variations (i.e. when doing spectroscopy) do not cause significant heating when the duty cycle is kept low.

Due to the heating from the Zeeman coil, we chose to balance the currents needed

to trap 84 and 87 by "centering" the pump-probe beams frequency such that the magnitude of the currents needed for both isotopes is similar, but with 84 requiring a (+) current and 87 a (-) current. However, trapping of 88 still requires the realignment of the sat. abs. pump-probe beams as this shift is just beyond the capabilities of the current drive. Care should be taken when adjusting this alignment as the paths are highly coupled as can be seen in Fig. 2.16a.

### 2.3.2 Narrowband cooling stage: 689 nm

#### 2.3.2.1 Overview

Arguably the most important transition for strontium is the  $^1S_0 \rightarrow ^3P_1$  intercombination line transition at 689 nm. In addition to cooling and trapping, most experiments performed in our lab utilize this transition as the primary spectroscopic probe owing to the long lifetime of the excited states. This allows for high precision measurements and large detunings using conventional techniques. This section describes the generation and trapping setups in use on the Neutral apparatus. The primary spectroscopy probe system and spin manipulation setup are outlined in section 2.3.5.

Recently, the 689 nm generation system has seen significant growth and undergone a complete restructuring. For notes on the original Neutral setup refer to App A.3 & A.4 in Natali's thesis. Most notably, the master laser system is now shared between multiple laboratories including the Rydberg apparatus, the Dunning lab, and the Neutral apparatus. This setup has required a modular approach to the master 689 nm system to ensure independence of the various lab activities.

Fig. 2.17 shows a block diagram outlining the relationships between the master laser setup and various Neutral systems which utilize this stable light source. In conjunction with the block diagram, Table 2.6 details the frequency shifts and AOMs in use. The block diagram denotes the position of AOMs by the grey squares and the red squares denote system frequencies determined by the various shifts. Lastly, the frequency axis beneath the block diagram illustrates the relative frequencies at various points of the complete red system specified with respect to the  $^{88}\text{Sr } ^1S_0 \rightarrow ^3P_1$  transition and shown along with the isotope shifts of the same transition.

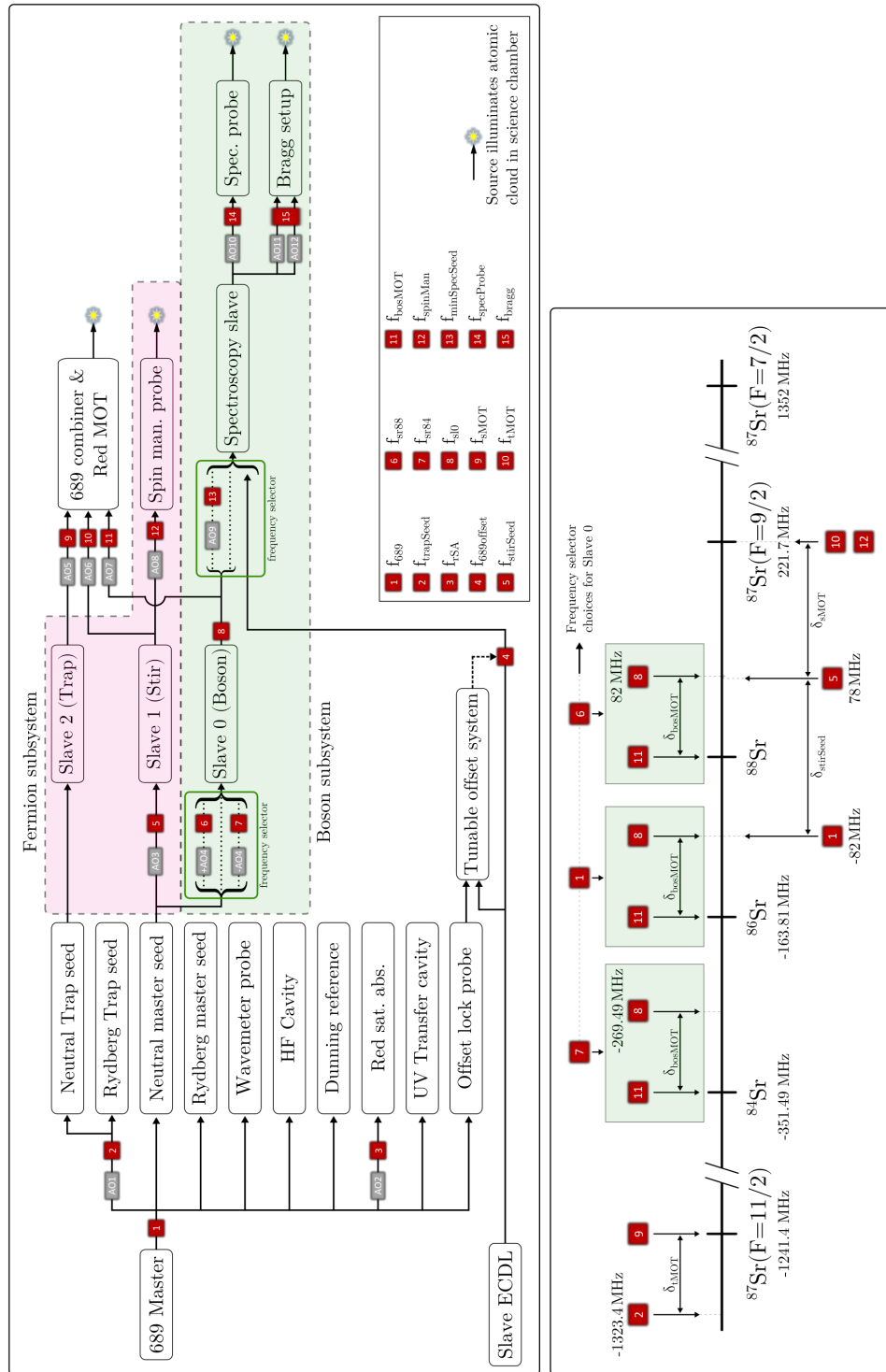


Figure 2.17 : 689 nm light generation system

Top - Block diagram showing various systems, AOMs, and the frequencies of red system. Table 2.6 gives further details on the AOMs. Bottom - Relevant isotopic shifts and system frequencies given relative to  $^{88}\text{Sr}$  intercombination transition.

Label	Ind.	Shift variable	Nominal Freq. [MHz]	Freq. Source	AOM Model
Trap Seed	AO1	$\delta_{trapSeed}$	-1241.44	Novasource G6	Brimrose TEF-1300-200-550
Red Sat. Abs.	AO2	$\delta_{rSA}$	+164±0.5	Novatech 409B (Dithered)	IntraAction ATM-1643DA1
Stir Seed	AO3	$\delta_{stirSeed}$	+160	Novatech 409B	IntraAction ATM-1602DA1
Boson isotope Selector	AO4	$\delta_{isoSel}$	+164 or -187.49	Novatech 409B	IntraAction ATM-2001A2
Trap MOT	AO5	$\delta_{tMOT}$	+82	Trap VCO / Novatech 409B	IntraAction ATM-852DA2
Stir MOT	AO6	$\delta_{sMOT}$	+143.7	Stir VCO / Novatech 409B	IntraAction ATM-1402DA1
Boson MOT	AO7	$\delta_{bosMOT}$	-82	Boson VCO / Novatech 409B	Isomet 1205C-2
Spin man. probe	AO8	$\delta_{spinProbe}$	-144±2	Novatech 409B	IntraAction ATM-1402DA1
Spec. slave seed	AO9	$\delta_{specSeed}$	-40	Novatech 409B	IntraAction AOM-402A1
Spec. probe	AO10	$\delta_{specProbe}$	-82±20	Novatech 409B	IntraAction ATM-902DA1
Bragg #1	AO11	$\delta_{bragg1}$	90±20	Novatech 409B	Crystal Tech. 3110-125
Bragg #2	AO12	$\delta_{bragg2}$		Novatech 409B	Crystal Tech. 3110-125

Table 2.6 : 689 nm system AOM details

Ind. labels the AOMs as shown in Fig. 2.17. The sign of the nominal freq. indicates the AOM order. The MOT AOMs are shown with two freq. sources which are used during the broadband red MOT and single frequency red MOT respectively.

The versatility of the 689 nm transition is apparent from Fig. 2.17 but comes at the cost of increased complexity. Unlike the blue system, where the overall system frequency was determined by varying the master laser frequency, the red master is locked at a fixed frequency relative to the  $^{88}\text{Sr}$   $^1S_0 \rightarrow ^3P_1$  transition. Nearly all frequency shifts are accomplished using AOMs driven with digital synthesizers such that each subsequent system derived from the master laser inherits the frequency stability and narrow linewidth of the master.

Fig. 2.17 also highlights the boson and fermion subsystems. These setups allow the Neutral apparatus to simultaneously trap and cool mixtures of a single bosonic isotope and fermionic strontium-87. The isotope selector AOM (A04) determines which bosonic isotope this system can trap. We denote the different frequencies available to injection lock slave 0 through the "frequency selector" box in the top part of the above figure. From each choice of input frequency, the output of slave 0 is also shown relative to other laser trapping frequencies and the isotope shifts of the  $^1S_0 \rightarrow ^3P_1$  transitions.

### 2.3.2.2 689 nm Master

Our master 689 nm source is a Toptica DL-pro. This is a Littrow configuration ECDL which outputs  $\sim 30$  mW of usable 689 nm light past its internal optical isolator. Fig. 2.18a shows how this power is distributed amongst the various subsystems and directed towards each laboratory. From the figure we see that the gigahertz AOM (AO1 is the first optic the light passes through since this AOM has a diffraction efficiency around  $\sim 20\%$ . The  $\sim 6$  mW of shifted light is then split between the Neutral and Rydberg experiments where it is used to injection lock a dedicated slave diode

used for the trapping MOT light needed for strontium-87.

Following the GHz AO, a series of waveplates and PBS cubes are used to apportion controllable amounts of power for providing light to various fiber paths and laboratories. A beam sampler along the path directs light into a mode-cleaning fiber which outputs to the high-finesse cavity system and the remaining power ( $\sim 2\text{ mW}$ ) is sent to a long heat pipe in order to interrogate the intercombination line transition.

The high-finesse cavity and heat pipe are used together to narrow the laser linewidth using the Pound-Drever-Hall (PDH) technique and subsequently lock the laser frequency to the atomic transition via saturated absorption, as illustrated in Fig. 2.18b. The atomic error signal is generated using standard frequency modulated Doppler-free saturated absorption where frequency modulation is performed via fast switching ( $\sim 11\text{ kHz}$ ) of the RF drive frequency applied to AO2. The high-finesse cavity is discussed in detail [section?](#) in Natali's thesis and has remained unchanged since her publication<sup>||</sup>.

### 2.3.2.3 Neutral red system

The Neutral 689 nm is composed of four slave diodes which may be designated into the Boson and Fermion subsystems as illustrated in Fig. 2.19. Light from the 689 master system is transported to the Neutral apparatus via the master seed and trap seed fibers. These fiber outputs provide approximately 3 mW and 1 mW for the master and trap respectively. This light is used to seed slaves 0-2, with spectroscopy slave (or slave 3) injection locked from the slave 0 output. Each of the three MOT systems

---

<sup>||</sup>As of April 2019, a ultra-low expansion cavity system is being implemented and tested to replace our homemade HF cavity.

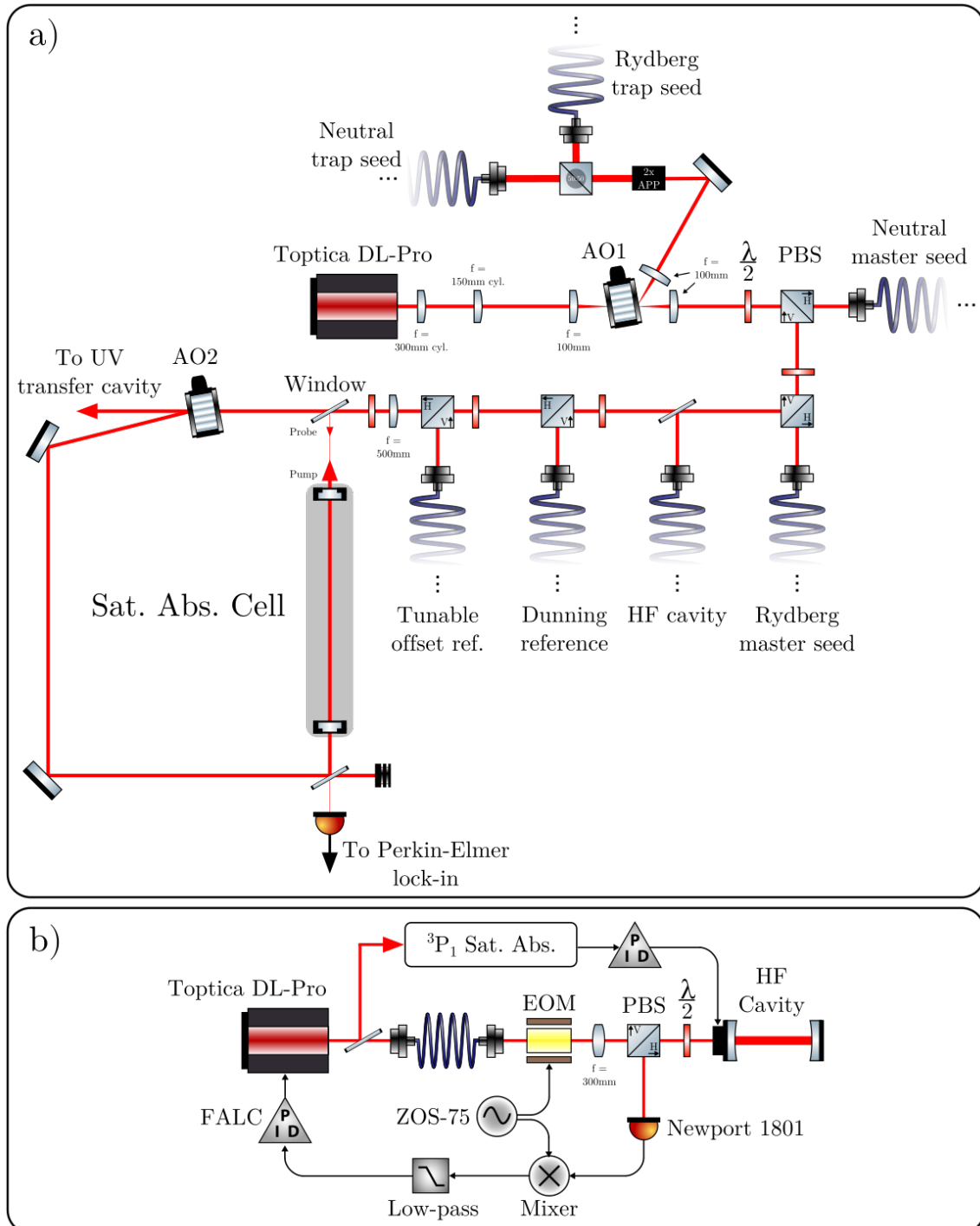


Figure 2.18 : 689 nm master system

- a) A simplified optical schematic showing the distribution of light as outlined in Fig. 2.17. b) Frequency stabilization scheme for the 689 nm master.

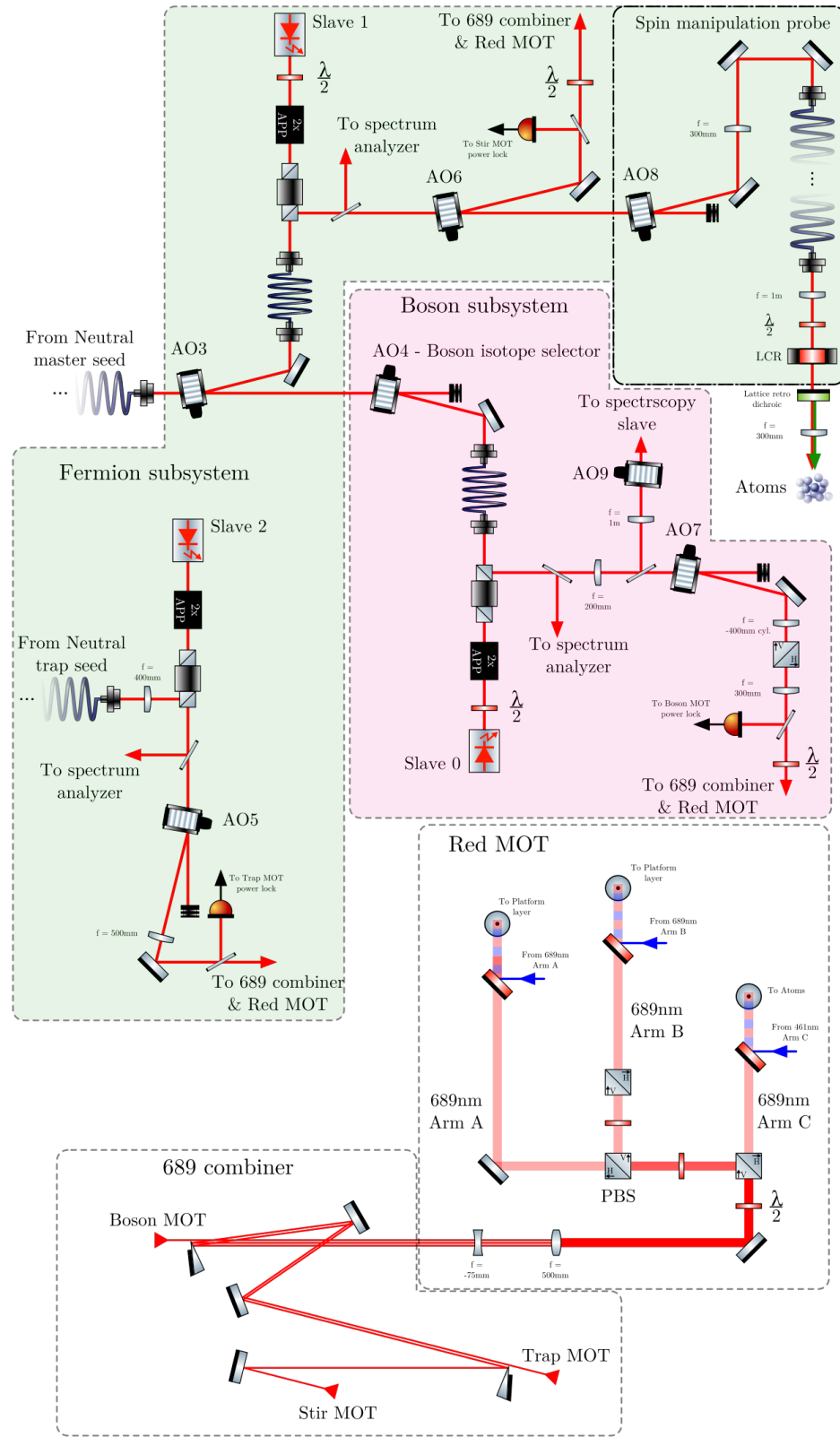


Figure 2.19 : Neutral 689 nm trapping and cooling setup

integrates an independent AOM which is used to provide dynamic intensity control and frequency offset & dithering during the 689 nm trapping and cooling stage. The gross detuning of these AOM's is fixed and specified in Table 2.6.

**Fermion subsystem:** Fig. 2.19 highlights the Fermion subsystem in green and is dedicated to a single isotope. This allows the seed laser frequencies to remain fixed as shown on the frequency axis given in Fig. 2.17.

As discussed in Sec. 2.1, trapping strontium-87 requires us to address two hyperfine transitions which we label the trap, operating along  $^1S_0 (F = 9/2) \rightarrow ^3P_1 (F = 11/2)$ , and the stir, operating along  $^1S_0 (F = 9/2) \rightarrow ^3P_1 (F = 9/2)$ . We generate these trapping and cooling photons using independent laser diodes, slave 1 and 2 for the stir and trap respectively, seeded with appropriately shifted light from the master laser. Light from slave 2 is used exclusively for the trap MOT while slave 1 is used for the stir MOT and spin manipulation probe, both of which operate along the ( $F = 9/2 \rightarrow F = 9/2$ ) transition.

**Boson subsystem:** Fig. 2.19 highlights the Boson subsystem in red. This setup enables the Neutral apparatus to individually trap each of the three bosonic isotopes of strontium. Additionally, this setup incorporates a spectroscopy probe which also features several choices for the input seed frequency. This system is detailed in Sec. 2.3.5.

Changing the bosonic isotope of interest is accomplished via switching the RF drive to the boson isotope selector AOM (AO4) and realigning through the mode-cleaning fiber to injection lock slave 0. This process has proven to be a fast and

robust means for switching between various isotopes without the need for dedicated diode systems for each isotope. Accounting for the boson MOT AOM (AO7) frequency, Table 2.6 gives the necessary drive frequencies for trapping strontium-88 and strontium-84. Strontium-86 is attainable by removing the drive frequency from the AOM such that slave 0 follows the 689 master frequency. Therefore, relative to the  $^{88}\text{Sr } ^1S_0 \rightarrow ^3P1$  transition, the input frequencies for slave 0 are [ $^{84}\text{Sr} \rightarrow -269.49\text{ MHz}$ ,  $^{86}\text{Sr} \rightarrow -82\text{ MHz}$ ,  $^{88}\text{Sr} \rightarrow +82\text{ MHz}$ ]. These details are represented schematically on the frequency axis of Fig. 2.17.

**689 combiner & MOT:** Finally, Fig. 2.19 also illustrates the 689 combiner & red MOT paths. The 689 combiner is a series of D-type mirrors for combining the boson, stir, and trap MOT beams such that these three light sources co-propagate onto the atoms. We find that long path lengths ensure acceptable alignment along the entire path length with the only major drawback that the individual arm powers are coupled for the three MOT beams.

As outlined in Fig. 2.15 and Sec. 2.3.1.4, the red MOT and blue MOT share the same path through the science chamber by utilizing beam combining dichroics and custom dual-wavelength waveplates.

### Historical notes and tips for usage

**Fiber usage for injection locking:** Optical fibers provide several key advantages when used to injection lock slaves. The foremost being a cleaner  $\text{TEM}_{00}$  output mode that can be easily mode-matched to the slave. Additionally, fibers provide a quick and effective means for ensuring optimal alignment of the injection locking

light by coupling the rejected light from the slave diode "backwards" through the fiber. Although rejected light is typically minimized when setting up a slave diode, by temporarily placing a waveplate before the isolator you can scramble the input polarization and increase the rejected power to facilitate alignment through the fiber. This process generally results in a quite robust alignment of the fiber output and the laser diode and is much faster than the free space method of coupling over a long distance. This alignment advantage along with improved mode matching has allowed us to injection lock a slave diode with as little as  $300\ \mu\text{W}$  while producing up to  $\sim 30\ \text{mW}$  of output power.

### 2.3.3 Optical dipole trap: 1064 nm

The ground state of strontium is a spinless  $J = 0$  state. Therefore, magnetic traps, which are common to alkali experiments, cannot be used for trapping the strontium ground state. Instead, we utilize optical dipole traps (ODT) which rely on the AC stark shift for trapping atoms.

The isotopes of strontium display a wide range of thermalization behavior due to their variation in scattering lengths. These differences in thermalization make it difficult to use a single ODT geometry for efficient trapping and evaporation of strontium. For this reason, the Neutral apparatus underwent a significant redesign of our ODT system as outlined in Ying Huang's thesis<sup>ref</sup>.

The experiments presented in chapter 5 of this thesis have relied on the trap configuration we call the independent arm ODT. Fig. 2.20 shows a simplified optical layout of this configuration which is composed of two 1064 nm beams labeled the loading and sheet traps which are controlled by independent AOMs. At the atoms, the approximate spot size of the loading trap is  $300 \mu\text{m} \times 60 \mu\text{m}$  and the sheet trap is  $400 \mu\text{m} \times 40 \mu\text{m}$ . Both beams have the short axis parallel to gravity to produce an oblate spheroid trapping volume which is useful for maintaining low density strontium-86 gases which reduces three-body recombination.

As shown in the figure, the two AOMs for the ODT are placed sequentially to better utilize the available 18W from the IPG. We typically load into a  $10 \mu\text{K}$  deep trap from the red MOT which requires  $\sim 4 \text{ W}$  in the loading trap and  $\sim 3 \text{ W}$  in the sheet trap. Once transferred into the ODT, we perform forced evaporation following a power law trajectory<sup>yohara</sup>, where the timescale for evaporation is isotope dependent.

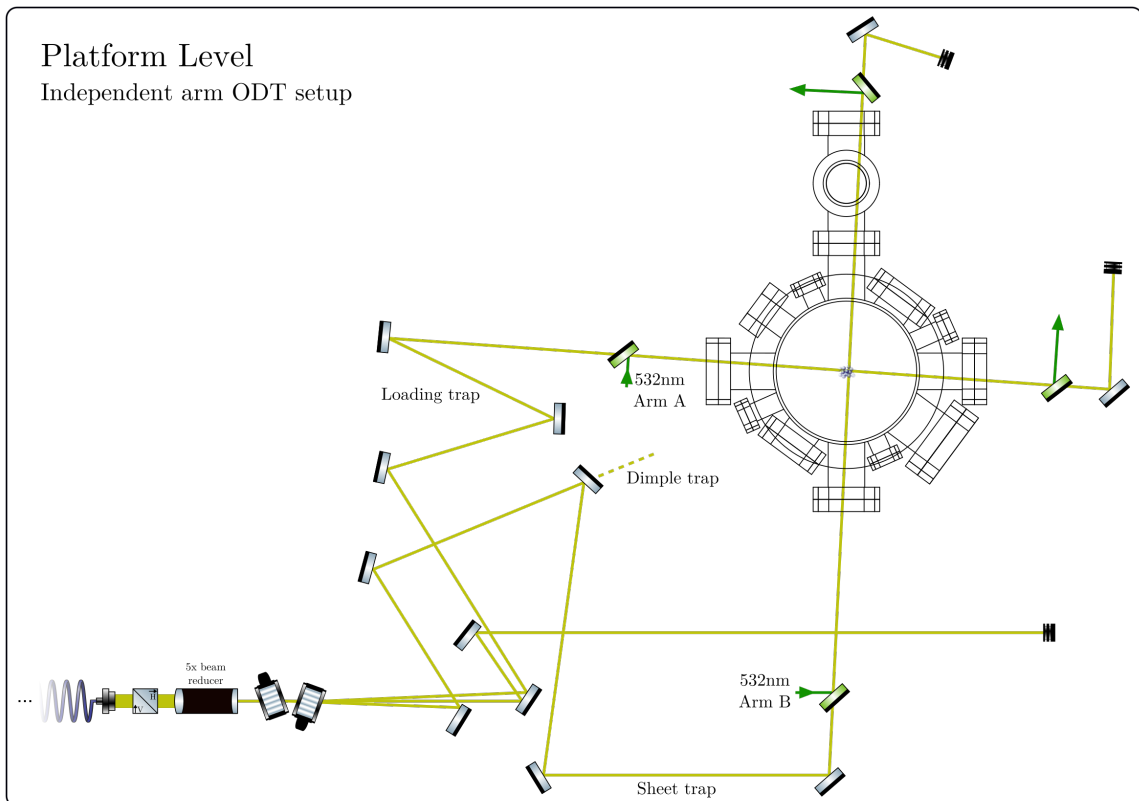


Figure 2.20 : 1064 nm optical dipole trap schematic

Paths for the loading and sheet traps are shown as they are realized on the apparatus. Also shown is the dimple trap path which is an optional configuration of the sheet trap. Please refer [Ying](#) for further information.

For our experiments with strontium-86, the evaporation timescales were on the order of 1-2 seconds for achieving sample temperatures near 100-200 nK and densities as high as  $10^{12} \text{ cm}^{-3}$ .

### 2.3.3.1 Modeling the potential

Optical dipole traps result from the AC stark shift present whenever an atom interacts with a light field [31]. In the simple two-level dressed atom model, the AC stark shift can be viewed as a mixing of the bare atomic states when the coupling light field is nearly resonant with the energy difference<sup>ref on dipole force as avoided crossing, CT book?</sup>. Fig. 2.21 shows a schematic avoided crossing of a two level system near resonance. Here the separation between states is defined as  $\Omega$ , or the Rabi frequency given by

$$\Omega = \frac{1}{\tau} \sqrt{\frac{I}{2I_{sat}}} \quad (2.2)$$

where  $\tau$  is the lifetime of the excited state,  $I_{sat}$  is the saturation intensity of the transition<sup>ref</sup>, and  $I$  is the applied intensity. Using this we can understand the origin of the potential which provides the trapping force in ODTs.

Considering an atom in the ground state,  $|1\rangle$ , a light field with red detuning,  $\Delta < 0$ , and the intensity dependence of Eq. 2.2. We see that at low intensity,  $\Omega^{\text{low}}$ , the energy of state  $|1\rangle$ ,  $E^{\text{low}}$ , is mostly unchanged from the non-interacting case. However, as intensity is increased,  $\Omega^{\text{high}}$ , the energy of state  $|1\rangle$  decreases. Thus, atoms in  $|1\rangle$  will experience a force,  $F(\mathbf{r}) = -\nabla U(\mathbf{r})$ , directed towards higher intensity regions when there is a spatial dependence of the potential energy.

With respect to the detuning,  $\Delta$ , from resonance, the potential energy of the atom

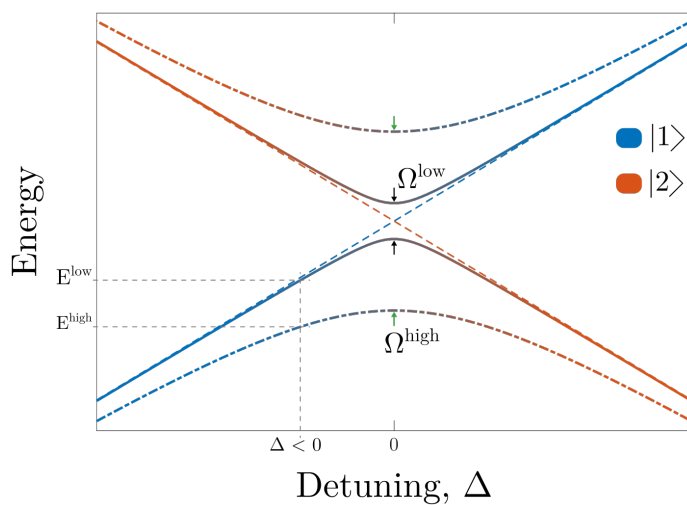


Figure 2.21 : Two-level avoided crossing

In the dressed atom model, coupling between the bare atomic states  $|1\rangle$  and  $|2\rangle$  results in an avoided crossing where the energy gap is determined by the coupling strength  $\Omega$ . The no coupling case is given by the dashed lines, while weak coupling is shown by the solid line, and strong coupling by the dash dotted line.

scales as

$$U(r) \propto \frac{\Gamma}{\Delta} I(r) \quad (2.3)$$

where,  $\Gamma$  is the natural linewidth of the transition determined by it's spontaneous decay lifetime, and  $I(r)$  is the spatial dependence of the light intensity. Optical dipole traps are also characterized by their off-resonant scattering rate. This rate is proportional to

$$\Gamma(r) \propto \left( \frac{\Gamma}{\Delta} \right)^2 I(r) \quad (2.4)$$

Comparing Eqs. 2.3 & 2.4, we find a favorable scaling for far off-resonant optical traps since the potential energy varies as  $1/\Delta$  and the scattering rate varies as  $1/\Delta^2$ .

The spatial dependence of  $U(\mathbf{r})$  derives from the TEM<sub>00</sub> gaussian intensity profile of the incident lasers given by

$$I(r, z) = \frac{2P}{\pi w(z)^2} \exp \left( \frac{-2r^2}{w(z)^2} \right) \quad (2.5)$$

where  $z$  is oriented along the beam propagation axis and  $r$  is transverse to this axis. Additionally,  $P$  is the incident laser power,  $w_0$  is the waist radius at  $z = 0$ , and the axial profile  $w(z)$  is given by

$$w(z) = w_0 \sqrt{1 + \left( \frac{z\lambda}{\pi w_0^2} \right)^2} \quad (2.6)$$

where  $\lambda$  is the laser wavelength.

Combining Eqs. 2.3 & 2.5 we find the three dimensional potential generated by two orthogonal lasers to be

$$U(x, y, z) = mgz + \frac{\alpha(\lambda)}{2\epsilon_0 c} \frac{2}{\pi} \left[ \frac{P_1}{w_1^y(x) w_1^z(x)} \exp \left( \frac{-2(y^2 + z^2)}{[w_1^y(x)]^2 [w_1^z(x)]^2} \right) \times \frac{P_2}{w_2^x(y) w_2^z(y)} \exp \left( \frac{-2(x^2 + z^2)}{[w_2^x(y)]^2 [w_2^z(y)]^2} \right) \right] \quad (2.7)$$

where  $mgz$  accounts for the influence of gravity on the atoms of mass  $m$ , labels 1, 2 specify the two intersecting laser, i.e. the load and sheet traps as illustrated in Fig. 2.20,  $\alpha(\lambda)$  is the AC polarizability of the ground state at a given wavelength,  $\epsilon_0$  is the vacuum permittivity, and  $c$  is the speed of light. This polarizability encapsulates the natural linewidth, detuning, and resonant behavior of the light field interaction with the bare atomic states [31]. Sec. 2.3.1 and App. A of Pascal's PhD thesis [57] outlines a calculation of the AC polarizability which at 1064 nm is  $\frac{\alpha(\lambda=1064 \text{ nm})}{2\epsilon_0 c} = -10.9 \text{ Hz}/(\text{W/cm}^2) = -5.23 \times 10^{-8} \mu\text{K}/(\text{W/cm}^2)^*$ . Furthermore,  $w_{(1,2)}^{(x,y,z)}$  generalizes Eqs. 2.5 and ?? for astigmatic laser profiles whereby the waist position and size are not common to both beam axes as assumed in these simple equations<sup>†</sup>.

The effects of gravity are a significant limiting factor for ultracold atoms as it is the dominant force that must be counteracted by the optical dipole trap. Fig. 2.22a shows the effects of gravity considering a simple one-dimensional gaussian potential,  $U(z) = mgz + A \exp\left(\frac{-z^2}{2\sigma^2}\right)$ . Here we've chosen a general form of the gaussian for illustrative purposes. In the figure, we define the trap depth as the difference between the trap minimum and the lowest saddle point. Additionally, by making the harmonic approximation, shown by the dashed line, we can Taylor expand Eq. 2.7 and determine the expected trap frequencies. Fig. 2.22b illustrates a realistic three-dimensional profile of an optical trap. Analyzing the 3D profiles, we find that the saddle points may not be along the  $X = 0$  line and therefore we must consider the full trap profile

\*Units here are convenient lab units for quick calculation of trap parameters. Polarizability of  ${}^1S_0$  in atomic units is  $\alpha = 232.857 \text{ au}$ .

<sup>†</sup>Eq. 2.7 is given assuming a coordinate system where one beam propagates along  $X$ , another along  $Y$ , and  $Z$  is parallel to gravity.

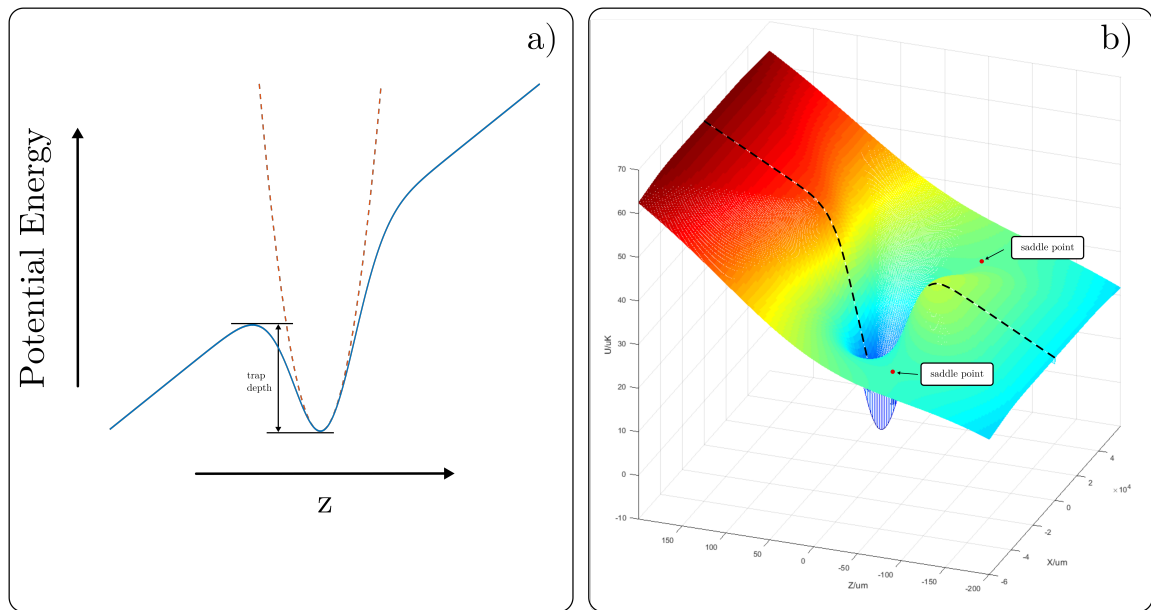


Figure 2.22 : Modeling an optical dipole potential

a) A one-dimensional view along the trap axis parallel to gravity. The trap depth is defined between the trap minimum and the nearest saddle point. Also shown is the harmonic approximation used for defining trap frequencies. b) A pseudo-color volumetric plot of a three-dimensional potential. Here we see a saddle point similar to the 1D case along  $X = 0$  but there is also a lower saddle point indicated by the black arrows.

when determining the trap depth. This is particularly important for shallow traps (low power) where the trap depth is more likely to be defined by a saddle point along a non-trivial trajectory. This realization has important repercussion for our analysis of the halo binding energy described in Ch. 4.

### 2.3.3.2 Trap frequency calibration

Measurement of the trap frequencies provides the link between our theoretical models and the experimental realization of the optical dipole trap. Previously, these measurements were performed by parametric heating via intensity modulation of the optical dipole trap [cite Ying thesis](#). This process causes atom loss via resonant heating when the modulation frequency matches a trap oscillation frequency. While convenient and simple, parametric heating can lead to a complicated spectrum to decipher since the heating process does not discriminate directional information and causes coupling of higher harmonics of the trap frequencies.

Recently, we have found excitation of center-of-mass (COM) oscillations to be a robust mechanism for measuring trap frequencies. Fig. 2.23 shows an example of trap frequency measurements taken via center-of-mass oscillations. This example illustrates the long-lived nature of these collective modes which can extend for hundreds of milliseconds. Furthermore, the frequency discrimination provides an unambiguous estimate of the underlying trap frequency.

Exciting vertical trap frequencies, along  $Z$ , is a straightforward process whereby we excite oscillations by quickly extinguishing one arm of the optical dipole trap for 1-2 ms before turning it back on and allowing the cloud to evolve in time. We measure the trap frequency by varying this evolution time subsequently performing a standard

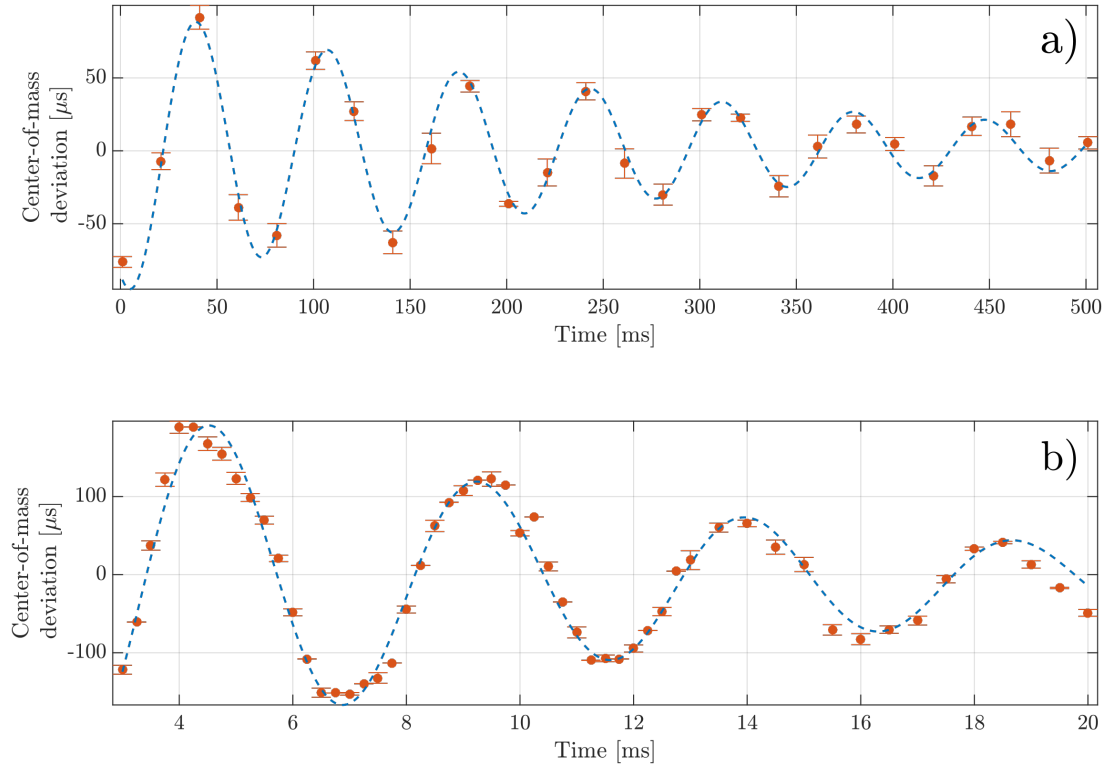


Figure 2.23 : Example center-of-mass oscillations

These measurements were taken in the independent arm ODT with strontium-84 which has a scattering length  $a = 124 a_0$  leading to slow decay of the oscillations. a) Horizontal trap frequency of  $\sim 13$  Hz extending over 500 ms. This mode was excited via the kicking method. b) Vertical trap frequency of  $\sim 220$  Hz. This mode was excited by momentarily pulsing one of the ODT beams off. Further details are given in the text.

time-of-flight absorption imaging step<sup>†</sup>.

Exciting oscillations along the horizontal directions, is a bit more challenging. We have developed two mechanisms for exciting these modes which we call the kicking method and the pulling method. The following sections provide further detail<sup>§</sup>.

**Kicking method:** The kicking method has been primarily used for measuring the trap frequencies of the independent arm ODT. In this configuration the two ODT beams intersect in a horizontal plane parallel to the optical table and orthogonal to one another. This method is useful here since the excitation of the center-of-mass oscillation occurs via an abrupt step of the AOM drive frequency. This changes the deflection angle of the IR beam out of the AOM which, in turn, "kicks" the cloud. Briefly, the kicking procedure is

- I. During the ODT loading phase, load into a trap with one beam offset
  - A. The beam which is offset will excite oscillations along the opposite beam and measure the confinement due to the beam being shifted.
  - B. We have found that, in our current configuration, an offset of  $\approx 1$  MHz results in a reasonable excitation amplitude.
- II. Once the red MOT is extinguished and ODT loading is complete, we evaporate down to the trap of interest in the offset trap.

---

<sup>†</sup>On a technical note, we find that this rapid on-off of the beams results in a brief overshoot of the power locks due to the reacquisition. However, the power lock equilibrium is restored after a few milliseconds and therefore we evolve for a time long compared to this perturbative behavior.

<sup>§</sup>Note that timescales specified below are given with strontium-84 as the example. This isotope has favorable scattering properties and is typically our prototyping isotope for new techniques.

A. We find it useful to follow the evaporation trajectory for the experiment at hand. This allows us to adequately model the experimental potential and evaluate the trap depth at various points of interest.

III. After evaporation, we let the atoms equilibrate for  $\approx 250$  ms then suddenly switch the frequency of the trap and hold for a variable evolution time before releasing and imaging.

We achieve the frequency shift that excites the kick by stepping the input of a voltage controlled oscillator (VCO) which is typically fixed by a static voltage source<sup>¶</sup>.

**Pulling method:** With the recent addition of the high power 532 nm for the optical lattice, we have explored an alternative method of inducing a center-of-mass oscillation. This method uses a single pass of vertically propagating green light (Arm C) to pull the atoms out of equilibrium to excite an oscillation. Details of the 532 nm setup are given below in ??.

The pulling method has become our preferred method of trap frequency measurement, as it does not require us to change any AOM frequency sources unlike the kicking method<sup>||</sup>. Additionally, the pulling method can be applied to traps where

<sup>¶</sup>During the experimental setup, we account for any voltage offsets between sources by measuring the output frequency of the VCO using an RF meter. This is also how we determine the needed voltage change for the  $\approx 1$  MHz shift.

<sup>||</sup>The loading trap uses a VCO so changing the voltage source is enough. However, the sheet/dimple is run from a IntraAction driver with a fixed digital synthesizer as the input. For kicking with the sheet, we temporarily replace the synth with a VCO, but be careful as this will also change the gain of the power lock circuit (Synth outputs  $\approx 0$  dbm but VCO outputs  $\approx 10$  dbm)

the 1064 nm light is recycled whereas previously our only recourse in this configuration was to measure trap frequencies via intensity modulation. Briefly, the pulling procedure is

- I. Using an unmodified ODT, load and evaporate down to the trap of interest.
- A. While evaporating, trigger the mirror pistons to withdraw and expose the Arm C path to the atoms.
- II. After evaporation, ramp up a slightly mis-aligned Arm C to high power over 250 ms then allow the atoms to equilibrate for another 250 ms in the combined two beam IR, one beam 532 ODT.
- A. The final power of the 532 nm beam when enabled should be adjusted to provide an adequate force without collapsing the IR ODT.
- III. Diabatically extinguish the 532 nm beam and hold in the optical dipole trap for varying evolution times before releasing and performing time-of-flight imaging.

The controlled mis-alignment of the 532 nm Arm C beam is facilitated by an absolute positioning mirror (model: Newport Conex-AG-M100D). This mirror provides a computer controllable interface for reproducibly changing the Arm C beam alignment and exciting center-of-mass oscillations along each of the IR beam directions.

### **Historical notes and tips for usage**

**IPG failure:** In the fall of 2018, the IPG YLR-20-LR, which had been in use for about a decade, died due to a thermal issue which led the internal fiber amplifier

to overheat and burn. As of April 2019, this laser is being replaced by an IPG YLR-50-1064-LR which is a diode pumped, multi-mode, linearly polarized Ytterbium fiber lasers with a maximum power output of 50 W. This system is being installed by Josh Hil, who is also reconstructing some elements of the paths reported in Ying's thesis.

### 2.3.4 Optical lattice trap: 532 nm

Until recently, experiments on the Neutral apparatus were confined to work with bulk gases in an optical dipole trap. While optical dipole traps are useful for efficient evaporation and thermalization of an ultracold gas, optical lattices greatly extend our capabilities for studying ultracold molecules and novel many-body quantum states give some refs.

Optical lattices are formed by a standing wave of light which creates a defect free periodic potential. These traps are extremely versatile and have enabled the observation of the superfluid - Mott insulator transition [28], artificial gauge fields for neutral atoms [47], quantum microscopy with single-site resolution [? ], and investigations of quantum magnetism [? ? ]. They are among the most well-established techniques for controlling a quantum state and have proven to be great tools for exploring the connection between few- and many-body systems [? ].

#### 2.3.4.1 Background

An optical lattice is created by counterpropagating two laser beams to form a standing wave pattern, which for two plane waves in one dimension results in a periodic potential given by

$$V(x) = V_{lat} \sin^2(k_L x) \quad (2.8)$$

where  $V_{lat}$  is the lattice depth determined by the polarizability of the atom for a given trapping wavelength  $\lambda$  and laser intensity  $I$ , and  $k_L$  is the lattice wavevector. This potential can be readily extended to three dimensions using two additional pairs of counterpropagating laser beams along the  $y$  and  $z$  directions which results in a

3D cubic lattice. Depth of the trapping potential,  $V_{lat}$ , is controlled by varying the intensity of the lattice beams.

Periodic potentials are powerful because they break the translational invariance of space which results in the formation of band structure and the opening of bandgaps or disallowed particle energies [4]. Because of this broken invariance,  $p$  is no longer a good quantum number and must be replaced by two new quantum numbers: the band index,  $n$ , and the quasimomentum,  $q$ . In one dimension, quasimomentum is specified by  $q = p - nG$ , where  $G = 2\pi/a$  is a reciprocal lattice vector, and  $a$  is the real space lattice constant. Fig. 2.3.4.1 shows how the band structure varies as the lattice depth is increased. Optical lattices have a lattice spacing  $a = \lambda/2$  which determines the reciprocal lattice vector  $G = 4\pi/\lambda = 2\hbar k_L$  and a natural energy scale  $E_r = \frac{\hbar^2 k_L^2}{2m}$  where  $m$  is the atomic mass and  $k_L$  is the lattice wavevector,  $k_L = 2\pi/\lambda$ . From the band structure, we see that the bandwidth of each band, given by  $\Delta E = E_{q=\hbar k_L} - E_{q=0}$ , decreases as the lattice depth is increased. In the limit that  $V_{lat} \rightarrow \infty$  the band structure reduces to a ladder of harmonic oscillator levels spaced by  $\hbar\omega_{ho} = \sqrt{4V_{lat}E_r}$ . Although, for moderately deep lattices,  $V_{lat} \gtrsim 5 E_r$ , this approximation is valid near the center of the Brillouin zone,  $q = 0$ , and provides a simple form to estimate the energy gaps between bands [38? ].

Solutions to the Schrödinger equation in a periodic potential are given by the Bloch functions [4]

$$\phi_q^{(n)}(x) = e^{iqx/\hbar} u_q^{(n)}(x) \quad (2.9)$$

These eigenstate wavefunctions are specified for a given quasimomentum  $q$ , and band index  $n$ . Their corresponding energy eigenvalues define the band structure of the

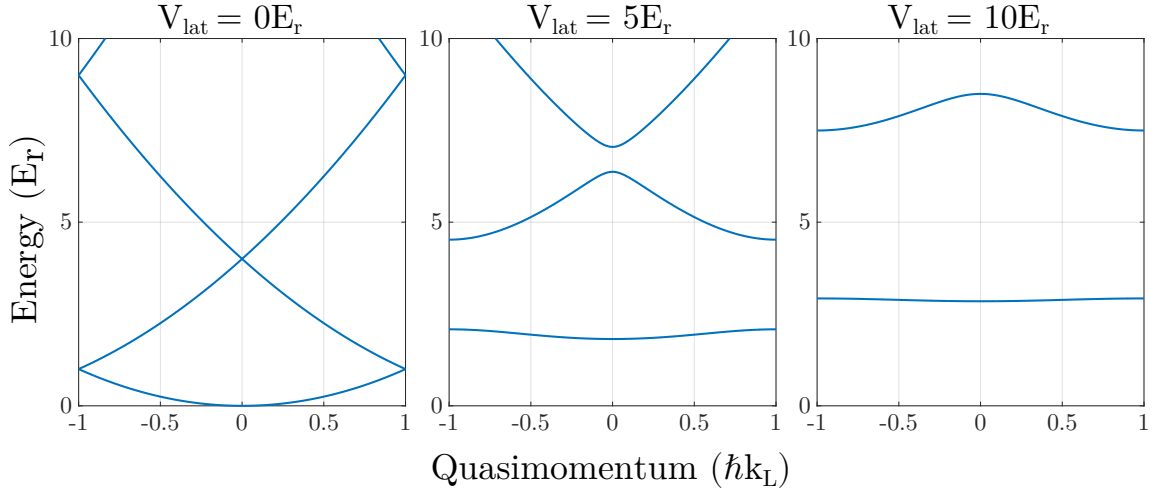


Figure 2.24 : 1D band structure as a function of lattice depth

One dimensional band structure for an optical lattice as the lattice depth is increased. The band energies are found by solving the Schrödinger equation using the Bloch functions of Eq. 2.9.

lattice shown in Fig. 2.3.4.1. From Eq. 2.9 we see that the Bloch functions are the product of plane waves modulated by a function  $u_q^{(n)}(x)$ , which shares the periodicity of the underlying lattice potential [4]. For an optical lattice this modulating function can be expanded in a basis of plane waves through a Fourier decomposition of the lattice potential in Eq. ??, which gives [1],

$$u_q^{(n)}(x) = \sum_l c_l^{(n,q)} e^{i2lk_L x} \quad (2.10)$$

Here  $c_l^{(n,q)}$  are the coefficients for each plane wave in the basis expansion that are found by diagonalizing the lattice Hamiltonian [1].

Often, we are interested in the dynamics of particles on a particular lattice site, but since Bloch functions are delocalized over the entire lattice, it is useful to instead

use the Wannier functions. These functions provide an orthogonal and normalized set of wavefunctions that are maximally localized to a specific lattice site. The Wannier function for a localized particle in the  $n^{th}$  band of a lattice site located at position  $x_i$  is given by [38]

$$w_n(x - x_i) = \mathcal{N}^{-1/2} \sum_q e^{iqx_i/\hbar} \phi_q^{(n)}(x) \quad (2.11)$$

where  $\mathcal{N}$  is a normalization constant and  $\phi_q^{(n)}(x)$  are the Bloch functions of Eq. 2.9. This localized description of particles allows us to calculate important physical quantities which govern dynamical properties of the lattice such as the tunneling rate,  $J/\hbar$ , and on-site interaction energy,  $U$ . As  $V_{lat} \rightarrow \infty$ , the Wannier functions approach the eigenfunctions of the harmonic oscillator, which allows us to estimate the spatial extent of an atomic wavefunction by  $a_{ho} = \sqrt{\frac{\hbar}{m\omega_{ho}}}$  [38].

### 2.3.4.2 Setup and alignment

#### Setup

Our optical lattice operates at  $\lambda = 532$  nm and is derived from a Coherent Verdi V-18 single mode laser which is sent through separate AOMs for intensity control of each arm before propagating in free space to the atoms. We label these arms A, B, & C as noted in Fig. 2.25. Figs. 2.26 - 2.28 show the detailed beam profiles for the lattice and specify the spot size at the atoms for each pass of all three arms. The horizontal arms are linearly polarized with the polarization vector aligned along the  $z$  direction, parallel to gravity. The vertically propagating beam is also initially linearly polarized, however when propagating vertically, this polarization appears as a superposition of  $\sigma+$  and  $\sigma-$  vectors in the frame of the atoms. With this configuration we can achieve

lattice depths  $\gtrsim 30E_r$  in an isotropic lattice.

### **Aligning the first pass:**

The following is a technique conveyed to our lab from Trey Porto. We have successfully used this technique to reproducibly align the first pass of the optical lattice to maximize overlap with the 1064 nm optical dipole trap. This process relies on co-locating the trapping regions of the 532 nm and 1064 nm traps by observing the change in amplitude of center-of-mass oscillations due to misalignment of 532 nm. Additionally, we have observed breathing mode oscillations when the 532 nm and 1064 nm traps are well overlapped due to the change in trap depth, and correspondingly the potential energy of the atoms, when flashing off the 532 nm light.

Below is our prescription for overlapping the first pass of the lattice with the IR trap.

I. This process requires the oscillations start from a consistent equilibrium. We achieve this through the following experimental sequence:

- A. Typical trapping sequence of blue MOT, repump, red MOT broadband, red MOT single frequency + ODT load
- B. After loading the ODT, evaporate to a reasonable depth for the given loading time. Note that we have observed thermal effects from the ODT which may lead to inconsistent spatial behavior. Therefore, the point where the beam overlap should be optimized is at or near the desired IR trap depth for the proposed experiments.
- C. Following the forced evaporation, hold in the 1064 nm trap while ramping

	Label	Part	Position [cm]	Distances [cm]	
Arm A	AOM	IntraAction AFM-804A1	-126.5	AOM → A1	24.1
	PBS	Thorlabs PBS12-532-HP	-117.8	A1 → A2	22.3
	Lens	CVI PLCX-25.4-772.6-UV-532	-106.5	A2 → A3	35
	Dichroic - 1	Thorlabs HBSY12	-30.6	A3 → A4	4.5
	Dichroic - 2	Thorlabs HBSY12	43.6	A4 → AD1	10
	Retro mirror	CVI Y2-1025-0-0.30CC	69.9	AD1 → Atoms	30.6
				Atoms → AD2	43.6
				AD2 → ARM	26.3
Arm B	AOM	IntraAction AFM-803A1	-167.1	AOM → B1	19
	PBS	Newport PBS-5811	-154.6	B1 → B2	25
	Lens	CVI PLCX-25.4-772.6-UV-532	103.1	B2 → B3	46
	Dichroic - 1	Thorlabs HBSY12	-36.1	B3 → B4	23.5
	Dichroic - 2	Thorlabs HBSY12	30.5	B4 → B5	14
	Retro mirror	CVI Y2-1025-0-0.30CC	73.5	B5 → BD1	3.5
					BD1 → Atoms
					Atoms → BD2
					BD2 → B6
				B6 → BRM	18
Arm C	AOM	IntraAction AFM-803A1	-117.5	AOM → C1	45.5
	PBS	Thorlabs PBS12-532-HP	-109.5	C1 → C2	25.5
	Lens-1	CVI PLCX-25.4-772.6-UV-532	-89.5	C2 → C3	15
	Retro lens	CVI PLCX-25.4-149.9-UV-532	14.6	C3 → C4	5.5
	Retro mirror	CVI Y2-1025-0	18.2	C4 → Atoms	26
					Atoms → CRM 18.2

Table 2.7 : Lattice optics details

All measurements are specified in centimeters. The optics position is given with respect to zero defined at the atom position. Distances are referenced to the optics labels given in Fig. 2.25.

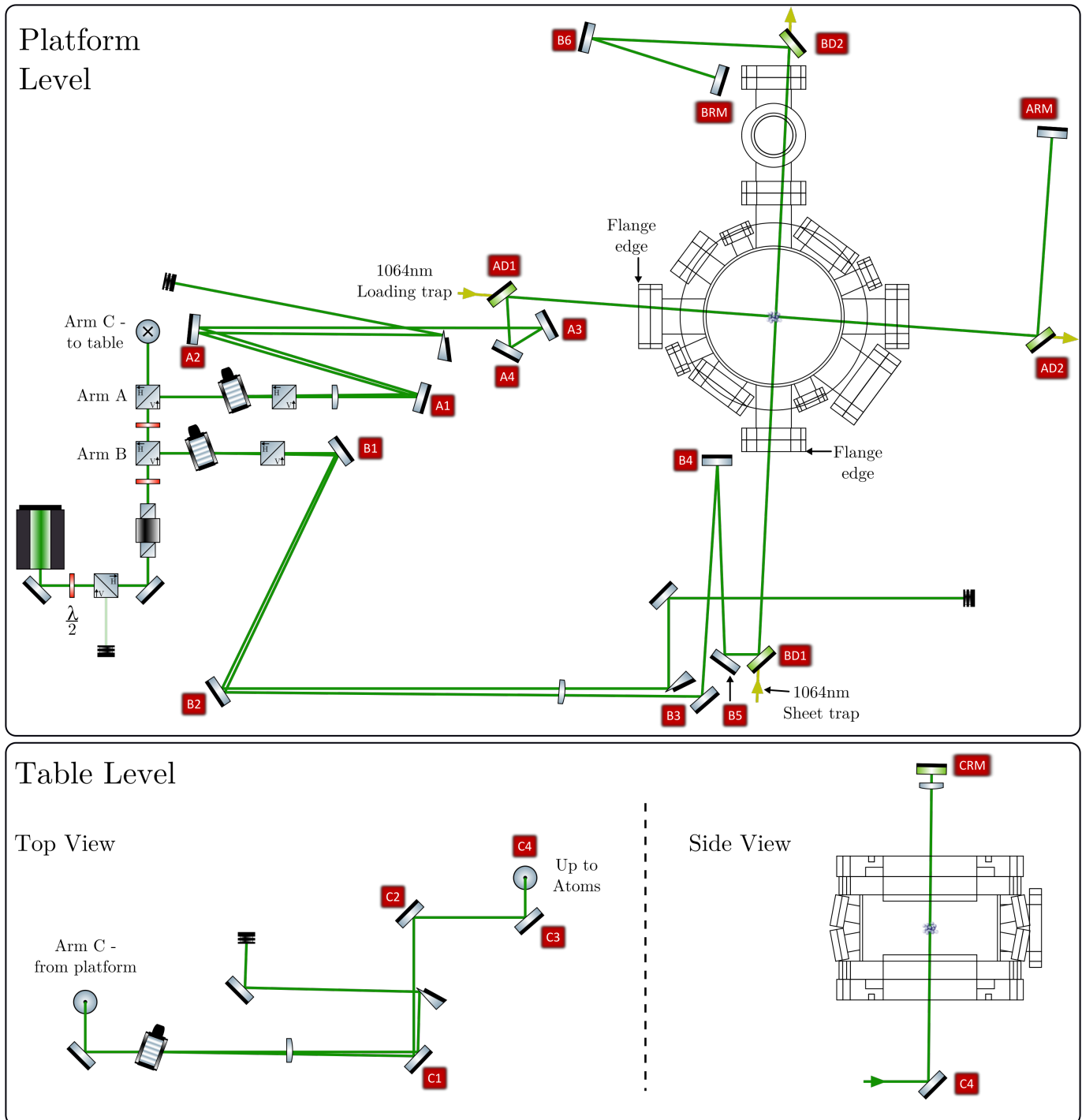


Figure 2.25 : Lattice optical schematic

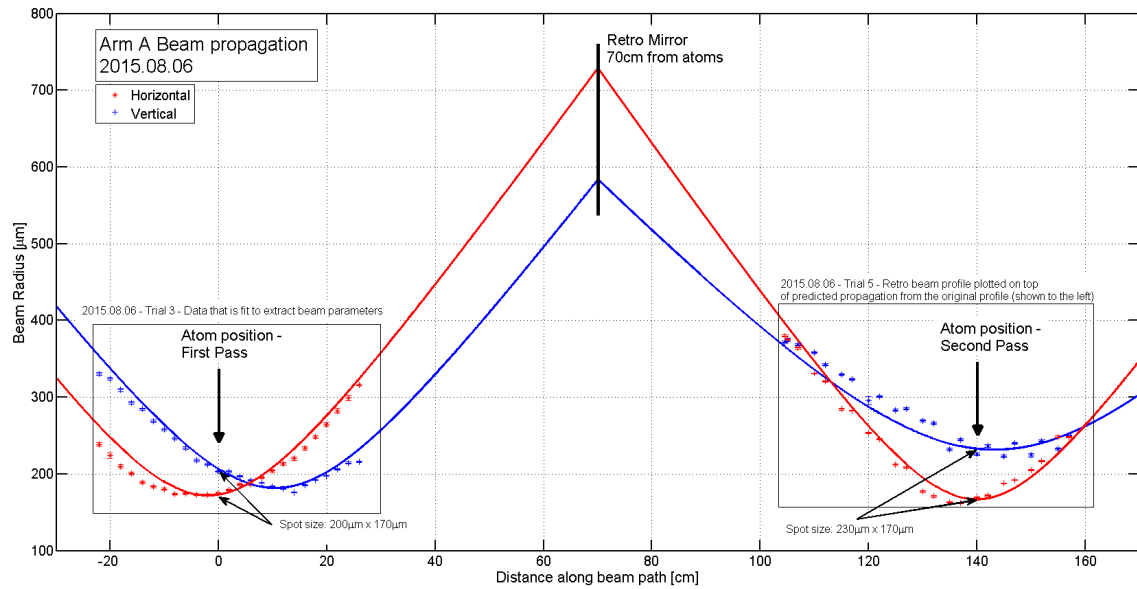


Figure 2.26 : Lattice Arm A profile

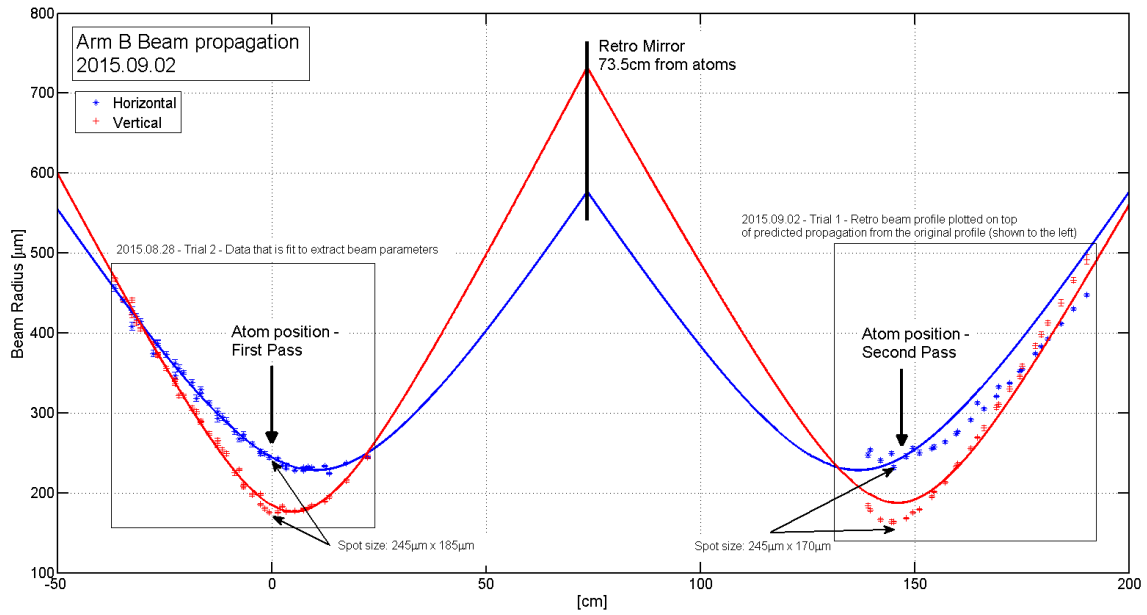


Figure 2.27 : Lattice Arm B profile

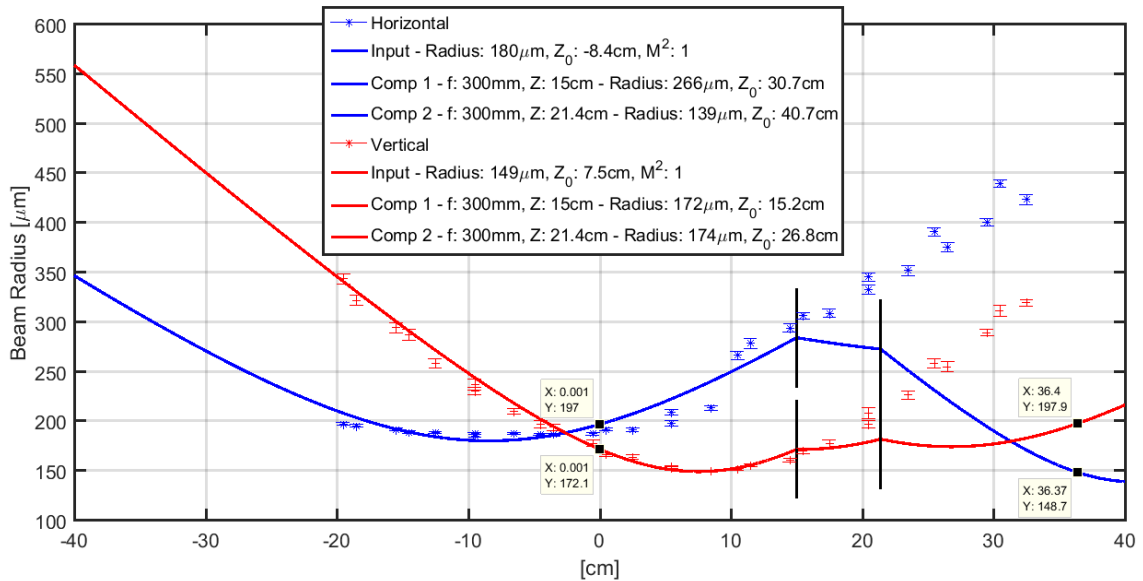


Figure 2.28 : Lattice Arm C profile

up the lattice arm being studied to full power. We generally find a ramp of approx. 200 - 300 ms worked best for strontium 84.

- D. Once the green is at full power, we additionally hold for approx. 250 ms in the combined 532 + Crossed IR ODT trap to allow for the equilibration of the atoms in the modified trapping potential.
- E. After the 250 ms hold, the green is flashed off to excite an oscillation within the IR ODT.
- F. Image the cloud as it oscillates

II. To evaluate the procedure above, first focus on in-situ images of the cloud,

where atoms are held in the combined 1064 + 532 nm trap\*\*.

III. When turning off the lattice and allowing the cloud to oscillate, identify the 1/4th period time of the oscillation. This is the point of maximum displacement and provides the most sensitive probe for observing how changes to the alignment may vary the oscillation amplitude. As the alignment is improved the maximum displacement is minimized, this is the signature of improving the overlap. If unsure about the oscillation period, vary the evolution time after extinguishing the 532 nm and observe the dynamics of the cloud to resolve a full oscillation.

IV. Each lattice arm (A,B,C) can then be varied along both dimensions (horizontal and vertical) while monitoring the oscillation amplitude. Lower amplitude indicates better alignment, but one must be extremely careful, as it is possible to obtain a flat response of the oscillation amplitude when severely misaligned. We have found that around the minimum in the oscillation amplitude, we are able to flip the phase of the 1/4 period oscillation as we move through the minimum. This phase flip along with the emergence of breathing mode oscillation are robust measures of good overlap between the beams.

Fig. 2.29 shows an example of the above process where for each scan we have varied the beam alignment slightly and can clearly observe a suppression of the oscillation amplitude. However, extended time series data in this fashion is arduous and we

---

\*\*Start by moving the VI cursor positions to be on the cloud center and drawing a box around the cloud location. This will help to identify small movements of the cloud as well as recording your start position.

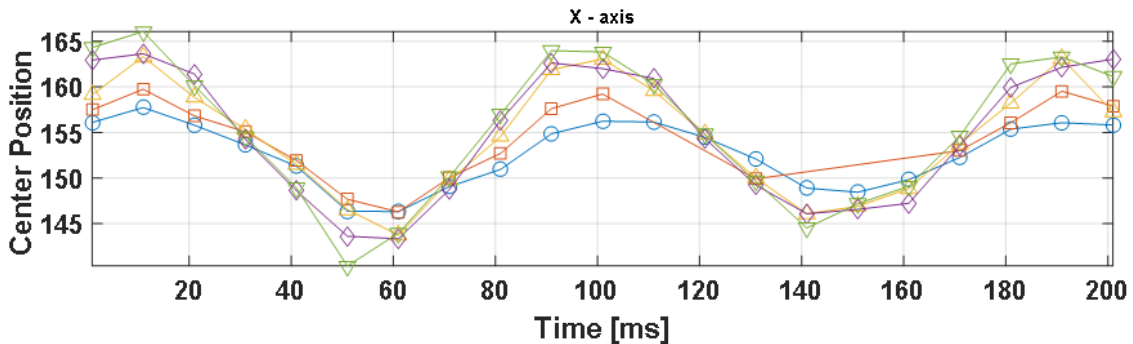


Figure 2.29 : Center-of-mass amplitude suppression when overlapping traps

Each subsequent scan is a small variation in the pointing of the last mirror directing the 532 nm light before the chamber. Note that the Y-axis is in arbitrary units.

have found similarly effective alignment to result from the single-point measurement as outlined above.

Additionally, Fig. 2.30 shows the emergence of a breathing mode when the traps are well overlapped. Observation of oscillatory behavior of the cloud radius with reduced deviation of the cloud center is a robust measure of the overlap of the 532 and 1064 traps.

### Aligning the retro-reflection:

The retro-reflection is optimized via the 2-band Kapitza-Dirac method. For a quantum degenerate gas in shallow lattice depths,  $\sqrt{10} E_r$ , only the  $\pm 1$  plane waves will be populated. Furthermore, for short pulses the amplitude of the population in these plane waves is linearly increasing with lattice depth. This provides a simple single point measurement which can be used for optimizing the lattice depth. However, an iterative approach may be needed to ensure that the alignment is only optimized dur-

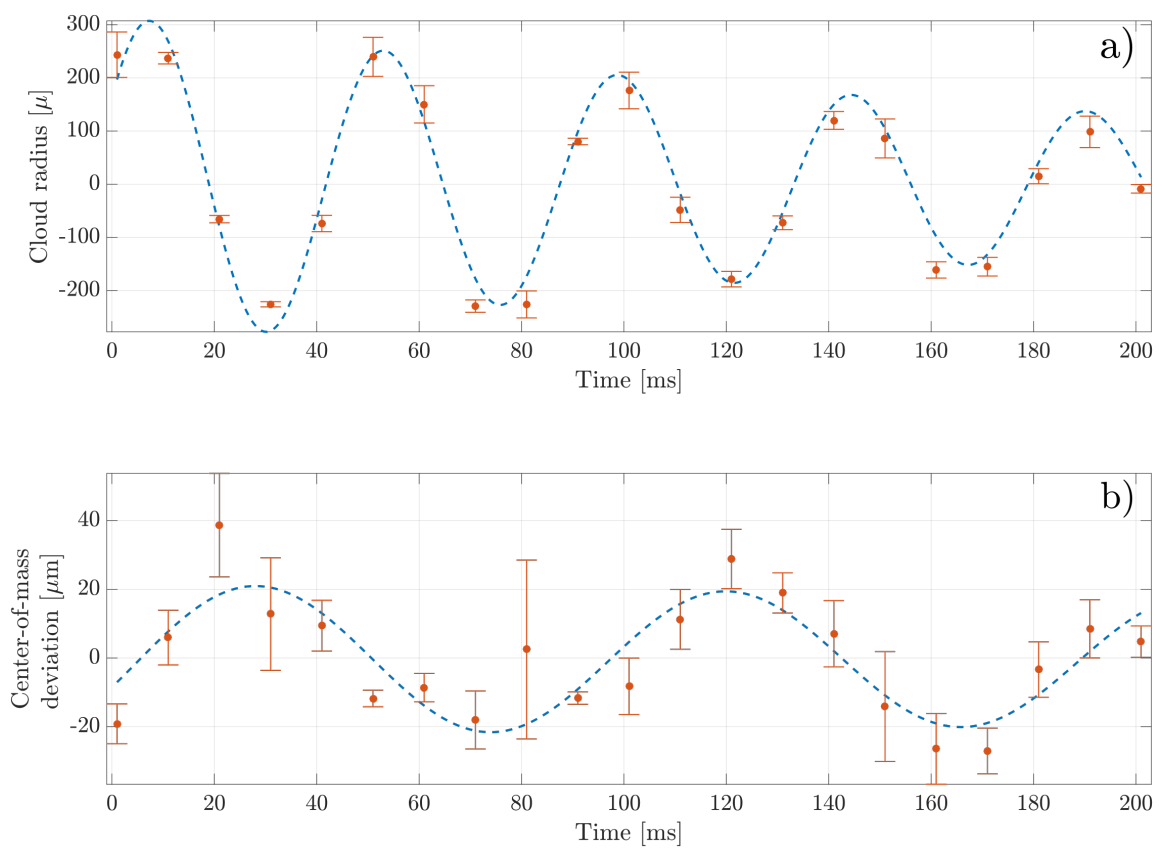


Figure 2.30 : Observation of breathing mode oscillation

a) The measured radius and b) the cloud center deviation along the horizontal axis.

ing the first quarter period before the population of the orders is maximized. Fig. 2.31 shows an example oscillation.

As our lattice is free space, the first order alignment of the retro-reflection is to overlap the incoming and retro-reflected beam over a long distance. This tends to overlap the two beams closely enough in the region of the atoms so as to begin observing diffraction effects when performing a short high intensity pulse of the 532 nm light.

Second, once we can observe diffraction, the gimbal mounted retro mirrors are adjusted to maximize the population of the diffracted plane waves<sup>††</sup>. As the diffracted population is oscillatory and depends on laser intensity we have found that using an exposure time of approx  $2 - 3 \mu\text{s}$  and varying the laser intensity has led to the most successful alignments of the retro. We generally start with this short time pulse of a few microseconds using the highest intensity pulse possible and systematically decrease the laser power into the lattice arm as the alignment is improved. Finally we note that, as Kapitza-Dirac happens on very short timescales, the power stabilization circuits must be bypassed for this procedure. Instead, we directly drive the RF sources with fast analog IC switches (switching time on the order of 10's ns) to apply the desired power to the lattice arm.

---

<sup>††</sup>This alignment is extremely sensitive and may ultimately benefit from a more reproducible method of adjustment as mount backlash can strongly effect this process.

### 2.3.4.3 Measurement and results

#### Kaptiza-Dirac Scattering

Kapitza-Dirac diffraction can be viewed as a diabatic projection from an initial eigenstate to a new set of eigenstates which results in an oscillation of the wavefunctions probability amplitudes over the new eigenstates of the system [33]. As was discussed in Sec. 2.3.4.1, the free space eigenstates are not the eigenstates of the lattice Hamiltonian. Thus a pure  $p = 0$  plane wave,  $|\phi_{p=0}\rangle$ , suddenly loaded into an optical lattice can be written as a superposition of the Bloch states given by Eq. 2.9, here denoted by  $|n, q\rangle$ .

$$|\Psi(t=0)\rangle = \sum_{n=0}^{\infty} |n, q\rangle \langle n, q| \phi_{p=0} \rangle \quad (2.12)$$

The time evolution of this state is then given by

$$|\Psi(t)\rangle = \sum_{n=0}^{\infty} |n, q\rangle \langle n, q| \phi_{p=0} \rangle \exp\left(\frac{-iE_n(q)t}{\hbar}\right) \quad (2.13)$$

where  $E_n(q)$  is the energy of the Bloch state at a specified  $q$  and  $n$  shown in Fig. 2.3.4.1. The exponential factor of Eq. 2.13 introduces oscillations among Bloch states and after a second diabatic projection back to the plane wave basis, we can relate evolution of plane wave population to the bandgap energy. From this analysis we find that for relatively weak lattices,  $V_{lat} \lesssim 10E_r$ , the plane wave population will vary as  $\omega_{osc} = (E_2 - E_0)/\hbar$ . Where  $E_i$  is the band energy of the  $i^{th}$  band with  $q = 0$  as is the case when performing Kapitza-Dirac with a Bose-Einstein condensate.

Fig. 2.31 shows a typical Kapitza-Dirac oscillation pattern which we use to maximize beam overlap near the atoms and calibrate our achievable lattice depths. Kapitza-Dirac is useful as an alignment tool since measurement of the population oscillation

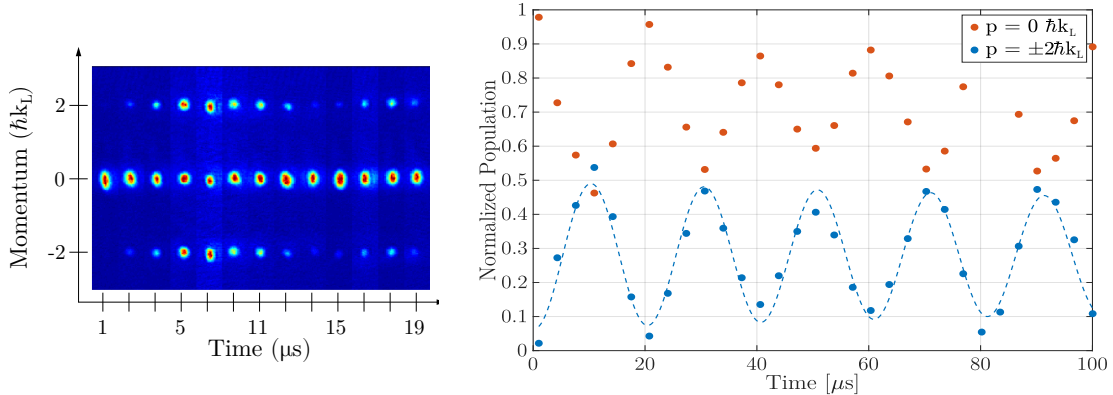


Figure 2.31 : Evolution of plane wave population using Kapitza-Dirac

Left: Time of flight slices for several realizations of Kapitza-Dirac with varying hold time in the lattice. Right: Normalized population from fits of time-of-flight images. Oscillations are fit with a decaying sinusoidal and the best-fit frequency is used to determine the lattice depth.

frequency can be highly accurate and directly relates to the bandgap energy in the lattice, shown in Fig. 2.3.4.1.

For reference, Fig. 2.33 shows the resulting lattice depth calibration for our most recent alignment.

**Higher order Kapitza-Dirac:** The simple two-band model is a straightforward method for determining the lattice depth but one that requires a time-series measurement over varying lattice depths. Gadway et. al. [25] derived a complementary depth calibration method which requires only a single time-series measurement at high lattice depth. This process relies on the quantum interference of the oscillating populations which produces a complex beat note. An undergraduate report

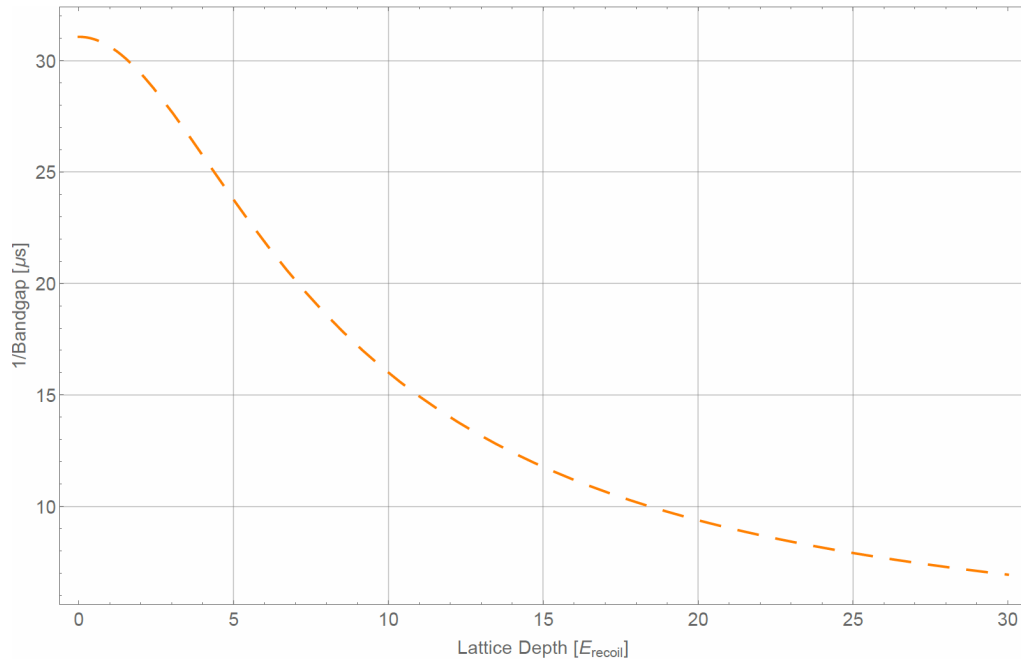


Figure 2.32 : Oscillation period between  $n = 0 \rightarrow n = 2$  band at  $q = 0$

Calculated for a 532 nm lattice acting on strontium-84.

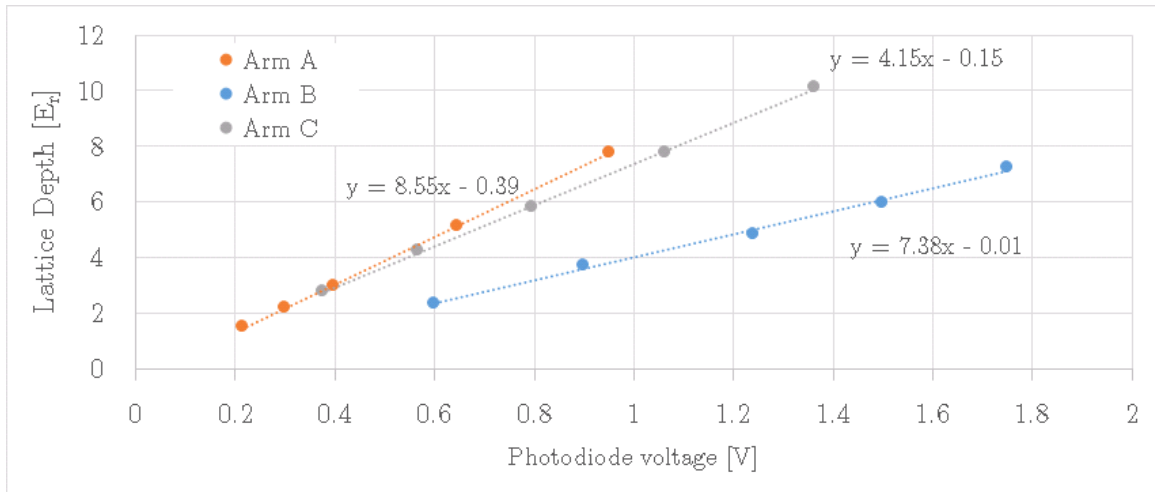


Figure 2.33 : Lattice depth calibration

Calibration was performed using the two-band Kapitza-Dirac technique. Maximum photodiode voltage for each arm is 10 V

from Alex Wikner [82], follows the original Gadway construction to develop an algorithm using Matlab<sup>TM</sup> for applying this technique to the Neutral apparatus. The cited report provides sample code as well as benchmark calculations for comparison. However, application of this work to calibrate the lattice depth has been stymied by a consistent heating concern we have observed when applying the lattice beams for significant periods at high lattice depths.

### **Heating of a quantum degenerate gas**

While Kapitza-Dirac diffraction is useful as a characterization tool, we typically wish to maintain equilibrium when loading condensates into the lattice. Thus slowly ramping up the lattice laser intensity will adiabatically transform a plane wave ground state into the ground Bloch state of the lattice [68]. Strictly speaking, in order to adiabatically connect the free space eigenstates and the lattice eigensates, the lattice must be turned on infinitely slowly due to the infinitesimal bandgaps which open near the band edges. Although near the band center,  $q = 0$ , the adiabaticity requirement relaxes to  $dV_{lat}/dt \ll 16E_r^2/\hbar$ , [33] which for strontium in a 532 nm lattice is  $\approx 5 \mu\text{s}/E_r$ . However, in practice we find that our condensate fraction is reduced during fast ramps into the lattice. Instead, we slowly ramp on the lattice over 100 ms which reduces heating caused by the ramp. We have experimented with various functional forms of this pulse shape and currently rely on an S-shaped curve given by Eq. 2.14

$$V_{sCurve}(A, B, C, t) = \frac{A - C}{2} [\tanh(2\pi B[t - 1]) + 1] + C \quad (2.14)$$

where A is the overall amplitude starting from zero, B is the timescale for one period, and C is a constant offset term.

As shown in Fig. 2.34, we observe a large condensate fraction after ramping the lattice up and back down in this manner to demonstrate restoration of BEC coherence. Further characterization of the lattice required us to measure the reduction of atom population over long times due off-resonant light scatter. For our red detuned optical lattice we expect the off-resonant scattering rate to be well approximated by a simple two level approach. In this model, the effective scattering rate is given by [38]

$$\Gamma_{eff} \approx \frac{\Gamma V_{lat}}{\hbar \delta_{lat}} \quad (2.15)$$

where  $\Gamma$  is linewidth of the dipole transition between the two states,  $V_{lat}$  is the lattice depth, and  $\delta_{lat}$  is the detuning of the optical lattice from the two level transition frequency. In strontium, the  $^1S_0 \rightarrow ^1P_1$  transition strongly dominates the polarizability of the ground state and therefore can be used to estimate the effective off-resonant scattering rate. For this transition  $\Gamma = 2\pi \times 30.5$  MHz and a 532 nm lattice is detuned by  $\delta_{lat} \approx 2\pi \times 87$  THz. With a lattice depth of  $V_{lat} = 10 E_r$  we expect a scattering rate of  $\Gamma_{eff} \approx 2 \times 10^{-1} \text{ s}^{-1}$ , which is negligible for the timescales of our proposed experiments. From Fig. 2.34, we see that there is not an appreciable loss of atoms over a one second timescale. Unfortunately, we have recently observed that attempts to load a degenerate gas into a deep lattice,  $\gtrsim 15 E_r$ , and hold over long timescales leads to unacceptable heating of the atomic sample. Currently, we hypothesize that this may result from the freespace nature of the lattice or an intrinsic instability (frequency or power) of the Verdi. The latter of these has been tested by monitoring the 532 nm light in a spectrum analyzer where no obvious deficiencies have been observed. To test our stability hypothesis, we are currently investigating fiber coupling one of the arms of the lattice but as of spring 2019, this project is ongoing.

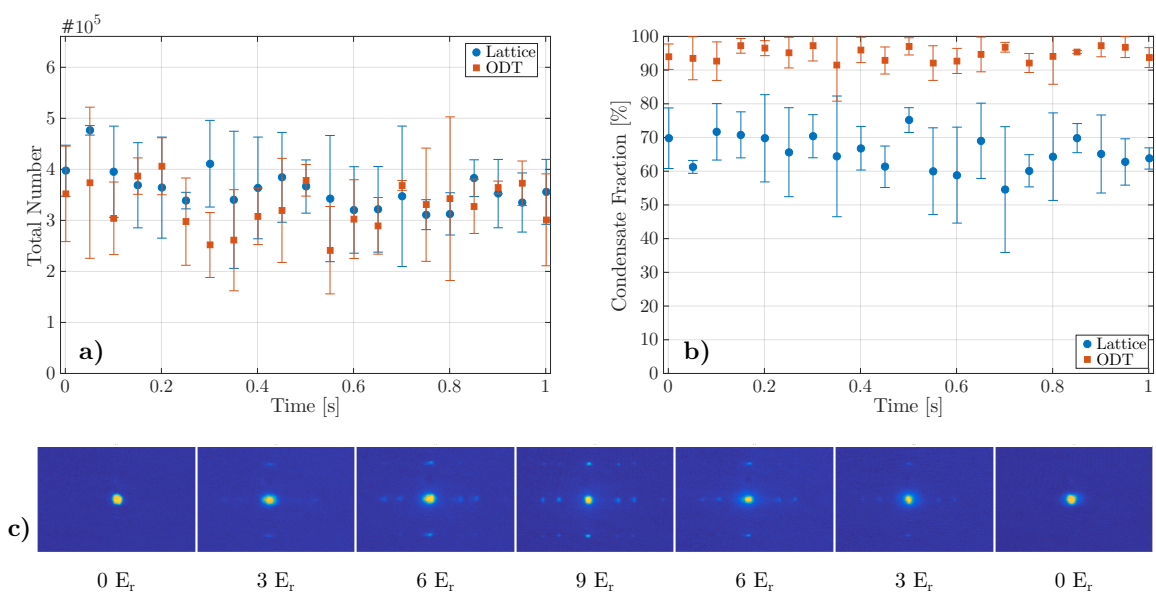


Figure 2.34 : Characterization of heating in the optical lattice

Evolution of condensate fraction over time after adiabatically ramping on the lattice to  $9 E_r$ . a,b) Comparison of total number and condensate fraction for a sample held in the optical dipole trap (red squares) or in a deep lattice (blue circles). c) Time of flight images after ramping on the lattice and diabatically projecting back to plane wave states.

### 2.3.5 Optical toolbox

#### 2.3.5.1 Absorption imaging system

Absorption imaging is a destructive measurement process which is predicated on measuring the spatially distributed attenuation of laser light after passing through an atomic cloud. In this section we will discuss the technical details of the Neutral absorption system and postpone the theoretical description of the process to Sec. 3.2.1. Additionally, we will reserve the discussion of image processing for App. B which details our software used to analyze the images and extract our physical measurements.

Fig. 2.35 shows a simplified schematic of the absorption imaging system. Light is derived from the MOT path subsystem and guided to the atom chamber via freespace propagation. After passing through the atoms an imaging system shapes and focuses the image onto a Cooke PixelFly CCD camera. The PixelFly is a 12 bit 1280x1024 CCD with a pixel size of  $6\ \mu\text{m}$ . The imaging relay system shown after the atomic sample was developed by Mi Yan and is outlined in detail in App. A of his PhD thesis [86]. Much of the imaging sequence is a standard procedure, however, day to day operation may be affected by system performance.

When taking images, we measure the optical depth to extract the properties of the atomic cloud, the physics of which is discussed in Sec. 3.2.1. For now, we will take as a given that each experimental sequence requires one image with the atoms in frame and another background image without the atoms. In the ideal scenario these two images would be identical except in the region of the atom cloud and thus information about the cloud could be inferred using Beer's law [ref](#). Although, practically we must wait for the atoms to exit the frame and thus introduce a time

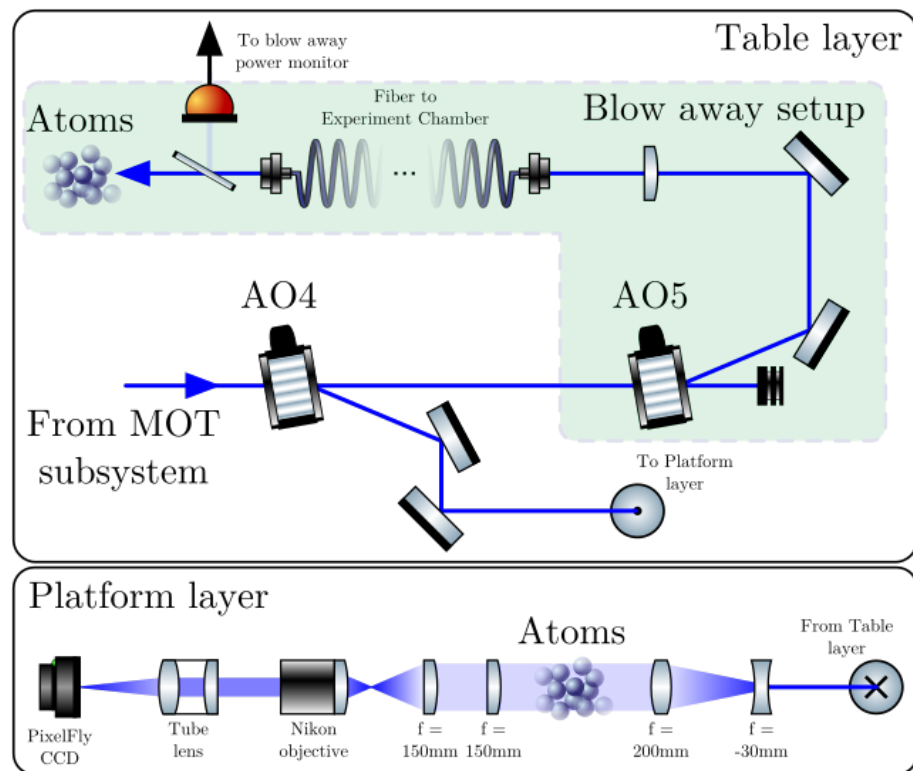


Figure 2.35 : Absorption imaging and blow away pulser optical schematic

Details on the construction and characterization of the blow away setup are available in Josh Hill's masters thesis [ref.](#)

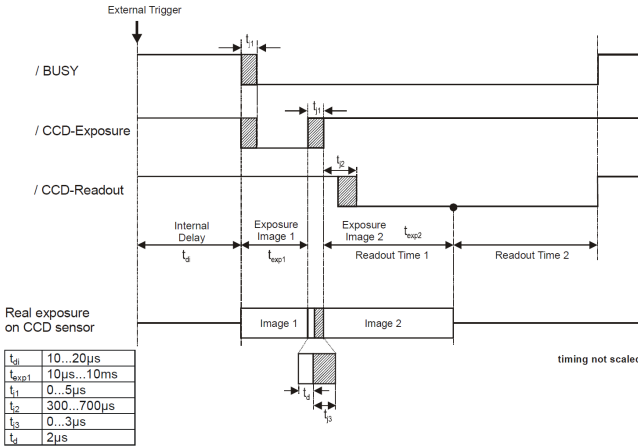


Figure 2.36 : Timing diagram of PixelFly doubleshutter mode

$t_j$  refers to timing jitter inherent to the camera. In this scheme the first exposure can be controlled via the external trigger but the second image exposure is fixed to the readout time of the first image.

delay between the consecutive images which we seek to minimize. For this reason we utilize a special feature of the PixelFly called "double-shutter" mode. This particular imaging mode of the camera utilizes a second hidden set of pixels that are interleaved with the active pixels of the CCD. Typically the acquisition time between consecutive images taken with a CCD is limited by the analog-to-digital conversion time needed to readout the image from the pixels into the camera's memory. However, the PixelFly's set of hidden pixels lets the first image taken, simply shift one row down from the active pixels into the hidden area once the externally triggered exposure time has elapsed. Once shifted down, the active pixels are free to be exposed again. With this process the time between images is reduced to 5μs. Fig. 2.36 shows a full overview of this process. The drawback of this scheme is that for exposure times less than the

readout time of an image, the second image is forced to have a minimum exposure of the readout time. This presents a challenge as our exposure time is about four orders of magnitude faster than the readout time. To overcome this, we rely on the fast response of the imaging system AOMs, a high extinction ratio of the 461 nm photons, and a narrow line filter centered at 461 nm attached directly to font face of the CCD. Fig. 2.35 shows two AOM's along the imaging path before the atoms. We found two AOM's necessary to attenuate leakage light along the path to acceptable levels while maintaining fast response times which a physical shutter cannot replicate.

Great care is taken to reduce the time between images since the laser intensity and frequency might drift between the atom and background images. Variations in intensity have straightforward implications for errors in measuring the optical depth since the characterization of the atomic number density assumes the only difference between the images is due to the presence of scattering particles and does not account for fluctuating photon number.

A more insidious source of error in absorption imaging is variation of the optical frequency. Coherent, frequency stabilized radiation is used to illuminate the atom cloud so that we may control the optical absorption cross section and accurately model the atomic number density. However, this laser light is passed through many optical components on it's path to the atoms and ultimately the imaging camera. Small reflections along this path result in a multitude of interferometers which cause small scale spatial intensity variation across the beam. Exacerbating this problem are short time frequency drifts that may occur between the atom and background images which result in slightly different fringe patterns in the atom and background images. Fringes patterns are a well known nuisance in experimental AMO images and

it has become routine to use linear algebra techniques (PCA, ICA, etc.) to create a composite background image for each atom image during analysis in order to create a higher quality image of the optical depth[70]. A brief discussion of the principal component analysis (PCA) algorithm employed by the Neutral analysis routine is outlined below.

Briefly, the PCA approach is as follows:

- I. Find a basis set of background images from a large set of raw background images.
- II. For a single atom image, construct an initial guess at a composite background image using coefficients to weight each basis image resulting in a superposition of the basis images.
- III. Segment the atom image into multiple regions by separating out the region of interest around the atom cloud.
- IV. Comparing similar regions between the composite background and the atom background region, perform a least-squares minimization by varying the weighting coefficients of the composite background.
- V. Once a suitable composite background has been found, calculate the optical depth using the atomic region of interest and the corresponding region of the minimized composite background image.

This procedure is repeated for each atom image using a static background basis set that is computed for each scan. Fig. 2.37 shows an example of using this technique with a background set of 20 other images (not shown). While PCA does not com-

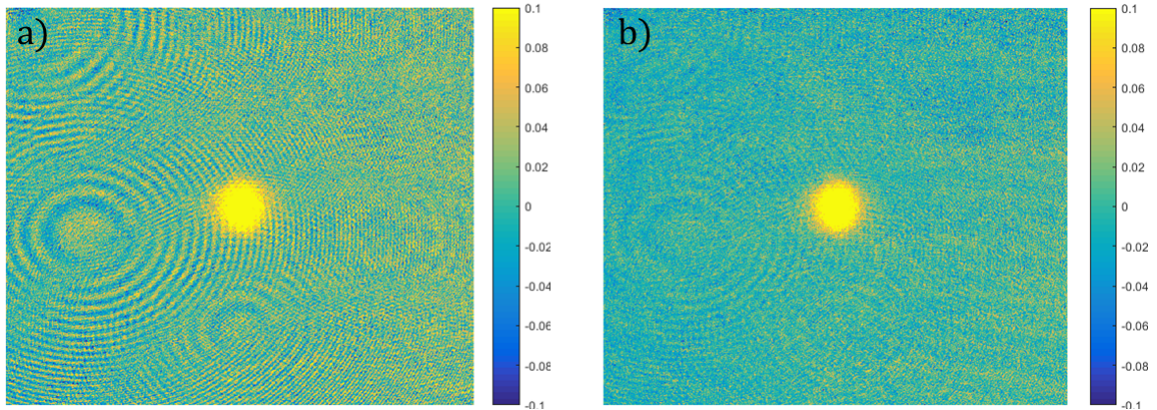


Figure 2.37 : Comparison of background subtraction methods

Background subtraction on the same image performed using two different methods and plotted on the same color scale. a) The partner-in-time background to the atom image is used. b) A composite background image formed via PCA is used.

pletely eliminate the visible fringe patterns, there is a noticeable reduction of the fringes in the PCA image versus the partner-in-time method.

### 2.3.5.2 Highly tunable 689 nm spectroscopy system

The spectroscopy laser is derived from a dedicated slave diode and is our primary 689 nm probe for bosonic isotopes, with the spin manipulation laser described below being used for fermions. This laser system is used for general intercombination line spectroscopy, photoassociation, Bragg scattering, and Rabi oscillation measurements.

Fig. 2.38 shows a simplified optical diagram. We found it necessary to increase the isolation out of the laser as the injection lock became unstable when coupling into the fiber couplers due to back reflections. We typically get  $\sim 25$  mW of usable power past the second isolator. As this is our primary spectroscopy laser, its optical setup

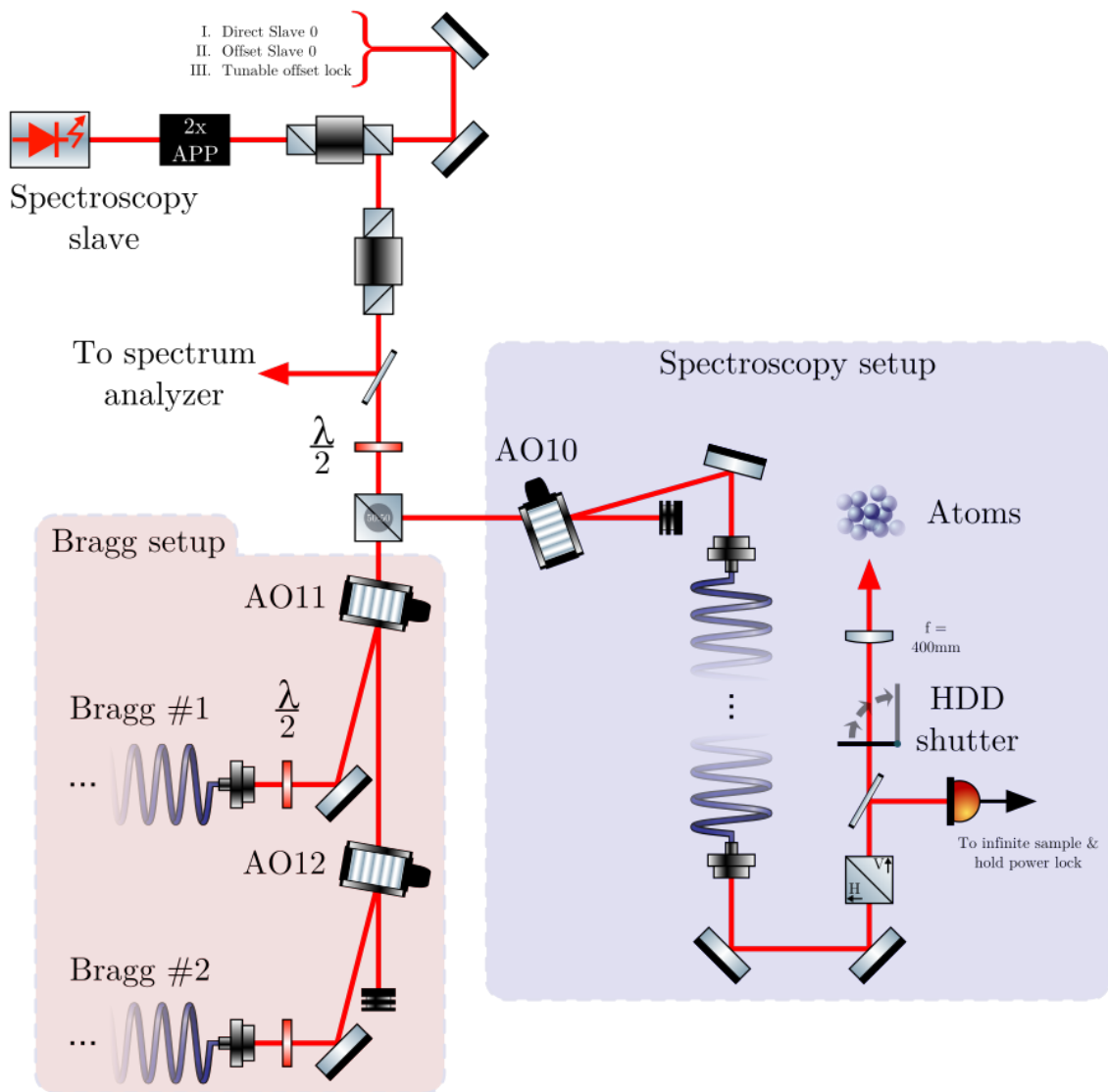


Figure 2.38 : Optical schematic: 689 spectroscopy laser

tends to be in flux but a couple of noteworthy innovations have been implemented in recent years. These include the development of an infinite sample and hold for intensity stabilization, a versatile injection locking scheme, and a shallow angle Bragg scattering setup which are discussed below.

**Infinite sample and hold:** The infinite sample and hold (ISH) circuit is used in conjunction with an intensity stabilization lock circuit and was built to allow for intensity stabilized "chirped" pulses on timescales much faster than the acquisition time of the intensity lock circuitry, typically  $\sim 70$  ms. This circuit was developed and built by Josh Hill and is based on the LTC1417 which is a low power 14-bit 400 kS/s ADC. Details of the circuit construction and characterization are left to Josh's forthcoming thesis. The ISH is currently placed on our spectroscopy probe and is situated between the intensity stabilization lock circuit and RF voltage controlled attenuator. This allows the ISH to passively sample the control voltage from the lock circuit. In sample mode the ISH output follows the input from the lock circuit. When the ISH is transitioned into hold mode, it begins ignoring changes on its input and outputs the last voltage that was sampled before the transition. A timing diagram of the infinite sample and hold usage is outlined in Fig. 2.39. Following our typical preparation sequence we place the ISH in sample mode and enable the spectroscopy probe with the HDD shutter blocking the beam. This allows the lock circuit time needed to acquire and stabilize the feedback voltage required to maintain the current intensity setpoint. Following lock acquisition, we transition the ISH into hold mode, open the shutter, and pulse the RF onto the spectroscopy AOM (AO10) via a fast RF switch, where the RF amplitude is attenuated via a voltage controlled attenuator and the

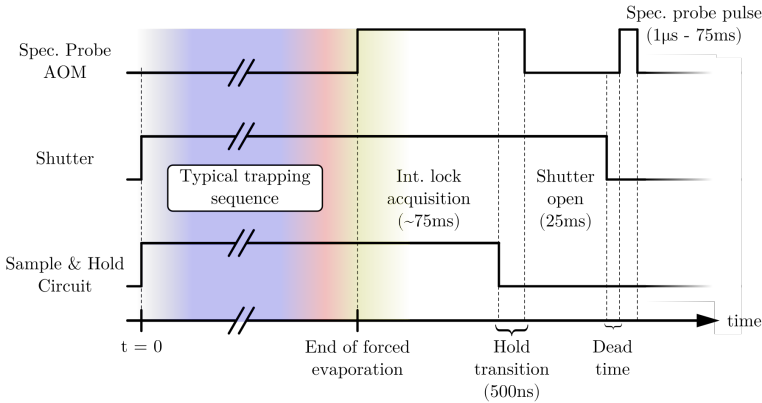


Figure 2.39 : Infinite sample and holding timing diagram

The HDD shutter in use has a full open time of  $\sim 15$  ms and the acquisition time of the sample and hold chip is on the order of  $\sim 500$  ns.

voltage input is the fixed output value from the ISH. This momentary transition to open-loop operation of the intensity stabilization circuit does suffer from slow long term fluctuations shot to shot, but provides a marked improvement on the intensity reproducibility without placing restrictions on the minimum pulse time required. Furthermore, by monitoring and recording the slowly varying intensity fluctuations, we can model any error introduced by the reduced intensity variation.

**Versatile injection locking scheme:** This scheme allows us to change the seed laser frequency via three different methods outlined below.

#### I. Directly following slave 0

- A. A small amount of light from slave 0 is coupled directly into the rejected port of the spectroscopy slave, resulting in the frequency of spectroscopy slave and slave 1 being shared. Fig. 2.19 shows the position of this pick-off

before the boson red MOT AOM. Recalling that slave 0 is always positioned +82 MHz of the bosonic isotope of interest, the direct method will position the frequency of the spec. slave to also be +82 MHz.

## II. Slave 0 minus 40 MHz

A. The light sent from slave 0 is shifted down 40 MHz by the spec. offset AOM. This positions the spec. slave frequency at +42 MHz of the intercombination line of interest.

## III. Programmable offset

A. In 2018 we re-purposed the original homemade 689 master ECDL described in Natali's thesis as a slave ECDL and directed light from this setup as a tertiary method for tuning the frequency of the spec. slave.

There are several things to note concerning the above descriptions. First, the "of interest" designation specifically refers to the variability of the laser frequency of slave 0 which is dependent on the configuration of the isotope selector AOM. Second, switching between case I and II is surprisingly trivial given the realized setup on the table. In practice, a flipper mirror and clever optical path alignment allow us to switch between these two injection methods in a matter of seconds and has demonstrated remarkable stability. Thirdly, while the programmable offset is the most versatile of the presented schemes, it also has the greatest frequency uncertainty and is fundamentally a different approach that we are still in the process of exploring.

The slave ECDL, beatnote generation, and phase locked loop (PLL) integrated circuit was a project begun by a visited student and later completed by Josh Hill. We

will leave the detailed description of the Neutral implementation for Josh's forthcoming thesis and instead reserve our current discussion to an overview of the technique. It is based on the 2009 work of Appel et. al. [89] which outlines a versatile optical phase locked loop with a claimed frequency range of sub-MHz to 7 GHz.

As a brief reminder, phase locking is a feedback scheme which seeks to maintain the frequency difference between two sources. This process is heavily used in the telecommunications industry and analog phase locking is a common technique in atomic physics laboratories as well. In atomic physics, the general idea is to generate a beatnote by interfering two single frequency lasers on a high bandwidth photodiode. From this optical beatnote we intrinsically observe the difference frequency of the two lasers as the summing frequency is well outside the bandwidth of photodiodes. The difference frequency can then be further interfered against an RF reference frequency and low-passed to generate an error signal which can be used to stabilize the difference frequency against the RF reference.

The versatile OPLL is a digital realization of this approach which we have used to lock the relative frequency difference between the Toptica master and slave ECDL from approx. 1 MHz to 1.2 GHz. The upper limited is currently bandwidth limited by our AC coupled photodiode and not by the OPLL circuitry. Fig. 2.40a) shows an example of the optical beatnote monitored via an RF spectrum analyzer. Notably, while we do observe suppression of frequency components around the set point which is characteristic of locking, we also see resonant peaking instead of a single narrow frequency peak as expected. Further investigations showed that the individual frequencies were fairly narrow as shown in Fig. 2.40b) where we observed atom loss on the  $F = 9/2 \rightarrow F = 11/2$  transition with linewidths on the order of 60 kHz.

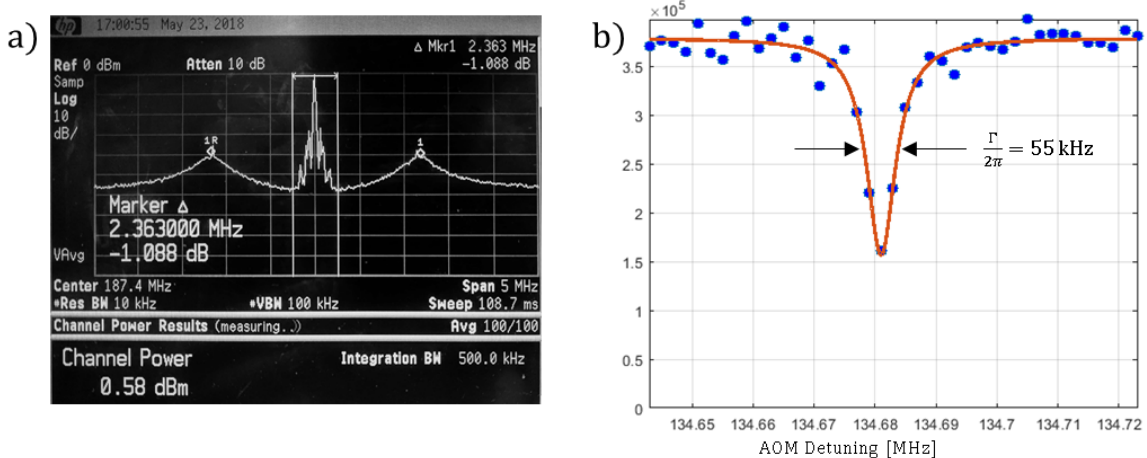


Figure 2.40 : Characterization of the OPLL performance

a) RF spectrum of the optical beatnote when the OPLL is engaged. Resonant peaking can be seen in the 500 kHz band around the center frequency. b) Atom loss spectrum which shows that the resonant features are at discrete frequencies. Differences between the AOM detuning shown and the center frequency of the OPLL are due to various AOM shifts between components.

Finally, we note that this system has also been used to perform Bragg spectroscopy as reported in the PhD thesis of Brian DeSalvo. Detailed drawings of the optical setup used for shallow angle Bragg scattering can be found in App. K.

### 2.3.5.3 Spin-manipulation laser with dynamic polarization control

Fermionic strontium-87 has become of particular interest for experiments studying quantum magnetism in a highly degenerate SU(N) system. Key to these studies is the creation and manipulation of arbitrary spin mixtures. We have recently implemented a spin manipulation laser probe (spin-man) acting on the  $F = 9/2 \rightarrow F = 9/2$  hyperfine transition of the intercombination transition for the purpose of creating well defined spin mixtures. Preliminary investigations using this system are reported in Ch. 6.

Fig. 2.19 illustrates the optical schematic of the spin-manipulation system which is derived from slave 1 and is related to the stir MOT system. The original construction of the output optics is outlined in Ch. 5 of Josh Hill's masters work [34] and is part of the layered optical systems added to the top of the optical chamber in 2017.

A key component of this layered system is the liquid crystal retarder (model: MeadowLark Optics LV-300 LCR) which allows us to dynamically control the polarization incident on the atoms. Additionally, a configurable high precision RF system for dynamically changing the spin-manipulation laser frequency allows us to perform optical pumping in a magnetic field by addressing each Zeeman transition independently. In concert, these devices allow us to, for instance, polarize to the  ${}^1S_0 (F = 9/2, m_F = 9/2)$  using  $\sigma+$  and once polarized use the LCR to rotate the light polarization to  $\sigma-$  and probe the polarized ground state along the

$^1S_0(F = 9/2, m_F = 9/2) \rightarrow ^3P_1(F = 9/2, m_F = 7/2)$ . Details of these experiments and further characterization of this system are presented in Ch. 6.

The RF tunability for optical pumping is based on the "table mode" feature of the Novatech 409B digital synthesizers which can be externally triggered to progress through a table of configured frequencies.

## 2.4 Apparatus interface

The Neutral apparatus interfaces to our digital infrastructure via a plenitude of specialized hardware implementations and custom written software. Over the last seven years nearly all of this digital infrastructure has been refactored, upgraded, or replaced. Therefore, the following sections will briefly outline these new constructs, providing references to code repositories when possible. However, detailed discussions on the usage of this infrastructure will be relegated to their respective appendices.

### 2.4.1 Software

The primary control software is a custom built Labview application based on a synchronous state machine\*<sup>ref</sup>. The Neutral implementation of this software is called neuKLEIN (Neutral Killian Lab Experimental Interface) and is based on a major overhaul, by Joe Whalen, of the original control software. A detailed overview of the capabilities, limitations, and instructions for use of neuKLEIN is available in App. C.

In short, an experimental sequence begins with serially programming each voltage output device. The pulseblasters are programmed last and are triggered via the global experimental trigger discussed in 2.4.3.3 below. Once all devices are ready the pulseblasters become the global clock and the neuKLEIN software begins polling the PixelFly camera waiting for a new image. Once an image is received various experimental parameters are recorded into text files and saved to disk. This process continues within the primary WHILE loop of the state machine and steps through

---

\*Currently this project can be found at <https://github.com/KillianRice/neuKlein>

the predetermined experimental settings array. Primary exit conditions for the loop are encountering an error, conclusion of the settings array, or manual abortion.

Once the files are written to disk, we perform image analysis using a custom Matlab<sup>TM</sup> routine imaginatively named Neutral imagefit routine<sup>†</sup>. An in-depth discussion on the usage, extensibility, limitations, and feature improvements is available in App. B.

#### 2.4.2 Hardware control and measurement systems

The hardware control system is composed of several primary components including the experimental clock, voltage output devices, and measurement instruments. We use a series of National Instruments<sup>TM</sup> data acquisition cards (NI-DAQs) and a re-configurable FPGA for generating output voltages. The experimental clock is based on a pair of SpinCore PulseBlaster TTL generators and a Cooke PixelFly camera is used for collecting absorption images. We also have access to a PicoScope 5000 digital oscilloscope for high resolution signal monitoring and recording. Typically this is used for recording experiment specific photodiode signals for later analysis.

Table 2.8 gives the models of the NI-DAQ cards and additional details such as the resolution, the shared FIFO (first-in, first out) buffer sizes, and the maximum sample rates as a function of the number of channels in use. Though these cards are known as acquisition cards, we instead rely heavily on the arbitrary waveform generation capabilities for dynamically generating analog output voltages. Furthermore, we do not stream data to cards during the experimental sequence but use only the on-board FIFO buffer for storing the arbitrary waveform.

---

<sup>†</sup>Currently this project can be found at [https://github.com/KillianRice/neutral\\_imagefit\\_routine](https://github.com/KillianRice/neutral_imagefit_routine)

Model	Resolution		FIFO buffer Size	Max sample rate	
	Bit depth	Voltage [mV]		Channels used	Rate [kS/s]
6713	12	5	16,384	1 - 5	1,000
				6	952
				7	833
				8	740
6221	16	0.03	8,191	1	833
				2	740
6229	16	0.03	8,191	1	833
				2	740
				3	666
				4	625
6733	16	0.03	16,384	1 - 5	1,000
				6	952
				7	869
				8	769

Table 2.8 : Arbitrary waveform generation details

All cards specified are the PCI model and interface with the experiment control computer directly through the motherboard or via a PCI expansion bin (model: StarTech PEX2PCIE4L). Sample rates are given in kilosample per second (kS/s) and is the same across all enabled channels. The FIFO buffer stores the individual waveform points and is also shared amongst all enabled channels. Full voltage output range is  $\pm 10\text{ V}$ .

It is important to remember that the finite buffer size and maximum sample rate define two extremes for time based waveform generation due to the discretization of the waveform. For short times, the maximum sample rate sets the minimum possible time step between two points on the voltage output. At long times, a fixed number of points between the start and end points may lead to unacceptably large voltage steps between two points on the voltage output. Balancing these two tradeoffs is essential and is the primary driver for the plethora of various cards so that we may dedicate their finite resources to specific tasks.

While arbitrary waveform generation is useful for dynamically varying voltages during an experimental sequence, there are a number of applications where a static voltage is needed or smoothly varying between two or more voltages is not required. Until recently, the NI-6713 was our only sources of experimentally controlled static voltages (in contrast to a static voltage from a supply) and switching between driving voltages was done via a bank of standalone fast analog IC switches (primarily the ADG419). Fast switching of the set point voltage has traditionally been how we control a number of systems through their feedback circuitry. For example, the 922 nm frequency is jumped from the optimal trapping frequency to the optimal imaging frequency at the end of the experimental sequence via the sat. abs. solenoid current. The change in magnetic field shifts the resonance frequency of the loss feature and the 922 nm frequency lock responds by varying the master laser frequency to restore the resonance condition. Therefore, while imperative to retain this functionality, the NI-6713 + switch bank limited in the number of controlled static voltages to eight and the simple standalone switches were insufficient for applying application logic for

dynamically choosing driving voltages<sup>‡</sup>.

These shortcomings led us to develop a real-time based NI-FPGA for the development of custom reconfigurable logic and static voltage output. This system is based on a NI cRIO-9063 with integrated Artix-7 FPGA, a NI-9403 32ch TTL input/output (I/O) module, and a NI-9264 16ch analog output module. The cRIO device manages the control layer of the system, hosting the embedded operating system and allows us to easily develop, compile, and deploy our custom control logic to the FPGA via Labview. The FPGA (field programmable gate array) executes the user-defined logic on a user-defined loop-time (minimum 50  $\mu$ s.) with the 32 TTL I/O channels and 16 analog output available for reading and writing each cycle. We typically do not use the output functionality of the TTL channels and instead opt for 32 input channels which can be dynamically assigned to control the 16 analog outputs. These analog outputs may be conditioned as static, simple switched, cascading switched, or simple boolean controlled outputs all configurable via software. Additional features include logic inputs which can be shared to multiple outputs and simple waveform generation such as linear ramps.

---

<sup>‡</sup>An example of this application logic might be any set point which could be controlled via boolean logic conditioning.

### 2.4.3 Ancillary laboratory systems

#### 2.4.3.1 MOT coils

#### 2.4.3.2 Trim coils

The trim coils are a cubic, 11.5" cage with current coils providing B-field in a Helmholtz configuration. These coils are used to trim out static residual magnetic fields and to apply dynamic and well controlled bias magnetic fields. We commonly use the coils along the Z-direction to apply bias magnetic fields during spectroscopy as shown in Fig. 2.41a).

The fine-structure magnetic sub-levels of the  $^3P_1$  state vary with B-field as 2.1 MHz/G. Compared to the natural linewidth of 7.5 kHz, this splitting of the  $^3P_1$  states provides a very sensitive probe for precisely zeroing the residual magnetic field. We determine the required bias fields by performing loss spectroscopy with unpolarized light along the  $^1S_0 \rightarrow ^3P_1$  transition using a bosonic isotope. Next we fit the  $m_j = \pm 1$  spectral features to a loss line-shape (either gaussian or lorentzian) and plot the line center as a function of applied magnetic field along each dimension. Fig. 2.41b) shows an example of the change in Zeeman splitting of the  $m_j$  levels using strontium-84. Finally, we perform a linear fit to the line center variation and extract the intercept which nulls the residual field and the slope which calibrates our applicable field strength per ampere. We have found these calibrations to be  $[\delta B_z = 0.985, \delta B_y = 0.982, \delta B_z = 0.987]$  G/A<sup>§</sup>.

---

<sup>§</sup>Further details available in Onenote under Research Projects → Routine Studies → B-field zeroing → Zeroing summary

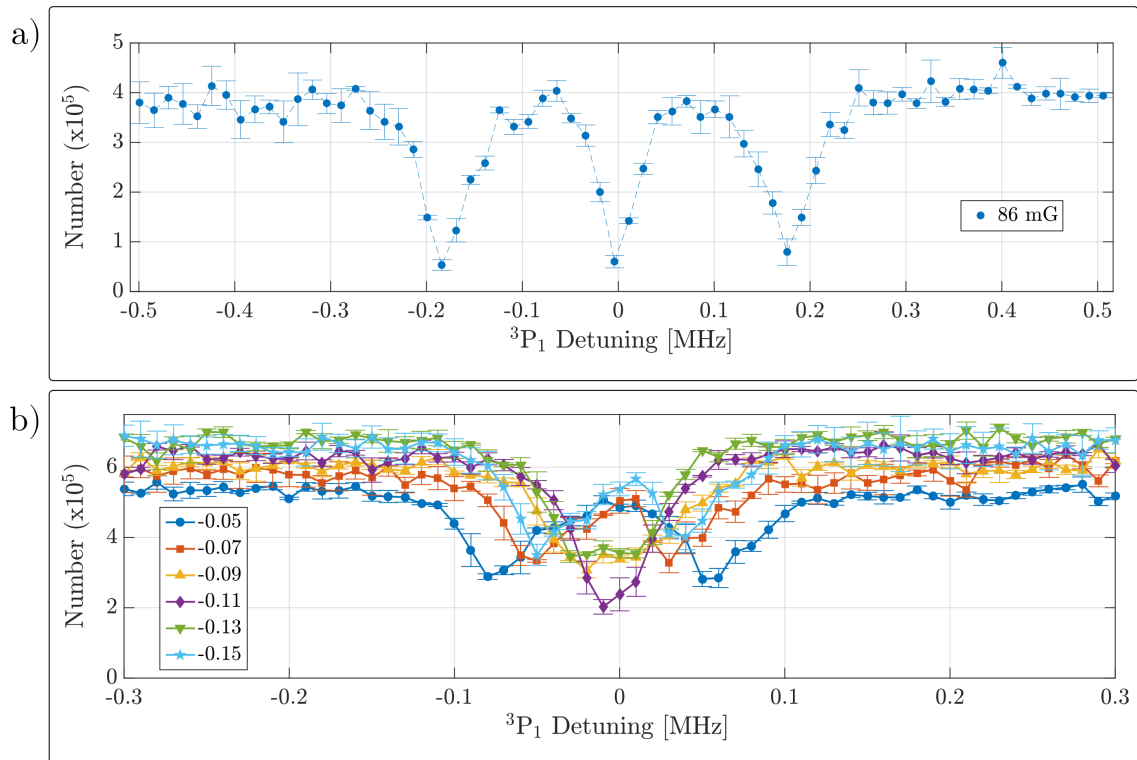


Figure 2.41 : Zeroing residual magnetic fields

Loss spectroscopy in various bias fields. a) Example of resolved Zeeman splitting of the  ${}^3P_1$  magnetic sub-levels. b) Typical B field variation for determining the zero field position. The applied bias is increased for each subsequent scan and a clear zero crossing is observed. The legend has been left in arbitrary lab units to emphasize the B-field zero crossing which occurs around -0.11.

### 2.4.3.3 Zero crossing AC line trigger

Fig. 2.42 shows the circuit used to start the Neutral experimental sequence. It is based on deriving a TTL pulse at the positive-going zero crossing of the 60 Hz building line. Manual triggering is essential since we do not share the same clock source between the two independent pulseblasters (PB0 & PB1). Instead relying on their relative precision and low timing jitter to maintain experimental synchronicity when triggered from a shared source.

Fig. 2.43 shows a comparison of the timing uncertainty when a short 200 ns pulse is output from both pulseblasters and the oscilloscope is triggered from the zero crossing of the AC line. While this measurement does not reveal the cause of the relative instability between the three sources (PB0, PB1, or AC line), we do observe a relative instability of approx.  $1\ \mu\text{s}$ . For most use cases with ultracold matter, this timing uncertainty is entirely reasonable and presents no practical limitation. However, this behavior does preclude the usage of cross-triggers between the pulseblasters when performing experiments with the optical lattice<sup>¶</sup>. This timing difference results in a similar consideration as the discrete timing issue discussed previously whereby, dependent on the dynamics under investigation, even small timing difference can lead to significant variation in the observed phenomena. We mitigate this effect by taking care to trigger all related processes from the same pulseblaster where the timing jitter is reduced to 50 ns.

We choose to trigger off the building wide 60 Hz line in order to maintain a fixed

---

<sup>¶</sup>Cross-triggers are defined as the mixing of timing signals between the two pulseblasters. For instance, using PB0 to trigger the turn on of lattice arm A and PB1 to trigger arm B.

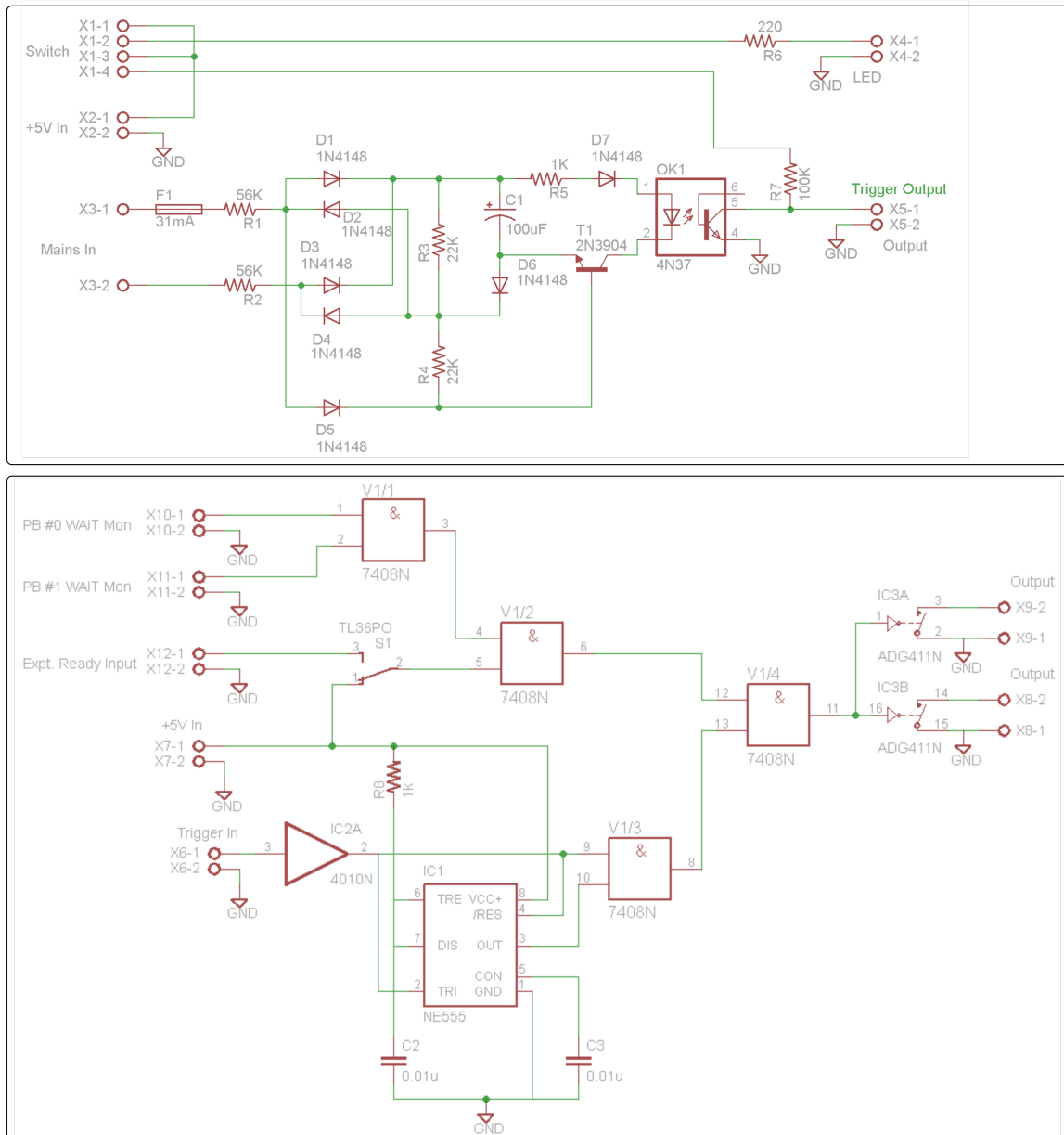


Figure 2.42 : Circuit diagram of the zero crossing AC line trigger

Top - 120 Hz square wave pulser which generates a short pulse on the 60 Hz zero crossing. Bottom - Synchronizer circuit between both pulseblasters, an optional expt. ready trigger (which ensures the atom shutter is open), and the AC zero-crossing trigger. Trigger input is from the top circuit and is used with the 555 timer in a one-shot configuration. This ensures only every other pulse from the AC trigger produces a HI output past the AND gate V1/3.

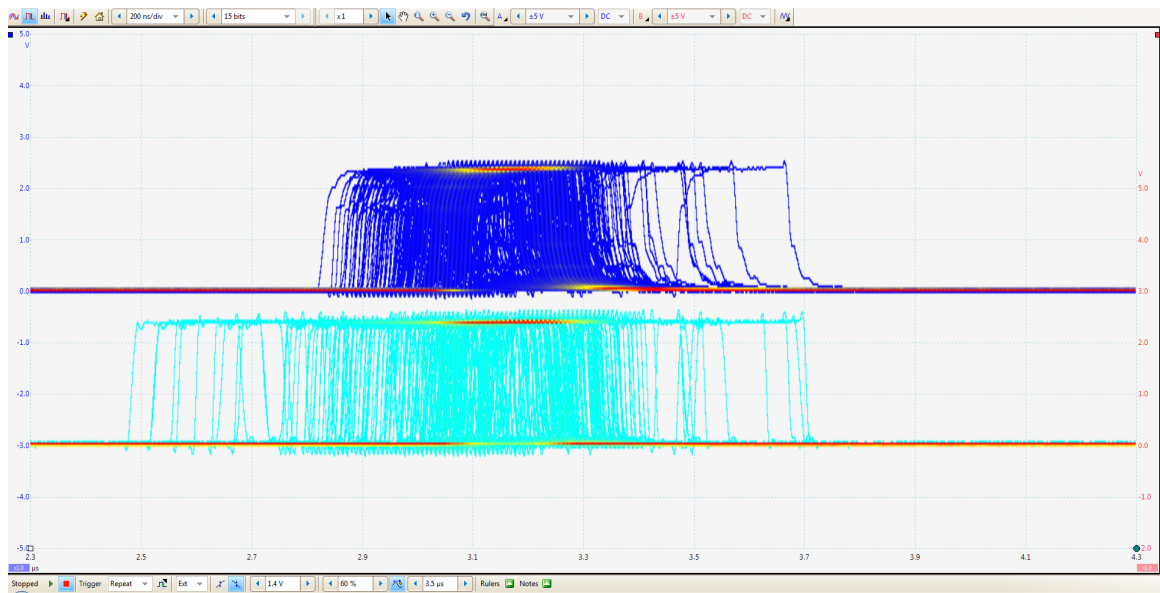


Figure 2.43 : Comparison of pulseblaster timing jitter

A persistent oscilloscope trace showing repeated measurements of a 200 ns logic pulse from each pulseblaster. The upper signal is PB0 and the lower is PB1. The scope is externally triggered by the zero crossing AC line trigger.

phase relationship from shot to shot. This is thought to act as a common-mode rejection of electrical noise which could couple into our measurements via intensity or frequency noise. However, we have not rigorously evaluated this hypothesis and no significant change was observed when changing the global experimental trigger.

Finally, the additional logic gates ensure that the pulseblasters trigger at the same time since they are programmed serially by the neuKLEIN software. This process is enabled by a WAIT signal that each pulseblaster outputs when in this state which is used to ensure proper initialization of the system before starting an experimental sequence.

#### **2.4.3.4 Pneumatic actuated mirror mounts**

The lattice arms in the plane of the atoms (A & B) are combined and separated along the 1064 nm ODT path using common harmonic beamsplitters as shown in fig. 2.25. Alignment of the vertical propagating beam presents a greater challenge as the numerical aperture into the chamber is limited and maintaining clean polarization of the MOT beams requires us to place the MOT waveplates along the vertical axis to avoid mirror reflections which may rotate the polarization. This restriction places prohibitive constraints on the availability of passive optical components which might combine the MOT and lattice traps along the vertical path. To overcome this, we employ industrial pneumatic valves and actuators to move the waveplates and requisite MOT mirrors out of the path before turning on the 532 nm light.

Fig. 2.44 shows the flow diagram for switches S1 and S2 for this system where the default position is the lower figure with the actuators extended. As one might expect, this abrupt movement does impart vibrations into to the table which we dampen by

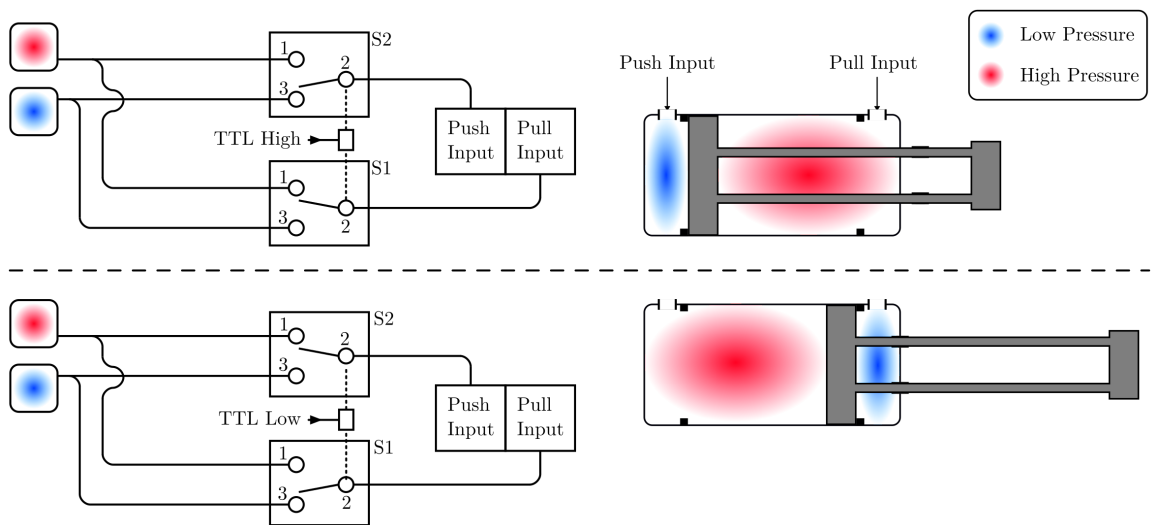


Figure 2.44 : Pneumatic actuators diagram

Example schematic for a single actuator. Three actuators are used on the apparatus to move several components simultaneously. Not shown is the 4-way cross which splits the output from each valve (S1 and S2) to each actuator.

slowing the movement and cushioning the stops. In practice we find that the system is fairly robust against these small "kicks"<sup>||</sup>. We have observed a settling of the actuators when extended as this is this default position. Future improvements may aim to provide a rail system for guiding the movement and supporting the actuators against gravity for smoother movement.

---

<sup>||</sup> Although occasionally the air pressure must be adjusted if the lasers are behaving erratically.

## Chapter 3

### Photoassociation in ultracold gases

#### 3.1 Introduction

This part needs to be brief and really should motivate the idea of PAS.

PA is not unique to atomic physics, chemists have been using light to interrogate molecular structure for a long time

physicists molecule

PA can come in many forms (in a lattice, in a bulk gas, via dissociating molecules)

Experimentally we observe PA by looking for trap loss **doublon paper**.

There are multiple flavors of PAS. Can do one-photon or two-photon.

Can even be used to modify the scattering length of atoms through mixing of atomic eigenstates.

Pioneering work done in the early 90's used PA to interrogate the sturucture of interatomic potentials to deduce the scattering lengths between atoms.

a photoassociation experiment can be used to map the square of the scattering wave function in the ground electronic state at the Condon points corresponding to the different excited bound levels. [9] What about the history of scattering? Most of what we know about quantum mechanics comes from either scattering experiments of spectroscopy. Definitely need some BS about how simple scattering theory has been a hallmark of atomic physics and Photoassociation spectroscopy is an important field

which relies on both of these properties.

Alkaline earth atoms, such as Sr, were hypothesized to take advantage of OFR's since there is a narrow transition easily accessible which could provide large changes in the elastic cross section while minimizing the losses due to the inelastic contribution. This was thought to be possible by controllable detuning the closed channel from the incoming open channel and balancing the loss rate (check this). While there were observations of a strontium OFR, notably work done on this very apparatus (citations), they were accompanied by unexpectedly high loss rates. Recent work by Nicholson et. al. were able to explain some of this behavior through a quantum interference effect whereby the elastic loss rate returns to zero between bound states as the effects of bound states cancel each other out. They used a coupled-channel description to describe the physics.

rabi oscilations between atomic and molecular condensates (cite ours and the lattice experiment that followed)

short-range PA This work is focused on long-range PA but in recent years groups have also developed short-range PA techniques for the creation of rovibrational ground state molecules. These techniques rely heavily on favorable overlap integrals betwwen molecular wavefunctions and typically searching for favorable intermediate states is a pain (that is why our large FCF might be useful)

While the general idea of photoassociation is straightforward, a rigorous theoretical understanding of the process requires discussion of several key topics related to the behavior of ultracold gases. fix this segue The photoassociation process is effected by the residual kinetic energy of the atoms, external potential energy from trapping potentials, and the internal potential energy due to inter-particle scattering between

atoms. In the following sections we will introduce how to determine the spatial and momentum density distributions of bulk atomic gases using a statistical mechanics approach. Next, we'll explore the two-body problem of cold collisions physics which is essential to understanding the photoassociation process. This approach will develop a quantum mechanical model describing interacting atomic particles. Finally, we'll extend this fully quantum theory with the addition of external fields and subsequently apply simplifying assumptions to formulate analytic expressions for modeling photoassociation spectra.

### 3.2 Theoretical description of trapped boson gases

Add equations Itrans from page 51 of natali's thesis

This section will briefly discuss the

Need to know the spatial and momentum distribution of atoms in the trap. Concerned with space as the likelihood of PA is dependent on the interatomic separation and the overlap integral between wavefunctions plays a big role. Highest probability of excitation is near the Condon point [citations?](#)

Momentum distribution needs to be known as this effects how the wavefunction looks as well as the distribution of energies within the cloud which can lead to line-broadening and asymmetric lineshapes

Essentially first part of chapter 2 from Res

We need

Since photoassociation is a two-body process, an accurate description of the spatial

[Ben](#) This chapter will briefly cover the statistical mechanics of trapped atomic

gases, both both at thermal temperatures and at near-zero temperatures for bosons and fermions. In our experiment, we typically acquire data by imaging the atomic density profile either in-situ or after releasing the atoms and allowing them to freely expand for a variable time-of-flight (TOF). I will discuss the expected density profiles for these various regimes and the related fit functions that we use to extract physical information from our samples. To illustrate the properties of trapped atomic gases, let us first consider a system in the grand canonical ensemble. For non-interacting particles at a temperature  $T$ , the average occupation of the state  $i$  with energy  $E_i$  is

**James** Typically our samples have a fixed number of particles,  $N$ , so the chemical potential,  $\mu$ , is constrained such that

In the limit of large particle number we can describe the gas semi-classically assuming that the occupation of the ground state is negligible.

The semi-classical distribution is defined such that the average number of particles in the phase-space volume  $d\mathbf{p}d\mathbf{r}$  is given by  $f(\mathbf{r}, \mathbf{p})d\mathbf{p}d\mathbf{r}/(2\pi)^3$  and

check the equation numbers in pethick and smith Consider the number density of atoms per phase space volume  $(2\pi\hbar)^3$  integrated from  $\epsilon > 0$

$$n(\mathbf{r}) = \int \frac{d\mathbf{p}}{2\pi\hbar^3} \frac{1}{\exp((E_r(\mathbf{r}) - \mu/k_B T) - 1)} \quad (3.1)$$

where we are neglecting the full quantum nature of the atoms and considering them as point masses with free particle energy  $E_r(\mathbf{r}) = \frac{p^2}{2m} + V(\mathbf{r})$

next we define the quantities

$$x = \frac{p^2}{2mk_B T} z(\mathbf{r}) = e^{\mu - V(\mathbf{r})/k_B T} \quad (3.2)$$

define  $\xi$

then performing a change of variables and plugging into above eq we find

$$n(\mathbf{r}) = \frac{2}{\sqrt{\pi} \lambda_T^3} \int dx \frac{\sqrt{x}}{z^{-1} e^x - 1} \quad (3.3)$$

where  $\lambda_T = \sqrt{\frac{2\pi\hbar^2}{mk_B T}}$  is the de Broglie wavelength cite?. This integral is of a certain form and can be rewritten using cite Demarco pg 237 footnote

need to put bound on these integrals from 0 to inf where does the 3/2 come from?

$$\begin{aligned} \int_0^\infty dx \frac{x^{\gamma-1}}{z^{-1} e^x - 1} &= \sum_{n=1}^{\infty} \int_0^\infty dx x^{\gamma-1} e^{-nx} z^n \\ &= \Gamma(\gamma) \text{Li}_\gamma[z] \end{aligned} \quad (3.4)$$

where  $\text{Li}_\gamma[z]$  is the polylogarithm function defined by cite something

$$\text{Li}_\gamma[z] = \sum_{n=1}^{\infty} \frac{z^n}{n^\gamma} \quad (3.5)$$

This function is also known as the bose enhancement function cite ketterle and describes the bunching of bosonic particles near degeneracy

Using this identity we can write the thermal distribution as

$$\begin{aligned} n(\mathbf{r}) &= \frac{\text{Li}_{\frac{3}{2}}[z(\mathbf{r})]}{\lambda_T^3} \\ &= \frac{1}{\lambda_T^3} \text{Li}_{\frac{3}{2}}[\exp(\mu - V(\mathbf{r})/k_B T)] \end{aligned} \quad (3.6)$$

For harmonic traps  $V(\mathbf{r}) = \frac{m}{2} \sum_i \omega_i^2 r_i^2$  where  $r_i$  represents the Cartesian coordinates. Plugging this into previous eq then the *in-situ* density profile is given by

$$n(\mathbf{r}) = \frac{1}{\lambda_T^3} \text{Li}_{\frac{3}{2}} \left[ \xi \exp \left( \sum_i \frac{-m\omega_i^2 r_i^2}{2k_B T} \right) \right] \quad (3.7)$$

Argue what  $z$  is what is it's range?, then say that it is small when  $T$  is large. Therefore, writing the first few terms of the series expansion of Eq.3.5

$$\text{Li}_\gamma[z] = z + \frac{z^2}{2^\gamma} + \frac{z^3}{3^\gamma} + \dots \quad (3.8)$$

we see that  $\text{Li}_\gamma[z] \approx z$  for  $z \ll 1$ . This corresponds to the high temperature limit which should result in recovery of the MB solution and indeed it does. In the classical, or high-temperature, limit  $\text{Li}_{\frac{3}{2}}[z(\mathbf{r})] \approx z(\mathbf{r})$ . From Eq. we see that this that in the limiting case we get the expected Maxwell-Boltzmann density profile what happens with  $\xi$ . In the following we will continue to use the full expressions with an explicit dependence on the polylogarithm as it is the most general form, however, we will use this approximation to ensure our expressions match those expected from a classical Maxwell-Boltzmann description of the gas.

this can be simplified

$$n(\mathbf{r}) = \frac{\xi}{\lambda_T^3} \exp \left( \sum_i \frac{-m\omega_i^2 r_i^2}{2k_B T} \right) \quad (3.9)$$

I'd like to put in something about the momentum distribution

MI PA [33] is a phenomenon in which two colliding atoms absorb a photon to create a bound, electronically excited molecule. Figure 1.1 shows the PA process of Sr: the bottom one is the  $1S0+1S0$  ground state potential, the long-range part of which is described by the R-6 van de Waals term, and the top one is the excited molecular  $1S0+3P1$  potential whose interaction at large separation is given by the R-3 dipole term. Two free ultracold Sr atoms in the ground state  $1S0$  with the thermal collision energy of  $E_g$  approach each other, and absorb a photon with the energy of  $h\nu$  to photoassociate to a molecular bound state of the excited potential around the Condon point  $R_c$ . The bound state  $\psi_e$  has the binding energy of  $E_b$ , and the Condon point  $R_c$  is the interatomic separation where PA occurs most likely which is characterized by the Franck-Condon overlap integral discussed later. The formation of the molecule is followed by spontaneous or stimulated decays, usually

creating either two free atoms with high kinetic energy or ground state molecule, both of which usually are lost due to extra high energies. Detecting the loss of atoms is a typical method to perform PA. According to the conventional treatment [33, 34], the strength of the PA transition is proportional to the Franck-Condon overlap integral between wave functions of ground-collisional and excited bound state. Since the wave functions oscillate fast at the short interatomic separation, the Franck-Condon overlap integral is dominated by the amplitude of the ground-state wave function near the Condon point  $R_c$  [33]. It is noticed that in  $^{88}\text{Sr}$  the Franck-Condon overlap between the second least bound state on the  $1\text{S}0+3\text{P}1$  potential and the ground-collisional state is large, which is a crucial feature to the applicability of experiments discussed in this thesis. PA has proven to be a very powerful tool in ultracold physics, such as determining absolute binding energies, extracting atomic collisions information, modifying collision strength, and making ultracold molecules [33].

### **3.2.1 Extracting data from column densities**

This description of the atoms in the trapping potential is useful but we need to go a step further because we use absorption imaging to determine properties of the atom after a time of flight.

Maybe put in something about different measurement techniques and reference the ketterle and pethick and smith again.

Removing the trap results in ballistic expansion with the above spatial density profile as the initial conditions. To derive how we find the properties of the atoms, consider the above spatial density profile as the initial conditions.

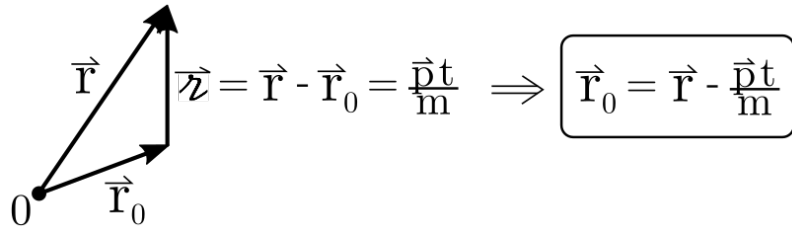


Figure 3.1 : Ballistic expansion of particles

Schematic representation particle displacement vectors used to determine how time-of-flight expansion transforms the initial density distribution

Atoms expand ballistically according to

$$\frac{d\mathbf{r}}{dt} = \frac{\mathbf{p}}{m} \text{ and } \frac{d\mathbf{p}}{dt} = 0 \quad (3.10)$$

Thus, an atom measured at position  $\mathbf{r}$  after the time-of-flight,  $t$ , will have moved a distance  $\zeta = \frac{pt}{m} = \mathbf{r} - \mathbf{r}_0$  from its initial position  $\mathbf{r}_0$

make the tof density  $n'$  the spatial density evolves then double check  $2\pi\hbar$  denom

$$\begin{aligned} n(\mathbf{r}, t) &= \int \frac{d^3\mathbf{r} d^3\mathbf{p}}{(2\pi\hbar)^3} \frac{1}{\exp\left(\left[\frac{p^2}{2m} + V(\mathbf{r}') - \mu\right] \frac{1}{k_B T}\right) - 1} \delta^3\left(\mathbf{r} - \frac{\mathbf{p}t}{m} - \mathbf{r}'\right) \\ &= \int \frac{d^3\mathbf{p}}{(2\pi\hbar)^3} \frac{1}{\exp\left(\left[\frac{p^2}{2m} + V\left(\mathbf{r} - \frac{\mathbf{p}t}{m}\right) - \mu\right] \frac{1}{k_B T}\right) - 1} \end{aligned} \quad (3.11)$$

Plugging in the harmonic potential we find that free expansion after release from a harmonic trap is self-similar and amounts to rescaling the the spatial coordinates by check Demarco's thesis. Thus the scaled spatial profile is given by

$$n'_{th}(\mathbf{r}, t) = \frac{1}{\lambda_T^3} \left( \prod_{j=1}^3 \frac{1}{1 + \omega_j^2 t^2} \right) \text{Li}_{\frac{3}{2}} \left[ \xi \exp \left( \sum_{i=1}^3 \frac{-m\omega_i^2 r_i^2}{2k_B T} \frac{1}{1 + \omega_i^2 t^2} \right) \right] \quad (3.12)$$

Using this description of the spatial distribution after time-of-flight expansion, we must now consider how to relate our absorption measurement to the physically

relevant variables of the gas.

Finally we must consider the column density along one direction since we are taking absorption images of the atoms. A brief description of absorption imaging and system used for this process is given in some sec.

Simply stated, absorption imaging is the process of illuminating a gas of atoms with resonant (or near resonant) laser light and taking a spatially resolved image of the laser beam. As the light is tuned near a resonant transition, the atoms will absorb and scatter photons out of the original laser beam resulting in a "shadow" which is proportional to the number of scatters within a certain spatial region. This shadow image is then normalized by taking another picture of the laser after the atoms have fallen out of the imaging region. This relation of the light attenuation to the number density of scattering particles is known as Beer's law and results

Using Beer's law cite, we can relate the total absorption of photons to the number density of scattering particles along the optical path multiplied by the absorption cross section. This results in a measurement of the "optical depth" of the gas along a column density. Measurement along a particular direction limits our description of the gas to the two-dimensional plane orthogonal to the laser beam as shown in some fig from ch 2.

Experimentally, the optical depth is trivially computed by taking the natural logarithm of the ratio of the images obtained from the camera. We then equate this OD image to be proportional to the spatial density profile after the time-of-flight

expansion integrated along the optical path through the atoms.

$$\begin{aligned} \text{OD} &= \ln \left( \frac{\text{Atom Image}}{\text{Background Image}} \right) = \sigma_{abs} \int_{-\infty}^{\infty} dz n'_{th}(\mathbf{r}, t) \\ &= \frac{\sigma_{abs}}{\lambda_T^3} \left( \prod_{j=1}^3 \frac{1}{1 + \omega_i^2 t^2} \right) \int_{-\infty}^{\infty} dz \text{Li}_{\frac{3}{2}} \left[ \xi \exp \left( \sum_{i=1}^3 \frac{-r_i^2}{2\sigma_i^2} \right) \right] \end{aligned} \quad (3.13)$$

where  $\sigma_i^2 = \frac{k_B T}{m \omega_i^2} (1 + \omega_i^2 t^2)$ . Need to say something about the integral in Eq.[prev](#) and evaluating the integral along  $z$  so going to write out the explicit spatial dependence in cartesian coordinates. Additionally, we'll rewrite the polylogarithm in terms of it's series representation in order to see an identity

$$\int_{-\infty}^{\infty} dz \text{Li}_{\frac{3}{2}} \left[ \xi \exp \left( \sum_{i=1}^3 \frac{-r_i^2}{2\sigma_i^2} \right) \right] = \int_{-\infty}^{\infty} dz \sum_{n=1}^{\infty} \frac{\xi^n}{n^{3/2}} \exp \left( \frac{-x^2}{2\sigma_x^2} - \frac{y^2}{2\sigma_y^2} - \frac{z^2}{2\sigma_z^2} \right)^n \quad (3.14)$$

Defining  $\rho = \exp \left( \frac{-x^2}{2\sigma_x^2} - \frac{y^2}{2\sigma_y^2} \right)$  and expanding the series out, Eq.[above](#) becomes

$$= \int_{-\infty}^{\infty} dz \xi \rho \exp \left( \frac{-z^2}{2\sigma_z^2} \right) + \frac{\xi^2}{2^{3/2}} \rho^2 \exp \left( \frac{-z^2}{2\sigma_z^2} \right)^2 + \frac{\xi^3}{3^{3/2}} \rho^3 \exp \left( \frac{-z^2}{2\sigma_z^2} \right)^3 + \dots \quad (3.15)$$

In this form we can readily separate out the dependence on  $z$  and perform the integral making use of the following identity [check identity](#)  $\int_{-\infty}^{\infty} dz \sum_{n=1}^{\infty} \exp \left( \frac{-z^2}{2\sigma_z^2} \right) = \frac{\sqrt{2\pi}}{n^{1/2}} \sigma_z$ . Eq.[above](#) then reduces to

$$\begin{aligned} &= \int_{-\infty}^{\infty} dz \sum_{n=1}^{\infty} \frac{\xi^2 \rho^n}{n^{3/2}} \exp \left( \frac{-z^2}{2\sigma_z^2} \right) \\ &= \sqrt{2\pi} \sigma_z \underbrace{\sum_{n=1}^{\infty} \frac{\xi^n \rho^n}{n^2}}_{\text{Li}_2[\xi \rho]} \end{aligned} \quad (3.16)$$

We are now ready to plug this result for the integral back into the full expression for the optical depth. Retaining the explicit expression in cartesian coordinates,

Eq.[above](#) becomes

$$OD(x, y) = \frac{\sqrt{2\pi}}{\lambda_T^3} \frac{\sigma_{abs}\sigma_z}{(1 + \omega_x^2 t^2)(1 + \omega_y^2 t^2)(1 + \omega_z^2 t^2)} \text{Li}_2 \left[ \xi \exp \left( \frac{-x^2}{2\sigma_x^2} - \frac{y^2}{2\sigma_y^2} \right) \right] \quad (3.17)$$

This equation still has one unknown,  $\sigma_z$ , that we cannot readily measure. This problem is solved by recognizing that we can readily calculate and measure a specific value of Eq.[something](#), namely the peak optical depth ( $OD_{peak}$ ) located at  $x = 0, y = 0$ .

$$OD_{peak} = \frac{\sqrt{2\pi}}{\lambda_T^3} \frac{\sigma_{abs}\sigma_z}{(1 + \omega_x^2 t^2)(1 + \omega_y^2 t^2)(1 + \omega_z^2 t^2)} \text{Li}_2[\xi] \quad (3.18)$$

thus the relation between the measured optical depth and the spatial density distribution is given by

$$OD(x, y) = \frac{OD_{peak}}{\text{Li}_2[\xi]} \text{Li}_2 \left[ \xi \exp \left( \frac{-x^2}{2\sigma_x^2} - \frac{y^2}{2\sigma_y^2} \right) \right] \quad (3.19)$$

and in the limit of long expansion time during time-of-flight, namely  $t \gg \omega_x^{-1}, \omega_y^{-1}, \omega_z^{-1}$  then the measured widths reduce to  $\sigma_i^2 = \frac{k_B T}{m} t^2$  and the atom temperature is given along each axis by

$$T_i = \frac{m\sigma_i^2}{k_B t^2} \quad (3.20)$$

Regarding the assumption that the expansion time is much greater than the trap frequencies, we should note that limiting factors in the expansion time are due to center of mass motion of the cloud under the influence of gravity. In the Neutral apparatus we typically utilize drop times are  $\approx 30$  ms. For shallow traps, where  $\omega_i$  is small, then the atoms may not have enough time during expansion to achieve fully ballistic expansion. In these cases it is typical to quote temperatures of the sample as measured along the tightest axis of confinement.

Last thing to do is to relate our expression for optical depth and number density to the total number of atoms in the trap. This task is straightforward by recalling the boson normalization requirement

$$\begin{aligned} N &= \int_{-\infty}^{\infty} d^3\mathbf{r} n_t h(\mathbf{r}) = \int_{-\infty}^{\infty} d^3\mathbf{r} n_t h'(\mathbf{r}, t) \\ &= \int_{-\infty}^{\infty} d^3\mathbf{r} \frac{\sigma_{abs}}{\lambda_T^3} \frac{1}{(1 + \omega_x^2 t^2)(1 + \omega_y^2 t^2)(1 + \omega_z^2 t^2)} \sum_{n=1}^{\infty} \frac{\xi^n}{n^{3/2}} \exp\left(\frac{-x^2}{2\sigma_x^2} - \frac{y^2}{2\sigma_y^2} - \frac{z^2}{2\sigma_z^2}\right)^n \end{aligned} \quad (3.21)$$

This equation is the same problem we saw above but integrated over all axes instead of just one. Therefore we can apply the same expansion and identity we employed to solve for the optical depth to find

$$N = \frac{(2\pi)^{3/2}}{\lambda_T^3} \frac{\sigma_x \sigma_y \sigma_z}{(1 + \omega_x^2 t^2)(1 + \omega_y^2 t^2)(1 + \omega_z^2 t^2)} \text{Li}_3[\xi] \quad (3.22)$$

From our expression for the optical depth, Eq.**some**, we can simplify this to

$$N = \frac{2\pi \sigma_x \sigma_y}{\sigma_{abs}} \text{OD}_{\text{peak}} \frac{\text{Li}_3[\xi]}{\text{Li}_2[\xi]} \quad (3.23)$$

Eq.**above**

All of our information comes from taking pictures of our atomic clouds and inferring the physical properties of the gas before the time-of-flight expansion. This is possible since we know the density profile of the gas in-situ. In the absence of external fields, other than gravity, turning off the trapping potential results in ballistic expansion described by  $\mathbf{r} = \mathbf{r}_0 + \frac{p^2}{2m}t$ , where  $\mathbf{r}_0$  and  $p$  are the position and momentum at the moment of release from the trap and  $t$  is the expansion time. Neglecting the center-of-mass motion due to gravity and assuming long expansion times, then we can easily find a regime where  $\frac{p^2}{2m}t \gg \mathbf{r}_0$  and therefore

$$\mathbf{r} \approx \frac{p^2}{2m}t \quad (3.24)$$

This

[43] get demarco thesis?. Thus, for atoms

Thus, for atoms starting at a position  $\mathbf{r}_0$

Density profile expands self-similarly

Time of flight is essentially a Fourier transform which turns the initial momentum information into spatial information.

### 3.3 Characterizing collisions

understand how to treat quantum two-body problem with external field coupling

Collisions are one of the key ways we learn things about atoms

In atomic physics, our low density gases are mainly within the regime of small interactions.

Here is where I cite sources of some of the original PA work, feshbach stuff collisions as an interferometer of the incoming and outgoing off the barrier, but also of different partial waves.

I want the reader to know that PA dis concerning the scattering wavefunction, that it comes from the overlap integral of the two wavefunctions (why do I need to know this? because this means that it is sensitive to positions of the nodes and can be used to map out the potentials. [this will motivate discussing low energy physics](#)

This spatial dependence is mapped onto the internal energy levels of each atom. I want to say dressed state model here (review atom-photon coupling, atomic physics book).

### 3.3.1 Classical

cross sections as a measure of the time between collisions

potentials where they come from centrifugal barrier analog - slide 16 Julianne just  
r xp of particles

center of mass coordinates only care about relative (generally) simplifies calculations

### 3.3.2 Single channel scattering

quantum solve time0independent SE just need potential, basis set, and boundary conditions

structureless pasrticles scattering free space plane waves de Broglie wavelength strontium de Broglie at 1uK

delta function unitarity limit supports one bound state - the true halo state where the wavefunction comes from

r-dependent potential show 1.1 from Hutson gneerally very complicated between atoms long-range part is typically has a power law drop off important that  $V_{-} \propto R^{-\zeta}$  as  $R \rightarrow \infty$  for ground state atoms dominant long-range part is  $R^6$

scattering states ( $E < 0$ ) repulsive barrier - particle scatter attrative well - particles accelerate

bound states boundary conditions dictate might have quasibound states (shape resonances)

wavefunctions General appraoch is incoming plane wave plus spherical wave common appraoch to expansion of wavefunction in partial wave expansion redefine

SE in terms of partial waves Asymtotic solution from WKB  $V \sim 0$  so must go to plane wave See phase shift

total cross section as sum over all partial waves

this results in a potential that supports bound states.

consider the two particle system as a single entangled particle long range part of this quasi-particle is just the eigenstates of the separate particles themselves (only composed of two parts) but the short range part is going to be determined by some complex physics (new eigenstates, what is the coupling mechanism?) the vdW point is the boundary distance? coupling is due to the interatomic potential, there is at least the long-range part falling off as  $R^{-6}$ , what are the types of interactions which make up the internal wall?

### 3.3.2.1 Low energy results

Simple form for scattering length gives limits on cross sections slide 24 (not sure I get the upper bound bit)

scattering length is a phase accumulation scattering length is very sensitive to details of potential can't really calculate ab initio

a number that represent all the complex physics within the interaction region

simple interpretation as peak shift at long range slide 12 julienne

Another way of seeing the origin of  $a$  is as the collisional  $E$  goes to zero wavefunction should go to a straight line plot from bertlett  $a$  is the intercept of that line on the internuclear axis this is one of the methods of actually determining  $a$

the scattering length as a coupling parameter in length units The mean field energy (I think I had a reference on this) slide 26

Determining  $a$  is not so easy because the interatomic potential is not known this was one of the pioneering uses for photoassociation PA is sensitive to the collisional wavefunction and therefore can help to map out the spatial distribution of the ground state Simple WKB estimation predicts zero-energy bound state as  $E \approx 0$  every atom would have infinite scattering length at low energy obviously not the case, GF first to determine analytic corrections due to long-range vdW interaction comes about because of phase contribution from the long-range part This is the regime we explored with our work in chapter 4 probing a bound state just near the dissociation threshold makes us extremely sensitive to the entire phase of the well

free atoms scattering as single particle state (different eigenstate) interaction determined by some gnarly stuff From scattering theory we know that the long range behavior is determined by short range physics how do we know this? (the dalibard intro) Can we come up with good enough pseudo potentials to describe the short range physics and then solve the schrodinger equation to extract wavefunctions? we want wavefunctions because that is the full characterization we don't know the right eigenbasis for the short range part but we can make some guesses (in particular Hund cases setup eigen states for various possible internal states) Bohn and Julianne theory guessed based on using quantum defect theory this pre-supposes that the bound and free wavefunctions are similar (I forgot in what respect) but that the bound ones must go to zero as  $R \rightarrow \infty$  If we have some notion of the wf then we can construct matrices which define interactions once we add additional coupling to the scattering problem now in a position where I need to connect scattering theory and the PAS

Once we have the ground state wavefunction of our new particle we can construct the internal structure by considering the internal energy structure of the constituent

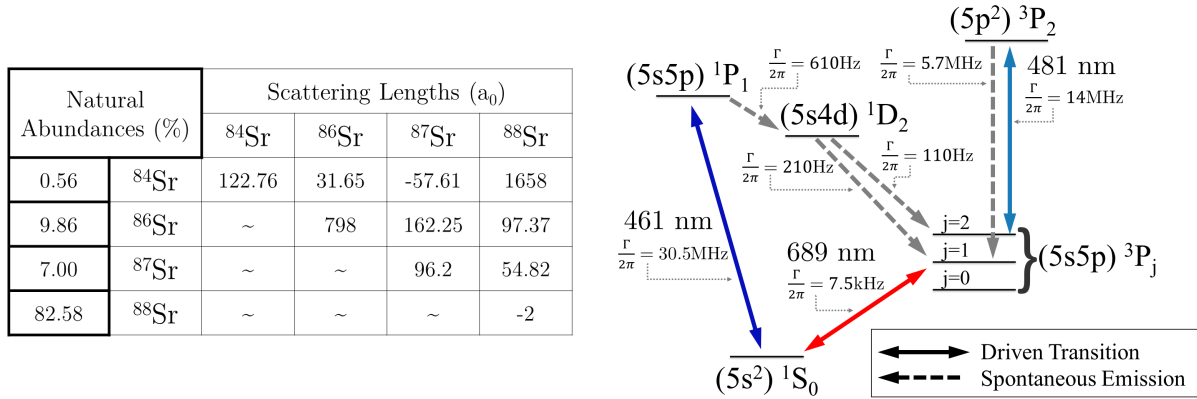


Figure 3.2 : Strontium interatomic wavefunctions

Res 6.3

atoms Can I make a connection that since it is a composite particle we must consider all the various configurations available?

### 3.3.3 Multichannel scattering

Everything we discussed was for unstructured particles this is the power of the scattering length

this would be the end of the story if all of these potentials were "separable" (or independent) you'd find your configuration, describe the potential, solve it, and you're done of course this isn't actually the case because the eigenstates of the separate potentials couple to one another. Even understanding the natural coupling between coupling between potentials is not easy tie back to complexity of understanding short range physics We don't really know what coupling exist and which energy levels are most important mostly effects the bound states of the system strontium example of the D state coupling in the 3P1 potential references to Res and other work

address somewhere that these types of problems are generally solved via coupled-channel methods which follow the same recipe for the scattering problem as in the single channel case but does so considering all channels simultaneously through matrices defining potentials and their couplings to one another. coupled equations are complicated point out references from Julienne, Mies, Bao, Hutson

But can match at asymptotic wavefunction again and get a lot of insight  
example: multichannel use to describe atom-diatom coupling multi-channel model  
(normal MFR diagram) other potentials are due to different combinations of atoms  
in hyperfine states these potentials can have different magnetic moments means that  
addition of a magnetic field can tune them relative to one another MFR has been  
extensively studied and is a common tool used in atomic physics

scattering resonances are due to off diagonal coupling between bound closed channels and scattering open channels give picture hand wavy explanation is that bringing a bound state close will modify the open channel (potential?) this results in a tweak of the phase shift which results in a change in scattering length can describe this as a change in the elastic cross section of the incoming open channel in general there is also an inelastic cross section that may contribute if the bound state has a finite lifetime.

define open and close channels  
S matrix - defines scattering phases and amplitudes due to couplings between various open and closed channels S found from the asymptotic solutions

if single channel then S reproduces above results if inelastic then get complex scattering length (need better way to segue, Julienne 2014 slide 19 - unitarity argument maybe) complex scat Real part is the elastic cross section Imag part if the inelastic

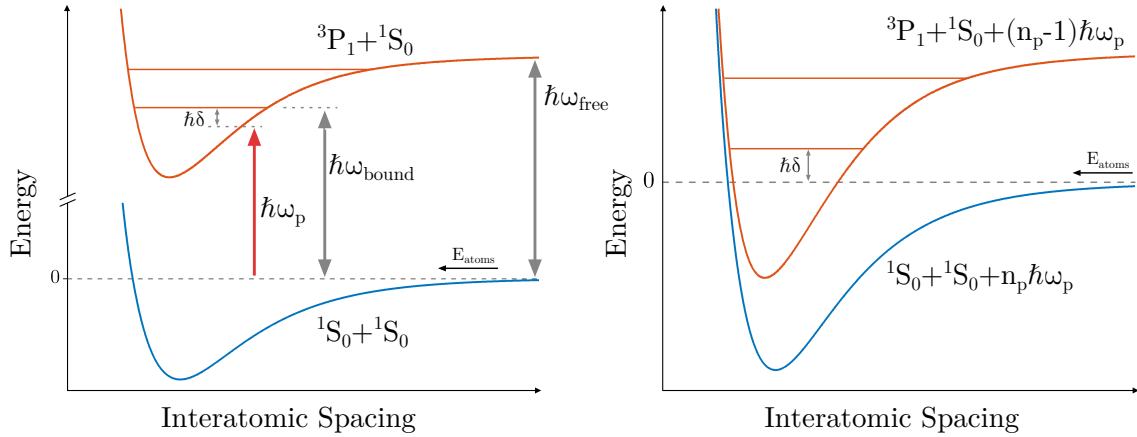


Figure 3.3 : Schematic representation of a Feshbach resonance

(a) Potentials for the open ( $^1S_0 + ^1S_0$ ) and closed ( $^3P_1 + ^1S_0$ ) channel of an optically coupled Feshbach resonance in strontium. (b) The same coupling shown in (a) in the dressed state model. Tuning of the excited potential is achieved by varying the laser frequency detuning,  $\delta = \omega_p - \omega_{bound}$ , and  $\omega_{free}$  is the  $^1S_0 \rightarrow ^3P_1$  atomic transition frequency.

Also the Chin '10 review on feshbach resonances

Follow the Nicholson 15 paper method of introing the elastic and inelastic cross sections

The use of a laser field as the coupling scheme in a Feshbach resonance introduces several advantages and complexities that must be considered when determining the expected properties of optical Feshbach molecules. In order to understand these differences, we will briefly outline the key concepts behind Feshbach resonances and the distinctions between optical and magnetic Feshbach resonances.

The basic idea of a Feshbach resonance is outlined in Fig. 3.3.3. Consider a simple

two channel system, denoted by the open channel and the closed channel. The open channel is generally a ground state potential for two free atoms near threshold. Atoms occupying this state can undergo elastic collisions and, in the absence of any external perturbation, will remain in the open channel. Conversely, the closed channel is a bound state of a higher lying potential who's energy can be tuned relative to the open channel. In the absence of coupling between the states, the open and closed channel remain eigenstates of the system as the tuning parameter, and therefore the energy of the closed channel, is changed. However, in the presence of coupling between the channels, the original eigenstates are mixed and develop an avoided crossing between the bare open and closed channels, when tuned across the resonance. The power of Feshbach resonances comes from the ability to externally manipulate the degree of state mixing, which results in control of the s-wave scattering length and the creation of low energy Feshbach molecules.

Magnetic Feshbach resonances (MFR) are used extensively in alkali metal systems to tune the scattering properties of ultracold gases since the ground states of these systems feature a magnetic moment due to an unpaired electron in the valence shell. Thus, MFRs utilize interactions between low lying ground state molecular potentials via spin-dependent couplings. Since both the open and closed channel are ground state potentials, MFRs often exhibit extraordinarily long lifetimes [15, 45]. Conversely, in strontium the ground state is a  ${}^1S_0$  state, as shown in Fig. 1.3. This state is not magnetically sensitive, so no MFRs exist near the  ${}^1S_0+{}^1S_0$  interatomic potential. Fortunately, optical Feshbach resonances (OFR) serve as another method to introduce coupling between the ground state potential (open channel) and a molecular state of an electronically excited potential (closed channel). Our work has utilized coupling

between the  ${}^1S_0 + {}^1S_0$  and  ${}^3P_1 + {}^1S_0$  two-body potentials via the narrow  ${}^1S_0 \rightarrow {}^3P_1$  atomic transition at 689nm. Fig. 3.3.3 shows a schematic of the potentials involved in the OFR of strontium in both the bare atomic and dressed state pictures. In the dressed basis we consider the combined atom + photon field system such that the channels become  $|{}^1S_0 + {}^1S_0 + n_p \hbar \omega_p\rangle$  as the open channel and  $|{}^3P_1 + {}^1S_0 + (n_p - 1) \hbar \omega_p\rangle$  for the closed channel. As the light field frequency,  $\omega_p$ , is varied the excited closed channel potential will experience an energy shift relative to the open channel, resulting in resonant coupling between the open and closed channels. [8, 18? ]

Both MFRs and OFRs can be treated by the same theoretical formalism, as a modification of the collisional properties between two particles [15, 62]. One of the hallmarks of ultracold physics is the simplicity of atomic collisions. As bosonic atoms get colder they can only collide via  $\ell = 0$  partial waves and thus the elastic collision rate between two atoms becomes energy independent and can be parameterized by a single fixed quantity,  $a_s$ . This parameter is known as the s-wave scattering length and is determined by the short range molecular potential between two colliding atoms. Through a similar approach, collisions near Feshbach resonances can be modeled by introducing a complex s-wave scattering length,  $\tilde{\alpha}$ . In this model, the magnitude of  $\tilde{\alpha}$  influences the elastic scattering rate between particles while the imaginary part describes losses through inelastic scattering. Under an isolated Feshbach resonance model at low energies, this complex scattering length is given by [15]

$$\tilde{\alpha} = a - ib = \frac{a_s \Gamma_0}{-E_0 + i(\gamma/2)} \quad (3.25)$$

where  $E_0$  and  $\Gamma_0$  are the energy independent parameters for, respectively, the resonance position and coupling strength between channels, and  $\gamma$  is a general decay

term associated with loss from the closed channel. Using Eq. 3.25, we can note the two main differences between MFRs and OFRs. Most experimentally useful MFRs, such as in Li and K, have negligible closed channel decay,  $\gamma = 0$ , and a fixed coupling strength between the open and closed channels. Thus, the change in the s-wave scattering length takes on a particularly simple form,

$$\tilde{\alpha} = a_s \left( 1 - \frac{\Delta}{B - B_0} \right) \quad (3.26)$$

where  $B_0$  is the resonance position and the coupling strength is parameterized by a magnetic width  $\Delta$ , such that  $\Gamma_0 = \delta\mu\Delta$  with  $\delta\mu$  the difference in magnetic moments between the open and closed channel.

Conversely, OFRs offer the possibility to tune the coupling strength between the open and closed channel, since the coupling depends on the transition matrix element which varies with the square root of laser intensity. Furthermore, since OFRs utilize electronically excited states which have a natural lifetime,  $\gamma$  is nonzero. This results in inelastic loss processes for OFRs. Similar to MFRs, we can define the change in scattering length as [6, 62, 87]

$$\tilde{\alpha} = a_s \left( 1 - \frac{w\delta}{\delta^2 + \gamma^2/4} + \frac{i}{2} \frac{w\gamma}{\delta^2 + \gamma^2/4} \right) \quad (3.27)$$

where  $\delta = \omega - \omega_0$  is the detuning from the chosen photoassociation resonance at  $\omega_0$  as shown in Fig. 3.3.3, and the width of the resonance is defined by  $w = -\ell_{opt}\gamma/a_s$ . Typically, the strength of OFRs are characterized by their optical length [15, 62] given by  $\ell_{opt} = a_s\Gamma_0/\gamma = \frac{\lambda_{OFR}^3 |\langle n|E\rangle|^2}{16\pi c k} I$ . Here  $c$  is the speed of light,  $\lambda_{OFR}$  is the wavelength of the coupling laser, and  $|\langle n|E\rangle|^2$  is the free-bound Frank-Condon factor between the bound state  $|n\rangle$  and scattering state  $|E\rangle$ . Additionally, it is useful to identify the

real and imaginary parts of Eq. 3.27 as defined in Eq. 3.25.

$$a_{OFR} = a_s + \ell_{opt}\gamma \frac{\delta}{\delta^2 + \gamma^2/4} \quad b_{OFR} = \frac{\ell_{opt}}{2} \frac{\gamma^2}{\delta^2 + \gamma^2/4} \quad (3.28)$$

Our previous work exploring the use of an optical Feshbach resonance took advantage of photoassociation transitions with large optical lengths to control the scattering length of an  $^{88}\text{Sr}$  BEC as described by Eq. 3.27. However, all studies of OFR to date have been limited by large atom loss rates [6, 23, 79, 80, 87] which can be modeled as a density evolution,  $\dot{n} = -K_{in}n^2$ , where  $K_{in}$  is the two-body inelastic loss rate constant. In the low energy limit,  $k \rightarrow 0$ , the inelastic loss rate is given by

$$K_{in} = \frac{8\pi\hbar}{\mu_r} b_{OFR} = \frac{4\pi\hbar}{\mu_r} \frac{\ell_{opt}\gamma^2}{\delta^2 + \gamma^2/4} \quad (3.29)$$

where  $\mu_r$  is the reduced mass,  $\delta$  is the laser detuning as shown in Fig. 3.3.3.

### 3.4 Modeling of photoassociation lineshapes

This section will concern the general theory used to describe photoassociative spectra. While a full quantum close-coupling calculation is the most complete and rigorous method for analyzing cold quantum scattering problems, useful approximations can be applied to realize relatively more "simple" closed analytic formulas describing photoassociation spectra.

This section will cover the theory of lineshapes in PAS.

Somewhere I read about three regimes of PAS as a comparison of relevant energy scales. Should explore that here

Pretty much have everything needed from our previous section. Relation of rate constant to cross sections is nice and simple Julianne 14 - slide 21 These fully coupled-channel models are not straightforward to evaluate. Can make assumption to simplify

### 3.4.1 One-photon excitation of free to bound transitions

Can recreate the type of model for MFR in a field dressed approach plot showing photon + potential

ANalytic forms for modeling compare all the forms of K the crazy one from BJ 99 the simple one with  $f(p)$  nicholson 42

show plot with all the terms defined

give loss rate (will need to have introduced before) define terms gammaStim as overlap gamma as molecular lifetime delta as detuning A as coupling strength

introduce reflection approximation evaluation of overlap reference BJ 99

give relative momentum distribution this results in an asymmetric profile give plot

Number equation vs. time

segue to narrow lines

#### 3.4.1.1 PAS near narrow intercombination transitions

quick note on the usage of the relative momentum distribution usually this is all we care about since the CoM part results in doppler shifts which would be negligible on the energy scales of broad dipole-allowed transitions using narrow intercombinations lines, the photon recoil energy is comparable to the bound state lifetime this means that individual lorentzians might be shifted (each by a different amount) in addition to the total line shape being asymmetric Integration over both degrees of freedom will be an important discussion in the next chapter as we fit spectra and determine the halo binding energy

ideas of limiting cases that can be explored with PAS [19]

### 3.4.2 Extension to two-color spectra

Pretty much the same things

Show new picture with all the couplings defined

Now that we have the theory of PAS covered.

$$N(t) = \frac{N_0 e^{-\Gamma t}}{1 + \frac{2N_0 \langle K \rangle V_2}{\Gamma V_1^2} (1 - e^{-\Gamma t})} \quad (3.30)$$

where  $N_0$  is the number at the beginning of the PAS interaction time, and  $\langle K \rangle$  indicates a spatial average of collision event rate constant  $K$  (Eq. 3.32). The one-body loss rate,  $\Gamma$ , is due to background collisions and off-resonant scattering from the PA lasers.

PA loss is described with a local equation for the evolution of the atomic density [Eq. (5.1)]. Integrating Eq. (5.1) over the trap volume yields the time evolution of the number of trapped atoms [Eq. (5.2)]. The effective volumes used throughout this analysis are defined by

$$V_q = \int_V d^3r e^{-\frac{qU(\mathbf{r})}{k_B T}}, \quad (3.31)$$

for trapping potential  $U(\mathbf{r})$ . The collision event rate constant can be expressed as a thermal average of the scattering probability for loss,  $|S(\epsilon, \omega_1, \omega_2, \dots, \mathbf{r})|^2$ , over the collision energy  $\epsilon$ . We also average over the trap volume to allow for the possibility that the scattering probability can vary with position in the trap due to inhomogeneity of laser intensity profiles and the density distribution [Eq. (3.32)].

$$\begin{aligned}\langle K \rangle &= \frac{1}{V_2} \int_V d^3r e^{-\frac{2U(r)}{k_B T}} \\ &\times \frac{1}{h Q_T} \int_0^{U_{max}-U(r)} d\epsilon |S|^2 e^{-\epsilon/k_B T}.\end{aligned}\quad (3.32)$$

where the partition function is  $Q_T = \left(\frac{2\pi k_B T \mu}{h^2}\right)^{3/2}$  for reduced mass  $\mu$ .

Bohn and Julienne [? ] provide an expression for  $|S(\epsilon, \omega_1, \omega_2, \dots)|^2$  for a collision on the open channel of two ground state atoms (g) with total energy  $\epsilon$  leading to loss-producing decay from the excited state  $b_1$  with rate  $\gamma_1$ . (See Fig. ??.) It yields

$$|S|^2 = \frac{(\Delta_2 + \epsilon/\hbar)^2 \gamma_1 \gamma_s}{\left[(\Delta_1 + \epsilon/\hbar)(\Delta_2 + \epsilon/\hbar) - \frac{\Omega_{12}^2}{4}\right]^2 + \left[\frac{\gamma_1 + \gamma_s}{2}\right]^2 (\Delta_2 + \epsilon/\hbar)^2}, \quad (3.33)$$

where all quantities are defined in the main text. For simplicity, we have omitted the light shift of  $b_1$  due to coupling to the scattering continuum [? ]. Equation (3.33) neglects all light shifts due to the trapping laser. Light shifts due to the photoassociation lasers coupling to states outside our model (Fig. ??) are also neglected. The thermal energy is much greater than the zero-point energy for trap motion,  $T \gg h\nu_{\text{trap}}/k_B$ , so confinement effects are negligible [? ].

and lights shifts of states 0 and 2 are approximately equal and will cancel in the determination of the binding energy of the halo state,  $E_2$  [64? ]. Neglecting

For the experiments reported here, we maintain significant intermediate-state detuning,  $|\Delta_1| \gg |\Omega_{12}|$ . Thus we are in a Raman configuration, and near two-photon resonance the expression for the scattering probability for a given initial scattering

energy Eq. (3.33) can be approximated as a Lorentzian

$$|S|^2 \approx \frac{A(\epsilon)}{\left(\Delta_2 + \epsilon/\hbar - \frac{\Omega_{12}^2}{4(\Delta_1 + \epsilon/\hbar)}\right)^2 + [\Gamma_L(\epsilon)/2]^2}, \quad (3.34)$$

where  $A$  and  $\Gamma_L$  are defined in Eqs. (5.8) and (5.9).

As discussed in the text, we analyze loss spectra using the effective expression, Eq. (5.10) to account for possible deviations from the single-channel theory [? ].

The total 689-nm intensity oscillates with 100% contrast according to  $I_{total} = I_1 + I_2 + 2\sqrt{I_1 I_2} \cos[(\omega_1 - \omega_2)t] = 2I \{1 + \cos[(\omega_1 - \omega_2)t]\}$ . Equation 4.1 The form of the AC Stark shift due to excitation lasers in Eq. 5.11 reflects the time average of the intensity and neglects the interference term. To confirm that this is the correct description, we numerically solved the time-evolution for a three-level system with similar optical couplings and oscillating optical intensity as present during halo photoassociation. The Hamiltonian is

$$H = \quad (3.35)$$

$$\begin{pmatrix} 0 & \Omega_{01} [\cos(\omega_1 t) + \cos(\omega_2 t)] & 0 \\ \cdot & E_{b1} & \Omega_{12} [\cos(\omega_1 t) + \cos(\omega_2 t)] \\ \cdot & \cdot & E_{b2} \end{pmatrix}$$

For  $\Omega_{01} \ll \Omega_{12} \ll \Delta_1 \equiv E_{b1}/\hbar - \omega_1$ , which is analogous to the experimental conditions used here

, the shift of the two-photon resonance condition follows  $\delta = \Omega_{12}^2/2\Delta_1$  in agreement with Eq. 4.1.

## Chapter 4

### Strongly coupled PAS of a weakly bound molecule

#### 4.1 Probing the ground state potential

Weakly bound ground-state dimers are of great interest in ultracold atomic and molecular physics. In this chapter we study the least-bound vibrational level of the  $X^1\Sigma_g^+$  electronic ground state of the  $^{86}\text{Sr}_2$  dimer in a high intensity regime, where the AC Stark shift is comparable to the unperturbed binding energy.

Previous studies of the molecular states of the  $X^1\Sigma_g^+$  ground state potential have primarily focused on strontium-88. Lots of properties of strontium derived from these studies and applied to other isotopes via mass-scaling. This work presents the first two-photon photoassociation study of the ground state of  $^{86}\text{Sr}$ , as all previous PA experiments have been one-photon PA to excited electronic states Yu 25-27. Direct excitation to the halo state provides an extremely sensitive probe of the long-range part of the ground state potential. The work presented in this chapter was followed by a low intensity study, presented in Ch. 5, which precisely determined the natural halo binding energy and presents a mass-scaled theory improving on the accepted scattering lengths of all strontium isotopes.

In these initial experiments, when varying the excitation laser intensity, we observed unexpectedly large bound-bound coupling between the intermediate molecular state, used for Raman coupling, and the halo state. Furthermore, by varying the in-

termediate state detuning, we observed a breakdown of the isolated resonance model which cannot explain the observed frequency dependence of the AC stark shift of the two-photon transition.

As discussed in the previous chapter, two-photon PAS can be used to directly populate molecular levels and can be described using the theory of Bohn and Julienne if the two driving lasers are of sufficiently different frequencies such that each laser independently drives a specific transition. This corresponds to the typical  $\Lambda$ -model Yu, 20 21. However, in the scenario of the halo state, the laser frequencies differ by only up to  $\sim 300$  kHz which is much smaller than the typical intermediate state detuning of several MHz. In this regime, each laser should be considered to act on both legs of the transition leading and in collaboration with the theory group of Kaden Hazzard, we developed simple theoretical models for describing this novel regime.

In the following we present our high-intensity results and discuss the theoretical development of several models focused on predicting the observed frequency dependence of the halo state and the bound-bound coupling to the intermediate state.

## 4.2 Experimental setup

Fig. 4.1 shows the excitation scheme used to probe the halo state in  $^{86}\text{Sr}$  using two-photon Raman photoassociation [? ], in which two laser fields couple colliding atoms to the least-bound state of the ground molecular potential. The sample temperature is low enough that collisions are entirely *s*-wave. The target state for the two-photon transition has total angular momentum  $J = 0$  and binding energy  $E_{b2}(< 0)$ .  $^{86}\text{Sr}$  has no nuclear spin and a  $^1S_0$  electronic ground state, leading to a single ground

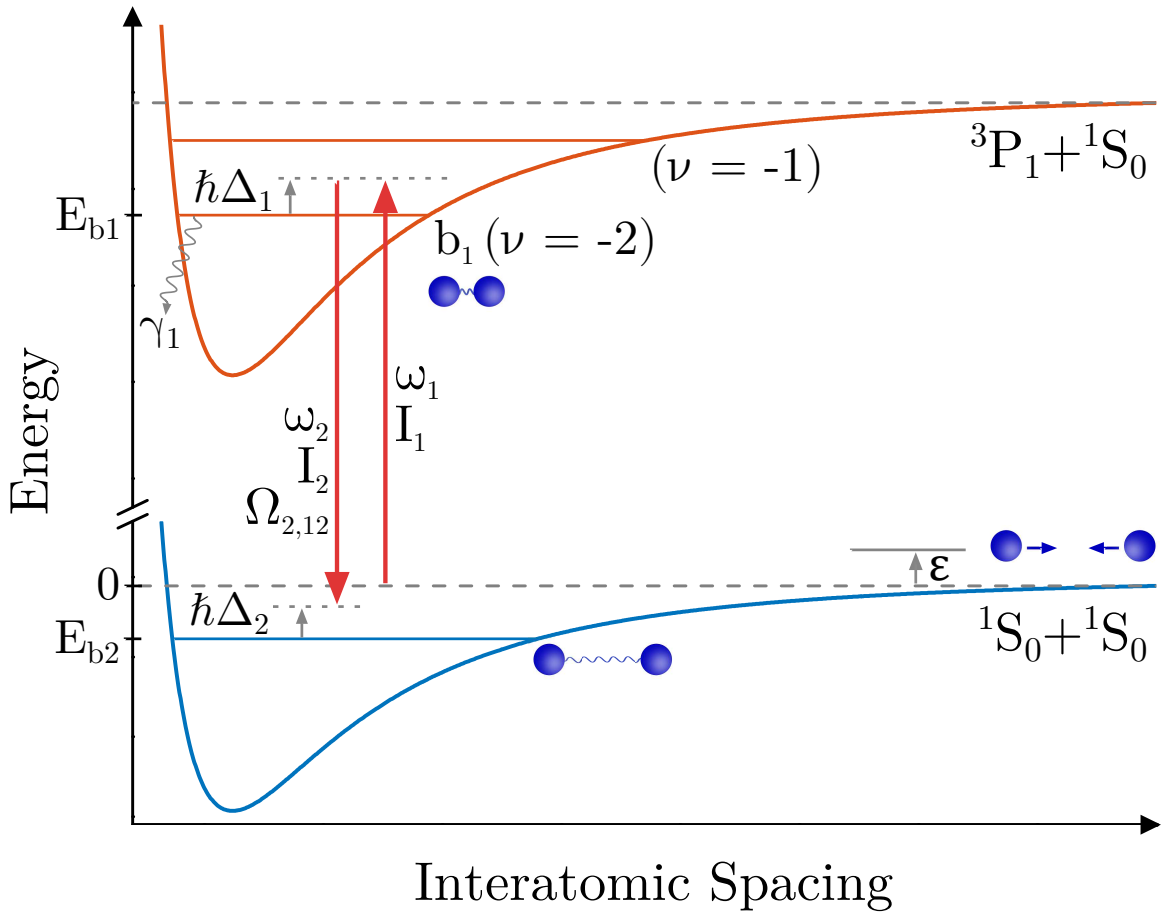


Figure 4.1 : Strontium PAS potential

Two-photon photoassociation diagram. The energy of two well-separated  ${}^1S_0$  atoms at rest is taken as zero.  $\epsilon$  is the kinetic energy of the colliding atom pair.  $E_{b1}$  is the unperturbed energy of the bound state of the excited molecular potential that is near resonance with the free-bound laser, which in these experiments is the second-least bound level of the excited molecular potential ( $\nu = -2$ ).  $E_{b2} (< 0)$  is the unperturbed energy of the least bound state of the ground molecular potential. The photon of energy  $\hbar\omega_1$  is detuned from  $E_{b1}$  by  $\hbar\Delta_1$  for  $\epsilon = 0$ , while the two-photon detuning from  $E_{b2}$  is  $\hbar\Delta_2$ . The decay rate of  $b_1$  is  $\gamma_1$ . Stark and collisional frequency shifts are neglected in this schematic.

electronic molecular potential ( $X^1\Sigma_g^+$ ). The dominant intermediate state ( $b_1$ ) is the  $J = 1$  rotational state of the second least-bound ( $\nu = -2$ ) vibrational level on the  $0_u^+$  molecular potential, which asymptotically connects to the  ${}^1S_0 + {}^3P_1$  asymptote at long range[? ]. This state is bound by 44.246(10) MHz [? ]. We define  $\Delta_1 = \omega_1 - E_{b1}/\hbar$  and  $\Delta_2 = \omega_1 - \omega_2 - E_{b2}/\hbar$  as the one-photon detuning from state  $b_1$  and two-photon detuning from state  $b_2$  respectively for an initial scattering state with collision energy  $\epsilon = 0$ .  $\Omega_{2,12}$  is the Rabi frequency for coupling between states  $b_1$  and  $b_2$  due to the laser field at  $\omega_2$  with single-beam intensity  $I_2$ . Because the binding energy of the halo molecule is very small compared to  $\Delta_1$ , both laser frequencies are near resonance with the  $\nu = -2$  state. The transitions to the least-bound ( $\nu = -1$ )  $J = 1$  excited molecular state, bound by 1.633(1) MHz, and the excited atomic state lie near enough in energy that they can effect our observations.

Photoassociation leads to loss of atoms from the trap through radiative decay from the intermediate, excited electronic state, and from collisions between molecules and background atoms. In addition to the relevant potentials, Fig. 4.1 also defines two possible relationships between the laser frequencies. In each of these scenarios, the frequency of  $\omega_1$  remains fixed while the frequency of  $\omega_2$  is varied. In the case that  $\omega_2 > \omega_1$ , then the standard Raman configuration is recovered where  $\Delta_1$  remains fixed while increasingly more energy is withdrawn from the system as  $\omega_2$  is increased. In the opposing scenario,  $\omega_2 < \omega_1$ ,  $\Delta_1$  is also varied slightly as  $\omega_2$  is varied, which in turn leads to a changing AC Stark shift over the course of a scan. Although, in our experiments  $\Delta_2 \ll \Delta_1$  and subsequently the variation of the AC Stark shift acting on the halo state is small. While experimentally, the data presented in this chapter is not accurate enough to measure the effects of this variation, our theoretical model does

predict slightly different binding energies in these two regimes as discussed below.

After an exposure time on the order of one hundred milliseconds, the number of ground-state atoms remaining and the sample temperature are measured with time-of-flight absorption imaging.

Two-photon spectroscopy is performed on ultracold  $^{86}\text{Sr}$  atoms in a single-beam optical dipole trap generated from a 1064-nm laser propagating perpendicular to gravity with beam waists of 260 and  $26\ \mu\text{m}$  [17,22]. The tight waist provides vertical confinement. The trap depth after an evaporative cooling stage determines the sample temperature, which is set between 30 and 1000 nK. Typical atom numbers are several hundred thousand and peak densities are as high as  $n_0 = 2 \times 10^{12} \text{ cm}^{-3}$ . The number of atoms and sample temperature are measured using time-of-flight absorption imaging operating on the 1S0-1P1 transition. Trap oscillation frequencies are determined by measuring dipole and breathing collective mode frequencies, which allow determination of trap volume and sample density

performed on ultracold Sr atoms in a single-beam optical dipole trap (ODT) generated from a 1064-nm laser propagating perpendicular to gravity. Typical atom numbers are several hundred thousand and peak densities are  $\approx n_0 = 1 \times 10^{12} \text{ cm}^{-3}$ . The number of atoms and sample temperature are measured using time-of-flight absorption imaging described in [some section](#). Trap oscillation frequencies are determined by measuring dipole and breathing collective mode frequencies, which allow determination of trap volume and sample density

We generate the two photons for spectroscopy as shown in Fig4.2. These photons are injection locked from the master laser and precisely controlled via two RF frequencies incident on a single acouto-optic modulator and delivered to the atoms with

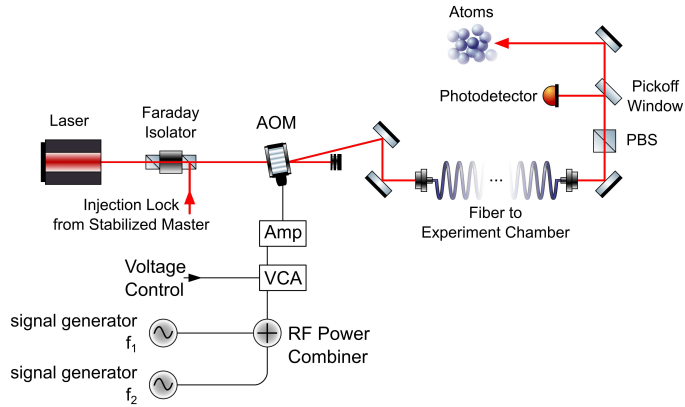


Figure 4.2 : Schematic of PAS light generation

Light for these experiments is generated by the spectroscopy slave laser setup discussed in Sec. 2.3.5.2.

an optical fiber. This fiber output is launched near the science chamber with output optics that yield a  $320\ \mu\text{m}$  waist at the atoms, much larger than the size of the atom cloud. Both PA beams are linearly polarized along the same direction. The beat signal of the two light fields after the fiber is monitored on a photodiode and the RF powers are adjusted to ensure matched intensities for the two frequency components ( $I_1 = I_2 \equiv I$ ).

The optical fiber ensures that the wavevector of the two photons will be parallel which allows us to neglect any effects of Doppler broadening which might result from imparting momentum into the atomic sample.

This is a simple system for generating multiple frequencies which are guaranteed to share the same wavevector, phase coherence, and gross frequency stability.

Primary reasons why we can't scan large distances. There will be a slight misalignment of the beams into the fiber and the RF may start to fall off. For these

experiments an AOM with a center frequency of 90 MHz was used.

We see a reduction in contrast when the two drive frequencies differ by more than  $\approx 250$  kHz.

Since the modulator is a narrowband device, scanning great care is taken to ensure the maximum amount of contrast is visible on the photodiode. This

This simple system has many advantages and a couple of drawbacks. Since both photons are aligned into the same fiber then they are guaranteed to have the same output wavevector and therefore the two photon process will be doppler free (since the absorption and emission processes will exactly cancel each other out).

Use of the AOM provides highly accurate control of the difference frequency with RF precision.

While versatile and simple, we are worried about the balance of the RF power onto the AOM. These devices are narrowband modulators (simple ones)

As described in [some section](#) the slave laser is frequency stabilized at +42 MHz of the 86Sr  $^1S_0 \rightarrow ^3P_1$  atomic transition. The AOM then shifts the light the remaining  $\approx 86$  MHz to set the detuning around the  $\nu = -2$  bound state of the  $^1S_0 + ^3P_1$  potential. Setting of  $\Delta_1$  is done by removing one of the frequencies, peaking up the diffraction angle and alignment into the fiber.

During the course of our experiments we found that mild environmental perturbations (loud noises, air currents due to fans, etc.) to the fiber resulted in slow variation of the light coupling through the fiber. Such amplitude modulations are not uncommon in laser systems and can typically be compensated for by using a closed loop locking mechanism. However, after construction of such a power lock the components

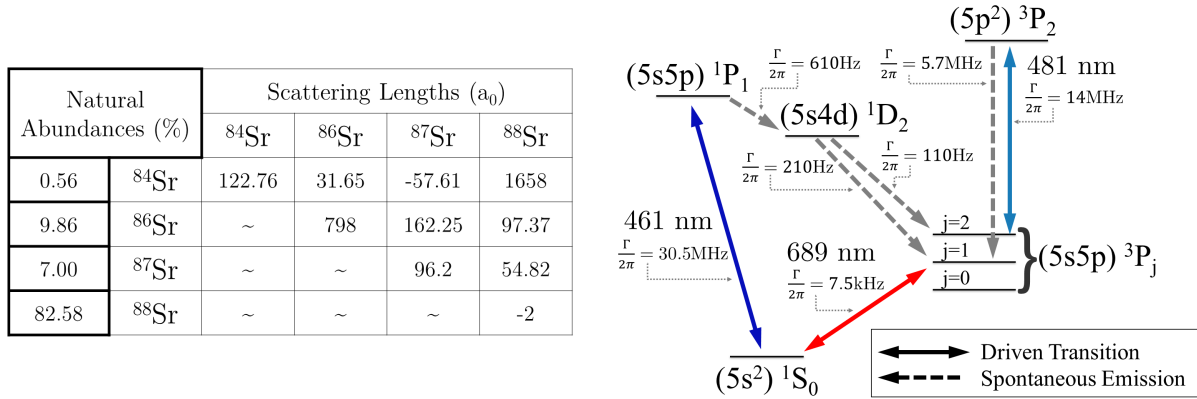


Figure 4.3 : Histogram of PAS beam intensity variation

One of the histograms from onenote. There are separate histograms for each experimental run (I should combine this so I don't have to discuss)

did not react quickly enough and there was a significant overshoot which resulted in an uncontrolled amount of light illuminating the atoms during short exposures. This led us to implement a digital based sample and hold mechanism for reduced intensity variability. This system is described in detail in some section. The sample and hold system in combination with the power lock provided intensity stability with a standard 5% standard deviation during a typical experiment. Fig shows a typical histogram of the recorded intensities.

The beat signal of the two light fields after the fiber is monitored on a photodiode and the rf powers are adjusted to ensure matched intensities for the two frequency components ( $I_1 = I_2 \equiv I$ ).

Regarding the general process

Using the  $^1S_0 + ^3P_1$  interatomic potential, we perform a raman process using the  $\nu = -2$  bound state which has a binding energy of  $E_b = -44\text{MHz}$  cite improved

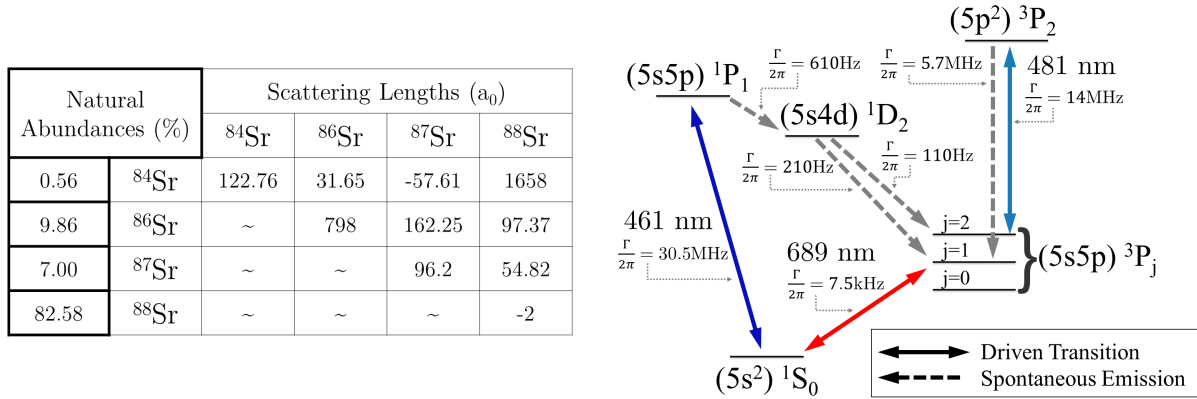


Figure 4.4 : Characteristic view of the PA beatnote

This is the picoscope plot of the beatnote

binding en. Sample pre

We used strontium 86 in a thermal gas at temperatures between 30 and 1000 nK.

Typical peak densities were around  $n_0 = 1 \times 10^{12} \text{ cm}^{-3}$ .

Raman process using the second bound state of the  $^1S_0 + ^3P_1$  interatomic potential

After the atoms have equilibrated in the final ODT configuration, the PA lasers are applied (Fig. ??). A single acousto-optic modulator, driven with two RF frequencies, is used to generate both PA beams. Light is derived from a frequency-stabilized master laser (Fig. 5.1) and coupled into a single-mode optical fiber

### 4.3 Estimating the halo binding energy

In this paper, we measure spectra in the high-intensity regime and develop a theory that accounts for the effects of the two-frequency drive when molecular binding energy is small and excitation laser intensity is high. The model neglects motional degrees of freedom for the initial state of two free atoms and considers only three levels a

dimer in the ground electronic state, the intermediate dimer state in the excited electronic potential, and two well-separated atoms. We numerically solve this model and analyze many of its features with analytic approximations. We also briefly consider extensions of this three-level model that add extra levels to capture some fine details of the ac Stark shift at large detuning. We show that the three-level model captures key experimentally observed features despite its simplicity. Numerical simulations show that it accurately predicts the appearance of additional spectral lines in the highintensity regime, and that these correspond to higher order non-linear processes. It accurately captures the location of the spectral peaks, including ac Stark shifts from both lasers when intermediate state detuning,  $\Delta_1$ , is comparable to E0 b . Furthermore, when the intensity of the lasers is not too small, the spectral lineshapes of individual lines are reasonably well-captured. This indicates that effects missing from this theory – the motion of the atoms [21], interaction shifts due to molecules and atoms scattering off of other molecules and atoms [22], and the varying density within the trap [18] – are less relevant in the regime of interest here.

#### 4.3.1 Frequency dependence of the AC Stark shift

The proximity of  $^{86}\text{Sr}$  to a scattering resonance and the susceptibility of the halo binding energy to the intensity of the excitation light suggests using light to tune the binding energy and scattering length as was done with optically assisted magnetic Feshbach resonances [3, 20], which is closely related to the use of optical Feshbach resonances [6, 80, 85, 87? ]. Understanding the frequency-dependence of  $\chi_{689}$  is important for investigating this possibility, so we extracted this parameter from spectra at a wide range of 689-nm laser intensities and detuning from the intermediate

resonance ( $\Delta_1$ ).

Figure 5.4 shows the resulting resonance positions,  $E'_{b2}$ , versus twice the single-beam intensity,  $2I = I_{689}$ . The shift in molecular binding energy is linear with intensity over the explored range, but varies greatly in magnitude and sign. From linear fits, we extract the AC Stark shift parameter  $\chi_{689}(\Delta_1)$  through  $E'_{b2} \equiv E_{b2} + h\chi_{689}(\Delta_1)I_{689}$  (Fig. 4.3.1).

In the experiment, the total 689-nm intensity oscillates with 100% contrast according to  $I_{\text{total}} = I_1 + I_2 + 2\sqrt{I_1 I_2} \cos[(\omega_1 - \omega_2)t] = 2I \{1 + \cos[(\omega_1 - \omega_2)t]\}$ . The functional form we use to fit the AC Stark shift reflects the time average of the intensity and neglects the interference term. To confirm that this is the correct description, we numerically solved the time-evolution for a three-level system with similar optical couplings and oscillating optical intensity as present during two-photon PA of a halo state. The Hamiltonian is

$$H = \begin{pmatrix} 0 & \Omega_{01} [\cos(\omega_1 t) + \cos(\omega_2 t)] & 0 \\ \Omega_{01} [\cos(\omega_1 t) + \cos(\omega_2 t)] & E_{b1} & \Omega_{12} [\cos(\omega_1 t) + \cos(\omega_2 t)] \\ 0 & \Omega_{12} [\cos(\omega_1 t) + \cos(\omega_2 t)] & E_{b2} \end{pmatrix}$$

For  $\Omega_{01} \ll \Omega_{12} \ll |\Delta_1| \equiv |\omega_1 - E_{b1}/\hbar|$ , which is analogous to the experimental conditions used here, we find that the two-photon resonance is shifted by

$$\frac{\hbar\Omega_{12}^2}{4\Delta_1} + \frac{\hbar\Omega_{12}^2}{4(\Delta_1 - E_{b2}/h)} \approx \frac{\hbar\Omega_{12}^2}{2\Delta_1}. \quad (4.1)$$

This agrees with our observation of a shift that is linear with intensity, and implies that the susceptibility is related to the Rabi frequency for a single-beam intensity  $I$  through  $\chi_{689} \approx (\Omega_{12}/\sqrt{I})^2/(8\pi\Delta_1)$ .

This single-resonance model [Eq. (4.1)] describes the observed shifts well for de-

tuning close to the  $\nu = -2$  state of the  $0_u^+$  molecular potential (small  $\Delta_1$ ). For large positive  $\Delta_1$ , however, at which  $\omega_1$  and  $\omega_2$  approach atomic resonance, deviations indicate coupling to one or more other states (Fig. 4.3.1). The most likely suspects are the  $\nu = -1$ ,  $J = 1$  excited molecular state, bound by 1.633(1) MHz, and the  ${}^1S_0 + {}^3P_1$  continuum. The sign of the deviation indicates that AC Stark shift of colliding  ${}^1S_0$  atoms due to coupling to the  ${}^3P_1$  state is dominant in this regime. We have neglected shifts due to collisions and the trapping laser, which are small at the large excitation-laser intensities used here.

A fit of the single-resonance model as shown in Fig. 4.3.1 yields  $\Omega_{2,12}/2\pi \equiv \Omega_{12}/2\pi = 800$  kHz for  $I = 1$  W/cm<sup>2</sup>. Note that  $\Omega_{2,12}$  as defined here would be the splitting of the Autler-Townes doublet [63], which differs from the Bohn-Julienne definition of the molecular Rabi coupling [? ]. From the measured  $\Omega_{2,12}$ , one can extract the Franck-Condon factor,  $f_{FCF}$ , reflecting the overlap of the ground and intermediate molecular states through

$$\Omega_{2,12} = \sqrt{f_{ROT}} \sqrt{f_{FCF}} \gamma_{atomic} \sqrt{\frac{I}{2I_{sat,atom}}} \quad (4.2)$$

where  $I_{sat,atom} = 2\pi^2 \hbar c \gamma_{atomic} / (3\lambda^3) = 3$   $\mu$ W/cm<sup>2</sup> is the atomic saturation intensity for the  ${}^1S_0 - {}^3P_1$  transition and  $I = I_{689}/2$  is the single-beam intensity. The rotational factor  $f_{ROT}$  accounts for the change in dipole moment from atom to molecule due to symmetry of the wave function and projection on a rotating molecular axis. Following the formalism described in [63],  $f_{ROT} = 2$  for the  $J = 1 \rightarrow 0$  bound-bound molecular transition studied here. This yields  $f_{FCF} = 0.03$ .

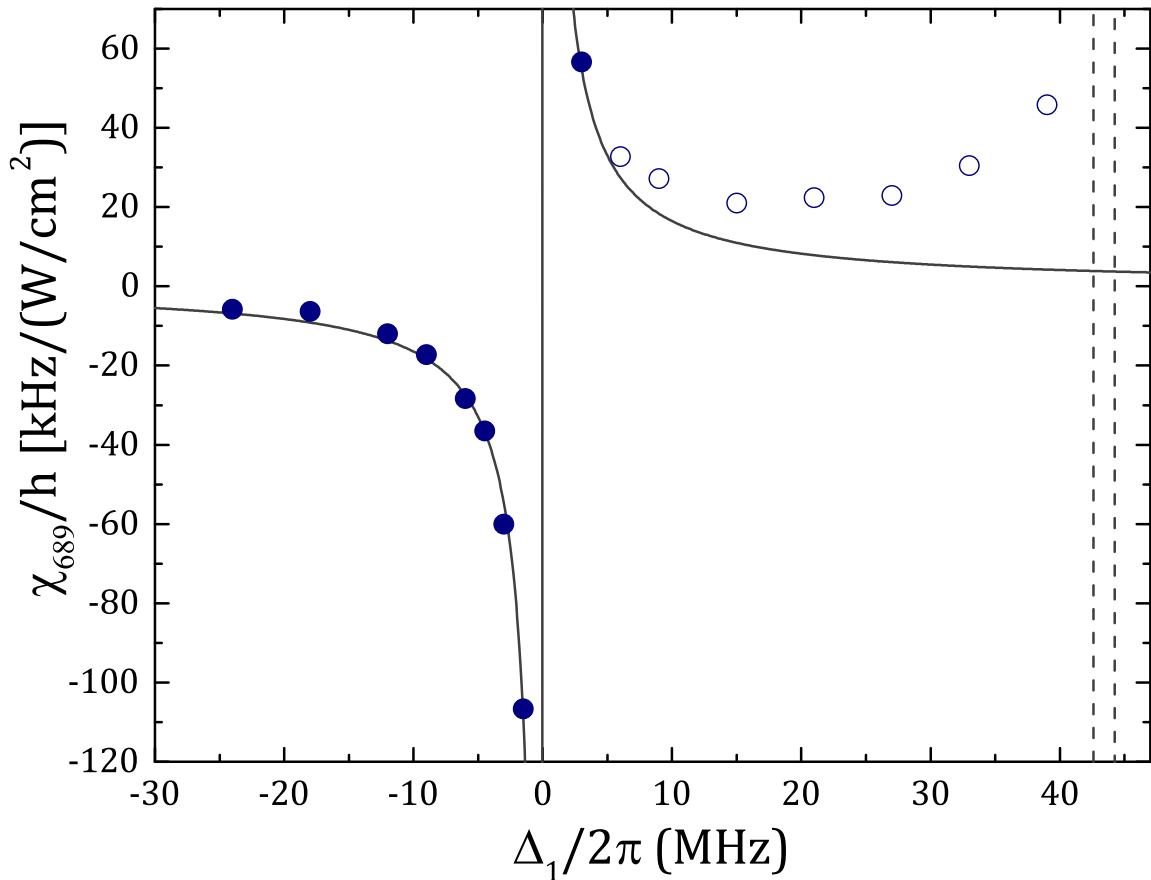


Figure 4.5 : Estimate of bound-bound coupling via isolated resonance model  
AC Stark shift susceptibility,  $\chi_{689}$ . Dashed lines indicate the positions of the  $\nu = -1$ ,  $J = 1$  excited molecular state, bound by 1.633(1) MHz, and the  ${}^1S_0 + {}^3P_1$  continuum. Solid and open symbols show experimental measurements of the susceptibility. Using only the solid symbols, we fit a single resonance model of the form  $\chi_{689} \approx (\Omega_{12}/\sqrt{I})^2/(8\pi\Delta_1)$  and show this fit result as a solid line.

#### 4.4 Multi-photon loss processes

A second case where treating each leg with a singlefrequency drive is inadequate is when the unperturbed binding energy is not much larger than the ac Stark shift. In this regime, additional peaks appear in the PA spectra at approximately  $E_b/2$ ,  $E_b/3$ , . . . , as shown in Fig. 1(c). This occurs at high intensities and/or low intermediate state detunings, and we will refer to this as the “highintensity” regime throughout this paper. We will discuss the origin of this effect in detail in Sec. VI. As per Fig. 1(c), we will refer to the most red-detuned line in the spectrum as the main negative peak, the most bluedetuned line as the main positive peak, and the additional peaks as higher order peaks.

## Chapter 5

### Binding energy of the $^{86}\text{Sr}_2$ halo molecule

conclusion of chapter 4 is that we measured the binding energy more accurately which can be directly related to a more precious value of the scattering length for 86. Also there is a straightforward experiment available to use to attempt to measure the efimov parameter for strontium.

Measurement of the binding energy precisely determines the associated *s*-wave scattering length ( $a$ ) for free-atom collisions. In the extreme case of a scattering resonance, the least-bound state represents an example of a quantum halo system [39] with spatial extent well into the classically forbidden region. Halo molecules show universality, meaning that molecular properties such as size and binding energy can be parameterized by the single quantity  $a$  independent of other details of the atom-pair interaction [10? ].

For potentials that asymptote to a van-der-Waals form, an additional parameter, the van der Waals length  $l_{\text{vdW}}$  can be introduced for a more accurate description. Efimov trimers also exist in systems near a scattering resonance, influencing dimer and atomic scattering properties and introducing additional universal phenomena [11, 61].

The known scattering properties of strontium are mass scaled from 88 is this somehow not as good for 86? Also, where are the most up to date scattering lengths for Sr from? - The '10 Fourier paper but by probing the 86 ground state potential

directly we can obtain a more accurate measurement of the 86-86 scattering length.

Strontium is a nice atom to work with because of the various properties of all of it's isotopes but access to such a variety of properties also comes with it share of complications.

The most abundant isotope, 88, has a nearly vanishing scattering length but served as the workhorse for many of our previous studies and those of other labs.

Using the universal prediction for the binding energy, including corrections derived for a van der Waals potential [26, 27, 30], we derive a more accurate value of the *s*-wave scattering length for  $^{86}\text{Sr}$  atomic collisions [? ? ].

We accurately determine the  $^{86}\text{Sr}_2$  binding energy, considering possible collisional frequency shifts and AC Stark shifts due to trapping and excitation lasers.

## 5.1 Experimental setup

Ecperimental methods expeirments in this chapter adn the following are very similar. biggest scientific differnece is that we explored different regimes of intensity experiments in this chapter were done on rydberg apparatus nearly identical machine to ours sample prep is the same but they have different ODT configurations specifics of general trapping procedure and characteristics can be found in some location used the PA light from my apparatus coupled through a long fiber pa generation talked abot below For the low E exp the general parameters were such and such generic tim-inf diagram (denote where physics is different) generation of photoassociation light Specifics of the low e experiment discuss optical setup propagation, polarization B field? ODT configurartion consideration of the trap depth during experiment we took

a lot of data over a wide range of parameters and assumed we were in a deeply trapped regime took data all the way down at 30nK and thought it was normal to not have a BEC at this point because it is 86 determined trap frequencies after we did the experiment during analysis we found a problem with the model not agreeing 30nK data did not fit well if we made the typical assumptions about a deep trap show plot of fit decided to model the trap numerically trap frequencies were measured at higher temps and extrapolated using model (reason to believe modeling) modeling found that the lowest point of the trap was an odd trajectory and was much lower than we naively thought show plot of fit hypothesized that the sample may not have been thermalized completely (non-ergodic) and thus was fooling us this is supported by the better fitting of 30 nK data over time Brings into questions the use of temperature, but will persist with that data where there is at least reasonable agreement Leads to a strong modification of the momentum distribution and will effect the energy integral due to large variation in the available energy range

In this work, we probe the halo state in  $^{86}\text{Sr}$  using two-photon Raman photoassociation (PA) [cite 16 from halo paper](#), in which two laser fields couple colliding atoms to the least-bound state of the ground molecular potential. We tune near resonance with an intermediate state that is bound in the  $0u$  potential corresponding to the  $^1S_0 + ^3P_1$  asymptote at long range as shown in Fig.5.1.

Photoassociation experiments follow the same general prescription. We start by trapping through the normal sequence as outlined in [some section](#). Then we evaporate down to the final trap depth. After evaporation

The two-photon PAS experiments described in the following chapters are performed under similar conditions but due to complications with the neutral vacuum

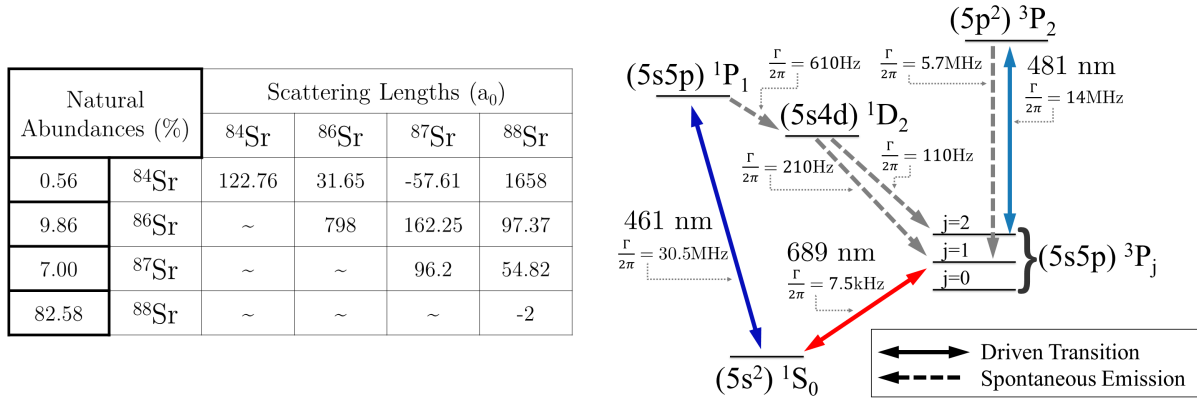


Figure 5.1 : Strontium two-photon photoassociation

fig 1 from the halo paper

system we performed the binding energy experiments using the Rydberg apparatus. While non-ideal from a consistency point of view, this did allow us to replicate and validate our previous findings which gives us great confidence in the robustness of this experimental approach.

The most significant difference between the two apparatus' is the trapping characteristics of the optical dipole traps and the beam parameters of the photoassociation beam. These differences are noted in the corresponding chapters but here we will outline the timing and generic characteristics that are shared between the two experiments.

performed on ultracold Sr atoms in a single-beam optical dipole trap (ODT) generated from a 1064-nm laser propagating perpendicular to gravity. Typical atom numbers are several hundred thousand and peak densities are  $\approx n_0 = 1 \times 10^{12} \text{ cm}^{-3}$ . The number of atoms and sample temperature are measured using time-of-flight absorption imaging described in some section. Trap oscillation frequencies are deter-

mined by measuring dipole and breathing collective mode frequencies, which allow determination of trap volume and sample density

Two-photon spectroscopy is performed on ultracold  $^{86}\text{Sr}$  atoms in a single-beam optical dipole trap (ODT) generated from a 1064-nm laser propagating perpendicular to gravity with beam waists of  $260\ \mu\text{m}$  and  $26\ \mu\text{m}$  [? ? ]. The tight waist provides vertical confinement. The trap depth after an evaporative cooling stage determines the sample temperature, which is set between  $30 - 1000\ \text{nK}$ . Typical atom numbers are several hundred thousand and peak densities are as high as  $2 \times 10^{12}\ \text{cm}^{-3}$ . The number of atoms and sample temperature are measured using time-of-flight absorption imaging operating on the  $^1S_0$ - $^1P_1$  transition. Trap oscillation frequencies are determined by measuring dipole and breathing collective mode frequencies, which allow determination of trap volume and sample density.

## 5.2 Modeling the PA spectra

### 5.2.1 Consideration of the trap depth

Show plots of the trap and how we determined what the trap depth was

Our previous discussion of the rate loss constant assumed we could describe the spatial distribution of the atomic density profile analytically. This is a valid superposition given two key assumptions, 1) the sample termperature remains constant during the PA exposure and 2) the trap is of sufficient depth that we can reasonably approximate it as a harmonic trap. cite Mi's trap paper.

Analysis of the trapping conditions after acquisition of the data revealed that this second assumption was not maintained during our experiment. In some figure we

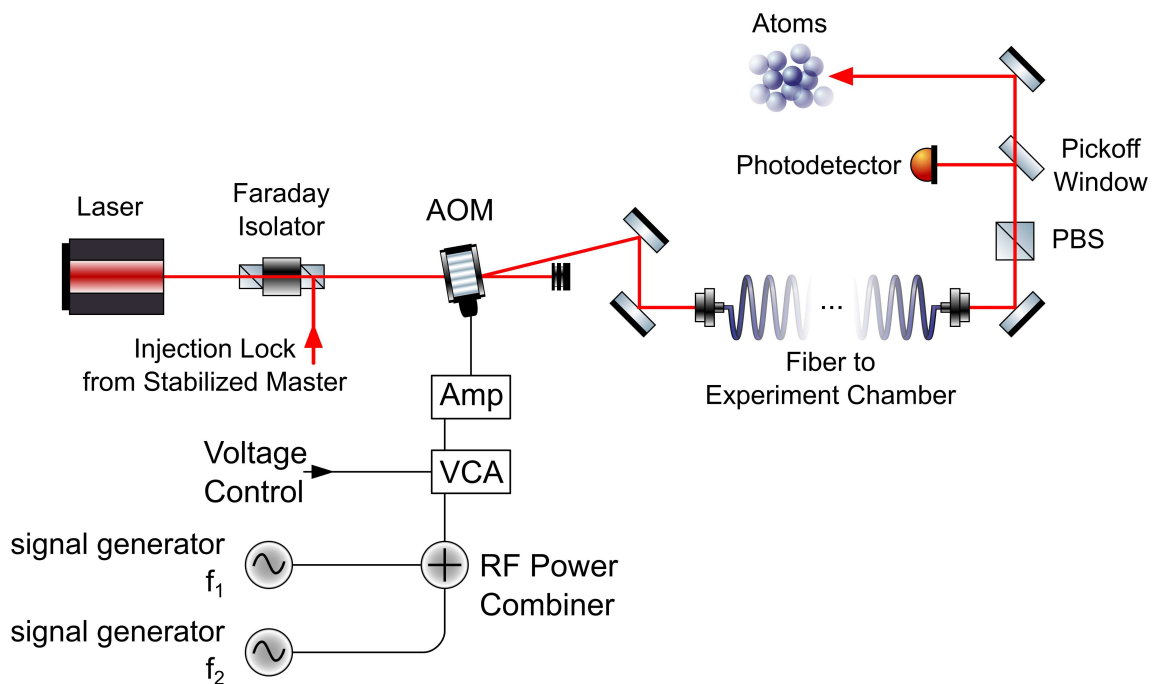


Figure 5.2 : PAS laser setup

Photoassociation laser schematic . A master laser is frequency-stabilized via saturated absorption spectroscopy to the  $^1S_0$ - $^3P_1$  atomic transition. After amplification with a diode slave laser, light at two controllable frequencies is generated with a single acousto-optic modulator (AOM) and delivered to the atoms with an optical fiber. The beat note between the two frequencies is monitored after the fiber.

can see that we only have an eta of 2. This is troublesome as it means we must numerically consider the density distribution over space when solvinf for the rate loss constant K.

In addition to the modified spatial distribution, we must also consider the effect of the trap depth on the energy profile of the trapped gas. In a typical high-eta trap, a typical Boltzmann profile is sufficient to describe the velocity distribution of the atoms and when we consider the distribution of relative energies that is important for PAS expeirments, we recover a simple bolztmann weighting for the distribution of energy probabilities. This is shown in [some app](#).

However, the case of a low-eta trap we must define a local cutoff energy at each point in space within the trap as atoms that have an energy higher than the local eta value are assumed to be lost from the trap. Derivation of this truncated relative energy probabillity distribution is given in [some app](#) and results in a stronger weighting of the coldest atoms near the bottom of the trap.

### 5.2.2 Fitting the trap-averaged thermal lineshape

This section develops the more groddy form of the BJ equation. Include the

In Ch. [somewhere](#) we discussed the usual situation for observing loss due to photoassocition. This experiment was similar to the 88 autler townes experiment.

PA loss is described with a local equation for the evolution of the atomic density

$$\dot{n} = -2Kn^2 - \Gamma n, \quad (5.1)$$

where the laser-frequency dependence of the collision-event rate constant,  $K$ , determines the spectrum of the PA loss. The one-body loss rate,  $\Gamma$ , is due to background

collisions and off-resonant scattering from the PA lasers. By integrating this equation over the trap volume, we can obtain the evolution of the total number of trapped atoms

$$N(t) = \frac{N_0 e^{-\Gamma t}}{1 + \frac{2N_0 \langle K \rangle V_2}{\Gamma V_1^2} (1 - e^{-\Gamma t})} \quad (5.2)$$

where  $N_0$  is the number of trapped atoms at the beginning of the PAS interaction time. The effective trap volumes  $V_q$  are

$$V_q = \int_V d^3r e^{-\frac{qU(\mathbf{r})}{k_B T}}, \quad (5.3)$$

for trapping potential  $U(\mathbf{r})$ .  $\langle K \rangle$  is the trap-averaged collision event rate constant

$$\begin{aligned} \langle K \rangle &= \frac{1}{V_2} \int_V d^3r e^{-\frac{2U(\mathbf{r})}{k_B T}} \\ &\times \frac{1}{h Q_T} \int_0^{\epsilon_{\max}(\mathbf{r})} d\epsilon |S|^2 e^{-\epsilon/k_B T}, \end{aligned} \quad (5.4)$$

which is itself a thermal average of the scattering probability for loss ( $|S(\epsilon, \omega_1, \omega_2, \dots, \mathbf{r})|^2$ ) over the collision energy  $\epsilon$ , with an energy cutoff  $\epsilon_{\max}$  to be discussed momentarily. The trapping potential is given by  $U(\mathbf{r}) = mgz + h\chi_{1064,g}I_{1064}(\mathbf{r}) - \tilde{U}_{\min}$ , where  $mgz$  is the gravitational potential at height  $z$ ,  $I_{1064}(\mathbf{r})$  is the intensity of the trapping light, and  $\chi_{1064,g} = 11 \text{ Hz}/(\text{W/cm}^2)$  [? ] is proportional to the polarizability of ground state atoms due to 1064 nm light.  $\tilde{U}_{\min}$  is subtracted to set the potential at the trap minimum to zero. The spatial integral is restricted to regions around the trapping local minimum with  $U(\mathbf{r})$  less than the trap depth [? ]. Downhill regions on the other side of the saddle point defining the trap depth are excluded. The laser intensity profile is measured independently, and the potential is found to be consistent with measured trap oscillation frequencies. The partition function is  $Q_T = \left(\frac{2\pi k_B T \mu}{h^2}\right)^{3/2}$  for reduced mass  $\mu = m/2$  and sample temperature  $T$ , for atoms of mass  $m$ .

Equation (3.32) provides the correct thermal average when the collision-energy distribution does not need to be truncated ( $\epsilon_{\max} \rightarrow \infty$ ). For our data, however, the ratio of sample temperature to trap depth is  $k_B T / U_{\text{depth}} \approx 3$  for samples with temperature above 100 nK and drops to unity for 30 nK samples, so truncation effects are important. If the single-particle kinetic-energy distribution function is a Boltzmann truncated at  $U_{\text{depth}} - U(\mathbf{r})$ , then the collision-energy distribution follows a Boltzmann distribution at low energies [ $\epsilon \ll U_{\text{depth}} - U(\mathbf{r})$ ] and falls off more quickly at larger energies, reaching zero at  $2[U_{\text{depth}} - U(\mathbf{r})]$ . We find that this treatment predicts a narrower distribution on the red side of the spectral line than we observe in our data, suggesting the presence of atoms in non-ergodic orbits with energies above the saddle point of the trap. This is not surprising given the large collisional loss rate associated with near-resonant scattering in this isotope. Fortunately, the molecular binding energy is strongly determined by the sharp edge of the spectrum on the blue side of the line, which is relatively insensitive to the description of the red tail. Our data is fit well with a truncated Boltzmann distribution of collision energies [Eq. (3.32)]. To estimate the systematic uncertainty introduced by this treatment, we perform fits with  $\epsilon_{\max}$  equal to  $2[U_{\text{depth}} - U(\mathbf{r})]$  and  $U_{\text{depth}} - U(\mathbf{r})$  and take the mean of the two results as the best value for the binding energy and half the difference as a systematic uncertainty  $\sigma_{\epsilon_{\max}} \approx 100 \text{ Hz}$ . This procedure does not correctly represent the overall normalization of  $\langle K \rangle$ , but we are not concerned with overall signal amplitude in this study. Atom temperatures vary by no more than 20% during the interaction time, so assuming a constant sample temperature is reasonable.

Bohn and Julienne [? ] provide an expression for  $|S(\epsilon, \omega_1, \omega_2, \dots)|^2$  for a collision on the open channel of two ground state atoms (g) with total energy  $\epsilon$  leading to

loss-producing decay from the excited state  $b_1$  with rate  $\gamma_1$  (Fig. ??),

$$|S|^2 = \frac{(\Delta_2 + \epsilon/\hbar)^2 \gamma_1 \gamma_s}{\left[ (\Delta_1 + \epsilon/\hbar)(\Delta_2 + \epsilon/\hbar) - \frac{\Omega_{12}^2}{4} \right]^2 + \left[ \frac{\gamma_1 + \gamma_s}{2} \right]^2 (\Delta_2 + \epsilon/\hbar)^2}. \quad (5.5)$$

For simplicity, we have omitted the light shift of  $b_1$  due to coupling to the scattering continuum [? ]. This approach was found to be sufficient for describing two-photon spectroscopy to a more deeply bound molecular level in  $^{88}\text{Sr}$  [? ]. Equation (3.33) neglects all light shifts due to the trapping laser. Light shifts due to the photoassociation lasers coupling to states outside our model (Fig. ??) are also neglected. The thermal energy is much greater than the zero-point energy for trap motion,  $T \gg h\nu_{\text{trap}}/k_B$ , so confinement effects are negligible [? ].  $\gamma_1 = 2\gamma_{\text{atomic}}$ , where  $\gamma_{\text{atomic}} = 4.7 \times 10^4 \text{ s}^{-1}$  is the decay rate of the atomic  $^3P_1$  level.  $\gamma_s(\epsilon)$  is the stimulated width of  $b_1$  due to coupling to the initial scattering state by laser 1, which for low energy can be expressed as [17, 63? ]

$$\gamma_s(\epsilon) = 2kl_{\text{opt}}\gamma_1, \quad (5.6)$$

where the optical length ( $l_{\text{opt}} \propto I_1$ ) is related to the overlap between the initial colliding state and  $b_1$ , and  $k = (2\mu\epsilon)^{1/2}/\hbar$ . We take the intermediate state  $b_1$  as the  $\nu = -2$  state, for which  $l_{\text{opt}}/I = (1.5 \pm 0.3) \times 10^4 a_0/(\text{W/cm}^2)$  [? ], where  $a_0 = 5.29 \times 10^{-11} \text{ m}$  is the Bohr radius.

For the experiments reported here, we maintain significant intermediate-state detuning,  $\Delta_1$ , for which  $|\Delta_1| \gg |\Omega_{2,12}|$ . Thus we are in a Raman configuration, and not in the Autler-Townes regime [? ]. In the Raman regime, Eq. 3.33 shows a maximum near two-photon resonance at  $\Delta_2 + \epsilon/\hbar = \Omega_{2,12}^2/4\Delta_1$ . Following a treatment discussed recently for a similar experiment in calcium [63], if the detuning is restricted to near

two-photon resonance then  $|S|^2$  can be approximated as a Lorentzian

$$|S|^2 \approx \frac{A(\epsilon)}{\left(\Delta_2 + \epsilon/\hbar - \frac{\Omega_{12}^2}{4(\Delta_1 + \epsilon/\hbar)}\right)^2 + [\Gamma_L(\epsilon)/2]^2}, \quad (5.7)$$

where

$$A(\epsilon) = \frac{\Omega_{2,12}^4 \gamma_1 \gamma_s(\epsilon)}{16(\Delta_1 + \epsilon/\hbar)^4} \quad (5.8)$$

$$\Gamma_L(\epsilon) = \frac{\Omega_{2,12}^2 [\gamma_1 + \gamma_s(\epsilon)]}{4(\Delta_1 + \epsilon/\hbar)^2}. \quad (5.9)$$

In practice, the variation of collision energy is negligible compared to the one-photon detuning  $\Delta_1$ .

There are several concerns regarding the rigorous application of the Bohn and Julienne theory [? ] to our experiment. The obvious one is that it assumes an isolated intermediate state, which is not always a good approximation because of the proximity of state  $b_1$  to the  ${}^1S_0 + {}^3P_1$  asymptote and to the  $\nu = -1$  state. Because of the small decay rate  $\gamma_1$  of the intermediate molecular state associated with metastable  ${}^3P_1$  atomic state, we also expect that loss from the ground molecular state cannot be neglected.

The more subtle issue is that Eq. (3.34) is derived assuming only a single laser beam is near resonant with each leg of the two-photon transition, which is not a good approximation for two-photon spectroscopy of a halo state and the resulting small laser-frequency difference  $\omega_1 - \omega_2 \approx -E_{b2} \ll |\Delta_1|$ . We can expect that coupling between pairs of states due to both photoassociation lasers will contribute to the transition strength and light shifts of the levels induced by the photassociation lasers [? ? ].

In the absence of a more complete theory treating these effects, we analyze loss

spectra using the effective expression given by Eq. (5.10), where the observed molecular binding energy ( $E'_{b2}$ ) includes any perturbations due to AC Stark or collisional

$$|S|^2 = \frac{\Gamma_L(\epsilon) + \gamma_{\text{eff}}}{\Gamma_L(\epsilon)} \times \frac{\eta A(\epsilon)}{(\omega_1 - \omega_2 + \epsilon/\hbar - E'_{b2}/\hbar)^2 + \left[\frac{\Gamma_L(\epsilon) + \gamma_{\text{eff}}}{2}\right]^2}, \quad (5.10)$$

shifts.

Parameters have been added in Eq. (5.10) to account for deviations of the signal strength ( $\eta$ ) and width ( $\gamma_{\text{eff}}$ ) from the predictions of [? ]. If deviations from Eq. (3.34) are small, we expect  $\eta \sim 1$ ,  $\gamma_{\text{eff}} \sim 0$ , and  $E'_{b2} \sim E_{b2} + \Omega_{2,12}^2/4(\Delta_1 + \epsilon/\hbar)$ .

Light shifts (AC Stark shifts) due to the trapping lasers and collisions with ground-state atoms (density  $n$ ) should contribute to shifts of molecular resonance. Similar effects were taken into account in a recent, high-precision study of weakly bound molecular states of ultracold ytterbium atoms [77]. In addition, we expect that both 689-nm excitation lasers will shift the line, not just  $I_2 \propto \Omega_{2,12}^2$ . We model the relationship between the measured resonance positions and the unperturbed binding energy  $E_{b2}$  as

$$E'_{b2} = E_{b2} + h\chi_{689}I_{689} + h\chi_{1064}I_{1064}(\mathbf{r}) + h\chi_n n(\mathbf{r}). \quad (5.11)$$

The susceptibilities, in Hz per unit intensity or density, will be determined from experimental data or theoretical considerations. The variation with position of the trapping laser intensity ( $I_{1064}$ ) and the density give rise to the spatial dependence of  $|S|^2$  and the need for a spatial average in Eq. (3.32). We take  $I_{689}$  as twice the single-beam intensity  $I_{689} = 2I$ . The 689-nm excitation beam is large enough compared to the atom sample to neglect spatial variation. The functional form for the AC Stark

shift due to the excitation lasers is discussed in Sec. ??.

### 5.3 Determination of energy shifts

Figure 5.2.2 shows a series of spectra for different final trap depths and sample temperatures. The characteristic asymmetric lineshape for excitation of a thermal sample is evident, with width decreasing as sample temperature decreases. The molecular binding energy is close to the sharp edge on the blue side of each spectrum.

We fit atom-loss spectra with Eq. (5.2) for the evolution of atom number with time, using the phenomenological expression Eq. (5.10) for the scattering probability and Eq. (3.32) for the average of the collision event rate constant over the trap volume and collision energy. The sample temperature, perturbed resonance frequency  $E'_{b2}$ ,  $\eta$ , and  $\gamma_{\text{eff}}$  are taken as fit parameters. In the final analysis, temperatures are set to values determined from time-of-flight imaging of the atoms, but when they are allowed to vary, the fit values differ by no more than 10%. Approximately 10 spectra are recorded for each set of experimental parameters, and the spread of resulting fit values are used to determine best values and uncertainties.

#### 5.3.1 AC Stark shift due to excitation lasers

The most significant perturbation to the resonance position is the AC Stark shift due to the excitation laser intensity, as shown in Fig. 5.3.1. For this data, the trap parameters, temperature ( $T = 30 \text{ nK}$ ), and initial peak sample density ( $n_0 = 2 \times 10^{12} \text{ cm}^{-3}$ ) are held constant. We vary the single-beam excitation intensity from  $I = 0.02 - 0.06 \text{ mW/cm}^{-2}$ , and the excitation time is 50 ms. The observed shifts are comparable to the thermal width of the spectrum, allowing a precise determination

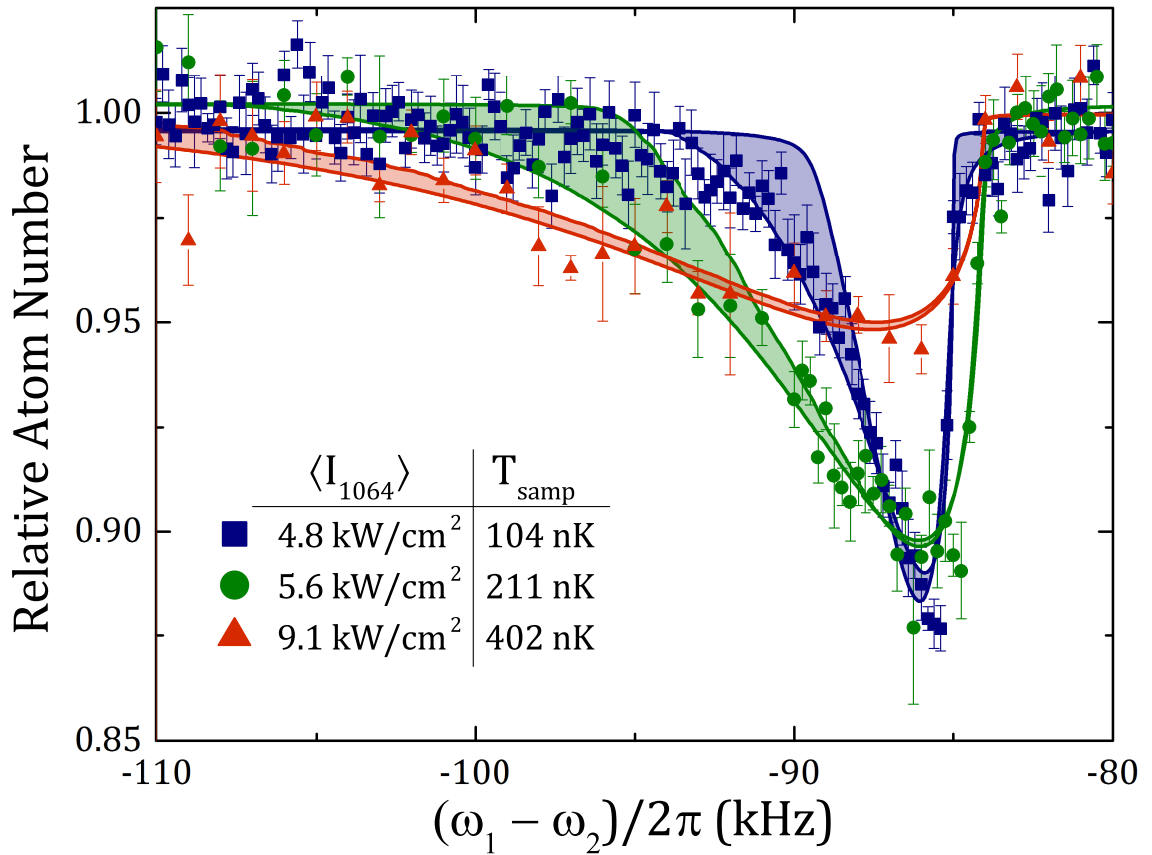


Figure 5.3 : Variation of 1064 nm trap depth

Atom-loss spectra as a function of two-photon difference frequency  $(\omega_1 - \omega_2)/2\pi$  for intermediate detuning  $\Delta_1/2\pi = -9 \text{ MHz}$ . Sample temperature and average trapping laser intensity are indicated in the legend. The single-beam excitation laser intensity is  $I = 25 \text{ mW}/\text{cm}^2$  for the 104 nK spectrum and  $I = 48 \text{ mW}/\text{cm}^2$  for the 211 nK and 402 nK spectra. Fits are described in the text, with the two boundaries of each band given by the fits with collision-energy truncation  $\epsilon_{\max}$  equal to  $2[U_{\text{depth}} - U(\mathbf{r})]$  and  $U_{\text{depth}} - U(\mathbf{r})$ .

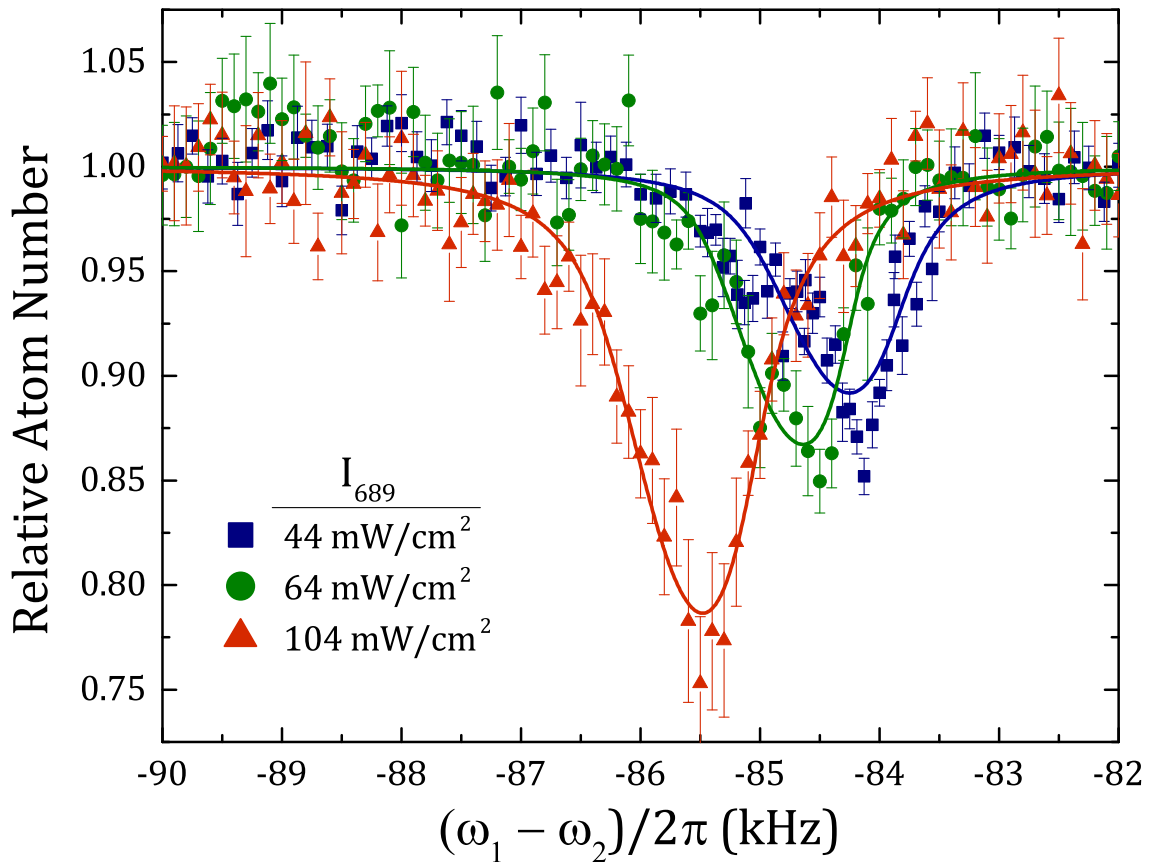


Figure 5.4 : Variation of 689 nm excitation

Atom-loss spectra as a function of two-photon difference frequency  $(\omega_1 - \omega_2)/2\pi$  for intermediate detuning  $\Delta_1/2\pi = -9 \text{ MHz}$  and various 689-nm excitation laser intensities . Twice the single-beam intensity  $I_{689} = 2I$  is indicated in the legend.

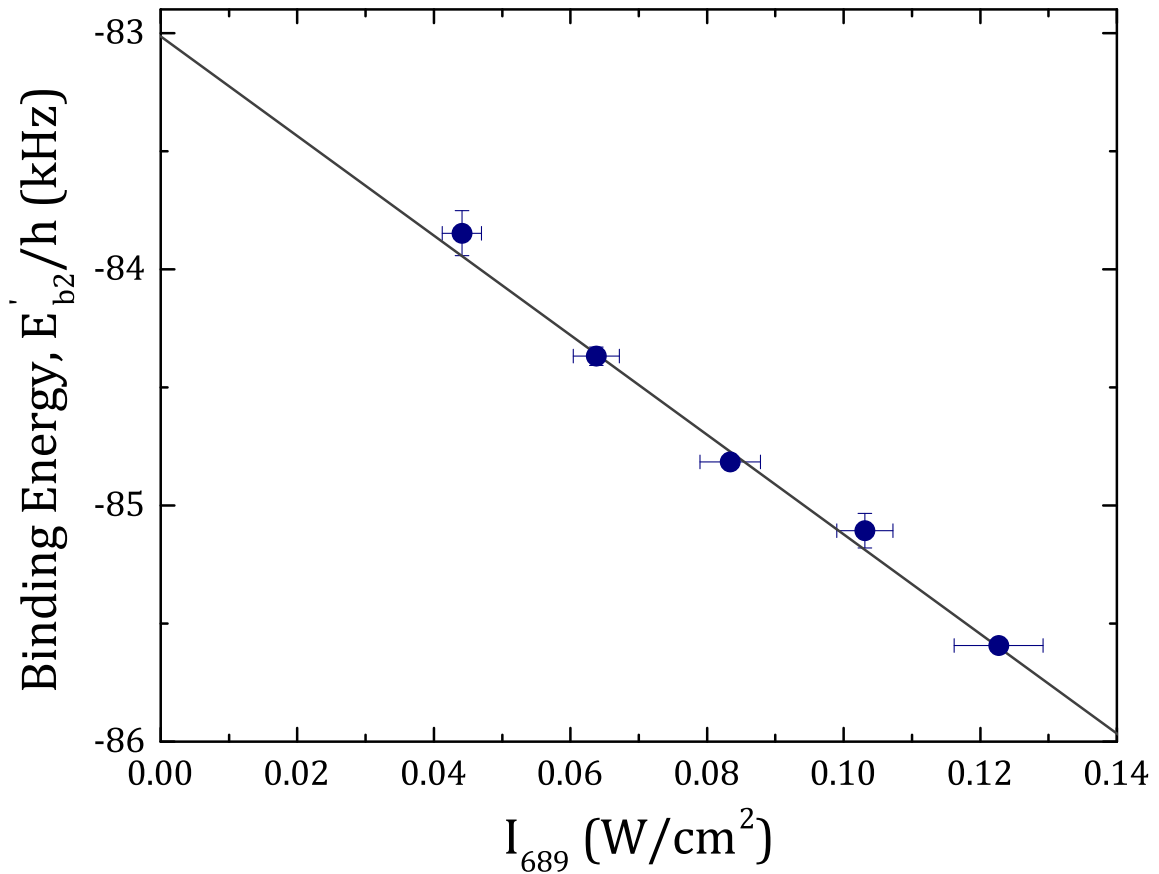


Figure 5.5 : Fit of 689 nm AC Stark shift

Measured resonance position  $E'_b$  plotted versus twice the single-beam intensity  $I_{689} = 2I$ . The linear fit provides the AC Stark shift parameter  $\chi_{689}$ .

of  $\chi_{689} = -21(1)(2) \text{ kHz}/(\text{W/cm}^2)$  from a linear fit to the resonance positions,  $E'_{b2} \propto h\chi_{689}I_{689}$  (Fig. 5.5). The first quoted uncertainty is statistical and it arises from variations in parameters and fluctuations in the measured intensity during the scans. The second value is systematic, reflecting uncertainty in laser-beam size and intensity profile at the atoms. All parameters beside the 689-nm laser intensity are held fixed for this data set, and the AC Stark shift is not correlated with any other variable, such as density or trap intensity. We thus obtain an accurate measure of  $\chi_{689}$  without attempting to account for other systematic shifts of  $E'_{b2}$  in this data. A study of the dependence of  $\chi_{689}$  on detuning from the excited molecular state will be discussed in Sec. ??.

Broadening to the red of the spectrum reflects the distribution of atom-atom collision energies, while broadening to the blue is most sensitive to decay of the intermediate state ( $\Gamma_L$ ) and the phenomenological broadening term  $\gamma_{\text{eff}}$  [Eqs. (5.9) and (5.10)]. The long lifetime of the excited state and the significant detuning  $\Delta_1$  result in a width  $\Gamma_L(\epsilon)$  less than 5 Hz for all conditions. This is extremely small compared to observed width, which yields values of  $\gamma_{\text{eff}}$  on the order of 300 Hz. We hypothesize that this width reflects decay of molecules in the electronic ground-state due to collisions with background atoms.

### 5.3.2 Density-dependent frequency shift

A shift of the two-photon resonance position is possible due to differing mean-field shifts of initial atomic and final molecular states arising from interaction with the background of ground-state atoms. Such a shift would be proportional to the atom density and depend upon the *s*-wave scattering lengths for atom-atom and atom-

dimer collisions,  $a_{86}$  and  $a_{\text{ad}}$  respectively. This was observed in a Rb Bose-Einstein condensate (BEC) in [84]. For a non-degenerate gas, this effect yields  $\chi_n = \hbar(\frac{a_{\text{ad}}}{\mu_{\text{ad}}} - 4\frac{a_{86}}{\mu_{\text{aa}}}) = \frac{\hbar}{m}(\frac{3}{2}a_{\text{ad}} - 8a_{86})$ , where  $\mu_{\text{ad}}$  and  $\mu_{\text{aa}}$  are the reduced masses for molecule-atom and atom-atom collisions respectively. Note that the shift would vanish for  $a_{\text{ad}} = (16/3)a_{86}$ .

The largest density used in our experiment ( $\sim 1 \times 10^{12} \text{ cm}^{-3}$ ) is relatively low compared to typical BEC densities, and at this time we are unable to accurately measure a variation of resonance position with density. However, the atom-atom scattering is close to resonance and thus Efimov physics can provide information on  $a_{\text{ad}}$  [11, 61] and an estimate of the systematic error introduced by any residual density-dependent frequency shifts. For a zero-range interaction, the atom-dimer scattering length is related to the atom-atom scattering length through the three-body Efimov parameter  $\kappa_*$  according to [11]

$$a_{\text{ad}} = a_{86} \{1.46 + 2.15\cot[s_0\ln(14.1\kappa_*a_{86})]\} \quad (5.12)$$

where  $s_0 = 1.006$ <sup>\*</sup>.

In principle, the atom-dimer scattering length can take any value. However, for a deep atom-atom potential, such as for the ground-state strontium dimer [?], there is a universality of the three-body physics that sets  $\kappa_* = 0.226(2)/l_{\text{vdW}}$  [81]. Here,  $l_{\text{vdW}} = (2\mu C_6/\hbar^2)^{1/4}/2 = 74.6 a_0$  is the van der Waals length associated with the  $C_6$  coefficient of the long-range  $\text{Sr}_2$  ground-state potential. We use  $C_6 = 3.03(1) \times 10^{-76} \text{ J m}^6$  found from a fit of potential parameters to spectroscopic data [?], which is consistent

---

\*The Efimov parameter is related to  $E_{3b}^0$  through  $\kappa_* = (m|E_{3b}^0|/\hbar^2)^{1/2}$ , where  $E_{3b}^0$  is the binding energy the lowest Efimov trimer would have in the case of resonant atom-atom interactions.

with a recent *ab initio* calculation [88]. This yields  $\kappa_* = 5.72 \times 10^7 \text{ m}^{-1} = (330 a_0)^{-1}$ . Equation (5.12) then predicts  $a_{\text{ad}} = 6.4 a_{86}$ , which leads to a small density-dependent frequency shift parameter of  $\chi_n = 50 \text{ Hz}/(10^{12} \text{ cm}^{-3})$ . A numerical calculation including a finite-range correction for the atom-atom interaction [55] results in  $a_{\text{ad}} = 3.5 a_{86}$  and  $\chi_n = -90 \text{ Hz}/(10^{12} \text{ cm}^{-3})$ . Thus, a very small shift is expected for the densities used here. We incorporate  $\chi_n = 0 \pm 90 \text{ Hz}/(10^{12} \text{ cm}^{-3})$  as a set parameter in our model of the spectrum, where we set the systematic uncertainty to reflect the spread of theory predictions. This uncertainty will be significant for our determination of the unperturbed halo binding energy.

### 5.3.3 AC Stark Shift due to Trapping Lasers

With an accurate determination of  $\chi_{689}$  and a value for  $\chi_n$ , we use the data shown in Fig. 5.2.2 to determine the susceptibility for the AC Stark shift from the trapping laser,  $\chi_{1064}$ , and the unperturbed halo binding energy  $E_{b2}$ . Figure 5.3.3 shows a plot of  $E'_{b2} - \chi_{689} I_{689} - \chi_n \langle n \rangle$  versus  $\langle I_{1064} \rangle$ , where  $E'_{b2}$  is the resonance position from each fit and  $\langle \dots \rangle$  indicates a weighted average of the quantity over the trapped sample, with a weighting given by the square of atom density. This weighting reflects the contribution to photoassociative loss, a two-body process. The plotted uncertainties in  $E'_{b2} - \chi_{689} I_{689} - \chi_n \langle n \rangle$  are from statistical variation in the fit parameters. The typical average density is  $\langle n \rangle \approx 1 \times 10^{12} \text{ cm}^{-3}$ . The linear fit function is to  $E_{b2} + \chi_{1064} \langle I_{1064} \rangle$ . In addition to statistical uncertainty, we have systematic uncertainty from  $\chi_n$  and treatment of the truncation of the collision-energy integral [Eq. (3.32)]. The dashed lines shown in Fig. 5.3.3 are resulting fits when the values of  $E'_{b2} - \chi_{689} I_{689} - \chi_n \langle n \rangle$  are shifted by the sum of these systematic uncertainties. The resulting value for the

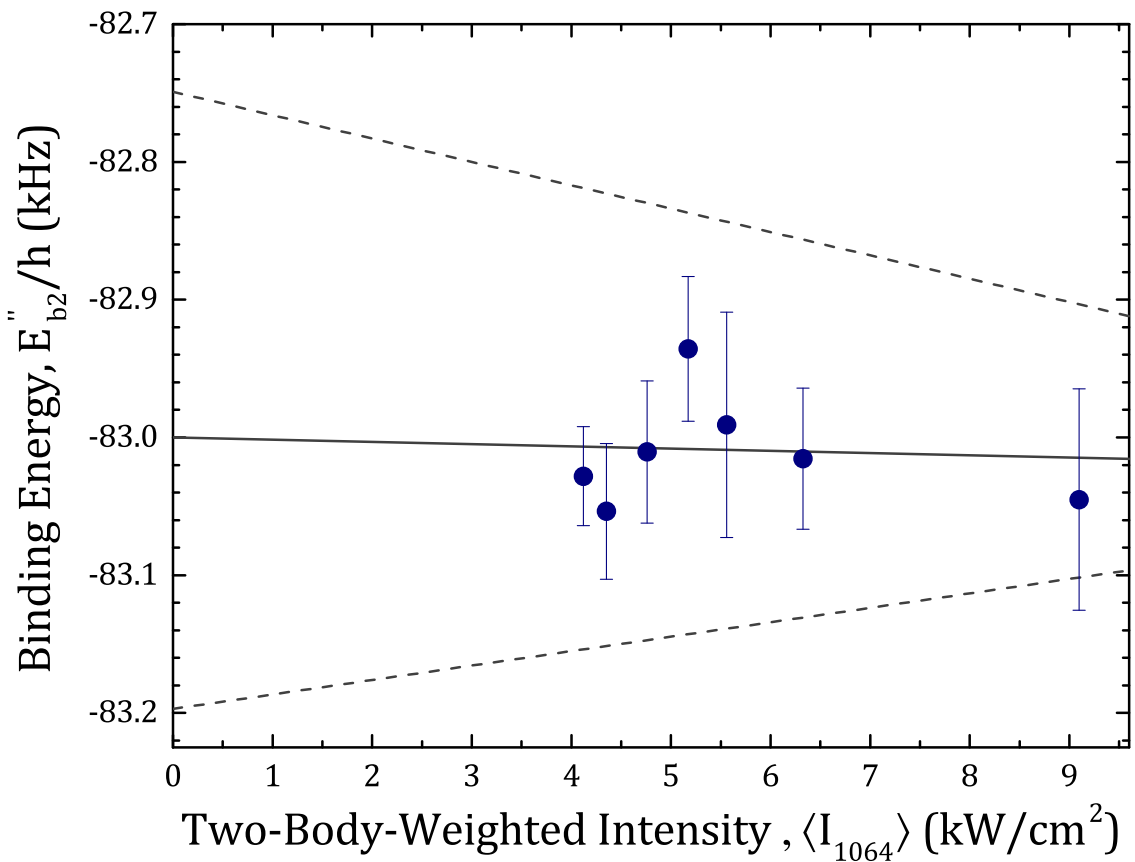


Figure 5.6 : Measurement of halo state susceptibility,  $\chi_{1064}$

Measured resonance positions corrected for excitation-laser AC Stark shift and collisional frequency shift,  $E'_{b2} - \chi_{689} I_{689} - \chi_n \langle n \rangle$ , as a function of average trap laser intensity  $\langle I_{1064} \rangle$  for the data such as in Fig. 5.2.2 . The trend line and confidence intervals are described in the text.

unperturbed binding energy is  $E_{b2}/h = -83.00(7)(20)$  kHz, where the first uncertainty is statistical, and the second is systematic. We observe a susceptibility to  $I_{1064}$  of  $\chi_{1064} = 0 \pm 10$  Hz/(kW/cm<sup>2</sup>).

For two-photon spectroscopy to a weakly bound dimer, it is typical to neglect any potential AC Stark shift due to far-off-resonant trapping lasers because the atoms contribute to the overall polarizability approximately as free atoms. But the high precision of our measurement allows us to detect a small shift. This corresponds to a relative differential polarizability of  $\chi_{1064}/2\chi_{1064,g}g = (\chi_{1064,b2} - 2\chi_{1064,g}g)/2\chi_{1064,g}g \approx xx$ .

## 5.4 Discussion of the halo binding energy

In the limit of extremely small binding energy, and thus resonant atom-atom interactions, the binding energy of a halo molecule is approximately given by [? ]

$$E_b = -\hbar^2/2\mu a^2. \quad (5.13)$$

For interactions described at long-range by the van-der-Waals form,  $V(r) = -C_6/r^6$ , as with ultracold atoms, a convenient figure of merit for quantifying how accurate this simple expression should be is given by the ratio of the *s*-wave scattering length to the mean scattering length or interaction range, closely related to the van der Waals length through [16, 30]

$$\bar{a} = l_{\text{vdW}} \frac{\Gamma(\frac{3}{4})}{\sqrt{2}\Gamma(\frac{5}{4})}. \quad (5.14)$$

Slightly away from resonance, corrections to the binding energy for the van der Waals potential were worked out in [26, 27], yielding

$$E_{b2} = -\frac{\hbar^2}{2\mu(a - \bar{a})^2} \left[ 1 + \frac{g_1 \bar{a}}{a - \bar{a}} + \frac{g_2 \bar{a}^2}{(a - \bar{a})^2} + \dots \right], \quad (5.15)$$

where  $g_1 = \Gamma(1/4)^4/6\pi^2 - 2 = 0.918\dots$  and  $g_2 = (5/4)g_1^2 - 2 = -0.947\dots$ . The range of validity of this expression is  $a \gtrsim 2\bar{a}$ . The accuracy of the first term in this expansion has been experimentally confirmed for various systems such as  $^{85}\text{Rb}$  [21, 44],  $^{40}\text{K}$  [59, 65] and  $^6\text{Li}$  [2]. This derivation of Eq. (5.15) assumes that the influence of short-range physics, which can be expressed through a quantum defect, varies negligibly from threshold to the molecular binding energy. We expect this to be an excellent approximation, since, as shown in Ref. [26] the corrections are typically less than about 1% even for GHz binding energies.

For ground-state  $^{86}\text{Sr}$  atoms,  $\bar{a} = 71.3 a_0$ . The most accurate value available for the s-wave scattering length is  $a = 798(12) a_0$  [? ], satisfying the requirement of  $a \gg \bar{a}$  for the least-bound state on the ground molecular potential to be a halo molecule. Nonetheless,  $\bar{a}/(a - \bar{a}) = .10$ , and the corrections given by Eq. (5.15) are significant. Figure 5.4 shows the importance of the correction terms.

Equation (5.15) and the previous best value of the scattering length [? ] predict a binding energy of  $E_{b2} = -86(3)$  kHz. This agrees with our measurement, but by inverting Eq. (5.15), we can use our increased accuracy in  $E_{b2}$  to extract an improved value of the scattering length of  $a = 810.6(3)(9) a_0$ , where uncertainties reflect statistical and systematic uncertainties in  $E_{b2}$  respectively. The next higher-order term in  $x_0 = \bar{a}/(a - \bar{a})$  is likely to introduce a correction on the order of 100 Hz in Eq. (5.15), creating a systematic uncertainty in  $a$  that is about one third of the uncertainty from our measurement.

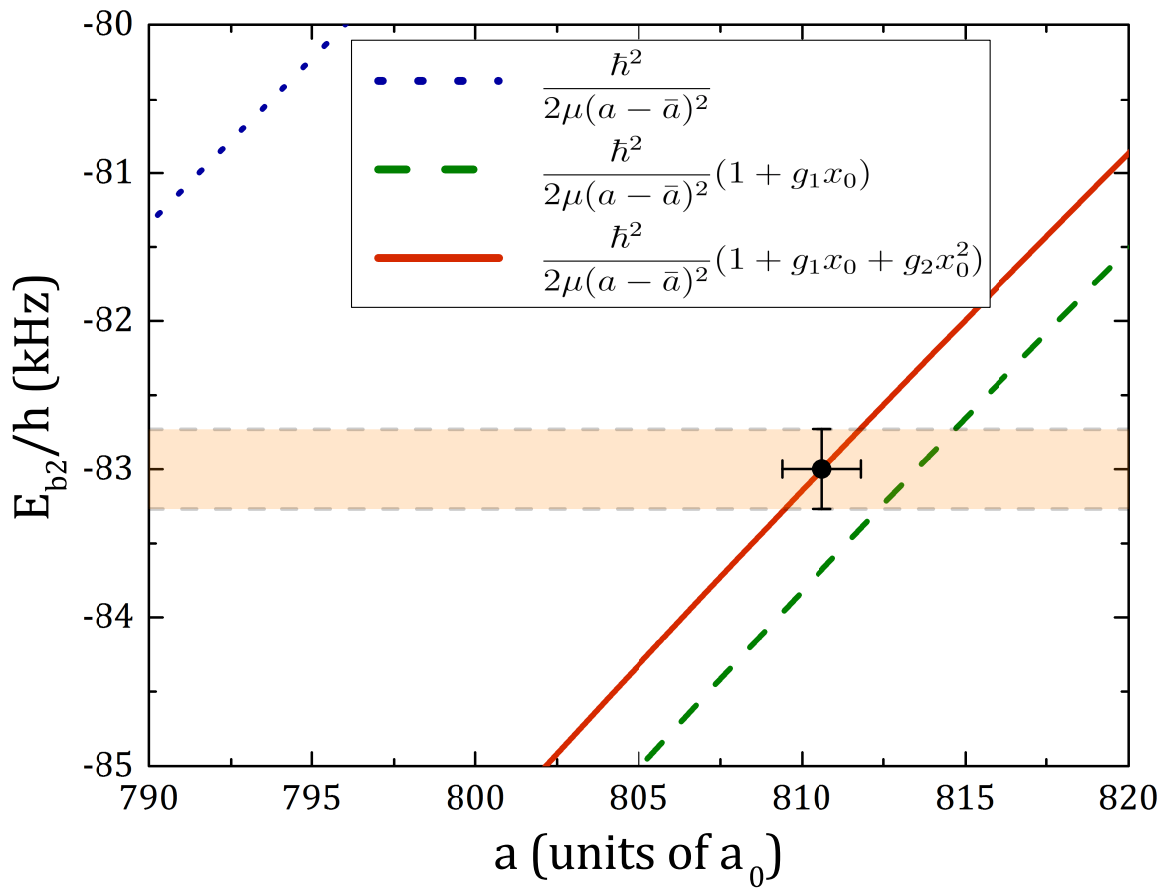


Figure 5.7 : Determination of  $^{86}\text{Sr}$  scattering length

Halo binding energy versus  $s$ -wave atom-atom scattering length for  $^{86}\text{Sr}$ . The shaded region indicates our experimental measurement. The lines are predictions of Eq. 5.15 retaining up to the first, second, and third terms as indicated in the legend [ $x_0 = \bar{a}/(a - \bar{a})$ ]. The data point is the prediction of Eq. (5.15) for the recommended value of the measured binding energy.

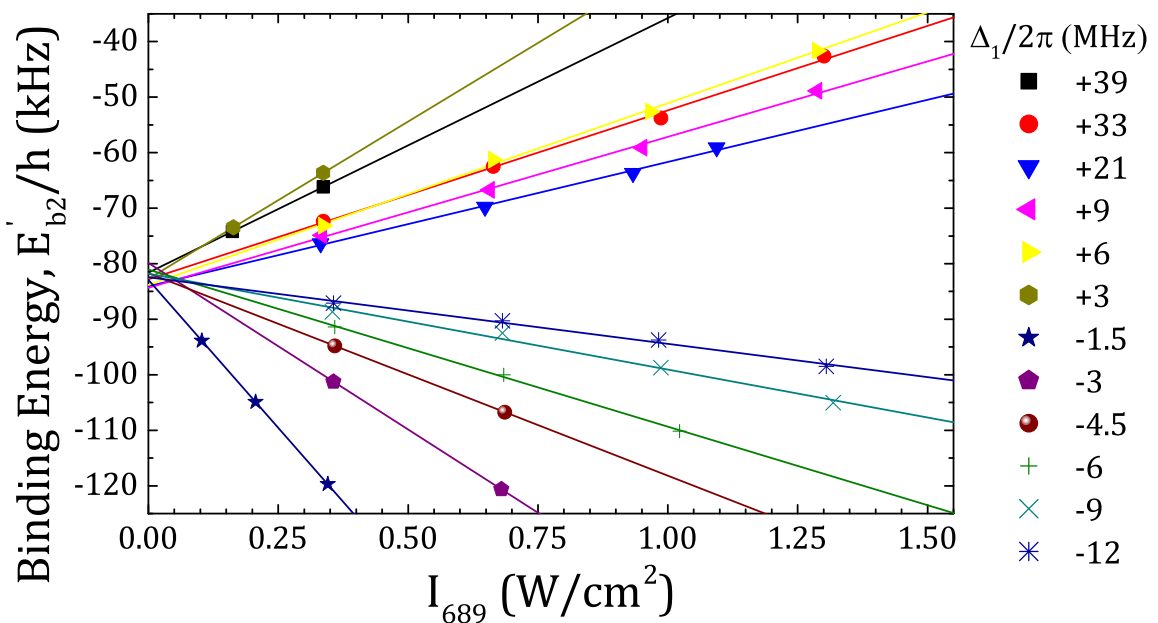


Figure 5.8 : Variation of halo susceptibility as a function of  $\Delta_1$

Two-photon PA resonance positions as a function of twice the single-beam excitation intensity,  $2I = I_{689}$  for various intermediate state detunings,  $\Delta_1$  .

### 5.4.1 Calculating the $X^1\Sigma_g^+$ $C_6$ coefficient

From the formula for the line shape we can see that it depends on the spatial distribution of the atoms. The standard approximation made when measuring these types of systems is to ensure loss does not cause heating of the atoms during photoassociation. Heating results in re-equilibration of the atomic density distribution, which in turn effects the rate of loss creation. Without independent controls to keep the system in thermal (and therefore spatial density) equilibrium.

What are the things the rate equation deals with?

We need the density distribution.

In a harmonic trap, there is a simple analytic form to the density distribution of a thermal gas. From Mi's work (and others) we know that this is only an approximation that is valid when  $\eta$  is approx greater than 4. When greater than 4 we can apply the high- $\eta$  approx and the trap frequencies along a particular direction reduce to  $\omega_{eqi}$ .

However, the trap we did this experiment in were at  $\eta$ 's of 1 or less so we don't have an analytic solution to the spatial distribution. Since this could be a problem we need to know what the trap looks like.

We measure trap oscillation freq. at several different powers and model the trap using the utility outlined somewhere else.

From the numeric model, we can define a spatially dependent  $\eta$  which is determined by the local trap depth which is simply the difference between the local potential energy and the global depth. This is illustrated in fig something.

The spatial information is not only important for the density determination, but

also for the range of available thermal energies. Consider two atoms near the local bottom of the trap. By definition, in equilibrium, a single atom may only have up to the trap depths worth of energy since any additional energy would result in its expulsion from the trap. In this case, in a relative momentum frame, the allowed collision energies range from zero to two times the trap depth. Similarly, as we move towards the edge of the trap the range of accessible collision energies shrinks. This additional weighting factor may be viewed as having a local truncated Boltzmann distribution at every point in space.

Normally the BZ dist goes to infinity but here we have a cutoff at 2 trap depth. The most naive approx would be to simply consider the BZ and harshly truncate at 2 trap depth. We tried this

We know this is unphysical since we should expect that the probability of observing a certain momenta at a certain point in space, should smoothly tend zero towards as we approach the edge of the trap. To see what this looks like we (and determine how important the effect is) we rederive the relative momentum distribution.

*{Some stuff about center of mass and relative}*

What were all the cases and conclusions of having done this? Remember to consider what the different cases are. If the total relative energy can be X then how does that get split up? Use the plots to show this limiting behavior. Like if particle 1 has all the energy then there is only one possible value for particle 2 (and vice versa).

DERIVATION for truncated trap below

Need to lookup references for this molecular chaos assumption. What about ergodicity? How to discuss that we may not be completely ergodic?

What does my potential look like? Can I make it a piecewise function? How

should I introduce this part?

Where does the f equation come from? I believe this is just the normalized boltzmann factor for probability to occupy a particular state.

We can truncate this single particle distribution by

$$f_{\mathbf{r}}(\mathbf{p}) = A \left( \frac{1}{2\pi k_B T} \right)^{3/2} e^{\left( \frac{-p^2}{2mk_B T} \right)} \Theta \left( \epsilon_{max} - U(\mathbf{r}) - \frac{p^2}{2m} \right) \quad (5.16)$$

where A is a normalization constant which ensures  $\int_0^\infty f_{\mathbf{r}}(\mathbf{p}) d\mathbf{p} = 1$  and  $\Theta(x)$  is the Heaviside function defined by

$$\Theta(x) = \begin{cases} 1 & \text{if } x \geq 0, \\ 0 & \text{if } x < 0 \end{cases} \quad (5.17)$$

We got a certain answer with the way shown in the paper.

We can also use a completely different method that ignores all the considerations of the last few sections. As was done in the calcium paper, we could simply fit the blue edge of the feature using a model function which can capture the high level features of the lineshape. Get the same answer. SHOW PLOTS TO THIS AFFECT AND COMPARE

Maybe go a little into the isolated resonance model (or at least recall), then tie into how we can measure the susceptibility across several different detunings which can give us the coupling to intermediate level. The first order analysis of this data suggest a bound-bound rabi frequency of **BLAH**.

Point out the curling up at the end and say how the simple isolated resonance model cannot predict. A full coupled channel calculation probably could but in the spirit of the Bohn and Julienne semi-classical approach, we set out to derive an

approximate analytic expression to determine the binding energies. THis is presented in the next chapter.

Lastly, we note that in the context of photoassociation, the center-of-mass component of Eq.A.3 is not typically considered as typical PAS experiments are performed utilizing broad dipole allowed transitions which have linewidths much greater than the doppler width thus only the relative momentum between particles is important for determining the loss rate coefficient K discussed in (somewhere).

The case of PA using narrow intercombination line transitions found in alkaline-earth-metal atoms

In general K is considered as a boltzmann average over a single loss rate constant This can be seen in [19] Eq. 1 where the loss rate constant is given by

$$\begin{aligned} K(\Delta, T) &= \langle \mathcal{K}(\Delta, \mathbf{P}_c, \mathbf{p}_r) \rangle \\ &= \int d^3\mathbf{P}_c f_M(\mathbf{P}_c) \int d^3\mathbf{p}_r f_\mu(\mathbf{p}_r) \mathcal{K}(\Delta, \mathbf{P}_c, \mathbf{p}_r) \end{aligned} \quad (5.18)$$

To this end we can integrate out the center of mass component to obtain the distribution most typically relevant to photoassociation.

By the time I've gotten to this I have already introduced K and that is not what I wanted to do.

conclusion here is the modified version of K we need for a trap that has a truncated energy disttribution

to get there normal version of K is given in ch3 this K can be given in terms of f? this version of f is given in the appendix why do I integrate out the com component? typical PAS experiments utilize dipole allowed transitions which have linewidths many times larger than the

We now perform a change of variables using Eq. and Eq.A.2 can be rewritten as  
In the s-wave limit I need to write K as a function of  $f(p)$  (should do this in the appendix proof and reference in body). Given the form of the loss rate constant K, our problem reduces to determining the form of  $f(p)$  when  $\eta$  is finite.

Ok, so need to reference [19] to motivate usage of center of mass. Then use [62] Eq. 43 to reference the particular form

what is the throughline I want to make? Develop  $K_{in} \rightarrow$  recast in terms of P distribution  $\rightarrow$  show how we can replace the normal dist with a truncated dist  $\rightarrow$  explore the effects of that truncation

## Chapter 6

### Progress towards studies of quantum magnetism

A straightforward extension of the work presented in this thesis would be to control interparticle spacing via an optical lattice. For these and additional experiments using quantum degenerate fermionic strontium we purchased and installed an optical lattice system. Our lattice is implemented using a Coherent Verdi V-18 which is shaped and propagated to our science chamber in free space. Fig shows the optical path for each arm of our cubic lattice.

Unfortunately, complications due to heating when loading the lattice has limited our success in this optical trap. I want to go over what we have been able to do so far with the lattice.

How did we characterize? Kaptiza-dirac extension

What convinced us we were having problems?

What are some ideas we could do in the lattice? Zeno faster cooling via stimulated raman potentially? (can I model this somehow?) repulsively bound molecules? use interaction control in lattice with the zeno thing

#### 6.1 Spin manipulation of $^{87}\text{Sr}$

Here is where I need to introduce and characterize the LCR

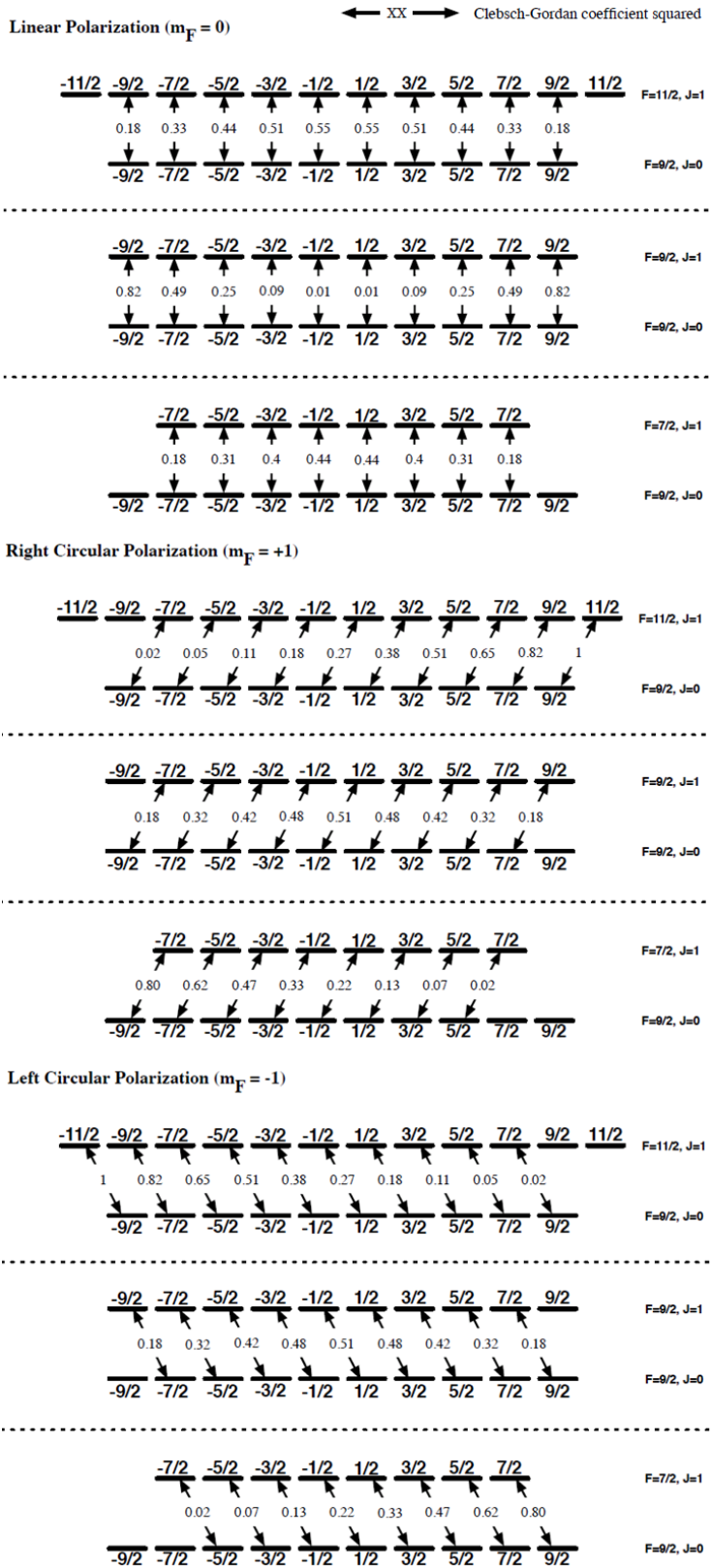
Averaging images together (how to use this code specifically)

don't forget to talk about optimizing the polarization of the fixed waveplate Fig. something shows the variation of the retardance angle for 689 nm light. For reference, Fig. 6.1 reproduces the Clebsch-Gordan coefficient diagrams originally created by Pascal. From this diagram we can easily see how optical pumping works. Let us consider an atom starting in the  $m_F = -9/2$  ground state and being exposed to *sigma+* photons acting on the  $F = 9/2 \rightarrow F = 11/2$  hyperfine transition. Absorbing a photon promotes the atom to the  $F = 11/2, m_F = -7/2$  state. From here we can consult Fig. 6.1 to find the dominate decay path to be to the  $F = 9/2, m_F = -5/2$  state due to the Clebsch-Gordan coefficients.

Now we have a couple of options, by taking advantage of the CG coefficients we see that we will probabilistically promote population towards a polarized state. In the absence of a bias field the magnetic sub-levels are degenerate so this could be an efficient process. In practice we find this to heat the atom population significantly. Therefore, in a bias field, we split out the levels by approx. 200 kHz to and address each sub-level transition individually. This allows us to minimize the number of photon scattering events which we hypothesize to be the cause of the observed heating.

can individually address the separate hyperfine sub-level transitions and sequentially pump population towards one a polarized state

Be sure to define convention for what we determined was plus and minus

Figure 6.1 :  $^{87}\text{Sr}^1S_0 \rightarrow ^3P_1$  hyperfine structure

## 6.2 Search for narrowline PA molecules using various spin mixtures

”Lorem ipsum dolor sit amet, consectetur adipiscing elit, sed do eiusmod tempor incididunt ut labore et dolore magna aliqua. Ut enim ad minim veniam, quis nostrud exercitation ullamco laboris nisi ut aliquip ex ea commodo consequat. Duis aute irure dolor in reprehenderit in voluptate velit esse cillum dolore eu fugiat nulla pariatur. Excepteur sint occaecat cupidatat non proident, sunt in culpa qui officia deserunt mollit anim id est laborum.”

## Chapter 7

### Conclusion

We have measured the binding energy of the least-bound vibrational level of the ground electronic state of the  $^{86}\text{Sr}_2$  molecule with two-photon photoassociative spectroscopy. Using the universal prediction for the binding energy of a halo state including corrections derived for a van der Waals potential [Eq. (5.15)] [26, 27, 30], we extract an improved value of the *s*-wave scattering length.

We also characterized the AC Stark shift of the halo-state binding energy due to light near resonant with the single-photon photoassociation transition. A model only accounting for a single excited-state channel [? ] cannot explain the observed frequency dependence of the AC Stark shift, which can be attributed to the proximity of other excited states.

Large AC Stark shifts of the halo state point to the possibility of optically tuning the  $^{86}\text{Sr}$  scattering length, similar to recent demonstrations of optical tuning of magnetic Feshbach resonances [3, 20]. This is attractive because ground-state strontium lacks magnetic Feshbach resonances. With improved measurement of the photoassociation resonance frequency and its dependence on background atom density, perhaps combined with optical manipulation of the scattering length, it may also be possible to study the landscape of Efimov trimers associated with this naturally occurring scattering resonance. This work also points to the need for improved theory, such as an improved calculation of the Sr ground-state molecular potential and  $C_6$  coefficient,

which could be compared with this high-accuracy measurement of the halo binding energy.

The work presented in this proposal is a natural extension of previous work done in our lab using an optical Feshbach resonance and one color photoassociation to manipulate the quantum state of a Bose-Einstein condensate. The creation and characterization of a novel type of Feshbach molecule is of fundamental interest to complete the analogy between optical and magnetic Feshbach resonances as well as to test the mechanism of Feshbach molecule stability in the presence of closed channel decay. This experiment provides a practical first demonstration of an optical lattice on our apparatus, which can be readily extended to a number of experiments such as out of equilibrium unitarity quenches [50], strongly interacting Bose gases stabilized by the quantum zeno effect [75, 83, 90? ], and the observation of exotic spin phases [5, 14? ]. Moreover, additional insight might also be drawn from revisiting OFR and photoassociation in an optical lattice and employing new measurement techniques in the lattice [76]. These and future experiments will take advantage of the variety of interactions and narrow intercombination transitions available in strontium as well as the control and selectivity afforded through an optical lattice.

## Bibliography

- [1] Anker, T., 2005, *Ultracold quantum gases in one-dimensional optical lattice potentials*, Ph.D. thesis, Ludwig-Maximilians-Universität München, URL [https://edoc.ub.uni-muenchen.de/968/1/Greiner\\_{ }Markus.pdf](https://edoc.ub.uni-muenchen.de/968/1/Greiner_{ }Markus.pdf).
- [2] Bartenstein, M., A. Altmeyer, S. Riedl, R. Geursen, S. Jochim, C. Chin, J. H. Denschlag, R. Grimm, A. Simoni, E. Tiesinga, C. J. Williams, and P. S. Julienne, 2005, Physical Review Letters **94**(10), 103201, ISSN 00319007.
- [3] Bauer, D. M., M. Lettner, C. Vo, G. Rempe, and S. Durr, 2009, Nature Physics **5**, 339.
- [4] Bergman, D. J., and D. Stroud, 1992, *Solid state Physics* (Saunders College), ISBN 047141526X.
- [5] Beverland, M. E., G. Alagic, M. J. Martin, A. P. Koller, A. M. Rey, and A. V. Gorshkov, 2016, Physical Review A **93**(5), 051601, ISSN 24699934, URL <http://link.aps.org/doi/10.1103/PhysRevA.93.051601>.
- [6] Blatt, S., T. L. Nicholson, B. J. Bloom, J. R. Williams, J. W. Thomsen, P. S. Julienne, and J. Ye, 2011, Physical Review Letters **107**(7), 073202, ISSN 00319007, URL <http://link.aps.org/doi/10.1103/PhysRevLett.107.073202>.
- [7] Boffard, J. B., M. L. Keeler, G. A. Piech, L. W. Anderson, and C. C. Lin, 2001,

- Physical Review A **64**(3), 032708, ISSN 1050-2947, URL <https://link.aps.org/doi/10.1103/PhysRevA.64.032708>.
- [8] Bohn, J. L., and P. S. Julienne, 1997, Physical Review A - Atomic, Molecular, and Optical Physics **56**(2), 1486, ISSN 10941622, URL <http://journals.aps.org/prabSTRACT/10.1103/PhysRevA.56.1486>.
- [9] Borkowski, M., R. Ciuryło, P. S. Julienne, S. Tojo, K. Enomoto, and Y. Takahashi, 2009, Physical Review A - Atomic, Molecular, and Optical Physics **80**(1), 1, ISSN 10502947, URL <http://arxiv.org/abs/0905.0958>.
- [10] Braaten, E., and H. W. Hammer, 2006, Physics Reports **428**, 259, ISSN 03701573.
- [11] Braaten, E., and H.-W. Hammer, 2007, Annals of Physics **322**(1), 120, ISSN 00034916, URL <http://linkinghub.elsevier.com/retrieve/pii/S0003491606002387>.
- [12] Bradley, C. C., C. A. Sackett, J. J. Tollett, and R. G. Hulet, 1995, Physical Review Letters **75**(9), 1687, ISSN 00319007, URL <http://link.aps.org/doi/10.1103/PhysRevLett.75.1687>.
- [13] Camargo, F., 2015, *Strontium Laser Cooling and Trapping Apparatus*, Masters, Rice University, URL <http://ultracold.rice.edu/publications/2015CamargoMasters.pdf>.
- [14] Chen, G., K. R. A. Hazzard, A. M. Rey, and M. Hermele, 2015, Physical Review

- A **93**(6), ISSN 24699934, URL <http://arxiv.org/abs/1501.04086>{%}0A<http://dx.doi.org/10.1103/PhysRevA.93.061601>.
- [15] Chin, C., R. Grimm, P. Julienne, and E. Tiesinga, 2010, Reviews of Modern Physics **82**(2), 1225, ISSN 00346861, URL <https://link.aps.org/doi/10.1103/RevModPhys.82.1225>.
- [16] Chin, C., and P. S. Julienne, 2005, Physical Review A - Atomic, Molecular, and Optical Physics **71**(1), 12713, ISSN 10502947.
- [17] Ciurylo, R., E. Tiesinga, and P. S. Julienne, 2006, Physical Review A **74**, 22710.
- [18] Ciurylo, R., E. Tiesinga, P. S. Julienne, R. Ciuryło, E. Tiesinga, P. S. Julienne, R. Ciurylo, E. Tiesinga, and P. S. Julienne, 2005, Physical Review A - Atomic, Molecular, and Optical Physics **71**(3), 030701, ISSN 10502947, URL <http://link.aps.org/doi/10.1103/PhysRevA.71.030701>.
- [19] Ciuryło, R., E. Tiesinga, S. Kotochigova, and P. S. Julienne, 2004, Physical Review A - Atomic, Molecular, and Optical Physics **70**(6), 062710, ISSN 10941622, URL <http://link.aps.org/doi/10.1103/PhysRevA.70.062710>.
- [20] Clark, L. W., L. C. Ha, C. Y. Xu, and C. Chin, 2015, Physical Review Letters **115**, 155301, ISSN 10797114.
- [21] Claussen, N. R., S. J. J. M. F. Kokkelmans, S. T. Thompson, E. A. Donley, E. Hodby, and C. E. Wieman, 2003, Physical Review A **67**(6), 60701, ISSN 1050-2947, URL <https://link.aps.org/doi/10.1103/PhysRevA.67.060701>.

- [22] DeSalvo, B. J., M. Yan, P. G. Mickelson, Y. N. Martinez de Escobar, and T. C. Killian, 2010, Physical Review Letters **105**(3), 030402, ISSN 0031-9007, URL <https://link.aps.org/doi/10.1103/PhysRevLett.105.030402>.
- [23] Fatemi, F. K., K. M. Jones, and P. D. Lett, 2000, Physical Review Letters **85**(21), 4462, ISSN 00319007, URL <http://link.aps.org/doi/10.1103/PhysRevLett.85.4462>.
- [24] Fisher, M. P., P. B. Weichman, G. Grinstein, and D. S. Fisher, 1989, Physical Review B **40**(1), 546, ISSN 01631829, URL <http://link.aps.org/doi/10.1103/PhysRevB.40.546>.
- [25] Gadway, B., D. Pertot, R. Reimann, M. G. Cohen, and D. Schneble, 2009, Optics Express **17**(21), 19173, ISSN 1094-4087, URL <http://arxiv.org/abs/0907.3507> <http://dx.doi.org/10.1364/OE.17.019173>.
- [26] Gao, B., 2001, Physical Review A - Atomic, Molecular, and Optical Physics **64**, 10701, ISSN 10941622.
- [27] Gao, B., 2004, Journal of Physics B: Atomic, Molecular and Optical Physics **37**(21), 4273, ISSN 0953-4075, URL <http://stacks.iop.org/0953-4075/37/i=21/a=004?key=crossref.2818e17c48ea9c152598f4de6d7b11ce>.
- [28] Greiner, M., O. Mandel, T. Rom, A. Altmeyer, A. Widera, T. W. Hänsch, and I. Bloch, 2003, Physica B: Condensed Matter **329-333**(6867), 11, ISSN 09214526, URL <http://www.nature.com/doifinder/10.1038/415039a>.
- [29] Greiner, M., C. A. Regal, and D. S. Jin, 2003, Nature **426**, 537.

- [30] Gribakin, G. F., and V. V. Flambaum, 1993, Physical Review A **48**(1), 546, ISSN 1050-2947, URL <http://link.aps.org/doi/10.1103/PhysRevA.48.546>.
- [31] Grimm, R., M. Weidemüller, and Y. B. Ovchinnikov, 1999, Optical dipole traps for neutral atoms, **9902072**, URL <https://arxiv.org/abs/physics/9902072>.
- [32] Hazzard, K. R. A., J. A. Aman, R. Ding, T. C. Killian, W. Y. Kon, and J. C. Hill, 2018, Physical Review A **98**(5), 053441, ISSN 2469-9926, URL <https://link.aps.org/doi/10.1103/PhysRevA.98.053441>.
- [33] Hecker Denschlag, J., J. E. Simsarian, H. Häffner, C. McKenzie, A. Browaeys, D. Cho, K. Helmerson, S. L. Rolston, and W. D. Phillips, 2002, Journal of Physics B: Atomic, Molecular and Optical Physics **35**(14), 3095, ISSN 09534075, URL <http://stacks.iop.org/0953-4075/35/i=14/a=307?key=crossref.143851fbd4f795110e47d745ef41278c>.
- [34] Hill, J. C., 2017, *Design and Construction of an Apparatus for Optically Pumping  $^{87}\text{Sr}$* , Masters, Rice University, URL [http://ultracold.rice.edu/publications/Hill{\\_}MS.pdf](http://ultracold.rice.edu/publications/Hill{_}MS.pdf).
- [35] Huang, B., R. Grimm, S. Stellmer, F. Schreck, and M. K. Tey, 2009, Physical Review Letters **103**(20), 200401, ISSN 0031-9007, URL <http://link.aps.org/doi/10.1103/PhysRevLett.103.200401>.
- [36] Huang, Y., 2013, *A New Optical Trap System for Ultracold Strontium*, Masters, Rice University, URL [http://ultracold.rice.edu/publications/Ying{\\_}Huang{\\_}master.pdf](http://ultracold.rice.edu/publications/Ying{_}Huang{_}master.pdf).

- [37] Ido, T., Y. Isoya, and H. Katori, 2000, Physical Review A - Atomic, Molecular, and Optical Physics **61**(6), 4, ISSN 10941622, URL <http://link.aps.org/doi/10.1103/PhysRevA.61.061403>.
- [38] Jaksch, D., and P. Zoller, 2005, Annals of Physics **315**(1), 52, ISSN 00034916, URL <http://linkinghub.elsevier.com/retrieve/pii/S0003491604001782>.
- [39] Jensen, A. S., K. Riisager, D. V. Fedorov, and E. Garrido, 2004, Reviews of Modern Physics **76**(1), 215, ISSN 00346861, URL <https://journals.aps.org/rmp/pdf/10.1103/RevModPhys.76.215>.
- [40] Jochim, S., M. Bartenstein, A. Altmeyer, G. Hendl, S. Riedl, C. Chin, J. Hecker-Denschlag, and R. Grimm, 2003, Science **302**, 2101.
- [41] Jones, K. M., E. Tiesinga, P. D. Lett, and P. S. Julienne, 2006, Reviews of Modern Physics **78**(2), 483, ISSN 00346861, URL <http://link.aps.org/doi/10.1103/RevModPhys.78.483><http://journals.aps.org/rmp/abstract/10.1103/RevModPhys.78.483>.
- [42] Katori, H., T. Ido, Y. Isoya, and M. Kuwata-Gonokami, 1999, Physical Review Letters **82**(6), 1116, ISSN 10797114, URL <http://link.aps.org/doi/10.1103/PhysRevLett.82.1116>.
- [43] Ketterle, W., D. S. Durfee, and D. M. Stamper-Kurn, 1999, Proc. Int. School of Physics-Enrico Fermi , 679904034, URL <https://arxiv.org/abs/cond-mat/9904034>.
- [44] Köhler, T., T. Gasenzer, and K. Burnett, 2003, Physical Review A **67**(1),

- 13601, ISSN 1050-2947, URL <http://link.aps.org/doi/10.1103/PhysRevA.67.013601>.
- [45] Köhler, T., K. Góral, and P. S. Julienne, 2006, *Reviews of Modern Physics* **78**(4), 1311, ISSN 00346861, URL <http://link.aps.org/doi/10.1103/RevModPhys.78.1311><http://link.aps.org/abstract/RMP/v78/p1311>.
- [46] Lang, F., K. Winkler, C. Strauss, R. Grimm, and J. H. Denschlag, 2008, *Physical Review Letters* **101**(13), 133005, ISSN 00319007, URL <http://link.aps.org/doi/10.1103/PhysRevLett.101.133005>.
- [47] Lin, Y. J., K. Jiménez-García, and I. B. Spielman, 2011, *Nature* **471**(7336), 83, ISSN 00280836, URL <http://www.nature.com/doifinder/10.1038/nature09887>.
- [48] Loftus, T. H., T. Ido, M. M. Boyd, A. D. Ludlow, and J. Ye, 2004, *Physical Review A - Atomic, Molecular, and Optical Physics* **70**(6), 063413, ISSN 10502947, URL <http://link.aps.org/doi/10.1103/PhysRevA.70.063413>.
- [49] Luo, F., G. C. Mcbane, G. Kim, C. F. Giese, and W. R. Gentry, 1993, *The Journal of Chemical Physics The Journal of Chemical Physics The Journal of Chemical Physics* **98**1(10), URL <http://dx.doi.org/10.1063/1.464079><http://aip.scitation.org/toc/jcp/98/4>.
- [50] Makotyn, P., C. E. Klauss, D. L. Goldberger, E. A. Cornell, and D. S. Jin, 2014, *Nature Physics* **10**(2), 116, ISSN 17452473, URL <http://www.nature.com/doifinder/10.1038/nphys2850>.

- [51] Martinez de Escobar, Y., P. Mickelson, M. Yan, B. DeSalvo, S. Nagel, and T. C. Killian, 2009, Physical Review Letters **103**, 200402, ISSN 0031-9007, URL <http://link.aps.org/doi/10.1103/PhysRevLett.103.200402>.
- [52] Martinez de Escobar, Y. N., 2010, *Bose-Einstein Condensation of 84Sr*, Ph.D. thesis, Rice University, URL <https://hdl.handle.net/1911/62163>.
- [53] Mazurenko, A., 2010, *Molecular Beam Nozzle Optimization*, Undergraduate, MIT, URL <http://ultracold.rice.edu/publications/2010mazurenkoOven.pdf>.
- [54] Méndez-Visag, C., 2014, Revista Peruana de Medicina Experimental y Salud Pública **31**(4), 725, ISSN 17264642, URL <http://www.ncbi.nlm.nih.gov/pubmed/10481000>.
- [55] Mestrom, P. M. A., J. Wang, C. H. Greene, and J. P. D’Incao, 2017, Physical Review A **95**, 32707, ISSN 24699934.
- [56] Michael Viray, 2014, *Zeeman Tunable Saturated Absorption Spectroscopy Cell for Locking Laser Frequency to the Strontium 1S0-1P1 Transition*, Undergraduate, Rice University, URL <http://ultracold.rice.edu/publications/MichaelVirayREUReport>.
- [57] Mickelson, P. G., 2010, *Trapping and Evaporation of Mixtures Sr*, Ph.D. thesis, Rice University, URL <https://hdl.handle.net/1911/62095>.
- [58] Mickelson, P. G., Y. N. Martinez de Escobar, M. Yan, B. J. DeSalvo, and T. C.

- Killian, 2010, Physical Review A **81**(5), 051601, ISSN 1050-2947, URL <https://link.aps.org/doi/10.1103/PhysRevA.81.051601>.
- [59] Moritz, H., T. Stoferle, K. Gunter, M. Kohl, and T. Esslinger, 2005, Physical Review Letters **94**, 210401.
- [60] Mukaiyama, T., H. Katori, T. Ido, Y. Li, and M. Kuwata-Gonokami, 2003, Physical Review Letters **90**(11), 113002, ISSN 0031-9007, URL <https://link.aps.org/doi/10.1103/PhysRevLett.90.113002>.
- [61] Naidon, P., and S. Endo, 2017, Reports on Progress in Physics **80**, 56001, ISSN 00344885.
- [62] Nicholson, T. L., S. Blatt, B. J. Bloom, J. R. Williams, J. W. Thomsen, J. Ye, and P. S. Julienne, 2015, Physical Review A - Atomic, Molecular, and Optical Physics **92**(2), 022709, ISSN 10941622, URL <http://journals.aps.org/prabstract/10.1103/PhysRevA.92.022709>.
- [63] Pachomow, E., V. P. Dahlke, E. Tiemann, F. Riehle, and U. Sterr, 2017, Physical Review A **95**(4), 043422, ISSN 24699934, URL <http://arxiv.org/abs/1702.00710> <https://link.aps.org/doi/10.1103/PhysRevA.95.043422>.
- [64] Ratcliff, L. B., J. L. Fish, and D. D. Konowalow, 1987, J. Mol. Spectrosc. **122**, 293.
- [65] Regal, C. A., C. Ticknor, J. L. Bohn, and D. S. Jin, 2003, Nature **424**, 47.
- [66] Rey, A. M., 2004, *Ultracold Bosonic Atoms in Optical Lattices*, Ph.D. thesis, University of Maryland, URL <http://hdl.handle.net/1903/1802>.

- [67] Saenz, A., 2005, *461nm Laser For Studies In Ultracold Neutral Strontium*, Masters, Rice University, URL <http://ultracold.rice.edu/publications/adsmastersthesis.pdf>.
- [68] Sakurai, J. J., 1994, *Modern Quantum Mechanics, Supplement I* (Pearson), ISBN 978, URL [http://www.amazon.com/gp/product/0805382917/ref=pd\\_lpo\\_sbs\\_dp\\_ss\\_1?pf\\_rd\\_p=1535523722&pf\\_rd\\_s=lpo-top-stripe-1&pf\\_rd\\_t=201&pf\\_rd\\_i=0201539292&pf\\_rd\\_m=ATVPDKIKX0DER&pf\\_rd\\_r=0F9ZVFXMSJ1718HT9VN2](http://www.amazon.com/gp/product/0805382917/ref=pd_lpo_sbs_dp_ss_1?pf_rd_p=1535523722&pf_rd_s=lpo-top-stripe-1&pf_rd_t=201&pf_rd_i=0201539292&pf_rd_m=ATVPDKIKX0DER&pf_rd_r=0F9ZVFXMSJ1718HT9VN2).
- [69] Schöllkopf, W., and J. P. Toennies, 1994, American Association fot the Advancement of Science **266**(5189), 1345, URL <http://science.sciencemag.org/content/sci/266/5189/1345.full.pdf>.
- [70] Segal, S. R., Q. Diot, E. A. Cornell, A. A. Zozulya, and D. Z. Anderson, 2009, 0905.1979, URL <http://arxiv.org/abs/0905.1979><http://dx.doi.org/10.1103/PhysRevA.81.053601>.
- [71] Stellmer, S., 2013, *Thesis: Degenerate quantum gases of strontium*, Ph.D. thesis, University of Innsbruck, URL <http://www.ultracold.at/theses/2013-stellmer.pdf>.
- [72] Stellmer, S., F. Schreck, and T. C. Killian, 2013, *Degenerate quantum gases of strontium*, Ph.D. thesis, University of Innsbruck, Singapore, 1307.0601, URL <http://arxiv.org/abs/1307.0601>[http://dx.doi.org/10.1142/9789814590174\\_0001](http://dx.doi.org/10.1142/9789814590174_0001)[https://doi.org/10.1142/9789814590174\\_0001](https://doi.org/10.1142/9789814590174_0001)

9789814590174{ }0001http://www.ultracold.at/theses/2013-stellmer.pdf.

- [73] Stellmer, S., M. Tey, R. Grimm, and F. Schreck, 2010, Physical Review A **82**, 41602, ISSN 1050-2947, URL <http://link.aps.org/doi/10.1103/PhysRevA.82.041602>.
- [74] Stenholm, S., 1988, *Laser cooling and trapping*, volume 9 of *Graduate Texts in Contemporary Physics* (Springer New York, New York, NY), ISBN 978-0-387-98728-6, NIHMS150003, URL <http://link.springer.com/10.1007/978-1-4612-1470-0>.
- [75] Syassen, N., D. M. Bauer, M. Lettner, T. Volz, D. Dietze, J. J. García-Ripoll, J. I. Cirac, G. Rempe, and S. Dürr, 2008, Science **320**(5881), 1329, ISSN 00368075, URL <http://www.ncbi.nlm.nih.gov/pubmed/18535241>.
- [76] Taie, S., S. Watanabe, T. Ichinose, and Y. Takahashi, 2016, Physical Review Letters **116**(4), 043202, ISSN 10797114, URL <http://link.aps.org/doi/10.1103/PhysRevLett.116.043202>.
- [77] Takahashi, Y., Y. Kikuchi, A. A. Buchachenko, K. Takahashi, P. S. Julienne, H. Yamada, M. Borkowski, Y. Takasu, and R. Ciuryło, 2017, Physical Review A **96**(6), 63405, ISSN 2469-9926, URL <https://link.aps.org/doi/10.1103/PhysRevA.96.063405>.
- [78] Tey, M. K., S. Stellmer, R. Grimm, and F. Schreck, 2010, Physical Review A - Atomic, Molecular, and Optical Physics **82**(1), 011608, ISSN 10502947,

- URL <http://journals.aps.org/prabSTRACT/10.1103/PhysRevA.82.011608>  
<http://link.aps.org/doi/10.1103/PhysRevA.82.011608>.
- [79] Thalhammer, G., M. Theis, K. Winkler, R. Grimm, and J. H. Denschlag, 2005, Physical Review A - Atomic, Molecular, and Optical Physics **71**(3), 033403, ISSN 10502947, URL <http://link.aps.org/doi/10.1103/PhysRevA.71.033403>.
- [80] Theis, M., G. Thalhammer, K. Winkler, M. Hellwig, G. Ruff, R. Grimm, and J. H. Denschlag, 2004, Physical Review Letters **93**(12), 123001, ISSN 0031-9007, URL <http://link.aps.org/doi/10.1103/PhysRevLett.93.123001>.
- [81] Wang, J., J. P. D’Incao, B. D. Esry, and C. H. Greene, 2012, Phys. Rev. Lett. **108**, 263001.
- [82] Wikner, A., 2017, *A MATLAB Script for Calibrating an Optical Lattice using Kapitza-Dirac Diffraction*, Ph.D. thesis, Rice University, URL <http://ultracold.rice.edu/publications/2017aWiknerKaptizaDirac.pdf>.
- [83] Wong, L. S., B. W. N. Voon, S. C. Teo, and A. Balakrishnan, 2016, Ecol-  
ogy, Environment and Conservation **22**(3), 1107, ISSN 0971765X, URL <http://link.aps.org/doi/10.1103/PhysRevLett.102.040402>.
- [84] Wynar, R., R. S. Freeland, D. J. Han, C. Ryu, and D. J. Heinzen, 2000, Science **287**, 1016.
- [85] Yamazaki, R., S. Taie, S. Sugawa, and Y. Takahashi, 2010, Physical Review Letters **105**(5), 050405, ISSN 00319007, URL <https://link.aps.org/doi/10.1103/PhysRevLett.105.050405>.

- [86] Yan, M., 2013, *Thesis: Optical Feshbach Resonances and Coherent Photoassociation in a BEC*, Ph.D. thesis, Rice University, URL <https://hdl.handle.net/1911/77594>.
- [87] Yan, M., B. J. Desalvo, B. Ramachandhran, H. Pu, and T. C. Killian, 2013, Physical Review Letters **110**(12), 123201, ISSN 00319007, URL <http://link.aps.org/doi/10.1103/PhysRevLett.110.123201> <https://arxiv.org/abs/0906.1837>.
- [88] Zhang, X., M. Bishof, S. L. Bromley, C. V. Kraus, M. S. Safronova, P. Zoller, A. M. Rey, and J. Ye, 2014, Science **345**(6203), 1467, ISSN 10959203, URL <http://www.sciencemag.org/cgi/doi/10.1126/science.1254978> <https://arxiv.org/abs/1403.2964>.
- [89] Zhang, X. L., R. S. Fletcher, S. L. Rolston, P. N. Guzdar, and M. Swisdak, 2008, Physical Review Letters **100**(23), 235002.
- [90] Zhu, B., B. Gadway, M. Foss-Feig, J. Schachenmayer, M. L. Wall, K. R. Hazzard, B. Yan, S. A. Moses, J. P. Covey, D. S. Jin, J. Ye, M. Holland, *et al.*, 2014, Physical Review Letters **112**(7), 070404, ISSN 00319007, URL <http://link.aps.org/doi/10.1103/PhysRevLett.112.070404>.

# Appendices

## Appendix A

### Two-particle momentum probability distribution

#### A.1 Standard form

Typical derivation of relative momentum probability distribution function

We begin by considering the single particle momentum probability distribution function (gotten how)? Single particle momentum probability distribution

$$f^1(\mathbf{p}) = \left( \frac{1}{2\pi k_B T} \right)^{3/2} e^{\left( \frac{-p^2}{2mk_B T} \right)} \quad (\text{A.1})$$

Extension of this simple Boltzmann equation into the two-particle regime is complicated due to dependence of each particle on the others. If however, we make the assumption that particle collisions are rapid (on some timescale) we can approximate the two particle momentum distribution as the product of two single particle functions. This is known as the molecular chaos assumption and is important for what???

The two particle distribution for a homogeneous system is then

$$\begin{aligned} f^2(\mathbf{p}_1, \mathbf{p}_2) &= f^1(\mathbf{p}_1)f^1(\mathbf{p}_2) \\ &= \left( \frac{1}{2\pi m k_B T} \right)^3 \exp \left( \frac{-(p_1^2 + p_2^2)}{2mk_B T} \right) \end{aligned} \quad (\text{A.2})$$

Next, we'd like to consider a center-of-mass frame for the distribution. So we'll define

we define the relative and center-of-mass momenta of the two particles by defining

$$\mathbf{P}_c = \mathbf{p}_1 + \mathbf{p}_2 \quad M = m_1 + m_2 = 2m$$

$$\mathbf{p}_r = \frac{\mathbf{p}_1 - \mathbf{p}_2}{2} \quad \mu = \frac{m_1 m_2}{m_1 + m_2} = \frac{m}{2}$$

from these equations we can use conservation of energy to determine the quadrature sum of the two momenta

$$\begin{aligned} \frac{p_1^2}{2m} + \frac{p_2^2}{2m} &= \frac{P_c^2}{2M} + \frac{p_r^2}{2\mu} \\ p_1^2 + p_2^2 &= \frac{P_c^2}{2} + 2p_r^2 \end{aligned}$$

thus the momentum probability distribution take the form

$$f^2(\mathbf{P}_c, \mathbf{p}_r) = \left( \frac{1}{2\pi M k_B T} \right)^{3/2} \left( \frac{1}{2\pi \mu k_B T} \right)^{3/2} \exp \left( \frac{-P_c^2}{2M k_B T} \right) \exp \left( \frac{-p_r^2}{2\mu k_B T} \right) \quad (\text{A.3})$$

## A.2 Truncated form

Here I will derive, motivate, and test limiting cases. Plots showing the effects of truncation will be in the main text

Two particle distribution (for correcting notation, use C and R when denoting CoM and Rel)

$$\begin{aligned} f_{\mathbf{r},trunc}^2(\mathbf{p}_1, \mathbf{p}_2) &= A^2 \left( \frac{1}{2\pi m k_B T} \right)^3 \exp \left( \frac{-(p_1^2 + p_2^2)}{2m k_B T} \right) \\ &\times \Theta \left( \epsilon_{max} - U(\mathbf{r}) - \frac{p_1^2}{2m} \right) \Theta \left( \epsilon_{max} - U(\mathbf{r}) - \frac{p_2^2}{2m} \right) \end{aligned} \quad (\text{A.4})$$

We have introduced a normalization constant  $A$  here to ensure the that integration over the truncated probability distribution remains equal to one.

The meaning of  $f_r$  is such that  $f$  should be evaluated at each point in space. Furthermore since the atoms are held in a trapping potential, each point in space has a local trap depth relative to the lip at the top of the trap [need some figure to try and denote this]

Want distribution of relative momenta so integrate out center of mass. Going to drop the two and trunc for now

$$\begin{aligned}\tilde{f}_r(\mathbf{p}_{rel}) &= \int d^3\mathbf{P}_c f_r(\mathbf{p}_1, \mathbf{p}_2) \\ &= \left(\frac{1}{2\pi Mk_B T}\right)^{3/2} \left(\frac{1}{2\pi\mu k_B T}\right)^{3/2} A^2 \int d^3\mathbf{P}_c e^{\left(\frac{-P_c^2}{2Mk_B T}\right)} e^{\left(\frac{-p_r^2}{2\mu k_B T}\right)} \\ &\times \Theta\left(\epsilon_{max} - U(\mathbf{r}) - \frac{P_c^2}{8m} - \frac{p^2}{2m} - \frac{\mathbf{P}_c \cdot \mathbf{p}}{2m}\right) \Theta\left(\epsilon_{max} - U(\mathbf{r}) - \frac{P_c^2}{8m} - \frac{p^2}{2m} + \frac{\mathbf{P}_c \cdot \mathbf{p}}{2m}\right)\end{aligned}\quad (\text{A.5})$$

Spherically symmetrix collisions so can integrate by transforming into spherical coordinates with the radius aligned along the interatomic axis

$$\begin{aligned}\tilde{f}_r(\mathbf{p}) &= \left(\frac{1}{2\pi Mk_B T}\right)^{3/2} \left(\frac{1}{2\pi\mu k_B T}\right)^{3/2} e^{\left(\frac{-p_r^2}{2\mu k_B T}\right)} A^2 \int_0^\pi \sin\theta d\theta \int_0^{2\pi} d\phi \int_0^\infty dP_c P_c^2 e^{\left(\frac{-P_c^2}{2Mk_B T}\right)} \\ &\times \Theta\left(\epsilon_{max} - U(\mathbf{r}) - \frac{P_c^2}{8m} - \frac{p^2}{2m} - \frac{P_c p \cos\theta}{2m}\right) \Theta\left(\epsilon_{max} - U(\mathbf{r}) - \frac{P_c^2}{8m} - \frac{p^2}{2m} + \frac{P_c p \cos\theta}{2m}\right)\end{aligned}\quad (\text{A.6})$$

$$X = \cos\theta$$

$$dX = -\sin\theta d\theta$$

Substitute and integrate over  $\phi$

$$\begin{aligned} \tilde{f}_r(\mathbf{p}) &= \left( \frac{1}{2\pi M k_B T} \right)^{3/2} \left( \frac{1}{2\pi \mu k_B T} \right)^{3/2} e^{\left( \frac{-p_r^2}{2\mu k_B T} \right)} 2\pi A^2 \int_{-1}^1 dX \int_0^\infty dP_c P_c^2 e^{\left( \frac{-P_c^2}{2M k_B T} \right)} \\ &\times \Theta \left( \epsilon_{max} - U(\mathbf{r}) - \frac{P_c^2}{8m} - \frac{p^2}{2m} - \frac{P_c p X}{2m} \right) \Theta \left( \epsilon_{max} - U(\mathbf{r}) - \frac{P_c^2}{8m} - \frac{p^2}{2m} + \frac{P_c p X}{2m} \right) \end{aligned} \quad (\text{A.7})$$

Recognize that the Heaviside functions cancel each other out on either side of zero, so can eliminate one of the Heavisides and multiply by 2

$$\begin{aligned} \tilde{f}_r(\mathbf{p}) &= \left( \frac{1}{2\pi M k_B T} \right)^{3/2} \left( \frac{1}{2\pi \mu k_B T} \right)^{3/2} e^{\left( \frac{-p_r^2}{2\mu k_B T} \right)} 4\pi A^2 \int_0^1 dX \int_0^\infty dP_c P_c^2 e^{\left( \frac{-P_c^2}{2M k_B T} \right)} \\ &\times \Theta \left( \epsilon_{max} - U(\mathbf{r}) - \frac{P_c^2}{8m} - \frac{p^2}{2m} - \frac{P_c p X}{2m} \right) \end{aligned} \quad (\text{A.8})$$

From here we can rewrite using the infinite relative momentum probability distribution  $f_{r,\infty}(\mathbf{p})$  from some equation

$$\begin{aligned} \tilde{f}_r(\mathbf{p}) &= \left( \frac{1}{2\pi \mu k_B T} \right)^{3/2} e^{\left( \frac{-p_r^2}{2\mu k_B T} \right)} \mathcal{G}(T, \epsilon_{max}, p_{rel}) \\ &= f_{r,\infty}(\mathbf{p}) \mathcal{G}(T, \epsilon_{max}, p_{rel}) \end{aligned} \quad (\text{A.9})$$

where  $\mathcal{G}(T, \epsilon_{max}, p_{rel})$  is given by

$$\begin{aligned} \mathcal{G}(T, \epsilon_{max}, p_{rel}) &= A^2 \left( \frac{4\pi}{2\pi M k_B T} \right)^{3/2} \int_0^1 dX \int_0^\infty dP_c P_c^2 e^{\left( \frac{-P_c^2}{2M k_B T} \right)} \\ &\times \Theta \left( \epsilon_{max} - U(\mathbf{r}) - \frac{P_c^2}{8m} - \frac{p^2}{2m} - \frac{P_c p X}{2m} \right) \end{aligned} \quad (\text{A.10})$$

Now define two dimensionless variables  $\tilde{\epsilon}$  and  $\tilde{E}$  which will be used to change variables once more

$$\begin{aligned}
\tilde{\epsilon} &= \frac{p_{rel}^2}{2\mu k_B T} & \tilde{E} &= \frac{P_c^2}{2Mk_B T} \\
p &= \sqrt{2\mu k_B T \tilde{\epsilon}} & P_c &= \sqrt{2Mk_B T \tilde{E}} \\
dpp^2 &= \frac{\sqrt{\tilde{\epsilon}}}{2} (2\mu k_B T)^{3/2} d\tilde{\epsilon} & dP_c P_c^2 &= \frac{\sqrt{\tilde{E}}}{2} (2Mk_B T)^{3/2} d\tilde{E}
\end{aligned}$$

Plugging these expressions into Eq.A.10 and rearranging

$$\begin{aligned}
\tilde{f}_{\mathbf{r}}(\mathbf{p}) &= A^2 \frac{e^{-\tilde{\epsilon}}}{(2\pi\mu k_B T)^{3/2}} \int_0^1 dX \frac{2}{\sqrt{\pi}} \int_0^\infty d\tilde{E} e^{-\tilde{E}} \sqrt{\tilde{E}} \\
&\quad \times \Theta \left( \eta(\mathbf{r}) - \frac{\tilde{E}}{2} - \frac{\tilde{\epsilon}}{2} - X\sqrt{\tilde{E}\tilde{\epsilon}} \right) \quad (\text{A.11})
\end{aligned}$$

would like to turn this distribution into a relative energy distribution. Collisions are isotropic so we can use the relation

$$\begin{aligned}
\int dpp^2 \int d\Omega_p \tilde{f}_{\mathbf{r}}(\mathbf{p}) &= \int d\tilde{\epsilon} \hat{f}_{\mathbf{r}}(\tilde{\epsilon}) = 1 \\
\Rightarrow 4\pi p^2 \tilde{f}_{\mathbf{r}}(\mathbf{p}) dp &= \hat{f}_{\mathbf{r}}(\tilde{\epsilon}) d\tilde{\epsilon} \quad (\text{A.12})
\end{aligned}$$

using  $dpp^2$  given above we then write

$$\hat{f}_{\mathbf{r}}(\tilde{\epsilon}) = A^2 \sqrt{\tilde{\epsilon}} e^{-\tilde{\epsilon}} \frac{2}{\sqrt{\pi}} \int_0^1 dX \frac{2}{\sqrt{\pi}} \int_0^\infty d\tilde{E} e^{-\tilde{E}} \sqrt{\tilde{E}} \Theta \left( \eta(\mathbf{r}) - \frac{\tilde{E}}{2} - \frac{\tilde{\epsilon}}{2} - X\sqrt{\tilde{E}\tilde{\epsilon}} \right) \quad (\text{A.13})$$

We can now choose the normalization constant  $A^2$  using

$$\int_0^{2\eta(\mathbf{r})} d\tilde{\epsilon} \hat{f}_{\mathbf{r}}(\tilde{\epsilon}) = 1$$

where we have used an energy cutoff of  $2\eta(\mathbf{r})$  since either particle may have an energy in the range  $[0 \rightarrow \eta(\mathbf{r})]$ . With the normalization, the complete expression for  $\hat{f}_{\mathbf{r}}(\tilde{\epsilon})$  is then

$$\hat{f}_{\mathbf{r}}(\tilde{\epsilon}) = \frac{2}{\sqrt{\pi}} \sqrt{\tilde{\epsilon}} e^{-\tilde{\epsilon}} \hat{\mathcal{G}}(\eta_{\mathbf{r}}, \tilde{\epsilon}) \quad (\text{A.14})$$

where all the effects of the truncation have been moved to  $\hat{\mathcal{G}}$ , given by

$$\hat{\mathcal{G}}(\eta_{\mathbf{r}}, \tilde{\epsilon}) = \frac{\int_0^1 dX \frac{2}{\sqrt{\pi}} \int_0^\infty d\tilde{E} e^{-\tilde{E}} \sqrt{\tilde{E}} \Theta \left( \eta(\mathbf{r}) - \frac{\tilde{E}}{2} - \frac{\tilde{\epsilon}}{2} - X \sqrt{\tilde{E}\tilde{\epsilon}} \right)}{\int_0^{2\eta(\mathbf{r})} d\tilde{\epsilon} \frac{2}{\sqrt{\pi}} \sqrt{\tilde{\epsilon}} e^{-\tilde{\epsilon}} \int_0^1 dX \frac{2}{\sqrt{\pi}} \int_0^\infty d\tilde{E} e^{-\tilde{E}} \sqrt{\tilde{E}} \Theta \left( \eta(\mathbf{r}) - \frac{\tilde{E}}{2} - \frac{\tilde{\epsilon}}{2} - X \sqrt{\tilde{E}\tilde{\epsilon}} \right)}$$

we can check the limiting behavior of this equation since we expect when

$$\lim_{\eta \rightarrow \infty} \hat{\mathcal{G}}(\eta_{\mathbf{r}}, \tilde{\epsilon}) = 1$$

. Indeed, remembering that

$$\int_0^\infty dx \sqrt{x} e^{-x} = \frac{\sqrt{\pi}}{2}$$

then this requirement is fulfilled.

## Appendix B

### Imagefit analysis routine

General procedure, should probably suggest moving to Github and warn about software migration breaking older versions of code.

Currently everything is working in 2015b? Can it work in a newer version?

#### B.1 Background removal

Covers *imagefit\_Background\_PCA*

Would like to remove noisy fringes to fit more easily

##### B.1.1 Principal component analysis

be sure to discuss tradeoffs such as matrix size, basis size, and number of images

The Anderson and Cornell groups have adapted two statistical techniques used in astronomical data processing to the analysis of images of ultracold atom gases. Image analysis is necessary for obtaining quantitative information about the behavior of an ultracold gas under different experimental conditions. Until now, the preferred method has been to find a shape (such as a Gaussian) that looks like the results and write an image-fitting routine to probe a series of photographs. The drawback is that information extracted this way will be biased by the model chosen.

The two groups recently employed model-free analysis techniques to extract re-

sults from interferometry experiments on Bose-Einstein condensates (BECs). The statistical processing techniques were able to rapidly pinpoint correlations in large image sets, helping the researchers uncover unbiased experimental results. Using the techniques, graduate student Steve Segal, former graduate student Quentin Diot, Fellows Eric Cornell and Dana Anderson, and a colleague from Worcester Polytechnic Institute calibrated their interferometer, identified and mitigated some noise sources, and unearthed signal information partially buried in the noise generated during the BEC experiment. By looking for correlations and relationships between pixels in a series of images (a), the researchers were able to clearly "see" changes in the overall number of atoms (d), changes in the vertical positions of three peaks in a momentum distribution (c), and changes in the fraction of atoms in the central peak (b), which was the primary experimental signal.

The results were obtained with principal component analysis (PCA) and independent component analysis (ICA). PCA identified simple pixel correlations and looked for areas of maximum variance. Such areas provided an idea about where to look for changes in size, structure, or position of the ultracold atom cloud. The PCA analysis was sufficient for calibrating the interferometer and debugging the experiment. It also provided an idea of size changes in one or more features of the experiment. However, the PCA analysis alone wasn't perfect. ICA was required to extract the most important information about the experiment, i.e., the fraction of the total number of atoms in one of three clouds. Using preprocessed data from a PCA analysis, ICA was able to test whether the values of neighboring pixels were statistically independent from one another. With this information, ICA could then determine relative differences in the experimental signal and separate its individual features.

Segal thinks physicists in the ultracold atomic physics field will be intrigued by the potential of using the PCA and ICA techniques to probe their experimental images. There are only two caveats: The techniques require 10–100 images, and their application to ultracold atom-cloud experiments is still in its infancy. - Julie Phillips

### B.1.2 Comparison of PCA implementations

## B.2 Fitting the spatial distribution

Covers *imagefit\_NumDistFit*

## B.3 Evaluating fit parameters

Covers *imagefit\_ParamEval*

### B.3.1 Writing new plug-ins

### B.3.2 Suggested improvement

The primary upgrade to this software would be an overhaul of the internal state variables. A complete rewrite of the `imagefit` routine was one of the first projects undertaken during this PhD, during such a time as the meanings of precise variable names was not well known. Unfortunately, this has led to vestigial variable names such as "imagevco\_atom" for the primary independent variable used for scan analysis. Additionally, while the plug-in nature of the `ParamEval` routine has proven to be incredibly useful for the development flexible experiment specific analysis routines, we have found the heavy reliance on structs [ref](#) for variable passing and storage to be prohibitively restrictive.

The imagefit routine was primarily written with the streamlining of first order image analysis as the design goal. We consider this to be the extraction of atom number and temperature versus a single scanned variable. However, the natural extension is to look for variations across higher dimensions, or what we deem second order analysis. Here is where structs are not useful since they tend to force a hierarchical variable relationship which complicates analysis where the variable of interest was not the explicit independent variable scanned. With this in mind, we highly recommend any future improvements to this process focus on the usage of tables [ref](#) for storing and passing data. These data structures consider all data at the same level and are widely used in data science. Finally, we note that this issue is not a new problem on the Neutral apparatus. But recent advancements to the experimental stability and control software have ballooned the amount of data we have been generating which is noticeably exacerbating this concern.

One of the key lessons I've learned is to be flexible when starting new projects. You don't know where the data is going to take you or what may come up as an interesting/useful perspective for developing and questioning hypotheses. Tables are a scheme that I've have realized are very common in data management and analysis. The popular python package Pandas, uses datatables exclusively and was the impetus for my interest in the data structure. Tables also make it easy to export and share your data via spreadsheet applications (assuming you use simple datatypes within each cell). Lastly, this is a warning that no matter what you end up doing with the data, you will inevitably have to spend time organizing and reorganizing it at times. With less structure imposed on the data you'll be able to manipulate things more easily and (most importantly to Tom) more quickly.

## Appendix C

### **neuKLEIN - Killian lab experimental interface**

During my time working on the neutral apparatus, Joe Whalen began a rewrite of the Labview based experimental control software which had grown organically through the first decade of the neutral apparatus' existence. Following this refactor, the user interface was also revamped to help reduce human errors and improve overall data collection efficiency. This chapter will outline the major components of the neuKLEIN software package and how this system integrates with the hardware control system and the software analysis algorithm.

#### **C.1 Labview code**

Need to have description of state machine.

Need to

Use of references for updating front panel

Need to get references for LV documentation for this stuff

Discuss triggered waveform oddity (retriggerable setup)

#### **C.2 FPGA code**

The versatility of FPGA led us to want to simple system for setting static voltages and switching them at will. We built such a system using an National Instrument

FPGA device (Xlinix something). The hardware details and circuitry are available in [appendix blah](#). This section will focus on the software side of programming and using the FPGA system.

This was originally a project started by a summer student named Weixuan Li in summer 2018. He did a good job.

Talk about special programs (the custom operation builder specifically)  
 Cycle time is  $50 \mu\text{s}$ . Uses a cRIO real time controller for managing the control layer and the FPGA executes the custom logic. Example of the flexibility this provides is the dynamic control of the blue frequency. Multiple voltage outputs define the different frequencies of the blue light. Originally achieved this same functionality by using a series of digitally controlled analog switches, but can recreate this in software. Additionally, the BOP has a weird behavior when you attempt to jump its frequency over large ranges. To alleviate this, we can add in logic that will ramp the set point if the change is bigger than some amount. This flexibility was not easily accessible before. Details on the interface boards and program software is available somewhere.

### C.3 Possible improvements

There are a number of possible improvements which I have realized through the usage of the systems. Here I'll detail the ones that I believe are the most straightforward and/or those things that have frustrated me most.

#### **Asynchronous state machine**

While conceptually simple, the synchronous state machine which neuKLEIN is based on has one significant drawback. The linear nature of this design pattern leads to

two drawbacks in particular. First, changes to the state variables are only read at the start of the while loop. Here, state variables refers to the value of all variables in the scope of neuKLEIN and should not be confused with the specific state flag enum for determining execution. While static state variable are desirable for the experimental parameters, neuKLEIN currently makes no distinction between program control variables and experimental parameters. An example where improved state handling would be useful is in the behavior of the "shutdown" button. Currently, when in the primary while loop and the shutdown flag triggered, this action does not exit the primary loop at the conclusion of the current cycle as might be expected. Instead, neuKLEIN continues execution for a number of cycles before exiting.

The second drawback is that sub-processes which take a long time block the overall progression of the program. This is most noticeable when program execution hangs due to an attempt to fit a cloud image when there is insufficient data to fit (or worse no atoms).

A straightforward solution would be to migrate to an asynchronous state machine. However, this is a fairly significant refactor and the above challenges have mostly presented inconveniences rather than practical limitations.

## **Network shared variables**

### **Standardize triggerable waveform VI**

### **Coupled scan parameters**

### **Update PicoScope VIs**

## Appendix D

### Experimental control computer hardware

”Lorem ipsum dolor sit amet, consectetur adipiscing elit, sed do eiusmod tempor incididunt ut labore et dolore magna aliqua. Ut enim ad minim veniam, quis nostrud exercitation ullamco laboris nisi ut aliquip ex ea commodo consequat. Duis aute irure dolor in reprehenderit in voluptate velit esse cillum dolore eu fugiat nulla pariatur. Excepteur sint occaecat cupidatat non proident, sunt in culpa qui officia deserunt mollit anim id est laborum.”

#### D.1 Overview of status

#### D.2 Migration to a new machine

Talk about expansion bin

#### D.3 PixelFly camera system

What is the datasheet? Where are the drivers? What OS is it compatible with?

Double shot system, the difference in camera exposure times, how we mitigate that difference and what errors might result because of this timing.

Get the double shot timing diagram.

Somewhere I need to talk about the discretization (in time) of the lattice card as it is not obvious

## Appendix E

### Neutral apparatus

”Lorem ipsum dolor sit amet, consectetur adipiscing elit, sed do eiusmod tempor incididunt ut labore et dolore magna aliqua. Ut enim ad minim veniam, quis nostrud exercitation ullamco laboris nisi ut aliquip ex ea commodo consequat. Duis aute irure dolor in reprehenderit in voluptate velit esse cillum dolore eu fugiat nulla pariatur. Excepteur sint occaecat cupidatat non proident, sunt in culpa qui officia deserunt mollit anim id est laborum.”

#### E.1 Opening vacuum - data and process

#### E.2 Nozzle redesign - neuNozzle 2018

We hypothesized that lack of a heat shield led to uneven distribution of the thermal energy throughout the oven. Therefore, fastening of the heat shield to the base flange was the primary goal of the redesign undertaken in late 2017 and further details can be found in App. E.

we did not install the gate valve before re-establishing vacuum.

The hope in doing this upgrade was to provide a better method for replacing the end cap window which the atom source directly points at.

With that fun aside, we order an extra window and the gate valve to replicate the system put in place on the Rydberg apparatus so that future needs to replace the

window could be accomplished by simply back filling the chamber with dry nitrogen or argon, closing the gate valve and simply replacing it quickly without the need to expose the main chamber body to direct atmospheric gas.

The second improvement that we attempted was to redesign the nozzle to include a heat shield. A CAD image is shown in figure. Unfortunately, due to the high tolerances of the base flange and surrounding enclosure the machining required for this custom piece was deemed prohibitively expensive. A prototype was designed following the machine drawings available in App [someplace](#) but was abandoned due to a bend that developed in the tubing which holds the fire rod.

However, the largest constraint was due to the flange size of 2 3/8" as the basis for the design. This provides very tight confinement and w

What is the model number for the firerod? What were the materials that were used?

Data about firerod I had some trouble finding the part number associated with the firerod in the Neutral chamber but luckily I found one of the broken firerods still had its part number on it, SK7J-2953. Below is the info from Valin Corporation who seems to be the local reseller of Watlow products.

SPECIAL DIAMTER HT FIREROD T/C CENTER CORE LOC "A" TYPE "J"  
120 Volts 240 watts 0.580 +/- 0.004 Diameter firerod 7.5" length 12" of MGT  
leads 12" of TC leads 6 13/32" of no heat section at lead end. Crimped of leads  
construction.

Don't forget the plan was to incorporate a design feature from Plasma's nozzle redesign which addressed the fragility of the feedthrough connection to the heater wire. This was a problem because the heater wire connection is very thin and we

used large clamp type connection for them before which was problematic due to the fragility of the heater wire and the necessity that the bulky clamp couldn't touch the nozzle body (as this would short the heater connection). The new connection would allow us to use a smaller crimp to the heater wire, use the rigidity of the feedthrough itself, and use alumina screws to insulate the connection from the nozzle body.

Other reason for redesign was to attach the heat shield directly to the flange.

All the pieces were ordered and built but a mistake on turning the nozzle body meant that we couldn't use the nozzle we built. As of April 2019, this construction is located in somewhere

## Appendix F

### Gaussian Beam Programs

”Lorem ipsum dolor sit amet, consectetur adipiscing elit, sed do eiusmod tempor incididunt ut labore et dolore magna aliqua. Ut enim ad minim veniam, quis nostrud exercitation ullamco laboris nisi ut aliquip ex ea commodo consequat. Duis aute irure dolor in reprehenderit in voluptate velit esse cillum dolore eu fugiat nulla pariatur. Excepteur sint occaecat cupidatat non proident, sunt in culpa qui officia deserunt mollit anim id est laborum.”

#### F.1 Simple beam propagation

Talk about normal ABCD matrix formalism and then extend to the M2 idea

#### F.2 Laser beam profile fitting

##### F.2.1 Data taking template

Give the data taking template here

Include a figure with all the distance measured off

Pictures of the profiler head and the important distance (I think this is in the manual on the drobo)

## Appendix G

### Concise derivation of effective volumes

The following derivation is meant to serve as a quick reference for finding the analytic form of the effective volumes for ultracold gases held in a optical dipole trap. This section follows the arguements presented by Mi's paper which considers and numerically evalutes the general case of power-law potentials and the corresponding ddensity distribution at arbitrary temperatures less than the trap depth.

If instead one restricts to the experimentally reasonable conditions of high- $\eta$  (recall  $\eta$  is the ratio of trap depth to sample temperature,  $\eta = \epsilon_t/k_B T$ ) and harmonic trapping potentials, then a useful analytic expression can be found for the effective volumes of the gas.

Following eff volume derivation from first year

## Appendix H

### Repair of 922 Lynx master

In early February 2017, the piezo actuator on the 922 shorted. I suspect it just got old or the Sacher driver killed it but whatever the cause we ordered a new one from Sacher (also ordered a spare which I put in the blue and beige cabinet in the Neutral lab). As of March 1st 2017 it seems that the 922 master is back up and running without issue.

The images below are how I changed the PZT. There was originally some more epoxy around the brass cup but Tom chipped that away so we could unscrew the cup from the flexure arm, this is what holds the PZT. The only other tricky part is removing the back circuit board to get access to the spring terminals that face down. Once you get access here replacing the PZT is fairly trivial.

I also include, at the end, a letter we received from Sacher once they sent us the new PZTs.

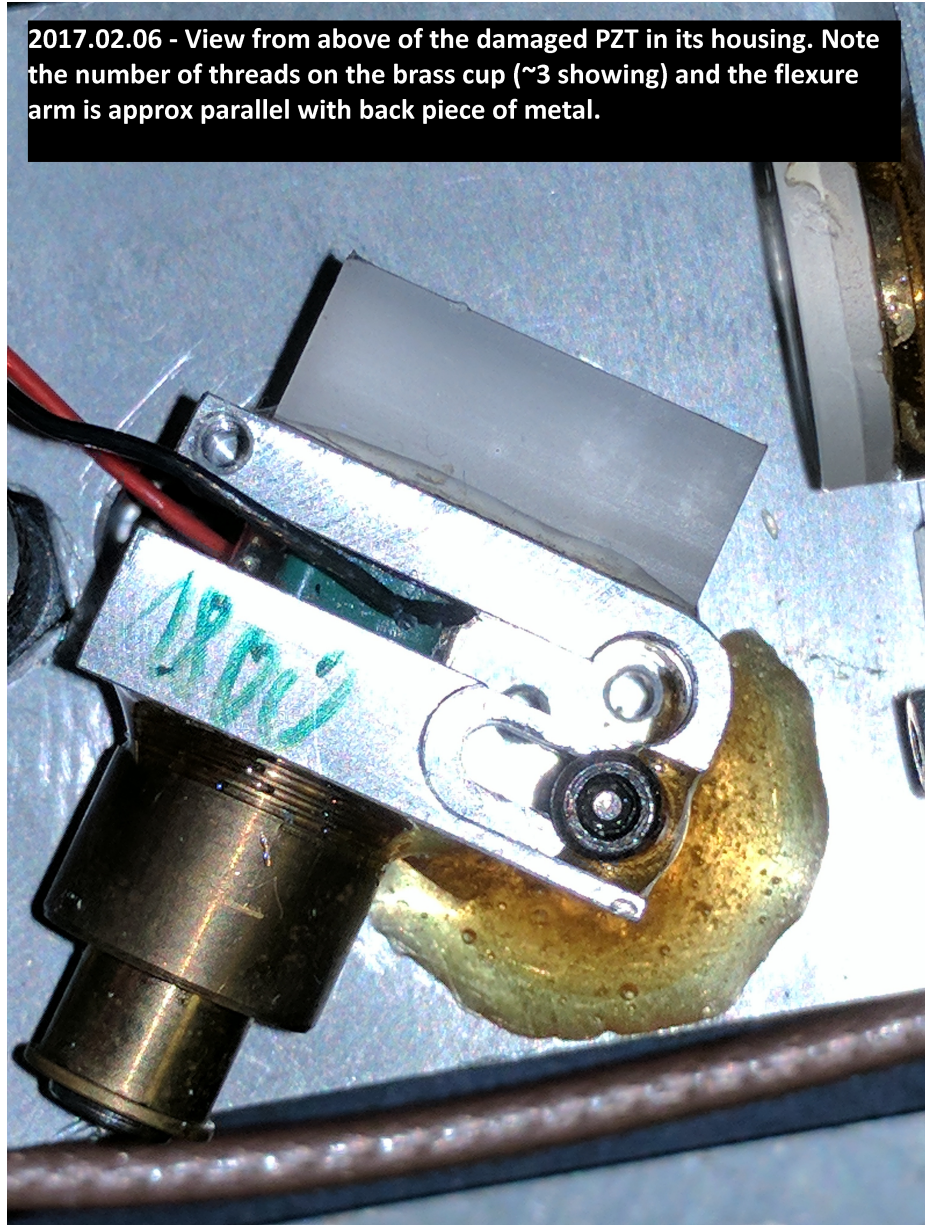


Figure H.1 : Damaged 922 master PZT

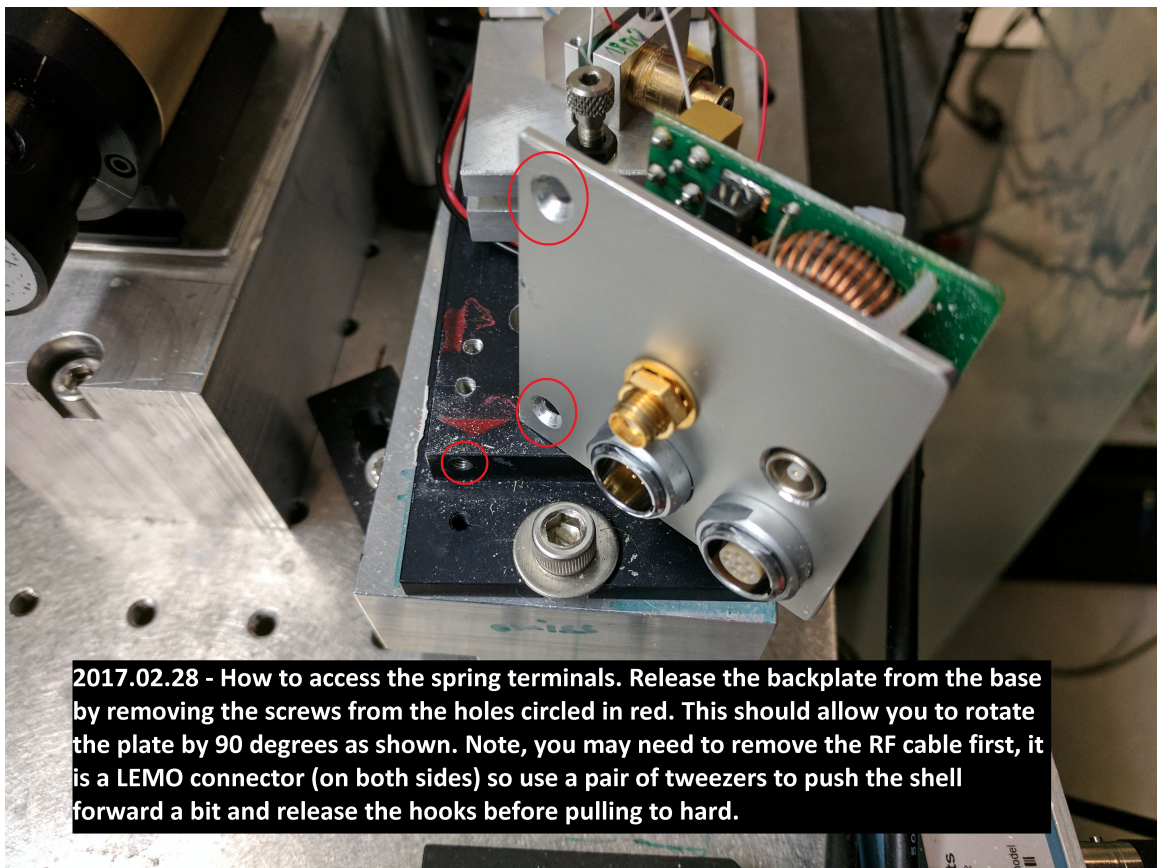
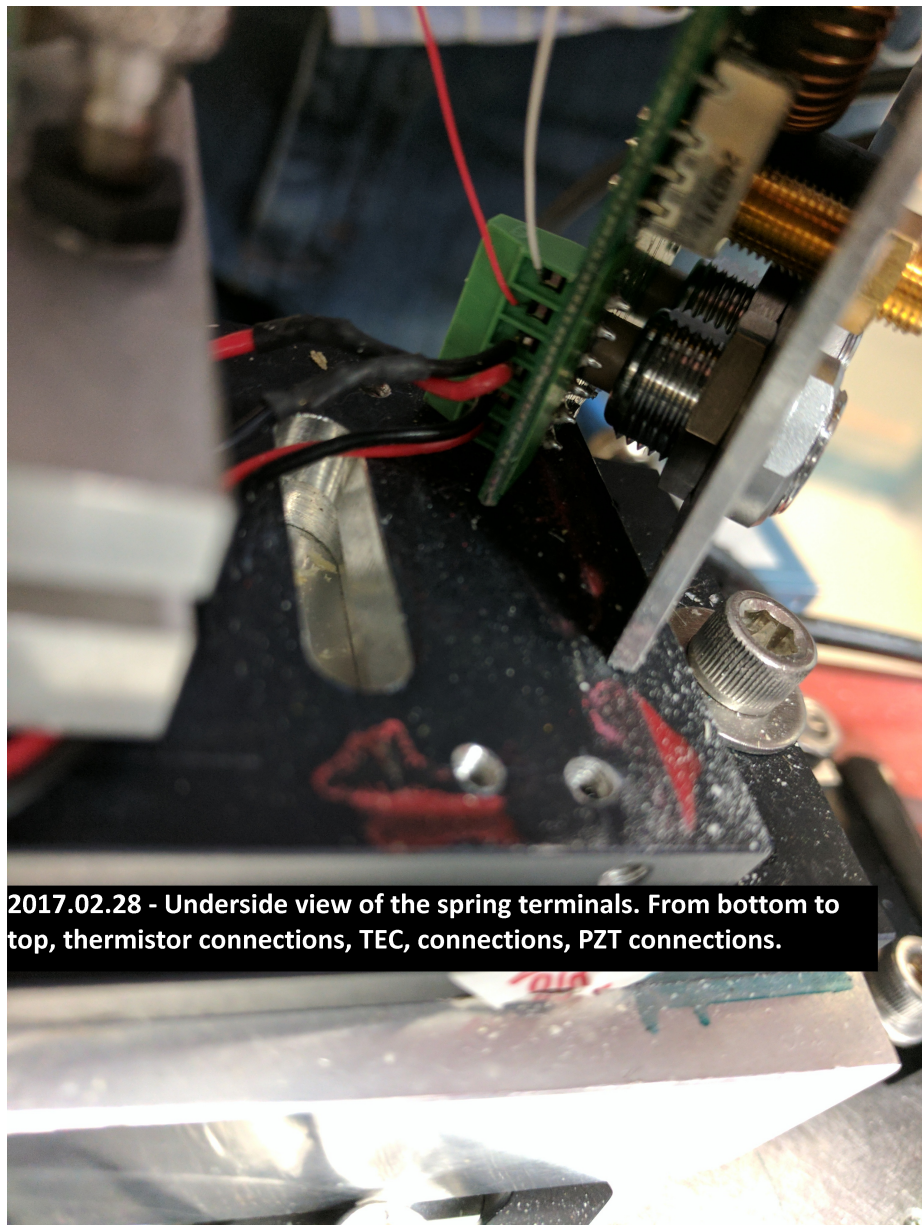


Figure H.2 : Removing the circuit board of the 922 master



2017.02.28 - Underside view of the spring terminals. From bottom to top, thermistor connections, TEC, connections, PZT connections.

Figure H.3 : Reference image of the spring terminal connections

2017.02.28 - Top view of the newly installed PZT. Unable to get back to three threads showing on the brass cup. Even having one thread in the flexure part caused a noticeable angle between the arm and the back piece of metal. Was able to fix with the internal screw no the brass cup.

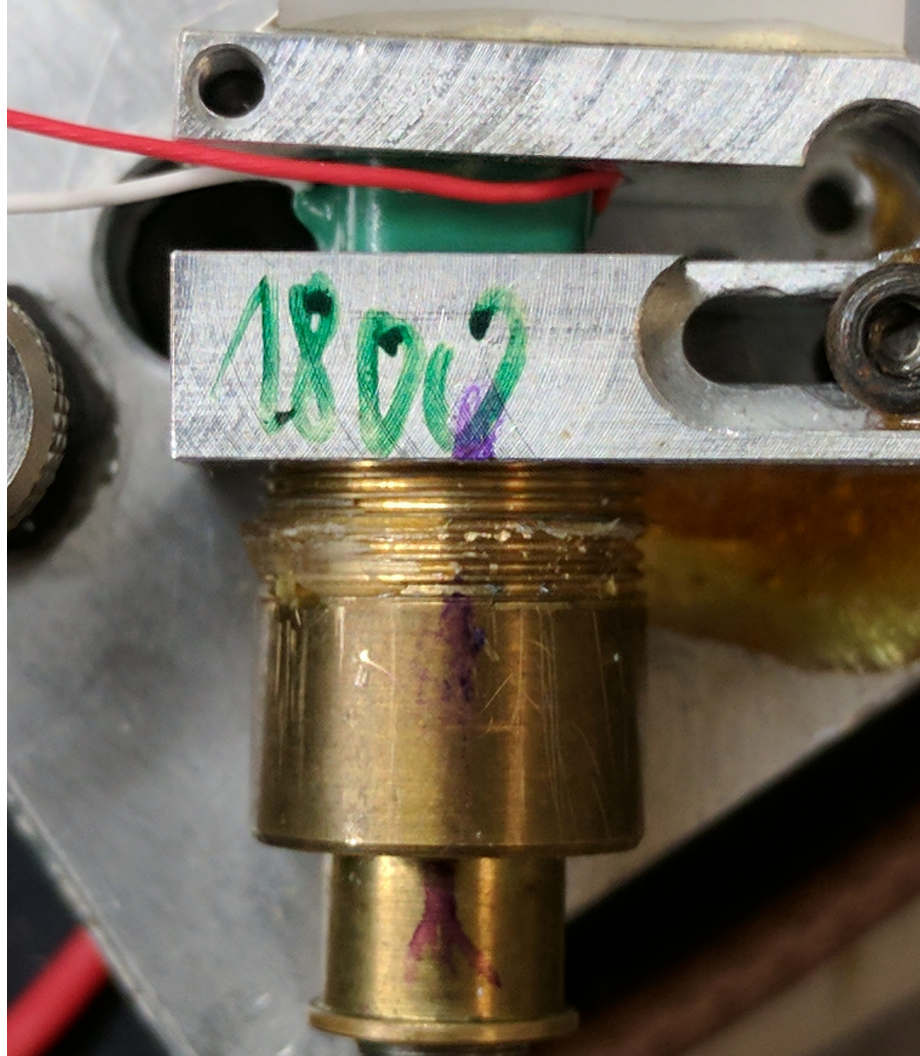


Figure H.4 : Newly installed 922 master PZT

## Exchanging the Piezo Actuator (PZT)

Purpose of this document is to support users of Sacher Lasertechnik Littrow Laser System with the exchange of the piezo actuator (PZT). Please note that there are security risks for the technician who performs the work as well as for the laser head accompanied with the exchange of the PZT.

- You are working with a Class IIIB laser system. Make sure to wear protective eyewear.
- The PZT is operated with high voltage up to 150V. Make sure to disconnect the laser system from the wall plug power supply prior to any action.
- Consult your security officer on all required security precautions prior to starting the scheduled exchange work.
- Laser Diodes are electrostatic discharge (ESD) sensitive devices. Make sure to take care on ESD protection, e.g. grounded wrist bands.
- The grating attached on the other side of the holder is a sensitive component which may be damaged by a single finger print.
- Avoid electrical short circuits of the piezo cables with the body of the laser head. A single electrical discharge may damage the laser diode.
- Avoid damages of PZT cables by holder's edges.

The customer should keep in mind that she/he are doing the exchange work at their own risk. Sacher Lasertechnik will not be liable in case of any damage to the laser system or any injury to the operating technician.

The holder is composed of diffraction grating, piezo actuator, brass-screw and coarse tuning screw (Figure 1). PZT shall be exchanged in the following procedure:

1. Unscrew the brass-screw (the yellow one) from the holder (Figure 2). You will find the PZT attached with glue within the holder.
2. Detach carefully the PZT from the holder (for example, by slightly waggling PZT from each side).
3. Remove the PZT from the holder (Figure 3).

For exchanging the PZT proceeds in the reverse order.

4. Put the new PZT and attach the front side of the PZT on the holder (using glue).  
The back side of the PZT has a small metal-plate attached to it to avoid damage caused by the coarse tuning screw.
5. Screw the brass-screw in.
6. Turn the coarse tuning screw a little bit to confirm the contact of the screw with the PZT.



Figure 1



Figure 2



Figure 3

Document: C:\Dokumente und Einstellungen\icksoon.park\SLT\_Arbeits\Tech-Dokus\Exchanging Piezo.doc  
Note: Specification are subject to change without further notice



# Appendix I

## Doppler Free Spectroscopy

Below we will quickly outline the derivation of the resonance condition when performing Doppler free spectroscopy. This method is commonly used when stabilizing a laser frequency to an atomic transition. In short, counter-propagating laser beams in a pump-probe configuration will can "burn a hole" through an atomic sample and lead to a Lamb dip. [refs](#)

Below we'll derive the resonance condition for when the two lasers will be resonant with the same velocity class. When used in conjunction with frequency modulation, an error signal useful for laser locking can be derived. Therefore, the resonance condition effectively defines the relationship of the laser lock point and any potential offsets.

The first section will cover the case where the two lasers share the same frequency as well as when one beam has an additional offset. Finally, for the case of the 461 nm sat. abs., we'll consider the resonance condition when using a Zeeman tunable transition.

### I.1 Common setup

Consider two laser beam at frequencies  $f_1 \& f_2 = f_1 + \delta$ , driving a 2-level atom with  $v \neq 0$  and transition energy  $E_0 = hf_0$ . Then the resonance condition for  $f_1 \& f_2$  is

given by

$$f_1 = f_0 + \mathbf{k}_1 \cdot \mathbf{v}_1 \quad f_2 = f_0 + \mathbf{k}_2 \cdot \mathbf{v}_2 \quad (\text{I.1})$$

Assume the beams are counter propagating such that  $k_1 = -k_2 = k$ , then the resonance condition becomes

$$f_1 = f_0 + kv_1 \quad f_2 = f_0 - kv_2 \quad (\text{I.2})$$

Finally, consider the case when the 2 beams interact with the same velocity class of atoms  $v_1 = v_2 = v$  then

$$f_1 = f_0 + kv \quad f_2 = f_0 - kv \quad (\text{I.3})$$

Rearranging these equation

$$\begin{aligned} kv &= f_1 - f_0 & kv &= f_0 - f_2 \\ &&&\\ &= f_0 - f_1 - \delta \end{aligned} \quad (\text{I.4})$$

Finally, combining these equations we find

$$\begin{aligned} f_1 - f_0 &= f_0 - f_1 - \delta \\ 2f_1 &= 2f_0 - \delta \\ f_1 &= f_0 - \frac{\delta}{2} \end{aligned} \quad (\text{I.5})$$

Therefore, if we use a single laser where  $f_{\text{laser}} = f_1$  and lock the frequency such that  $f_1 \& f_2$  are resonant with the same velocity class of atoms then the laser frequency will be given by  $f_{\text{laser}} = f_0 - \delta/2$ .

We can also see what would happen if  $f_1 = f_2 = f + \delta$ . Then instead of locking to  $f_0 - \delta/2$  the resonance condition would become  $f_{\text{laser}} = f_0 - \delta$ .

## I.2 Addition of Zeeman shift

Expanding on the previous case we now consider the effects of adding a magnetic field. This addition will let us controllably tune the resonance condition and thereby change the frequency of the locked laser. As before we consider two laser beams,  $f_1$  &  $f_2$  where  $f_2 = f_1 + \delta$ , and take the beams as counter propagating and interacting with the same velocity class. With the additional Zeeman shift, the previous resonance condition becomes

$$\begin{aligned} f_1 &= f_0 + \mathbf{k}_1 \cdot \mathbf{v}_1 + g_j \mu_B m_1 B = f_0 + kv + g_j \mu_B m_1 B \\ f_2 &= f_0 + \mathbf{k}_2 \cdot \mathbf{v}_2 + g_j \mu_B m_2 B = f_0 - kv + g_j \mu_B m_2 B \end{aligned} \quad (\text{I.6})$$

where  $g_j$  is the Lande g-factor,  $\mu_B$  is the Bohr magneton,  $m_i$  is a specified magnetic sub-level, and  $B$  is the magnetic field. Proceeding as we did previously, with the additional assumption that  $m_1 = m_2 = m$ , then we find

$$\begin{aligned} f_1 - f_0 - g_j \mu_B m B &= f_0 - f_1 - \delta + g_j \mu_B m B \\ 2f_1 &= 2f_0 - \delta + 2g_j \mu_B m B \\ f_1 &= f_0 - \frac{\delta}{2} + g_j \mu_B m B \end{aligned} \quad (\text{I.7})$$

As before, the resonant frequency depends on the constant offset  $\delta$  but now applying a controllable B-field we can tune the frequency  $f_1$ . Therefore, once we include feedback to maintain  $f_{\text{laser}} = f_1$  then the tunability gives a know for dynamically varying the laser frequency.

Note that the above case has only been considered for a simple two-level system,  $m_1 = m_2 = m$ . Physical systems can simulate this case if the light polarization is well determined. However, non-pure polarization can result in coupling to additional Zeeman sub-levels and may lead to "crossover" resonances.

## Appendix J

### Bose-Hubbard model

When bosons are confined to the lowest energy band of a lattice, a particularly simple model known as the Bose-Hubbard Hamiltonian is used to describe the lattice system [? ].

$$H_{BH} = -J \sum_{\langle i,j \rangle} (\hat{b}_i^\dagger \hat{b}_j + \hat{b}_j^\dagger \hat{b}_i) + \frac{U}{2} \sum_i \hat{n}_i (\hat{n}_i - 1) \quad (\text{J.1})$$

Where  $\langle i, j \rangle$  denotes a sum over nearest-neighbors. This model is the simplest example of a non-trivial interacting many-body system for dynamics in a lattice. The first term describes hopping of bosons from site to site at a rate  $J/\hbar$ . The second term describes an interaction energy which is related to the s-wave contact interaction term,  $g = 4\pi\hbar^2 a_s/m$ , where  $a_s$ , is the s-wave scattering length of the particles.  $J$  and  $U$  can be calculated directly using the Wannier functions of Eq. 2.11 and are given by [38]

$$\begin{aligned} J_{ij} &= - \int d^3x w_0(x - x_i) \left( \frac{p^2}{2m} + V(x) \right) w_0(x - x_j) \\ U &= \frac{4\pi\hbar^2 a_s}{m} \int d^3x |w_0(x - x_i)|^4 \end{aligned} \quad (\text{J.2})$$

Using Eq. J.2 we have calculated the expected tunneling rates and interaction energies for atomic strontium and plot the results in Fig. J for homonuclear samples of strontium as a function of lattice depth. This single band calculation is valid under the assumption that the interaction energy of a site is smaller than the bandgap between the  $n = 0$  and 1 bands, namely  $UN \lesssim \hbar\omega_{ho}$  where  $N$  is the mean number of

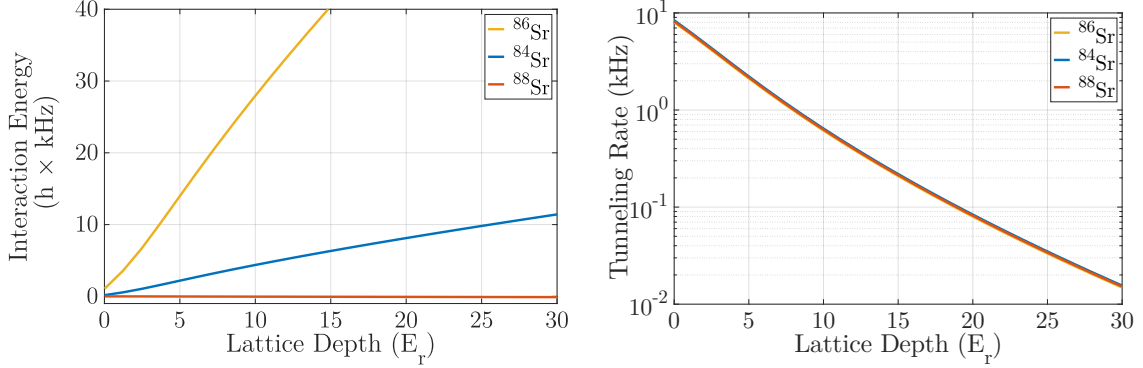


Figure J.1 : Calculated interaction energies and tunneling rates for each isotope of strontium

The interaction energy shows a large variation because of its dependence on the s-wave scattering length. However, the tunneling rate is approximately the same for all isotopes since the change in mass is negligible between isotopes.

particles per site and  $\hbar\omega_{ho}$  is the approximate energy spacing between bands [66].

Alternatively, Eq. J.2 can be simplified through considering appropriate limits to the Bose-Hubbard model. In the limit that  $U \rightarrow 0$ , the Bose-Hubbard model becomes exactly solvable and the energy of the  $n = 0$  band is given by  $E_q^{(0)} = -2J \cos(qa)$  [38]. Thus, the tunneling rate,  $J$ , can be related to the bandwidth of the lowest band as expressed in Eq. J.3. Under a separate limit,  $V_{lat} \rightarrow \infty$ , then the tunneling rate goes to zero and the localized wavefunctions can be approximated by a Gaussian wavefunction which yields the form for the on-site interaction  $U$  given in Eq. J.3 [66].

$$\begin{aligned} J &= \frac{E_{q=\hbar k_L} - E_{q=0}}{4} \\ U &= \frac{\hbar a_s}{\sqrt{2\pi}} \frac{\bar{\omega}_{ho}}{\bar{a}_{ho}} \end{aligned} \tag{J.3}$$

Here  $\bar{a}_{ho}$  and  $\bar{\omega}_{ho}$  are the geometric means of the one-dimensional harmonic oscillator length and frequency given previously.

Competition between  $J$  and  $U$  results in a phase transition known as the superfluid - Mott insulator transition [24, 28]. When  $J/U \gg 1$  atoms are free to delocalize over the lattice and the many-body ground state is a superfluid. In the opposite limit that  $J/U \ll 1$ , particle fluctuations between sites are no longer energetically accessible and the system transitions into an interaction induced insulating state known as a Mott insulator. This state is characterized by fixed particle number per site and in a 3D cubic lattice near unit filling, this phase transition occurs at  $J/U \approx 35$  which, for  ${}^{84}\text{Sr}$ , corresponds to a lattice depth of  $V_{lat} \approx 13E_r$  [24].

## Appendix K

### Shallow angle Bragg setup

”Lorem ipsum dolor sit amet, consectetur adipiscing elit, sed do eiusmod tempor incididunt ut labore et dolore magna aliqua. Ut enim ad minim veniam, quis nostrud exercitation ullamco laboris nisi ut aliquip ex ea commodo consequat. Duis aute irure dolor in reprehenderit in voluptate velit esse cillum dolore eu fugiat nulla pariatur. Excepteur sint occaecat cupidatat non proident, sunt in culpa qui officia deserunt mollit anim id est laborum.”